UNIVERSIDADE D
COIMBRA

Md Nazmul Azim Beg

DETAILED UNCERTAINTY ANALYSIS OF URBAN HYDRAULIC STRUCTURES IN LARGE CATCHMENTS

PhD Thesis in Civil Engineering, with specialization in Hydraulics, Water Resources and Environment, supervised by Professor Maria Rita Lacerda Morgado Farnandes de Carvalho and Professor Jorge Eduardo Teixeira Leandro and submitted to the Faculty of Sciences and Technology, University of Coimbra.

September of 2018

Faculty of Science and Technology
University of Coimbra

Detailed uncertainty analysis of urban hydraulic structures in large catchments

Md Nazmul Azim Beg

PhD thesis in Civil Engineering, with specialization in Hydraulics, Water Resources and Environment, supervised by Professor Maria Rita Lacerda Morgado Fernandes de Carvalho Mesquita David and Professor Jorge Eduardo Teixeira Leandro and submitted to the Faculty of Sciences and Technology, University of Coimbra.

Coimbra, September of 2018

UNIVERSIDADE D
COIMBRA

To my parents…

Preamble

This work was carried out within the framework of the Marie Skłodowska Curie Initial Training Network QUICS. The QUICS project has received funding from the European Union's Seventh Framework Programme for research, technological development and demonstration under grant agreement no 607000.

An acknowledgement is owed to the following institutions that provided logistical and technical supports during this thesis:

- University of Coimbra
- MARE - Marine and Environmental Sciences Centre
- The University of Sheffield
- Technical University of Munich
- CTGA, Portugal

Financial Support:

Host Institutions:

Co-host institutions:

All CFD modelling part was accomplished by using the Open Source CFD toolbox OpenFOAM®. OpenFOAM® is a registered trademark owned by OpenCFD® Limited (www.openfoam.com). OpenFOAM® is produced by OpenCFD® Limited, freely available and opensource, licensed under the GNU General Public License.

All the CFD modelling results showed in the thesis were performed on the Centaurus and the Navigator Clusters of the Laboratory for Advanced Computing of University of Coimbra, Portugal.

The hydrological model results showed in this work was completed by using LARSIM (Large Area Runoff Simulation Model). The model is a licenced product and licenced for the Technical University of Munich, Germany.

Acknowledgements

I would like to express my deepest gratitude to my Supervisor Prof. Rita Fernandes de Carvalho for the motivation and inspiration she provided me throughout the PhD. I am very much grateful to my co-supervisor Prof. Jorge Leandro for the encouragement and support he has provided during my Thesis. Special thanks to Prof. Simon Tait and Prof. Wernher Brevis for their precious time and invaluable comments in different parts of my research project.

I would also like to give a heartiest thanks to all my colleagues at the University of Coimbra for hosting during my PhD. A special appreciation to Pedro Lopes and his family for the support he gave to start a new life in Coimbra, Joao Marques and Ricardo Martins for their support in needs and helping me to set a foundation at the beginning of my research. Thank you Mousinho, Babar, Rafael, Fabiana and Lincoln for sharing the PhD Journey together.

Cheers to all my QUICS colleagues for spending a memorable time together. Thanks to all the colleagues in university of Sheffield and Technical University of Munich for welcoming me like one of their own during my secondments. Especially I would like to mention Manoranjan, Vivian, Ambuj, Punit and Iris for the memorable time we spent together in Sheffield and Munich. Some special people include Arif vai, Zehan vabi, Iftekhar vai and Mithila vabi for making me feel at home while I was away from my family. Thanks to all the friends who were there in times of necessity and happiness and shared their life pieces during these years: Poonam, Ruku vai, Thuel, Kamal vai, Alice, Sadid, Raihan, Ishtiaq, Milcan, Feroz, Tania and all my WRE'03 friends.

Last but not the least gratitude from the core of my heart to my parents Md Gausul Azim Baigh and Dalia Mahbub for their blessings, unconditional support and sacrifice, without them it was impossible to chase my dreams. I would like to thank my sister Papia for inspiring and taking care of me in hard times also my sisters Mistah and Nusaiba for their love.

The most special person who supported me unconditionally without questioning my goal is my wife, Sayma. Without her help and understanding I would have never finished my PhD. My heart feels proud to say that all the giggles, singing and dancing by my daughter Sarah filled my stressful time with joy.

Md Nazmul Azim Beg

Coimbra, August 2018

Abstract

Quantifying and reducing uncertainty in a numerical model improve model reliability and enhance model performance. For an urban drainage flow, the state-of-the-art modelling method is dual drainage modelling where the surface drainage system is represented as two dimensional, and the buried piped network is represented as one dimensional. Most of these models use the St. Venant equation to calculate the flow, which does not help with the modelling of drainage structures such as manholes and gullies as they have complex three-dimensional flow. These structures are represented as point entities using head loss coefficients and discharge coefficients. This involves uncertainty in results as the values of these coefficients are highly case dependent. Urban drainage models also require hydrological input boundaries such as discharge and water levels, for which they are dependent on measurements or outputs of a hydrological model. A major part of this thesis focuses on finding the uncertainty of manhole head loss coefficients and gully discharge coefficients (Chapter 3 to Chapter 6). The last part of the thesis (Chapter 7) focuses on quantifying uncertainties in rainfall-runoff hydrological model results to ensure efficient flood forecasting.

In analysing the uncertainty of the manhole and gully modelling, the primary focus was given to understanding the hydraulics and the flow through these structures correctly. Three different sets of laboratory experiments were conducted in characterising the manhole and the gully flow. In the first measurement set, velocity measurements were done in a small-scale manhole. Stereoscopic Particle Image Velocimetry was utilised to record the three velocity components in three different two-dimensional planes at various hydraulic conditions. In the second experimental measurement set, a prototype scale manhole was utilised to measure its flow and surcharge depths at different surcharges. In the third experimental work, velocity measurements were conducted in a prototype gully using ADV.

Computational fluid dynamics (CFD) was used to investigate the flow behaviour and inspect the manhole head loss coefficients and gully discharge coefficients at distinct conditions. The scaled manhole model was replicated primarily utilising OpenFOAM® CFD modelling tools. A multiphase Volume of Fluid (VOF) model was constructed by applying four different Reynolds Averaged Navier Stokes (RANS) turbulence models. The PIV measurement data was used to validate the CFD modelling procedure. The comparison showed that among four different RANS models the RNG k-ε model is the best choice considering model result quality of velocity and pressure as well as time requirement in model simulation. Later, RNG k-ε model was applied in replication of the

prototype scale manhole used in the laboratory. The model also showed good performance when model data were compared with the experimental measurement of discharge and pressure. Lastly, the validated CFD model was used to find uncertainty of manhole head loss coefficients in prototype scale manhole models. Three different manhole moulds found in the drainage systems were analysed numerically: Type A with sump zone, Type B without a sump and Type C with benching. The effect of small bending angles and manhole of inlet diameter ratios were further checked for Type A manhole. Results showed that at very small bending angles, jet flow core region can still dissipate through the outlet pipe and causes a minimal increase of head loss at the post threshold surcharge. At higher bending angles, the core jet flow disappears in the manhole, and higher head loss coefficients are observed for all surcharge. The Type A manhole showed an alternation of the hydraulic regime at manhole diameter ratio of 3.0. Over this ratio, manholes showed indication of threshold surcharge zone, which was absent in lower ratios.

CFD model of prototype gully showed good agreement when compared to ADV velocity data. The validated gully model was used to check different gully discharge coefficients for different gully outlet water levels. Three different downstream surcharge levels were identified for which the gully flows show different discharge coefficients.

The last part of the dissertation focuses on quantifying uncertainty in a rainfall-runoff model. A tool was developed which can be used for automated flood forecasting including estimation of input and parameter uncertainties. It can also forecast flood discharge using ensemble-based Monte Carlo method. The tool was successfully applied at the city of Kulmbach located within Upper Main river catchment in Germany. A new methodology is proposed for flood forecasting named ‘Discharge Interval Method’. When compared with the traditional Monte Carlo method, the Discharge Interval Method was also found to efficiently hindcast historical flood events in a fraction of time without downgrading forecast quality.

Keywords: Manhole, Gully, PIV, Head loss coefficients, Discharge Coefficients, Uncertainty, OpenFOAM®, LARSIM, Flood Forecasting, Monte Carlo

Resumo

Quantificar e reduzir as incertezas de um modelo numérico pode melhorar tanto a sua confiabilidade como melhorar o seu desempenho. Os modelos atuais de drenagem urbana utilizam o conceito de drenagem dual, onde o sistema de drenagem superficial é calculada como bidimensional e a rede enterrada é calculada como unidimensional. A maioria desses modelos usa as equações de Saint-Venant para calcular o escoamento no qual as estruturas de drenagem, como caixas de visita e sumidouros, não são simulados pois têm um comportamento claramente tridimensional. Estes elementos são normalmente traduzidos por valores de perda de carga pontuais e coeficientes de vazão, potenciando incerteza nos resultados. Os modelos de drenagem urbana também requerem fronteiras de entrada de origem hidrológica, tais como caudais e alturas de água, que dependem de medições experimentais ou saídas de outros modelos hidrológicos. A presente tese foca-se maioritariamente na formulação da incerteza dos coeficientes em caixas de visita e dos respetivos coeficientes de vazão. A última parte da tese concentra-se em encontrar incertezas da modelação hidrológica de chuvadas e escoamentos para garantir uma previsão eficiente de cheias.

Ao analisar a incerteza na simulação numérica de caixas de visita e sumidouros, o foco principal foi o de compreender os fenómenos hidráulicos que ocorrem nessas estruturas. Três estruturas experimentais em laboratório foram usadas para adquirir dados experimentais do escoamento. No primeiro ensaio foram retirados dados de velocidade numa caixa de visita. A técnica de velocimetria por imagem de partículas (PIV na sigla inglesa) foi utilizada para recolher a velocidade do escoamento nas três componentes em três planos bidimensionais para diferentes condições hidráulicas. No segundo ensaio foi usada uma caixa de visita à escala real a fim de se conhecer o escoamento e as profundidades de escoamento para diferentes caudais. No terceiro ensaio foram medidas as velocidades pontuais num sumidouro à escala real recorrendo a um equipamento de Doppler (ADV na sigla inglesa).

Modelos de Dinâmica de Fluidos Computacional (CFD na sigla inglesa) foram usadas para investigar o comportamento do escoamento e inspecionar as perdas de carga na caixa de visita e os coeficientes de drenagem do sumidouro para diferentes condições hidráulicas. A caixa de visita foi numericamente simulada usando a ferramenta de CFD OpenFOAM recorrendo a um modelo baseado na técnica de Volume de fluido (VOF na sigla inglesa) em conjunto com quatro tipos de modelos de turbulência baseados na decomposição de Reynolds (RANS na sigla inglesa). As medições de PIV foram usadas para calibrar o modelo numérico. A comparação mostrou que entre

os diferentes modelos RANS, o modelo RNG k-ε foi o que melhor representou a velocidade e pressão medida experimentalmente e apresentou um menor tempo computacional. Este modelo foi posteriormente usado para a simulação da caixa de visita com bons resultados relativamente à simulação dos caudais e pressões. A calibração deste modelo foi definitiva para a quantificação da incerteza dos coeficientes de perda de carga na caixa de visita considerando diferentes geometrias normalmente usadas nos sistemas de drenagem, Tipos A, B e C. Foram estudados os efeitos de pequenos desvios entre a entrada e a saída da caixa e diferentes rácios entre o diâmetro da caixa de visita e a conduta de entrada para o Tipo A. Os resultados mostraram que para pequenos desvios entre a entrada e a saída, o jato principal é dissipado pela saída e causa uma pequena perda de carga. Já para os desvios maiores, o jato desaparece dentro da caixa de visita gerando grandes perdas de carga. Na caixa de visita do Tipo A foi identificado um regime hidráulico alternado para um rácio de 3.0 entres os diâmetros caixa/entrada. Acima deste rácio foi encontrada uma zona de sobrecarga bem identificada.

O modelo CFD do sumidouro mostrou excelente performance quando comparado com os dados de velocidade do ADV. A validação deste modelo permitiu verificar os coeficientes de vazão para diferentes alturas de água. Foram identificados três regimes de escoamento a jusante do sumidouro com implicações nos coeficientes de drenagem.

A última parte desta tese está focada na quantificação da incerteza de um modelo numérico hidrológico com escoamento superficial. Foi desenvolvida uma ferramenta que pode ser utilizada para antecipar automaticamente as cheias urbanas com a inclusão de parâmetros de incerteza na entrada do modelo e previsão do caudal usando o método de Monte Carlo. Esta ferramenta foi testada com sucesso na cidade de Kulmbach, na bacia do Rio Meno (Alemanha). Foi proposta uma nova metodologia para a previsão de cheias chamada de 'Discharge Interval Method'. Quando comparada com o tradicional método de Monte Carlo, o 'Discharge Interval Method' foi também bastante eficiente na previsão inversa de eventos de cheias numa fração de tempo que não diminui a qualidade da previsão.

Palavras-Chave: Caixa de visita, Sumidouro, Velocimetria por Imagem de Partículas (PIV), Coeficientes de perda de carga, Coeficientes de vazão, Incerteza, OpenFOAM, LARSIM, Previsão de cheias, Monte Carlo

List of Publications

The content in this thesis is based on works either published, submitted, under review, or in preparation (as listed below). Though these works have different co-authors, the intellectual, research and writing effort was that of the first author. Prof. Rita F. Carvalho and Prof. Jorge Leandro provided their guidance throughout the work, helped in organising the workflow and supervised during the data processing. Prof. Simon Tait and Prof. Wernher Brevis helped in building the PIV experimental setup and corresponding data processing, as well as provided their guidance and technical support in assuring data quality.

A full list of papers or presentations submitted during this thesis, from the period starting from April 2015 and in which Md Nazmul Azim Beg is an author or co-author are presented herein:

Works published/submitted since the beginning of the PhD and are parts of the thesis:

Chapter 3:

Beg, M.N.A., Carvalho, R.F., Tait, S., Brevis, W., Leandro, J. Flow characterisation in a scaled surcharged manhole using stereoscopic PIV. (submitted)

Chapter 4:

Beg, M.N.A., Carvalho, R.F., Tait, S., Brevis, W., Rubinato, M., Schellart, A., Leandro, J., 2017. A comparative study of manhole hydraulics using stereoscopic PIV and different RANS models. Water Sci. Technol. 87–98. https://doi.org/10.2166/wst.2018.089

Beg, M.N.A., Carvalho, R.F., Leandro, J., Tait, S., Schellart, A., Brevis, W., 2017. Comparison of manhole hydraulics using PIV and different RANS model, in: Marsalek, J., Kabelkova, I. (Eds.), 14th IWA/IAHR International Conference on Urban Drainage. ICUD2017, Prague, Czech Republic, pp. 241–249.

Chapter 5:

Beg, M.N.A., Carvalho, R.F., Leandro, J., 2018. Effect of surcharge on gully-manhole flow. J. Hydro-environment Res. 19, 224–236. https://doi.org/10.1016/j.jher.2017.08.003

Beg, M.N.A., Carvalho, R.F., Leandro, J., 2017. Effect of surcharge on gully and manhole flow, 2º FOAM @ PT / 1º FOAM IBÉRICO, 2 July 2017, University of Coimbra, Coimbra, UK

Chapter 6:

Beg, M.N.A., Carvalho, R.F., Leandro, J. Uncertainty in manhole hydraulics due to different

manhole mould and small bending in the pipe. (submitted)

Beg, M.N.A., Carvalho, R.F., Leandro, J., 2017. Comparison of flow hydraulics in different manhole types, in: Ghani, A.A. (Ed.), Managing Water for Sustainable Development: Learning from the Past for the Future: Proceedings of the 37th IAHR World Congress. IAHR & USAINS HOLDING SDN BHD, Kuala Lumpur, Malaysia, pp. 4212–4221.

Chapter 7:

Beg, M.N.A., Leandro, J., Bhola, P., Konnerth, I., Amin, K., Köck, F., Carvalho, R.F., Disse, M. Flood forecasting with uncertainty using a fully automated flood model chain : a case study for the City of Kulmbach, (submitted)

Beg, M.N.A., Leandro, J., Bhola, P., Konnerth, I., Amin, K., Köck, F., Carvalho, R.F., Disse, M., 2018. Flood forecasting with uncertainty using a fully automated flood model chain : a case study for the City of Kulmbach, in: 13th International Hydroinformatics Conference. Palermo, Italy, pp. 1–9.

Other works published/submitted/under preparation since the starting of the PhD, but are not included of the thesis:

International Journals:

Muthusamy, M., Tait, S., Schellart, A., **Beg, M.N.A.**, Carvalho, R.F., de Lima, J.L.M.P., 2018. Improving understanding of the underlying physical process of sediment wash-off from urban road surfaces. J. Hydrol. 557, 426–433. https://doi.org/10.1016/j.jhydrol.2017.11.047

Bellos, V., **Beg, M.N.A.**, Leandro, J., Carvalho, R.F.; Investigating uncertainty due to grid size in 2D and 3D hydrodynamic modelling (under preparation)

Beg, M.N.A., Carvalho, R.F., Rubinato, M., Shucksmith, J., Leandro, J. Numerical and experimental investigation on solute transport in through a overflowing manhole (under preparation)

Technical Report:

Beg, M.N.A., Carvalho, R.F., Leandro, J., Schellart, A., 2018. Deliverable 2.2: Report on software tools for investigating the influence of hydraulic structures and their uncertainty in sewer network modelling. Available at: https://www.sheffield.ac.uk/polopoly_fs/1.783804!/file/D2.2_QUICS_v2-2_Final.pdf.

Publications in proceedings of international conferences and workshops:

Beg, M.N.A., Carvalho, R.F., Leandro, J., 2018. Suspended sediment transport model for urban drainage structures, in: OpenFOAM 2nd Iberian Meeting. Santiago de Compostela, Spain.

Beg, M.N.A., Carvalho, R., Lopes, P., Leandro, J., Melo, N., 2016. Numerical Investigation of the Flow Field inside a Manhole-Pipe Drainage System, in: Crookston, B., Tullis, B. (Eds.), Hydraulic Structures and Water System Management. 6th IAHR International Symposium on Hydraulic Structures. Utah State University, Portland, Oregon, USA, pp. 1–11. https://doi.org/10.15142/T370628160853

Beg, M.N.A., Carvalho, R.F., Leandro, J., Lopes, P., Cartaxo, L., 2016. Investigation of the Flow Field inside a Drainage System: Gully - Pipe - Manhole, in: International Junior Researcher and Engineer Workshop on Hydraulic Structures. Utah State University, Lübeck, Germany, pp. 1–11. https://doi.org/10.15142/T3859Z

Carvalho, R.F., Lopes, P., **Beg, M.N.A.**, Leandro, J., 2018. Performance of different gully bottom pipe outlet characteristics, in: 5th IAHR Europe Congress - New Challenges in Hydraulic Research and Engineering. Trento, Italy.

Muthusamy, M., Carvalho, R.F., **Beg, M.N.A.**, Tait, S., Schellart, A., Lima, J.P. de, 2017. Effect of rainfall intensity, surface slope and sediment build-up on sediment wash-off process: An experimental study, in: Marsalek, J., Kabelkova, I. (Eds.), 14th IWA/IAHR International Conference on Urban Drainage. ICUD2017, Prague, Czech Republic, pp. 109–112.

Posters or presentations without proceedings

Beg, M.N.A., Carvalho, R.F., Leandro, J., 2017. Numerical and experimental flow investigation in a surcharged manhole (Poster), QUICS Final Dissemination Event, International Water Week, 2 November 2017, Amsterdam, The Netherlands

Beg, M.N.A., Carvalho, R.F., Leandro, J., 2017. Comparison of Gully Flow Due to Different Gully Outlets, 12th OpenFOAM Workshop. 24-27 July 2017, University of Exeter, Exeter, UK

Beg, M.N.A., Carvalho, R.F., Leandro, J., 2016. Flow investigation in a Gully-Manhole drainage system. Poster Sess. Present. QUICS Ind. Dissemination Event, 15 June 2015, Aquafin, Aartselaar, Belgium

Table of Content

Preamble i

Acknowledgements iii

Abstract v

Resumo vii

List of Publications ix

Table of Content xiii

List of Figures xviii

List of Tables xxiii

Nomenclature xxv

Chapter 1 Introduction 1

1.1 Motivation 1

1.2 Aims and scope 3

1.3 Thesis Structure 4

Chapter 2 Literature Review 7

2.1 Flow in Urban Drainage Structures 7

2.2 Manhole 9

2.3 Gully 15

2.4 Sediment in drainage system 20

2.5 Experimental flow measurement technique in a drainage structure 26

2.5.1 ADV 26

2.5.2 PIV Method 30

2.6 CFD Modelling of urban drainage structure and its challenges 35

2.6.1 CFD modelling 35
2.6.2 Prediction of water surface 36
2.6.3 Choice of turbulence modelling 38
2.6.4 Choice of appropriate CFD tools 40
2.7 Description of OpenFOAM model 41
2.7.1 interFoam Solver 41
2.7.2 Algorithms 44
2.8 The uncertainty involved in urban drainage modelling 44
2.9 Uncertainty analysis in large-scale hydrological modelling 46
2.10 Uncertainty analysis procedure in this research 47
2.10.1 Uncertainty analysis in hydraulic structure modelling 48
2.10.2 Uncertainty analysis in large-scale catchment modelling 49

Chapter 3 Flow characterisation in a scaled surcharged manhole using Stereoscopic PIV 51

3.1 Abstract 51
3.2 Introduction 51
3.3 Methodology 53
3.3.1 Laboratory setup 53
3.3.2 PIV Setup 54
3.3.3 Data collection 56
3.3.4 Data processing 57
3.4 Uncertainty estimation in the measurement 58
3.5 Results and discussions 61
3.5.1 Statistical Convergence 61
3.5.2 Spatial mean velocity patterns 62
3.5.3 Secondary flow and vortex formation in the manhole 69
3.5.4 Turbulent kinetic energy 71
3.5.5 Reynolds shear stresses 73
3.5.6 Changes in core and diffusion region at different conditions 76
3.6 Conclusions 78
3.7 Acknowledgement 79

Chapter 4 A comparative study on manhole hydraulics using stereo PIV and different RANS models 81

4.1 Abstract 81

4.2 Introduction 81

4.3 Methods and Materials 82

4.3.1 Experimental model 82

4.3.2 PIV measurement 83

4.3.3 Numerical model 85

4.4 Results and Discussion 88

4.5 Conclusions 96

4.6 Acknowledgements 97

Chapter 5 Effect of surcharge on gully-manhole flow 99

5.1 Abstract 99

5.2 Introduction 99

5.3 Methodology 102

5.3.1 Experimental Setup 102

5.3.2 Experimental Test Cases 103

5.3.3 Numerical Model Description 104

5.3.4 Mesh Generation 106

5.3.5 Definition of boundary conditions and simulation control parameters 108

5.4 Results and Discussion 109

5.4.1 Comparison with experiments 109

5.4.2 Velocity field and manhole head loss at different surcharge 113

5.4.3 Effect of manhole surcharge on the gully flow 118

5.5 Conclusions 123

5.6 Acknowledgements 124

Chapter 6 Uncertainty in manhole hydraulics due to different manhole mould and small bending in the pipe 125

6.1 Abstract 125

6.2 Introduction 126

6.3 Methodology 128

6.3.1 Manholes considered for uncertainty analysis 128

6.3.2 Computational domain and mesh 128
6.3.3 Numerical Model 130
6.3.4 Modelling procedures and boundary Conditions 131
6.3.5 Identification of Manhole head loss coefficient and threshold surcharge 133
6.4 Mesh analysis 134
6.5 Results and discussions 136
6.5.1 Comparison of head loss values with the literature 136
6.5.2 Head loss coefficient at different manhole moulds 137
6.5.3 Free surface location at different manhole moulds 139
6.5.4 Change in head loss coefficient due to pipe bending 141
6.5.5 Effect of manhole to pipe ratio 143
6.6 Conclusions 145
6.7 Acknowledgements 146

Chapter 7 Flood forecasting with uncertainty using a fully automated flood model chain: A case study for the City of Kulmbach 149

7.1 Abstract 149
7.2 Introduction 150
7.3 The FloodEvac Tool 151
7.4 Pilot catchment and datasets 153
7.5 Methods 155
7.5.1 Generation of rainfall uncertainty 155
7.5.2 Generation of parameter uncertainty 156
7.5.3 Forecast of flood discharge 157
7.6 Uncertainty analysis in the model results 158
7.7 Towards reducing the forecast time requirement 160
7.8 Hindcasting other flood events 161
7.9 Determining the forecast quality 163
7.10 Conclusions 166
7.11 Acknowledgements 167

Chapter 8 FInal Remarks 169

8.1 Conclusions 169
8.2 Research Questions 171

8.3 Future works 173

References 175

List of Figures

Figure 2.1: Head loss measurement in a surcharged manhole (adapted from Pang and Loughlin (2011, fig. 1)) 10

Figure 2.2: Typical manhole types in urban drainage systems. Type I, II, III and IV are adapted from Asztely (1995) fig. 2.3 11

Figure 2.3: Proposed shape factors for different manholes, adapted from Bo Pedersen and Mark (1990). 12

Figure 2.4: a to d) Different shape and gratings type of a typical roadside gully and e) the cross section of a gully 16

Figure 2.5: Geometry of road channel flow for gully water intake (exaggerated vertical scale) (top panel), Gully hydraulic efficiency curve (bottom-left panel) and typical captured flow vs approached flow of a gully (bottom-right panel); adapted from (Butler and Davies, 2011) 18

Figure 2.6: Solids transport and accumulation process (adapted from (Ashley et al., 2004)) 21

Figure 2.7: Fall velocity about the diameter of a spherical grain of quartz, adapted from (Hickin, 1995, p. 75) 26

Figure 2.8: Schematic of Sontek ADV Probe adapted from *Palmer (2002)* (left panel) and Sontek web page (http://www.sontek.com/productsdetail.php?10-MHz-ADV-2) (right panel) 28

Figure 2.9: Example of cleaned data (upper panel) and contaminated data (bottom panel), adapted from *Goring and Nikora (2002)* 29

Figure 2.10: PIV measurement at the horizontal plane of a scaled manhole (adapted from Lau (2007) p. 185, their figure 5.28) 30

Figure 2.11: Three different camera placement options for stereo PIV (a) Lens Translation Arrangement, (b) Angle Displacement Arrangement and (c) Angle Displacement Arrangement with Sheimpflug Condition. Image adapted from (Hu, 2013, fig. 4.3). 31

Figure 3.1: Clockwise: a) Top scheme of the PIV setup on the manhole at the laboratory, b) Two cameras focusing calibration plate in the manhole, c) Nd:YAG Double cavity double pulsed laser, d) a 45° mirror under the manhole to reflect the laser light sheet vertically, and e) Agitation tank mixing polyamide 12 seeding particles. The vertical laser light sheet is not shown in the figure. 54

Figure 3.2: Plane of view of each camera, calibration plate and acquired particle image view from both cameras 55

Figure 3.3: Comparison between two different velocity data from the scenario at 2×10^{-3} m^3/s inflow and 210 mm water level. The dotted contour and red vectors showing data after averaging all the instantaneous measurement. Solid contour and the blue vectors are showing data after stitching from different measurements allowing smaller Dynamic Velocity Range 59

Figure 3.4: Checking of temporal convergence of the measured velocity data 61

Figure 3.5: Left panel: Mean normalised velocity vectors at three planes in the manhole at inflow, Q = 2×10^{-3} m^3/s with the water level of 210 mm, Right panel: Zoomed view of the central plane with schematic locations of different velocity zones 62

Figure 3.6: Mean velocity magnitude at CVP for different inflow and surcharge conditions 63

Figure 3.7: Normalized Mean velocity magnitude at CVP at different inflow and surcharge conditions 64

Figure 3.8: Out of the plane normalised mean velocity at CVP at different inflow and surcharge conditions. Positive values are showing velocity away from the camera, and negative values are showing velocity towards the camera 66

Figure 3.9: Normalised mean velocity magnitude at LVP and RVP 67

Figure 3.10: Out of the plane normalised mean velocity component at LVP and RVP. Positive values are showing velocity away from the camera, and negative values are showing velocity towards the camera 68

Figure 3.11: Mean normalised vorticity at LVP, CVP and RVP. Positive (red) values showing clockwise rotation and negative values (blue) showing anti-clockwise rotation 70

Figure 3.12: Mean normalised turbulent kinetic energy at CVP 71

Figure 3.13: Mean normalised turbulent kinetic energy at LVP and RVP 73

Figure 3.14: Magnitude of mean normalised Reynolds stress component R_{xy} at CVP 74

Figure 3.15: Magnitude of mean normalised Reynolds stress component R_{yz} 75

Figure 3.16: Magnitude of mean normalised Reynolds stress component R_{zx} 76

Figure 3.17: Location of the core and diffusion regions from all the measurements at CVP 77

Figure 4.1: Experimental setup for 2D3C stereo PIV measurement at the manhole 83

Figure 4.2: a) Numerical model mesh (top left panel), b) Boundary locations (top right panel) and c) Mesh convergence test (bottom panel)..... 88

Figure 4.3: Comparison of non-dimensional velocity components from the numerical models and PIV measurement at both CVP and RVP of the manhole. The flow direction is from right to the left 90

Figure 4.4: Out of the plane velocity component at the CVP from PIV and four RANS models.... 91

Figure 4.5: Temporal standard deviation of different velocity component at CVP and RVP, measured from PIV data and four RANS models..... 92

Figure 4.6: Flow streamline through the manhole and water level range from different models 93

Figure 4.7: Bottom pressure comparison from different RANS models and the experimental pressure sensor data..... 94

Figure 5.1: Upper Panel: Experimental setup; Lower panel: Computational mesh of different parts of the domain A: Gully with outlet pipe, B: Outlet Pipe, C: Manhole and D: Pipe connected with Manhole..... 103

Figure 5.2: Velocity measurement locations using ADV. Left panel shows the location of the three planes and the right panel shows the point measurement locations at each plane..... 104

Figure 5.3: Mesh analysis using three different mesh sizes. Left panel shows longitudinal velocity profile at the manhole centre and the right panel shows longitudinal velocity profile at the outlet pipe 107

Figure 5.4: Pressure level vs Discharge in the two manholes from experimental and numerical simulation (after Beg et al. (2016a) 110

Figure 5.5: Comparison of pressure head between numerical and experimental model..... 110

Figure 5.6: Comparison of velocity between numerical (upper panel) and experimental (bottom panel) study at three longitudinal planes of the gully..... 111

Figure 5.7: Velocity profile at different locations of the gully. Firm lines showing numerical model data and cross (x) markers showing data from experimental study 112

Figure 5.8: Transverse velocity (V_y) at the gully..... 113

Figure 5.9: Longitudinal velocity at the centreline of the manhole from different simulations. Left panel shows vertical section and right panel shows horizontal section through the axis of the inlet-outlet pipe. a, b, c and d show velocities at 30 l/s-0.45 m depth, 30 l/s-1.21 m depth, 120 l/s-0.54 m depth and 120 l/s-1.27 m depth of water at the manhole centre respectively 115

Figure 5.10: Coefficient of head loss vs Surcharge ratio at the manhole 116

Figure 5.11: Velocity distribution and diffusion region in circular free jet (adapted from the works of Guymer et al. (2005) and Pedersen and Mark (1990)..... 117

Figure 5.12: Schematic diagram of gully flow to the manhole..... 118

Figure 5.13: Computed intercepted flow at the gully vs surcharge heights at the manhole..... 119

Figure 5.14: Cross section through the gully outlet jet at different surcharges. The figure at left panel represents Zone 1, the middle panel represents Zone 2 and the right panel represents Zone 3. 120

Figure 5.15: Gully discharge vs square root of head difference at the gully at left panel and Gully discharge vs head difference at the gully at right panel 121

Figure 5.16: Manhole bottom shear stress at different surcharge height of the manhole. The flow direction is from left to the right..... 122

Figure 6.1: Schematic views of the sides of the three manholes showing sizes and positions of different components (upper panel) and their computational meshes (bottom panel). Left panel shows Type A, middle panel shows Type B and the right panel shows Type C 129

Figure 6.2: Top view of different orientations of inlet-outlet pipe for Type A manhole 129

Figure 6.3: Three open boundaries of the model 130

Figure 6.4: Head loss in a surcharged manhole, adapted from Pang & O'Loughlin (2011) 134

Figure 6.5: Mesh analysis using three meshes for Manhole Type C. Left panel shows longitudinal velocity profile at the manhole centre and the right panel shows longitudinal velocity profile at the outlet pipe..... 135

Figure 6.6: Head loss coefficients comparison for manhole Type B (left panel) and Type C (right panel). Data adapted from Bo Pedersen and Mark (1990), Stovin et al. (2013) and Guymer et al. (2005) respectively. 137

Figure 6.7: Manhole Head loss coefficient (K) vs Surcharge ratio (s/Φ_p) for manhole types A, B and C..... 137

Figure 6.8: Instantaneous velocity profile at the central axis of the manhole. From left to right: Manhole Type A, Type B and Type C. The flow direction at each manhole is from left to right . 139

Figure 6.9: Bottom pressure in three types of manhole at different upstream (u/s) and downstream (d/s) cases. Red, Green and Blue lines show the pressure data of Manhole Type A, B and C respectively. Manhole centre is at x = 0 m..... 140

Figure 6.10: Flow velocity at different inlet conditions of the manhole. All figures representing inlet condition of 60×10^{-3} m^3/s and outlet condition of 0.6 m of water column pressure. The flow direction is from left to right..... 141

Figure 6.11: Manhole head loss coefficients for different horizontal angle difference between inlet and outlet..... 142

Figure 6.12: Effect of head loss on manhole to pipe ratio..... 144

Figure 6.13: Instantaneous velocity at the vertical cross section of the manhole at all manhole ratio and surcharge conditions..... 145

Figure 7.1: FloodEvac Tool and Model chain 151

Figure 7.2: LARSIM water balance model 153

Figure 7.3: Case study: Upper-Main Catchment..... 153

Figure 7.4: Historical observed discharge data at the Ködnitz gauge. The flood event marked with red shade was chosen for the analysis 154

Figure 7.5: Uncertainty quantification of rainfall distribution..... 156

Figure 7.6: Probability distribution curve of the eight considered parameters at one sub-catchment 157

Figure 7.7: All forecast uncertainty results..... 158

Figure 7.8: Scatter plots of observed vs simulated data for each hourly forecast leads..... 159

Figure 7.9: Confidence intervals in flood forecasting 159

Figure 7.10: Observed discharge with updated forecasts using Discharge Interval method..... 161

Figure 7.11: Hindcasting three events using traditional Monte Carlo (left panel) and the Discharge Interval method (right panel). The three flood events are January 2011 (top), January 2012 (middle) and May 2013 (bottom). The ninety percentile discharge forecasts from the MC method is shown with the Discharge Interval method data. 162

Figure 7.12: ROC plot of the four hindcasted events at 6 hrs lead time using Monte Carlo approach and Discharge Interval Method 165

List of Tables

Table 2.1: List of related studies on in line manholes using physical modelling 13

Table 2.2: List of related studies on inline manholes using Computational Fluid Dynamics (CFD) modelling 14

Table 2.3: Grain size indicator values of D10, D50 and D90 and %<100 µm for suspended solids in urban wet weather discharge (adapted from (Ashley et al., 2004) 25

Table 2.4: Typical mean values of settling velocity (adapted from (Chebbo, 1992; Stahre and Urbonas, 1990) 25

Table 3.1: List of PIV measurement conditions 56

Table 4.1: Different values of head loss coefficient (K) at different models 95

Table 5.1: Quality parameters of the computational mesh 108

Table 5.2: Numerically determined discharge coefficient of the gully outlet for different surcharge conditions 121

Table 6.1: Combinations of numerical simulations to check manhole mould effect 131

Table 6.2: Combinations of numerical simulations to check manhole inlet orientation effect ... 132

Table 6.3: Combinations of numerical simulations to check manhole inlet orientation effect ... 132

Table 6.4: Parameters for the CFD simulations 132

Table 6.5. Comparison between different mesh properties 135

Table 7.1: Likelihood table for calculating a forecast category 164

Table 7.2: Average area under the ROC curve for all the four events with both forecasting methods and different forecast leads. MC refers to Monte Carlo; DI refers to Discharge Interval Method 166

Nomenclature

Acronyms

1D	One Dimensional
2D	Two Dimensional
3D	Three Dimensional
ADV	Acoustic Doppler Velocimetry
ASM	Algebraic Stress Models
CAE	Computer-Aided Engineering
CDF	Cumulative Distribution Function
CFD	Computational Fluid Dynamics
CFL	Courant Friedrichs Lewy
DD	Dual Drainage
DNS	Direct Numerical Simulation
EPS	Ensemble Prediction System
FDM	Finite Differences Methods
FFT	Fast Fourier Transform
FVM	Finite Volume Method
GCI	Grid Convergence Index
GUI	Graphical User Interface
LES	Large Eddy Simulation
OpenFOAM®	Registered trademark of a CFD tool box naming: Opensource Field Operation and Manipulation
PDF	Probability Distribution Function
PIV	Particle Image Velocimetry
PTV	Particle Tracking Velocimetry
RANS	Reynolds-Averaged Navier-Stokes
RNG	Re-Normalization Group
RSM	Reynolds Stress Models
SGS	Sub-Grid Scale
SST	Shear Stress Transport
STL	Stereo Lithography file
SWE	Shallow Water Equations
TKE	Turbulent Kinetic Energy

VOF	Volume of Fluid

Symbols

C_α	Binary coefficient to activate the compressive term
D	Diameter
E	Efficiency
$\mathbf{f}_\sigma$	Volumetric surface tension force
F_r	Froude number
g	Gravity vector
H	Hydraulic head
I	Turbulent intensity
K	Head loss coefficient
k	Turbulent kinetic energy
$Ø_m$	Diameter of manhole
$Ø_p$	Diameter of pipe
p^*	Difference between total and hydrostatic pressure
p, P	Pressure
Q	Flow rate
q	Unit discharge
r	Radius
R_e	Reynolds number
u	Velocity vector
u, v, w	Velocity component towards x, y, z directions
V_x, V_y, V_z	Velocity component towards x, y, z directions
x	Position vector
y^+	Dimensionless wall distance
α	Volume fraction
ΔH	Energy drop
η	Kinematic viscosity
η_t	Turbulent eddy kinematic viscosity
μ	Dynamic viscosity
μ_t	Turbulent eddy dynamic viscosity
ρ	Density
U_{avg}	U mean velocity
τ	Shear stress

CHAPTER 1
INTRODUCTION

1.1 Motivation

Numerical modelling is never free of uncertainties mainly due to the complexity of the physics involved in the natural processes as well as due to the inability of mathematical equations to represent them in the simplified and computationally efficient way. Quantifying and reducing uncertainties in a numerical model improve model reliability and increase model performance. Most urban drainage models are one or two dimensional in which the pipe network is represented as a one-dimensional object while the paved road or infiltration area is considered as two dimensional (Chen et al., 2015; Djordjević et al., 2005; J. Leandro and Martins, 2016). This methodology keeps a balance between computational cost and accuracy in the model results. However, urban drainage network also contains different structures such as street gully and manholes. When the flow enters these structures, it experiences some local phenomena such as flow contraction, expansion, rotation and recirculation. The flow becomes more turbulent and possibly involves air entrainment and sediment mixing. Most drainage models use Shallow Water Equations (SWE) at its depth-averaged or both depth and width averaged form (Barthélémy et al., 2018; Martins et al., 2016) and are not able to represent the physics of the flow through the structures properly (Leandro et al., 2009b). For this purpose, the hydraulic structures are considered in these models as point entities, and the flow effects are represented using empirical equations of head loss coefficients and discharge coefficients, calculated from previously tested experimental models. This introduces uncertainty in the model results as a very few existing models are available to calibrate these coefficients (Djordjević et al., 2005).

In most busy cities, the urban drainage system is the only pathway to convey the flood water from urban areas. Local flooding is a recurrent problem for many European cities, whose sewers and stormwater systems are often affected by surcharging problems, pipe deterioration and construction flaws, due to a combination of ageing infrastructures and growing urbanisation (Freni et al., 2010). Estimation of flood risk management in urban areas has also become a significant theme in recent engineering researches as even a small-scale flood in a busy urban area can cause a great economic loss. Elaboration of the drainage network is often an essential requirement of urbanisation, yet, relatively little attention has been given to the of urban drainage structures

(Meierdiercks et al., 2010). After a storm event, the urban drainage system collects and conveys the runoff through its surface and underground system. Gully maintains the connection between the overland and underground systems and manhole maintains the connection between drainage pipes. With the advancement of the weather and flood forecasting system, it is possible to estimate the flood discharge before the flood event with the help of proper hydrological models. Moreover, by using a proper flood routing model, possible inundation and local flooding can also be estimated.

When considering a flood routing model, it is desired to calculate the local losses related to manholes and gullies to calculate possible local flooding accurately. Several works have been done to characterise manhole hydraulic losses (Arao et al., 2013; Bo Pedersen and Mark, 1990; Carvalho and Leandro, 2012; Gisonni and Hager, 2002; Guymer et al., 2005; Lau et al., 2008; Lopes et al., 2018; Mark et al., 2004; Marsalek, 1984, 1981; Sangster et al., 1958; Stovin et al., 2013; Zhao et al., 2006). Researchers pointed out many factors that act as the key points in determining the head loss in a manhole. From which, the most important factors are the inflow velocity, surcharge ratio, manhole diameter to pipe diameter ratio, the angle between inflow and outflow pipes and so forth. (see section 2.2 for a complete list). Still, researchers report that the list of factors that affect head loss is yet to be completed (Arao et al., 2013).

Compared to works on manholes, less works are reported about characterising hydraulic efficiencies of a gully pot (Ackers et al., 2001; Carvalho et al., 2011; Gómez and Russo, 2009; Leandro et al., 2014c; Lopes et al., 2016a, 2015; Martins et al., 2014; Romagnoli et al., 2013). Researchers have also described the solid entrance procedure through the gully (Butler and Karunaratne, 1995; Butler and Memon, 1999; Ellis and Harrop, 1984; Osborne et al., 1998; Pratt et al., 1987). From the literature, it has been found that runoff flow enters the underground sewer system through the roadside gully and carries suspended sediment loading to the sewer. However, the hydraulic efficiency of the gully is a function of the grate (Butler and Davies, 2011) and there are several grate variation can be found in Portuguese drainage system (Lopes et al., 2016a). However, the discharge coefficient of the gully may also be dependent on its geometry, upstream and downstream flow condition (Galambos, 2012) as well as the orientation of the outlet pipe. The changes in these affecting properties may introduce uncertainty in the model results.

Many uncertainty sources are connected to hydrological modelling to calculate discharge flow from rainfall data. Forecasting of flood events is a non-deterministic process in which uncertainty stems from different sources (Deletic et al., 2012). The accuracy of flood forecast is also connected to the accuracy in predicting atmospheric condition, which is a non-linear and complex system and hard to predict the exact state (Lorenz, 1969). Additionally, there are also inherent issues with hydrological model structures in representing the rainfall and runoff process. For these reasons,

hydrological model forecasts contain uncertainty in a great extent (Beven and Binley, 1992; Boyle et al., 2000; Refsgaard et al., 2007; Wani et al., 2017). This makes uncertainty assessment an integrated part for hydrologic modelling and considered necessary in many scientific literature (Barbetta et al., 2017; Beven, 2002; Refsgaard et al., 2007, 2005; Todini, 2009; Vandenberghe et al., 2007).

This motivation leads to the research question that this thesis intends to provide an insight on:

1. ***What are the uncertainty sources in modelling urban drainage flow related to hydraulic structures such as manholes or street gullies?***
2. ***How to reduce the uncertainty caused by the non-representation of the hydraulic structures and their 3D effects on the flow?***
3. ***How to quantify the uncertainty in flood discharge forecasting so that the predicted discharge can be used more reliably for drainage flow model?***

In this research, the primary focus is given to find the uncertainties involved in calculating the head losses and drainage efficiencies of a manhole and gully. Uncertainty of head losses and efficiencies calculation due to geometrical change of inlet/outlet orientation in the structure has been analysed. The analysis is done using experimental measurements in the laboratory and numerical modelling using open source CFD tool OpenFOAM®. The workflow follows the sequence to develop CFD models and validate them with experimental modelling techniques. Later, the validated CFD model procedure is applied to analyse several scenarios to account gully drainage efficiency and manhole head losses in the real cases.

To predict the risk of urban flooding, it is also essential to be able to forecast the amount of flood discharge with reasonable accuracy. In the latter part of the thesis, application of a flood forecasting tool is described, which is capable of automated flood forecasting with the calculation of possible input and parameter uncertainties using Monte Carlo based ensemble method. A new flood forecasting methodology is also proposed which can calculate flood forecast band very fast. The forecast band calculated by the proposed method is quantitatively similar to the 90-percentile band of Monte Carlo ensemble results.

1.2 Aims and scope

In order to provide answers to the mentioned research questions, the thesis is structured keeping an aim and some objectives. The aim is to reduce uncertainty in urban drainage flow modelling through: a) better prediction of drainage structure flow and b) better estimation of hydraulic model boundary values. In this thesis, prediction of urban drainage flow means to calculate manhole head loss coefficients and gully discharge coefficients with more certainty. Prediction of

hydraulic model boundary means to evaluate the discharge and water levels at the upstream and downstream points of the drianage points in case of calculation or forecasting drainage flow and local innundation.

To answer the research questions mentioned above, and to fulfil the aim the research is intended at keeping the following objectives:

- To review the literature related to experimental modelling of manhole and gully in both laboratory and real scales as well as using CFD models.
- To review the experimental measurement techniques commonly applied in multi-dimensional and turbulent flow measurements.
- To conduct experimental measurements on manholes and street gullies at different scales.
- To test the capacity of VOF based CFD models in replicating the flow behaviours of drainage structures and validate the CFD modelling procedures using the experimental measurement data.
- To explore manhole head loss coefficients and gully discharge coefficients at various scenarios using validated CFD models
- To develop a tool to quantify modelling uncertainties in flood discharge forecasting to ensure reliable boundary data for the urban drainage model

1.3 Thesis Structure

This thesis is divided into eight chapters, including the present introduction. The detailed descriptions of the contents of the chapters are as follows:

Chapter 1 introduces the topic of the research with the research objective and research questions.

Chapter 2 presents a literature review about manholes and gullies; sediment flow modelling in an urban drainage system, CFD modelling techniques and its challenges in modelling an urban drainage system, experimental measurement techniques, governing equations of interFoam model, uncertainties involved in urban drainage structure and uncertainties involved in a hydrological rainfall-runoff model.

Chapter 3 describes an experimental investigation of stereo PIV measurement in a scaled manhole. The work investigates mean velocity and turbulence structures at the scaled manhole at the different inflow and surcharge conditions.

Chapter 4 investigates a scaled manhole experimentally and numerically to find the best turbulence modelling approach to model the manhole hydraulics. The work compares PIV velocity data with four different RANS models. Water levels and pressure measurements at the manhole were also compared with the four CFD models.

Chapter 5 explores a full-scale manhole and gully model through experimental and numerical modelling. The work compares numerical model data with velocity measurement data at the gully using ADV and discharge and pressure measurement data at the manhole. The model also finds different gully discharge coefficients for different surcharge conditions and different manhole head loss coefficients at different inflow and surcharge conditions.

Chapter 6 applies the validated CFD modelling procedures in finding manhole head loss uncertainties for different types of prototype scale manholes. In the first part, three commonly found manhole mould designs are investigated. Later one type of manhole design is further explored to see the effect of small bending angles between the inlet and the outlet pipes. The last part describes the effect of manhole to pipe ratios in assessing the manhole head loss coefficients.

Chapter 7 presents a tool to make automated flood forecasting with added estimated uncertainty. The tool calculates the input and parameter uncertainties of a large-scale hydrological model by applying a Monte Carlo based ensemble approach. Hindcasting historical flood events were performed at the city of Kulmbach, Germany. The work also proposes a new methodology to forecast flood discharge in a much shorter time.

Chapter 8 concludes the work and suggests some possible topics for future research.

CHAPTER 2
LITERATURE REVIEW

2.1 Flow in Urban Drainage Structures

The history of urban drainage system is more than 5000 years old (Chocat et al., 2004; Cooper, 2007). Still today, people are facing new challenges due to the increase in demand on runoff quantity and quality, landscape aesthetics, ecological benefits and advancement in pollution and runoff control. Scientists are always searching for advanced treatment of urban wet-weather effluents, and tools for analysis and operation of drainage systems. The increasing threat of climate change is also a concern for the researchers. Extreme precipitation will become more frequent (Arnbjerg-Nielsen, 2011) and this will eventually increase the risks of sewer surcharge and flooding (Arnbjerg-Nielsen et al., 2013; Willems, 2013; Willems et al., 2012). However, adopting an integrated approach, optimal operation of the existing infrastructure, advanced pollution and runoff source controls, improved resilience of receiving waters, and adaptive water management can be the key to achieve additional improvements (Chocat et al., 2011). One critical issue still concerning is the management of risk and uncertainties and utilising more efficient design of the drainage system.

An urban drainage system is divided in two parts, the below ground system is termed the "minor system" and includes hydraulic structures such as gully systems, manholes as well as pipes which comprise the conventional urban drainage infrastructure. The above ground system is termed as "major system" that consists of different surface flood pathways, which includes roads, paths, car parks and playing fields.

The drainage system disregarding to its type plays an important role in routing the excess water during a flooding event. Efficient drainage system also stops/ minimise the spread of water-borne pollutions during a flooding event. According to the water framework directive of European Union, urban flooding is defined as: "*condition where wastewater and/or surface water escapes from or cannot enter a drain or sewer system and either remains on the surface or enters buildings*". A flood event can cause different kinds of damages. The damages may be categorised as (König et al., 2002; Mark et al., 2004; Rubinato et al., 2013):

- Direct damage: typically, material damage caused by water or flowing water. These damages are visible and can be measured;
- Indirect damage: such as traffic disruption or production losses. These are the secondary effects of the flood. These are also visible damages, and the losses can be measured.
- Social consequences: such as psychological problems for inhabitants as well as effects on health due to contact with flood water. These damages are hard to measure.

An urban flood event is unsteady and complex phenomena, in a flooding event, the water volume moves through both above grounds and below ground systems. When modelling it, one needs to consider the whole drainage system consists of two interconnected subsystems. In case of modelling the surface runoff, the flow can be accumulated according to the surface slope which may be spatially varied. This phenomenon is usually accurately modelled with a two-dimensional flow modelling. When modelling an underground pipe network, the pipe slope and pipe orientation can drive the flow to a specific direction. This makes the problem a one-dimensional flow model. There are certain models that uses both 1D and 2D flow equations (known as 1D-2D model); using 1D equations for underground pipe networks and 2D equations for overland flow. This combination can represent the flow with reasonable accuracy as well as minimise the computational effort in modelling them (Leandro et al., 2016). This type of different dimensional models are known as Dual Drainage (DD) models (Bazin et al., 2014; Jorge Leandro and Martins, 2016; Martins et al., 2017; Nanía et al., 2014). The coupling between the two types are done using one way (surface to sewer only) or both ways linking systems.

The concept of dual drainage modelling first surfaced in the urban storm drainage manual of the city of Denver (UDFCD, 1969) and later strengthened in the work of Ellis et al. (1982). They, however, did not model the surface and the sewer system simultaneously, instead applied synthetic hydrograph simultaneously and neglected the interactions in between. Later, different dual drainage models were proposed in literature where proper interaction between the two system was applied effectively. In the later stage, some modelling tools like SIPSON (Djordjević et al., 2005), SWMM (Rossman and Huber, 2016), MIKE Flood (DHI, 2017), SOBEK (Deltares, 2018) were developed and applied to different urban and peri-urban areas in simulation of sewer network and surface inundation works.

The application of different dual drainage models to represent the urban drainage flow is described in different literature (Chen et al., 2015; Leandro et al., 2009b; Martins et al., 2016; Verwey, 2001; Vojinovic and Tutulic, 2009). The primary equation in these models is Saint Venant equations, which is a combination of mass and momentum conservation equations, averaged towards one or two directions:

$$\frac{\partial h}{\partial t}+\frac{\partial (hu)}{\partial x}+\frac{\partial (hv)}{\partial y}=0 \tag{2.1}$$

$$\frac{\partial (hu)}{\partial t}+\frac{\partial (hu^2)}{\partial x}+\frac{\partial h(uv)}{\partial y}+gh\frac{\partial h}{\partial x}=-gh\frac{\partial z_b}{\partial x}-\tau_{bx} \tag{2.2}$$

$$\frac{\partial (hv)}{\partial t}+\frac{\partial h(uv)}{\partial x}+\frac{\partial (hv^2)}{\partial y}+gh\frac{\partial h}{\partial y}=-gh\frac{\partial z_b}{\partial y}-\tau_{by} \tag{2.3}$$

where, u and v are the depth averaged velocity components, h is the depth of flow, t is the time, τ is the bed friction stress value, g is the acceleration due to gravity, z_b is the bed elevation and x & y are the two directions in Cartesian co-ordinate system.

When the flow enters a structure within drainage system, the flow is not necessarily a 1D or 2D flow anymore instead becomes a 3D flow. Conventional 1D, 2D or 1D-2D models cannot represent the 3D flow. The representation can be done using empirical minor head loss relationships (Leandro et al., 2014b; Rubinato, 2015; Rubinato et al., 2013). As the flow within the structures is not fully resolved, the representation of the structures in these flow models may have some uncertainties. Manholes and gullies are the two most common structures found in an urban drainage system. In this work, these two hydraulic structures will be focused in view of finding uncertainties in modelling them.

2.2 Manhole

Manhole can be found in both combined and separated drainage system. It is usually built as a utility hole to inspect and access the underground drainage system. Apart from inspections reasons, manholes are usually provided in pipe flow for the following cases (Butler and Davies, 2011, p. 138):

- changes in direction
- heads of runs
- changes in gradient
- changes in size
- major junctions with other sewers
- every 90m

The complex flow pattern in a manhole may include the effects of retardation, acceleration, rotation in different planes. The head loss in the manhole may depend on several factors (Marsalek, 1984):

- retardation of the fluids at the upstream of the fluids
- the sudden expansion of the flow in manhole
- secondary flow inside the manhole
- resonance oscillations in the manhole
- acceleration of the fluid at the outlet

The energy of fluid at a section can be represented as head, which is a summation of pressure head, velocity head and potential head. This equation is derived from Bernoulli's equation.

$$H = \underbrace{\frac{P}{\rho g}}_{Pessure\ head} + \underbrace{\frac{v^2}{2g}}_{Velocity\ Head} + \underbrace{z}_{Potential\ head} \tag{2.4}$$

where, P is the pressure, v is the velocity of the fluid, ρ is the fluid density, g is the acceleration due to gravity and z is the height of the fluid from a certain datum. The head loss is calculated using the following equation:

$$H_L = \frac{P_1 - P_2}{\rho g} + \frac{{v_1}^2 - {v_2}^2}{2g} + z_1 - z_2 \tag{2.5}$$

where, subscript 1 and 2 denotes upstream and downstream respectively.

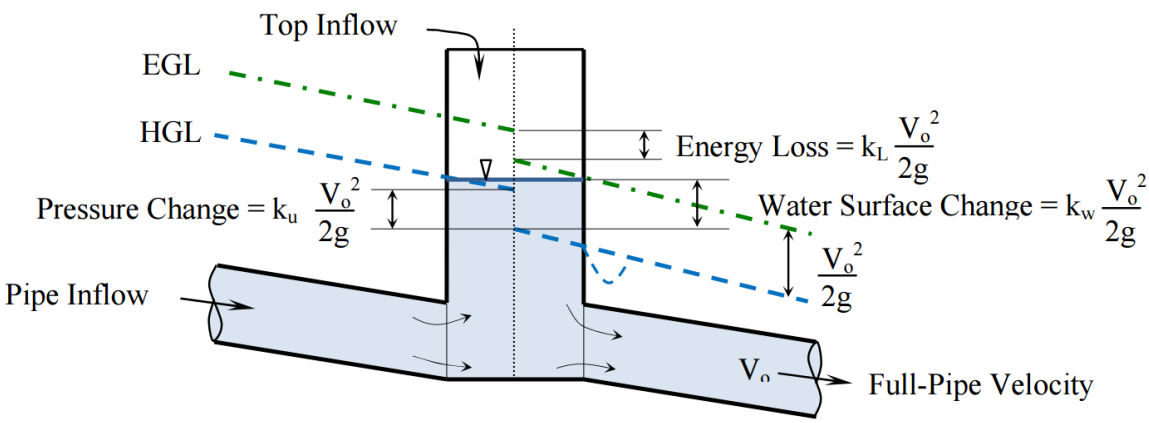

Figure 2.1: Head loss measurement in a surcharged manhole (adapted from Pang and Loughlin (2011, fig. 1))

The line that shows the energy head through the length of fluid flow is known as Energy Grade line. When determining the head loss of a manhole, the energy grade lines are extrapolated to the middle of the manhole, and the difference between the extrapolated lines at the middle of the manhole gives the measurement of head loss (Figure 2.1). The energy loss coefficient (K) for manhole structures are commonly denoted as a the ratio between head loss and inflow velocity

head (Arao et al., 2013; Carvalho and Leandro, 2012; Marsalek, 1984; Pfister and Gisonni, 2014; Stovin et al., 2013; Zhao et al., 2006) and defined as:

$$H_L = K\frac{{V_0}^2}{2g} \tag{2.6}$$

From the connectivity point of view, manholes can be divided in two types: inline manhole and junction manhole. Inline manholes are with a single inlet and a single outlet only. In a junction manhole, there could be two or more inflow pipe connected.

Due to the difference in design practice, the four types of inline manholes (Figure 2.2) can be seen in different countries.

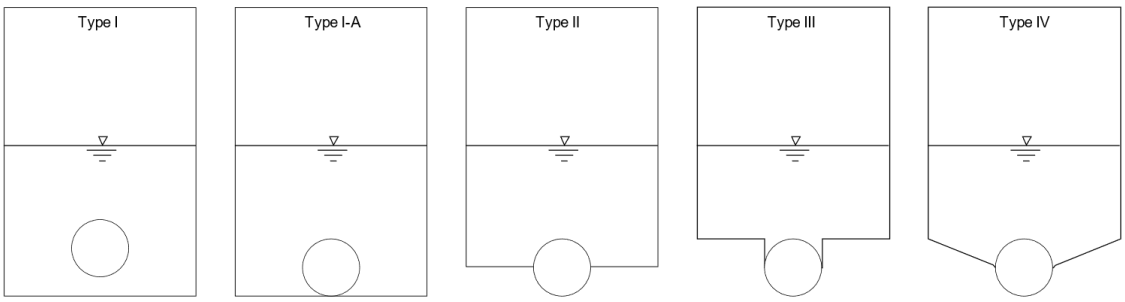

Figure 2.2: Typical manhole types in urban drainage systems. Type I, II, III and IV are adapted from Asztely (1995) fig. 2.3

Different researches have been conducted for finding the head loss coefficient K for different manhole types. Experimental models done by Sangster et al. (1958) showed the value of K for Type I manholes stays between 0.1-0.2. Marsalek (1984) studied Type I, II and III manholes with experimental models and found K values within the range of 0.124 to 0.221 for circular manholes and 0.102 to 0.344 for square shaped manhole. His results showed decreasing value of K with decreasing manhole widths. Pedersen and Mark (1990) also did experimental modelling for different manhole types with equal inflow and outflow pipe diameters. He defined different shape factors (ε) which quantify the relative impact of the different geometries on the observed K. His calculated ε values were 0.24, 0.07 and 0.025 for Type I, II and III manholes respectively (Figure 2.3). List of some researchers' work on in line manhole can be seen in Table 2.1

Shape ($D_m/D \leq 4$)	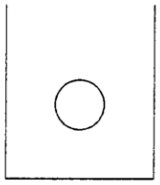 A	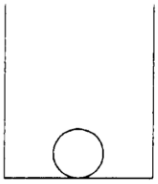 B	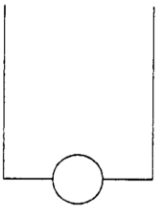 C	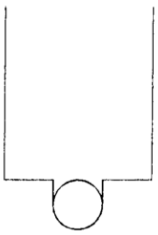 D
ζ	0.24	0.12	0.07	0.025

Figure 2.3: Proposed shape factors for different manholes, adapted from Bo Pedersen and Mark (1990).

Table 2.1: List of related studies on in line manholes using physical modelling

	(Sangster et al., 1958)	(Ackers, 1959)	(Yevjevich and Barnes, 1970)	(Archer et al., 1978)	(Hare, 1981)	(Marsalek, 1984, 1981)	(Howarth, 1985)	(Bo Pedersen and Mark, 1990)	(Wang et al., 1998)	(Gargano and Hager, 2002)	(Guymer et al., 2005)	(Mrowiec, 2007)	(Kim et al., 2008)	(Granata et al., 2014, 2011)	(Arao et al., 2012)	(Mark and Ilesanmi-jimoh, 2016)	(Rubinato et al., 2018)
Type of Manhole	I	IV	II	IV	I	I, II, III	III, IV	I, II, III	I, I-A	I-A	I-A	I-A, II, III	I-A, II, III	I-A	I, I-A	I-A	I-A
Part-Full pipes	-	X	X							X	X			X			
Filled pipes	X	X		X	X	X	X	X	X	X	X	X	X	X	X	X	X
Straight through flow	X	X		X	X	X	X	X		X	X	X	X		X		X
Varying pipe Diameter	X								X						X		
Varying manhole diameter	X					X	X	X			X			X			
Rectangular manhole	X	X	X	X	X	X	X										
Circular manhole	X			X		X	X	X	X	X	X	X	X	X	X		X
Varying drop in manhole	X												X	X	X	X	
Varying water depth in manhole	X	X		X		X	X	X	X		X	X	X		X	X	X
Supercritical flow										X				X			
Bend between inlet-outlet pipe									X				X		X		

Table 2.2: List of related studies on inline manholes using Computational Fluid Dynamics (CFD) modelling

	(Zhao et al., 2008)	(Lau, 2008)	(Stovin et al., 2013)	(Bennett, 2012)	(Saiyudthong and Guymer, 2005)	(Isenmann et al., 2016)
Type of Manhole	I	I-A	I-A	I-A	I-A	I
Part-Full pipes	X	X				X
Totally filled pipes	X	X	X	X	X	X
Circular manhole		X	X	X	X	
Square manhole	X					X
Bend between inlet-outlet pipe					X	
Software used	ANSYS	ANSYS	ANSYS	ANSYS	ANSYS	OpenFOAM
Free surface consideration	VOF	Rigid lid	Rigid lid	Rigid lid	Rigid lid	VOF

Studies have pointed out the very complex matter of energy losses in manholes. Some of the parameters which have found to affect the head losses include:

- The ratio between surcharge in the manhole and inflow pipe diameter (Mrowiec, 2007; Stein et al., 1999; Stovin et al., 2013)
- Diameter ratio between inflow pipe and manhole (Bo Pedersen and Mark, 1990; Stein et al., 1999; Stovin et al., 2013)
- Depth ratio between the upstream branches and the downstream channel (Taylor E.H., 1944)
- Upstream and Downstream hydraulic conditions (i.e. subcritical or supercritical), (Gargano and Hager, 2002; Zhao et al., 2008, 2006, 2004)
- Effect of bed discordance on the channel junction flow (Biron et al., 1996)
- Different flow rates for main pipe and combined lateral pipe (Ramamurthy and Zhu, 1997; Zhao et al., 2006)
- Different joining angle between lateral pipe and the main pipe (Arao et al., 2013; Mrowiec, 2007; Pfister and Gisonni, 2014; Stein et al., 1999; Zhao et al., 2008)
- Different ratio between water depth in the manhole and pipe diameter (Ramamurthy and Zhu, 1997)
- Different ratio between pipe diameter and manhole diameter (Ramamurthy and Zhu, 1997)
- Existence of sump inside the manhole and benching effects (Arao et al., 2012)
- Diameter ratios between inflow and outflow pipes (Arao et al., 2013)
- Ratio of flow rates between inflow pipes and outflow pipes (Arao et al., 2013; Stein et al., 1999)

- Drop gaps between the inflow pipe and outflow pipe (Arao et al., 2013)

Works from different researchers on measuring energy losses in manhole showed many different aspects of manhole characteristics. It has been found that the head loss coefficient is dependent on many variables. When considering junction manholes, it is crucial to calculate energy loss at manholes considering all variables of structural elements of the pipes and of the manhole which has not been accomplished yet (Arao et al., 2012; Rubinato et al., 2013).

Many authors explained the flow through the surcharge manhole in-line with the submerged jet theory (Bo Pedersen and Mark, 1990; Guymer et al., 2005; Guymer and O'Brien, 2000; Lau et al., 2008; Stovin et al., 2013). The theory was originally proposed by Albertson et al. (1950). Arao and Kusuda (1999) and Guymer et al. (2005) introduced the concept of 'Threshold surcharge' when describing the hydraulics of a surcharge Type I-A manhole. Their works showed that at a surcharge of approximately 20% of the manhole diameter, the manhole shows a very high head loss coefficient. The concept was followed by the work of Stovin et al. (2013) as the work introduced another term 'Threshold diameter ratio', describing that at a manhole to pipe diameter ratio of 4.4 for Type I-A manhole, the manhole hydraulic regime alters as well. At ratios over the described value, manholes are characterised with high head loss coefficients.

2.3 Gully

A gully is a small settling chamber or sump that can be found at the along the kerb of a road (Memon and Butler, 2002a, 2002b). Gully is also known as catch basin in some countries (Osborne et al., 1998). Primary task of a gully (inlets, catch pits) is to collect surface runoff and convey it to the drainage network below ground containing manholes and pipes.

Gullies consist of the grating to collect heavy material in the flow. An underlying connecting pipe connects the gully to the below-ground drainage system. Sometimes, a water seal is provided with the gully to block odour from coming outside; especially with the ones connected to a combined sewer system. (Butler and Davies 2011 p. 139).

Gully pots have been used historically to prevent coarse debris from entering the underlying drainage system. The prevention of sewer clogging was especially important before the existence of good quality street pavements (Scott, 2012). Even today, roadside gully structure is an important integral structure to collect surface water for both storm and combined sewer system (Butler et al., 1995). They are widely used in urban drainage networks, predominantly to prevent surface runoff from carrying solids and sediment into drains and sewers, and so that it cannot create obstruction or hydraulic constraint in the drainage system (Butler et al., 1995; Butler and

Memon, 1999; Deletic et al., 2000; Memon and Butler, 2002a, 2002b; Osborne et al., 1998). Some secondary uses of gully pots can be listed below:

- Preventing odours from combined sewers from escaping to the atmosphere (as mentioned above) in case connected to a combined system (Butler et al., 1995; Butler and Davies, 2011; Osborne et al., 1998);
- Retaining some fine sediment and so reducing the polluting load (Begum et al., 2008; Osborne et al., 1998);
- Retaining oil and other floating pollutants (Osborne et al., 1998)
- Reducing the risk of accidents caused by the build-up of water on the roads and in the gutters (Begum et al., 2008)

Inlets of gullies are rectangular and placed at the same level of the street or pavement. The inlet is covered by a grate of different sizes and shapes. In some countries, gully is replaced by a small drop manhole and covered with a grate and placed on streets following the same rules as for the gullies (Lopes et al., 2016a).

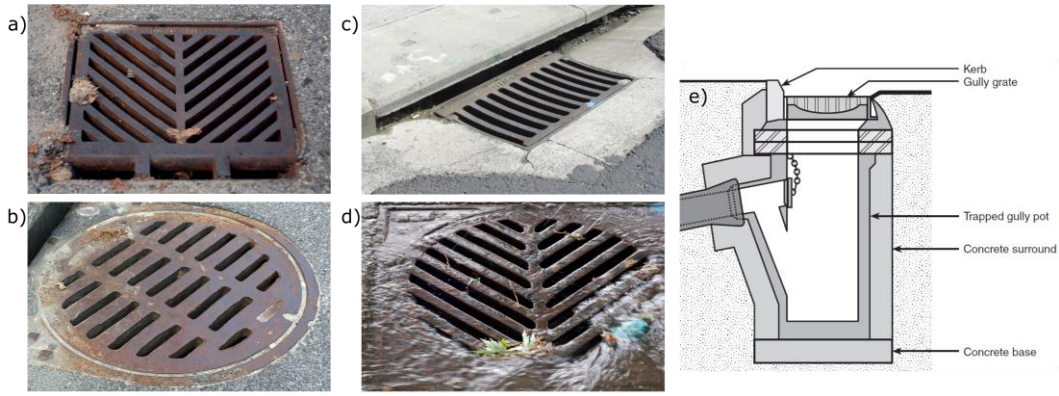

Figure 2.4: a to d) Different shape and gratings type of a typical roadside gully and e) the cross section of a gully[1]

Dry and wet weather condition

The operation of gully pot is different according to the wetness of the weather. During dry weather condition, biochemical processes connecting to degradation of bio matter (for example dry leaves) dominates. It creates a rapid drop in dissolved oxygen (DO) concentrations, especially in the

[1] Image sources of Figure 2.4: a) https://en.wikipedia.org/wiki/Storm_drain;
b) http://www.greateraugustautilitydistrict.org/wastewater-stormwater/stormwater-catch-basins
c) http://www.hynds.co.nz/product/stormwater-superpit/
d) https://www.smithsonianmag.com/smart-news/millions-dollars-worth-gold-and-silver-lurk-sewage-180953960/
e) adapted from (Butler and Davies, 2011, p. 141)

summer, creates an anoxic condition and anaerobic degradation (Butler et al., 1995; Memon and Butler, 2002a). Low DO levels result in the build-up of anoxic conditions and anaerobic degradation of the bottom sediments. Re-aeration occurs when sufficient rainfall passes through the pot. After a storm event inflow into the gully pot ceases and conditions become rapidly quiescent (Butler et al., 1995).

However, during wet weather condition, physical process connecting drainage and sediment flow govern. Incoming runoff rapidly displaces the standing liquor containing dissolved and suspended pollutant load (Butler et al., 1995). The wet weather processes usually include sedimentation, sediment bed build up, erosion of the top sediment layer, dilution and washout of the dissolved and suspended pollutants in the top liquor and re-aeration of gully liquor (Butler and Memon, 1999). As our focus is only on the physical processes, we shall not go into detail on the dry weather conditions.

Gully hydraulic efficiency

Gully hydraulic efficiency is dependent on the depth of water at the upstream, the flow width and the grating geometry (Butler and Davies, 2011). A typical efficiency curve is given at the bottom-left part of Figure 2.5.

The curve indicates that at low flow, almost 100% of the incoming flow is captured and the efficiency decreases with the increase of incoming flow after a certain maximum approached discharge (Q_1).

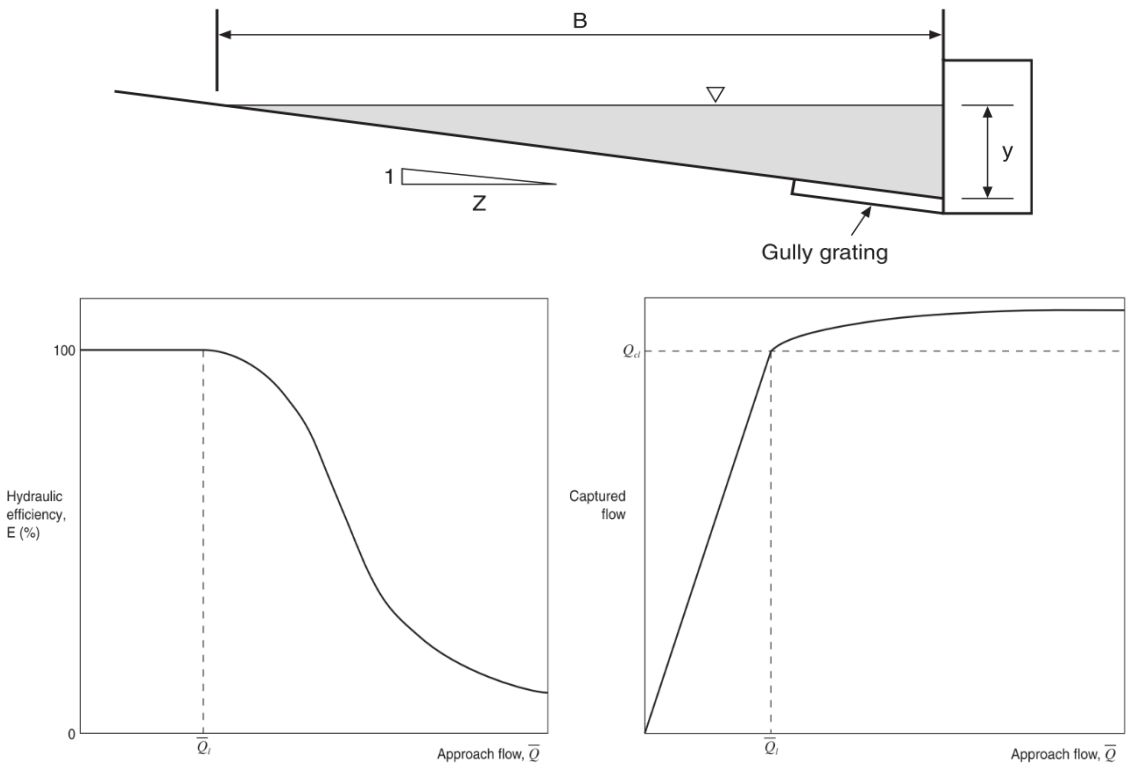

Figure 2.5: Geometry of road channel flow for gully water intake (exaggerated vertical scale) (top panel), Gully hydraulic efficiency curve (bottom-left panel) and typical captured flow vs approached flow of a gully (bottom-right panel); adapted from (Butler and Davies, 2011)

However, the plot of Captured flow vs Approached flow (Figure 2.5: bottom-right) shows that the captured flow can be more than Q_1, which was corresponding flow with 100% efficiency. A gully can intake additional flow due to higher flow depth. Thus, the capacity (Q_c) can be increased due to a bypass flow, which can be around 20%.

The hydraulic capture efficiency (E) for an individual gully become:

$$E = \frac{Q_c}{\overline{Q}} \tag{2.7}$$

where, E is a function of the type of grate, water flow width, road gradient and cross-fall.

The flow through a gully outlet follows the orifice equation (Carvalho et al., 2011; Lopes et al., 2016a; Mark et al., 2004; Martins et al., 2014). The equation can be described as:

$$\mathrm{Q} = \mathrm{C_d A_o} \sqrt{2\mathrm{gh_o}} \tag{2.8}$$

where, Q is discharge from the gully, $\mathrm{A_o}$ is cross-sectional area of the orifice, $\mathrm{h_o}$ is the head difference between the gully and the outlet, $\mathrm{C_d}$ is the coefficient of discharge of the orifice and g is acceleration due to gravity, which is 9.81 ms^{-2}.

However, in a practical scenario, the gully discharge coefficient is also connected to other variable of the flow. Li et al. (1954) conducted hydraulic tests at a ½ scale gully model with grating and proposed that the flow over the grate is

$$q = Q_0\left(1 - \frac{L^2}{{L_0}^2}\right)^2 \tag{2.9}$$

where, L_0 is the length of grating required to capture all the flow travelling on grating. The discharge coefficient also increase with the increase in longitudinal slope of the grate (Burgi and Gober, 1978). However, according to Johnson (2000) the traverse length of the gully can have almost no influence on the discharge coefficient.

The discharge coefficient can also be connected to the Froude's number of the flow and can be related as (Galambos, 2012):

For F_R < 0.6:

$$C_d = 0.611\sqrt{1 - \frac{3{F_R}^2}{{F_R}^2 + 2}} \tag{2.10}$$

For 0.6 < F_R < 1.0:

$$C_d = 0.45 - 0.06(F_R - 0.6) \tag{2.11}$$

For 1.0 < F_R < 1.8:

$$C_d = 0.95\sqrt{2 - \frac{3{F_R}^2}{{F_R}^2 + 2}} \tag{2.12}$$

For F_R > 1.8:

$$C_d = 0.632 - 0.018(F_R - 1.8) \tag{2.13}$$

Many experiments have been conducted to calculate hydraulic drainage efficiency (E) of a street gully. The results have been summarised in the design manual by the US Department of Transportation (Brown et al., 2013).

Gómez & Russo (2009) investigated several continuous grates and their hydraulic efficiency for storm events using physical experimental setup. Djordjević et al. (2013) investigated a full-scale cylindrical gully with grate using both experimental and numerical models. They used OpenFOAM VOF model to check the three dimensional model of the gully. They checked that the influence of

surface transverse slope on flow characteristics and showed that re-circulation zones could form downstream from the gully.

Martins et al. (2014) also investigated the drainage flow of the gully using experimental and numerical models. They showed that weir and orifice equations can characterise the flow at the gully outlet. During standard scenarios, gullies allow the water to be drained from the surface to the sewer system. However, the opposite directional flow may occur due to an exceptional event when gully may become pressurised and surcharged water may flood the surface area (Leandro et al., 2014c; Lopes et al., 2015). However, there has not been much work done considering gully hydraulic efficiency at reverse flow.

Both Lopes et al. (2015) and Martins et al. (2014) employed full-scale VOF based OpenFOAM model to analyse the flow behaviour. The investigated gully was represented by a rectangular box having a dimension of 0.6×0.3×0.3 m^3. They proposed different pressure vs flow curve and compared them with the experimental data.

Romagnoli et al. (2013) presented the gully turbulence characteristics at drainage condition. They observed higher turbulent kinetic energy at inlet centreline with anisotropy in Reynold's stress. A fast-flowing gully flow contains not only the liquid but also a lot of air bubble within it. Lopes et al. (2016b) investigated the air-entrainment in gully using CFD modelling tool. They specifically validated their model result for air bubble concentration in a gully with free surface flow.

2.4 Sediment in drainage system

Sedimentation and sediment deposits in urban drainage creates hydraulic overloading and loss of conveyance. This may lead to surcharging, surface flooding and premature operation of a combined system (Alvarez-Harnandez, 1990; Butler and Davies, 2011; Skipworth et al., 1999). Nevertheless, it creates problem to the ecosystem of the receiving water body as well. Much research has been conducted on the transport, settling, and scour of solids in sewers in especially in Europe (Ashley and Crabtree, 1992; Butler et al., 1995; Butler and Karunaratne, 1995; Cheng and Hsu, 2014; Larrarte and Chanson, 2008; Mark et al., 1996; Pitt, 2004; Schellart, 2007). Researchers have focused on the origin, processes and the flow of sediments of solids in the drainage system.

The source of solids in sewer system may originate from the flowing sources (Ashley et al., 2004):

- Atmosphere, containing dusts and aerosols,
- Surface of catchments, as solids accumulate during dry periods and wash off during storm events,

- Domestic sewerages, containing large organic contents
- Environmental processes in the water body, such as degradation, decay, infiltration/exfiltration, interaction
- Industrial and commercial effluents mainly from construction sites, which could be relatively high in terms of solid loads entering sewer

In most of the drainage system, the solids accumulates in the kerb, then passes to the gully. Part of the solids in gully is confined in the gully-trap and the rest transferred to the underground drainage system. The transport system of sediment in sewer is shown in Figure 2.6.

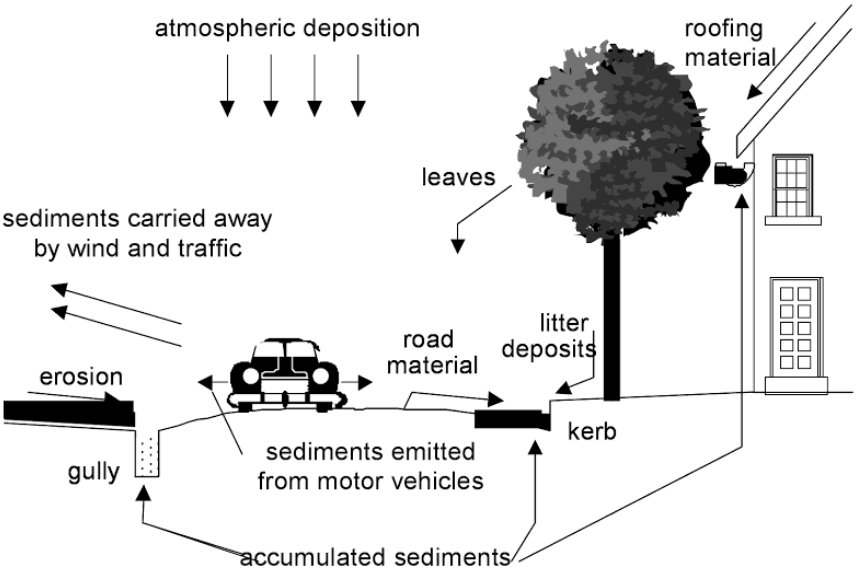

Figure 2.6: Solids transport and accumulation process (adapted from (Ashley et al., 2004))

During the storm event, solids gain access to the sewerage system as a suspension in the runoff (Butler and Karunaratne, 1995). There are other mechanisms involved, such as wind action, vehicle-generated turbulence, vibration, street sweeping and deliberate dumping of material (Butler et al., 1995; Butler and Karunaratne, 1995). The material supply rate within the same catchment area is highly variable, both spatially and temporally. The spatial variability may be connected to the land use pattern and human activities (Pratt et al., 1987). Pratt et al. (1987) found evidence that variability exists both between measurements of the contents of the gullies in the same 14-day period and between the results of one gully obtained in different periods of the year.

The peak time in solid accumulation can be different in different locations depending on the local climate and environment. Research in UK showed that November to December may be crucial

time for the locations with deciduous trees (Pratt et al., 1987). As an alternative example, in the work of Pratt et al. (1987), they found the peak gully solid accumulation in North London during June, when soil surfaces dried and water- or wind-mobilised material were readily available due to gardening and other human and animal activities. From June to February of the following year, material supply decreased with the decrease in outdoor activities. Ellis and Harrop (1984) checked the removal of sediment from the gully at a highway of metropolitan London and found seasonal variation influenced by both rainfall and surface flow characteristics.

Furthermore, total sediment weight removed from the road surface during the spring period was only 18- 20% of the summer loadings, which showed a close correspondence to both seasonal rainfall and flow characteristics (Ellis and Harrop, 1984). Grottke (1990) checked the loss on ignition analysis as a measurement of organic matter from dry gully pot samples. His findings were 6% – 10% greater in autumn than spring.

The sediment inside the gully pot mixes with gully liquor and the following can occur (Deletic et al., 2000):

- deposition of some of the input sediment and overall build-up of gully sediment deposits, or
- erosion of part of the existing sediment deposits, with a reduction in the depth of deposits

It has been found that in the invert of pipes there is often coarse, loose, granular, predominantly mineral material overlain by a mobile, fine-grained deposit (Skipworth et al., 1999). During low flow rates, deposition tends to occur, while erosion will occur only during the most intense storm events (Deletic et al., 2000). Roadside gully pots have been identified as potential sources and can make significant contributions to stormwater pollutant loadings (Morrison et al., 1995). A significant amount of sediment transport process takes place during the first flush storm of the wet season which may carry a significant mainly pollutant load as well (Butler and Davies, 2011, p. 300; Deletic, 1998). The likely sources of the first flush flood sediments are (Butler and Davies, 2011):

- Catchment surface wash off and gully pots: The first flush from this source would be expected as a result of the early rainfall washing off pollutants accumulated on the catchment surface and in gully pots since the last rainfall.
- Wastewater flow: Since the storm wave moves faster than the wastewater ‘base flow’, the front of the wave can consist of an ever-increasing volume of overtaken undiluted base flow. However, this is generally diluted to some extent by the inflow from intermediate branches.

- Near-bed solids: In many sewer systems, high concentrations of organic solids have been observed in a layer moving just above the bed. The added turbulence as the storm flow increases causes these solids to become mixed with the stormwater.
- Pipe sediments: Increasing storm flows provide suitable conditions for re-erosion of the deposited material.

Between storm events, the gully pot sediments and liquor change to the composition as a result of biochemical reactions (Morrison et al., 1995).

The particle sizes

Sediment flow within the sewer system is dependent on the type, particle size and specific gravity of the sediment. Many authors have worked on particle size distribution, e.g. (Bertrand-Krajewski, 2006; Verbanck, 1990). They have found variability in the size of particles according to their origin (Bertrand-Krajewski, 2006):

- particles deposited along roads and kerbs: diameter usually between 200 and 1000 µm; d50 of about 300-400 µm; specific gravity: 2.6;
- particles in domestic sewage: d50 is about 30-40 µm; specific gravity: 1.5;
- particles transferred in sewers by rain weather: very fine, d50 is about 30-40 µm, and are transported primarily in suspension; specific gravity: 2.4
- particles deposited in sewers: larger than those transported by suspension; d50 is about 200- 1000 µm, and they are transported primarily by rolling and saltating along the sewer invert; specific gravity: 2.6

Within the sewer trunk, d50 value diminishes within the distance from to inlet to outlet as a granulometric sorting. Although, some authors reported an increasing d50 of deposited particles at the same location with time, due to the consolidation of deposits by organic matter and/or by chemical precipitation (Roberts et al., 1988).

Transport process

The transport process of the sediment inside a drainage system is the most complicated part due to the following reasons (Bertrand-Krajewski, 2006):

- the insufficiency of available data for sewer systems
- the complexity of the physical process which involves bed and suspended loads, deposition and erosion processes
- the high number of parameters to be accounted for: velocities, shear stresses, collector's geometry, particles characteristics

Many researchers have worked on sediment transport, especially for fluvial hydraulics and solid transport in closed pipes. Although the transposition of their results and relations to urban hydrology and sewer systems is challenging due to different site conditions, like particle sizes, cohesiveness due to the presence of organic matters, turbulence and unsteadiness of flow, partial filling of pipe and presence of free surface flows. These factors may lead to a different mechanism in sediment transport.

Usually, solids are transported through the sewer in three ways:

- the bed load transport: the particles are sliding, rolling and saltating, without to leave the bed;
- the suspended load: the particles from bed material or other sources remain in suspension in the flow without definitive deposition, but temporary deposition is possible;
- the wash load: very fine particles which are permanently transported in the flow, without any deposition

The transport of solids by water in closed pipes has been studied by several authors, due to its economic interest. Durand (1953) proposed a distinction between different transport regimes about the particle diameter for graded sediments:

- **Homogeneous mixture**: for, d < 25 µm: particles always remain in suspension without deposition and with a homogeneously distributed concentration
- **Intermediary mixture**: for, 25 µm < d < 50 µm: this is a transition domain
- Heterogeneous mixture:
    - for, 50 µm < d < 200 µm: particles are transported in suspension with heterogeneous concentrations
    - for, 0.2 mm < d < 2 mm: particles are transported with intermediate conditions
    - for, d > 2 mm: particles are transported by saltation

Here, we shall focus on the transport process of cohesion less sediment particles as most of the sediment flow is transported through this process.

The suspended solids in the sewer may settle and accumulate as a deposit as biofilm during dry weather condition. The situation changes at a successive period of increased flow due to urban wet weather runoff. In addition to the suspended solids already in the runoff, a relative increase in the suspended solids concentration may occur during a successive period of increased flow due to erosion process (Ashley et al., 2004). Table 2.3 shows the size characteristics in suspended sediment in a sewer flow. The grain size characteristics for suspended solids in wet weather discharge can be generalised as:

- Fine particle: (<100 µm) dominate in the suspended phase at the downstream section of a sewer network. Particles smaller than 100 µm represent between 66 to 85% of the total mass with a median diameter ranging from 25 to 44 µm.
- Fine particle (< 100 µm) tend agglomerate.
- Results of size measurements are similar for a range of sewer systems and also for combined and separate systems.
- Solids entry in man-entry size sewers (< 1 m) are generally coarser than the solids transported in suspension in a storm or dry weather flow.

Table 2.3: Grain size indicator values of D10, D50 and D90 and %<100 µm for suspended solids in urban wet weather discharge (adapted from (Ashley et al., 2004)

Type of network	D10 (µm)	D50 (µm)	D90 (µm)	%<100 µm
Storm sewer networks	6-9	29-38	265-1375	76-85
Combined networks	4-13	25-44	183-497	66-82

The suspended sediment loads are kept in suspension by the upward flux of turbulence generated by the channel bed (Hickin, 1995). To keep the materials in suspension, the upward velocity has to be equal or higher than the particle fall-velocity. The settling velocity of suspended sewer solids is frequently represented by means of the median settling velocity (w50). Other indicators like w10, w35 or w90 are used in some models. Some typical values are given in Table 2.4.

Table 2.4: Typical mean values of settling velocity (adapted from (Chebbo, 1992; Stahre and Urbonas, 1990)

	Settling velocities (m/h)		
	W10	W50	W90
Combined sewer	<0.06	8.1	67
Separate sewers	0.37	7.2	89
Separate sewers (USA)	0.10	4.9	213

Several authors described mathematical equations to calculate settling velocities for non-cohesive sediment particle using properties of similar particle sizes. Some of the well-practised formulas are Rubey formula (1933), Stokes formula, Zanke formula (1977) and Van Rijn formula (1948). Although, it should be noted that these formulas consider two fundamental principles:

- the particle is spherical and uniform density
- the particle is isolated in an infinite water volume (i.e. free from particle-to-particle interaction)

Many transport relationships have examined the transport of sediment in pipes concentrated on the movement of non-cohesive sediment (Ackers et al., 2001; May, 1993; Nalluri and Alvarez, 1992). Some transport relationships have been derived to describe thresholds as the limit of deposition or to estimate the transport capacity of the flow (Skipworth et al., 1999). However, many of these relationships have been developed at a laboratory scale, which has yielded unique estimates of transport rate for a range of granular particles, typically sands, under a limited range of hydraulic conditions and, in some cases, with deposited beds (Ackers et al., 2001; Skipworth et al., 1999). So, in case of analysis with field level problems, where the sediments are a combination of different sizes and a significant proportion have cohesive properties (Nalluri and Alvarez, 1992; Skipworth et al., 1999), care should be taken in the analysis in order to obtain fewer uncertainties.

Figure 2.7 shows settling velocities measured using spherical quartz grains (Hickin, 1995, p. 75)

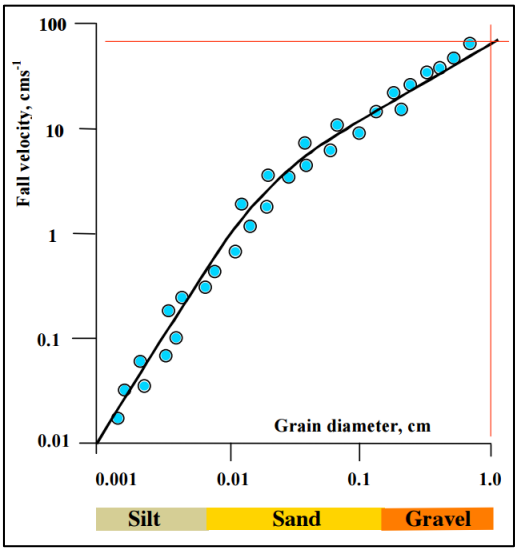

Figure 2.7: Fall velocity about the diameter of a spherical grain of quartz, adapted from (Hickin, 1995, p. 75)

2.5 Experimental flow measurement technique in a drainage structure

2.5.1 ADV

Use of Acoustic Doppler Velocimetry (ADV) (Figure 2.8) is one of the most common methods in measuring the velocity of fluids. It measures the three-dimensional velocity with the help of Doppler shift. An ADV measurement probe consists of three main component: sound emitter, three or four sound receivers and a signal conditioning electronic module (García et al., 2005). It uses Doppler principle to measure the velocity of an object. The principle is here described as explained by McLelland and Nicholas (2000) and Nortek (2013).

An ADV cannot measure the velocity of fluid if there is no impurity or seeding. The sound receivers of the ADV instrument can only collect the signals when it reflects from another particle in the fluid.

The ADV uses the shift to estimate velocities using the Doppler relationship shown below:

$$\Delta f = 2 f_{ADV} c v_{rel} \tag{2.14}$$

where, Δf is the change of frequency, C is the sound speed and f_{ADV} is the operating frequency (10 MHz at most cases). A Doppler shift is estimated from a pair of two signals. According to McLelland and Nicholas (2000), the ADV uses this pair of pulse scheme with unequal pulse repetition rates (τ_1 and τ_2) which are separated by a time duel (τ_D). The phase-shift is calculated from the auto and cross-correlations computed from a single pulse-pair. McLelland and Nicholas (2000) reported that, τ_D = 560x10^{-6} s for a Nortek ADV. Thus the time difference between two pulse pair dt becomes:

$$dt = \tau_1 + \tau_D \tag{2.15}$$

The signal phase change (dΦ) is proportional to the velocity component along the bisector of the transmitted and received signals. The phase change is related to the radial flow velocity (v_i) according to the following Doppler relation:

$$v_i = \frac{C}{4\pi f_{ADV}} \frac{d\emptyset}{dt} \tag{2.16}$$

A MicroADV performs a sequential sampling of each receiver while a Vectrino performs a simultaneous sampling for all the receivers (Carvalho, 2015). Hence, the total time for a sample velocity collection T for a MicroADV becomes:

$$T = 3(\tau_1 + \tau_D + \tau_2 + \tau_D) \tag{2.17}$$

and for a Vectrino:

$$T = (\tau_1 + \tau_D + \tau_2 + \tau_D) \tag{2.18}$$

This makes the sampling rate of a vectrino higher than a microADV. ϕ is unambiguously defined for ±π. This leads to a maximum measurable velocity, V_{max}:

$$v_{max} = f_{pr} \frac{C}{4\, f_{ADV}} \tag{2.19}$$

where, fpr is known as pulse repetition rate (PRT), which is inverse to the time between pulses 1 and pulse 2 transmissions and also known as the pulse repetition frequency (PRF), distance, or lag:

$$f_{pr} = \frac{1}{dt} \tag{2.20}$$

There is also a specific range for coherent pulse operation, r_{max}:

$$r_{max} = \frac{C}{2f_{pr}} \tag{2.21}$$

Combining equation (2.19) and (2.21) becomes,

$$r_{max} v_{max} = \frac{C^2}{8f_{ADV}} \tag{2.22}$$

This equation shows the limitation of a particular ADV. In case of measuring higher velocity, the sampling range becomes small. In case of measuring in water, C=1500 m/s and f_{ADV}=10 MHz, the value is close to 0.03.

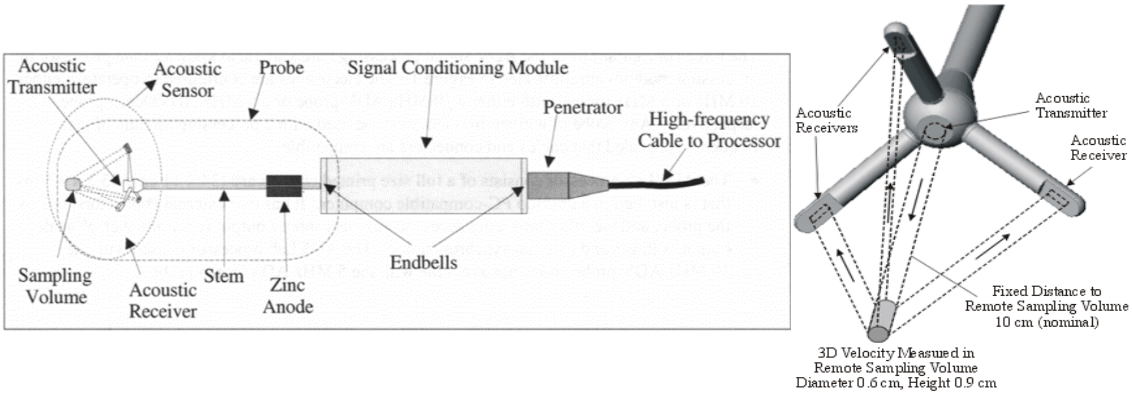

Figure 2.8: Schematic of Sontek ADV Probe adapted from *Palmer (2002)* (left panel) and Sontek web page (http://www.sontek.com/productsdetail.php?10-MHz-ADV-2) (right panel)

There might be several source of error in using ADV. Some of them has been enlisted here as per Carvalho (2015).

- errors due to the experimental setup (e.g. misalignment of the instrument);
- errors due to physical constraints of the measurement technique (e.g. the size of the sampling volume and sampling frequency of the instrument);
- statistical errors due to sampling a random signal, and
- errors due to the methodology used to compute the parameters (e.g. scaling relations only provide order of magnitude estimates of a parameter)

Sometimes, echoes from past pings can affect the present measurements. This is known as pulse interference and Weak Spots. The user always needs to do a proper post-processing before using the data. There are a lot of theories published about cleaning the spikes in an ADV data sample. One well adept method is described by (Goring and Nikora, 2002; Nikora and Goring, 2000). It has the added advantage that it requires no parameters method combines three concepts:

1- differentiation enhances the high frequency portion of a signal,
2- the expected maximum of a random series is given by the Universal threshold, (Phase-Space Thresholding)
3- good data cluster in a dense cloud in phase space or Poincare

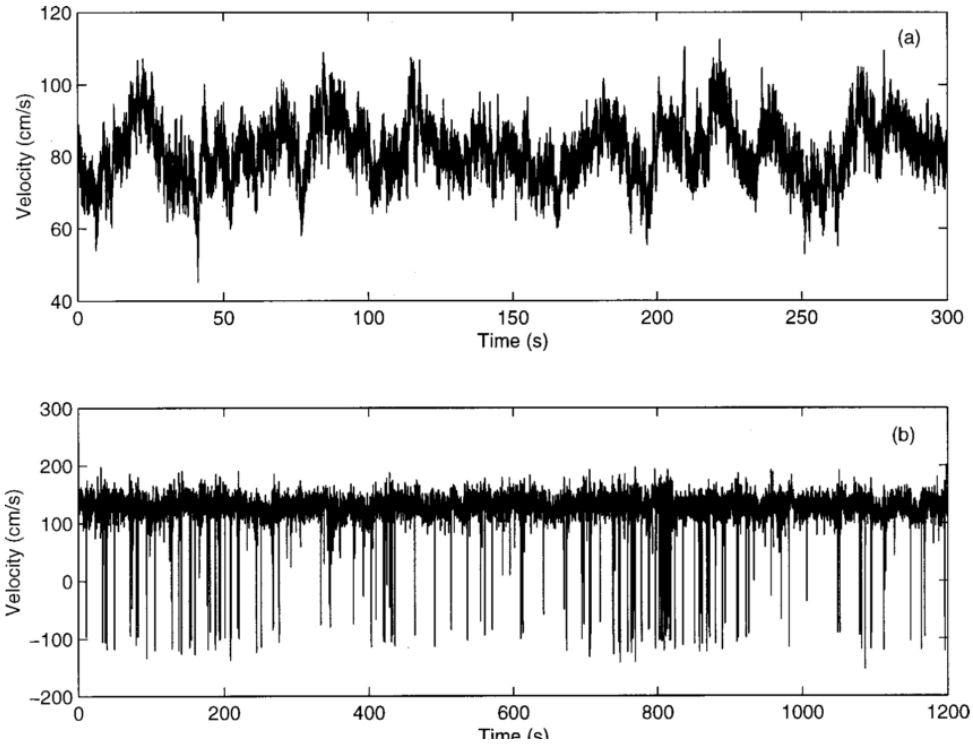

Figure 2.9: Example of cleaned data (upper panel) and contaminated data (bottom panel), adapted from *Goring and Nikora (2002)*

The uses of ADV is well practised for different purposes at both in the laboratory and in the field. The main uses of ADV as measuring the three dimensional velocity field reported by Leandro et al. (2014c), Lopes et al. (2014) and Lopes et al. (2015). As ADV can be used for very frequent velocity data acquisition, this method is also used in characterization of turbulence structure of a fluid. Voulgaris and Trowbridge (1998) and Nikora et al. (2001) used ADV data to characterise an open channel flow over a rough bed, while Romagnoli et al. (2013) used similar procedure in characterizing turbulence phenomena of a surcharged gully. Unlike previously mentioned works,

Chanson et al. (2008) also described the use of ADV backscatter data in measuring suspended sediment concentration in an estuary.

2.5.2 PIV Method

Particle Image Velocimetry (PIV) is an image-based technique and becoming widely used for observing fluid flow. Laboratory Particle Image Velocimetry (PIV) experiments provides high-resolution 2D spatial flow field data (Stovin et al., 2008). In PIV measurement, a sheet of light (usually laser light sheet) is used to illuminate the observing particles and some particles are seeded in the fluid. One or more high speed camera is used to record the positions of the seeding particles at a very short interval. The displacement of an individual particle is measured from two successive image frames. The time interval between the two images can give the velocity of the particle. Thus, the velocity of the fluid is measured assuming that the particle moves with the same speed as the fluid. A group of discrete particles inside the fluid can give the flow velocity of the whole fluid plane. Figure 2.10 shows a 2D plane PIV velocity measurement of a scaled manhole.

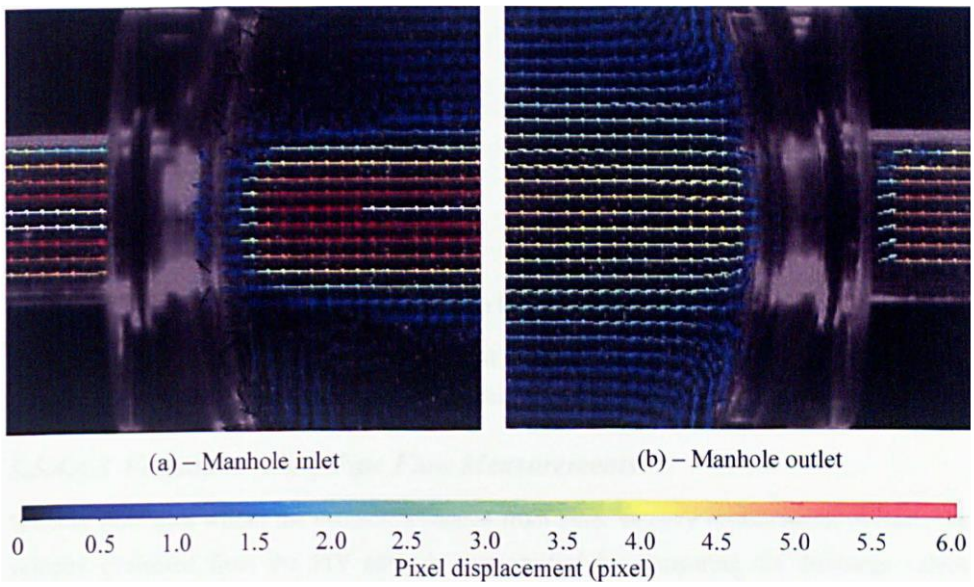

Figure 2.10: PIV measurement at the horizontal plane of a scaled manhole (adapted from Lau (2007) p. 185, their figure 5.28)

However, in a classical PIV measurement technique only one camera is used, and the resultant velocity can be obtained only at a 2D plane parallel to the plane of camera. The velocity component at the perpendicular to the camera frame cannot be determined as the camera cannot capture it. So classic PIV approach is not favourable for measuring three dimensional complex velocity field (Prasad and Adrian, 1993). For this reason, recent advancements in PIV technique include the holographic PIV (HPIV) technique (Barnhart et al., 1994), three-dimensional (3D)

particle-tracking velocimetry (3D-PTV) (Virant and Dracos, 1997), tomographic PIV (Elsinga et al., 2006), and the stereo PIV (SPIV).

The stereo PIV technique has some advantages in comparison to the other methods mentioned. Three dimensional PTV and tomographic PTV use three or more cameras and generate a 3D image, and thus 3D displacements of the tracer particles are determined by using particle tracking (3D PTV) or 3D correction-based algorithm. In these methods, the position of all the tracer particles in the measured volume is required to be recorded with each recording cameras; which is very difficult in most cases. It becomes more difficult in case of high-resolution cameras. Consequently, these methods involve lower resolution images and the results may miss small-scale vortex structures in the flow (Hu, 2013). Stereo PIV method can overcome this issue and take a simultaneous measurement with higher resolution images. It uses two cameras with separate viewing angles. Later, two velocity fields are combined using geometrical equations derived from corresponding camera positions relative to a target object and the third velocity component is calculated (Martínez-Suástegui, 2012).

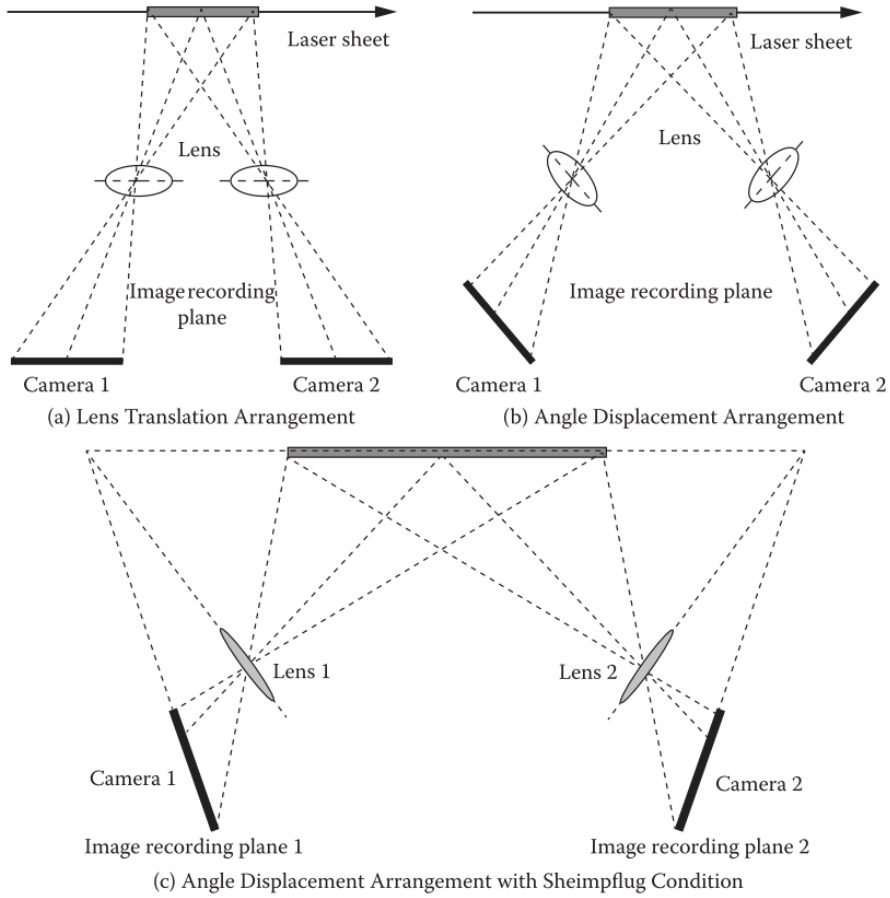

Figure 2.11: Three different camera placement options for stereo PIV (a) Lens Translation Arrangement, (b) Angle Displacement Arrangement and (c) Angle Displacement Arrangement with Sheimpflug Condition. Image adapted from (Hu, 2013, fig. 4.3).

Three different camera arrangements are well practised in stereo PIV method (Figure 2.11). They are:

- Lens Translation Arrangement: This is the most straightforward approach for stereoscopic image recording. The two cameras are placed side by side and parallel to the target object (Figure 2.11 a). Due to parallel geometry, the ratio of image distance to object distance is the same throughout the image plane. It makes the combining of the two image vectors easier. Nevertheless, in case of applying this method in liquids, the change of air to liquid refractive index, and the magnification varies over the image field which violates the main merit of using lens translation arrangement at the first place. Again, a larger angle between the two cameras is desirable for good accuracy of the velocity vector which is absent in this method. As a result, the camera sensors are usually moved closer to the outer edge of the image circle. Then again, sometimes this may affect the image quality of the recorded image due to lens aberration issue.
- Angle Displacement Arrangement: At this arrangement, the two cameras are set at a particular angle (Figure 2.11 b) with the measurement plane. It gives the freedom to have a larger overlapped view region that allows the user to have a larger flow field in common. However, this arrangement has certain disadvantages as the best focal plane for each camera is the plane parallel to the corresponding camera plane; but not the plane of the target object/illuminating plane (Hu, 2013, p. 76). To overcome this issue, the depth of field of the camera needs to be increased by increasing the aperture of the lens. This lowers the image intensity and may require stronger intensity/power of the laser source.
- Angle Displacement Arrangement with Sheimpflug Condition: This method has been described by Prasad and Jensen (1995). In this arrangement, the image sensor plane of the camera is tilted in such a way, so that the sensor plane, lens principle plane and the target plane intersect at a line (Figure 2.11 c). In this approach, the best focus plane of the camera remains the same as the target plane and thus overcomes the focussing issue in angle displacement method. It also enables the image sensors to be near the optical axis of the camera lens, so that the acquired image quality is better compared to those of lens translation approach. For these reasons, Sheimpflug Condition approach is the most common approach for stereo PIV measurement.

Uncertainty associated with Stereo PIV measurement

One of the main uncertainties in the stereo PIV measurement comes from the viewing angle of the two cameras. While considering the accurate measurement of the out of the plane velocity component, it is very crucial to have a good camera angle. According to Adrian and Westerweel

(2011), the random error within the plane and out of the plane are related according to the following equation:

$$\frac{\delta_y}{\delta_x} = 1/\tan\alpha \tag{2.23}$$

where, δ_y and δ_x are the random errors towards out of the plane and within the plane respectively and α is the camera viewing angle. Setting the camera viewing angle to 45° degree makes the vector measurement accuracy unbiased to any direction.

The spatial resolution of the PIV plays a crucial role in determining the measurement accuracy. In PIV measurement, it is crucial to pinpoint the centre of each particle in the image, and it is directly related to the spatial and the temporal resolution of the PIV instruments.

In a PIV measurement, if the pulse interval of the laser light is Δt, the vector calculated at the image plane due to particle displacement will be calculated using the following relation (Adrian, 1997):

$$\Delta \boldsymbol{X}_p \cong M_o \boldsymbol{v}_p \Delta t \tag{2.24}$$

where, M_o is the optical magnification of the object which is determined internally by the image accusation software from the calibration data as the ratio of the distances: a) *from the camera lens to the image plane* and b) *from the camera lens to the image sensor*, the $\boldsymbol{v}_p$ is the velocity vector of a particle and $\Delta \boldsymbol{X}_p$ is the displacement of a single particle in the image plane. Small value of Δt is desirable for an instantaneous velocity observation; however, it cannot be made too small for two reasons. Firstly, there is always an uncertainty associated with the response time of the particle. Secondly, to make an accurate measurement, the particle displacement needs to be considerably bigger than the uncertainty in particle position. According to Adrian (Adrian, 1986), this uncertainty is directly associated with the optical resolution. Each PIV system accuracy is defined by a constant of the system. Moreover, due to the noise in the image, the shape of one particle in two successive images may also appear differently and contribute to uncertainty in determining the particle location. This particular uncertainty is associated to the seeding particle diameter (Adrian, 1997).

To pinpoint the positioning of each particle in the image, the sub-pixel accuracy method using three-point Gaussian interpolation (Nobach and Honkanen, 2005) is known to be the best method. In this method, the positioning accuracy can be reached up to 0.01 pixel of the image considering each particle are visible as 2-3 pixels in the image (Nobach et al., 2004; Nobach and Honkanen, 2005).

Each PIV instrument has a range considering the minimum to maximum resolvable length, (known as the Dynamic Spatial Range, DSR) and maximum to minimum resolvable velocity (known as Dynamic Velocity Range, DVR) (Adrian, 1997). They are related as:

$$(DSR)(DVR) = \frac{L_x}{c_\tau d_\tau} = constant \tag{2.25}$$

where, L_x is a constant depending on the pixels size of the camera, c_τ is a constant concerning the ability of the analysis procedure to calculate the particle displacement between two consecutive images and d_τ is the particle diameter in the recorded image. If the measurement plane has both high and low velocity particles, the DVR increases. This effectively decreases DSR.

The influence of seeding particle in PIV measurement is connected to two fundamental properties of the particles: particle size and particle density (Van Overbrüggen et al., 2016). A primary source of error is the influence of the gravitational forces of the seeding particles, which would introduce an additional velocity component towards the gravity (Raffel et al., 2007). This induced velocity can be calculated using Stoke's law:

$$U_g = {d_p}^2 \frac{\rho_p - \rho}{18\mu} \tag{2.26}$$

where, d_p is the particle diameter (normally in the range tens of micron), ρ_p is the particle density, ρ is the density of water (998 kg/m^3 at 20 ˚C), and μ is the dynamic viscosity of water (1.0016×10^{-3} Pa at 20 ˚C). It is recommended to use a particle which has a density very similar to water which makes the downward velocity small.

The velocity measurement may also have a strong dependence on the particle diameter (Van Overbrüggen et al., 2016) considering Stokes number in the cases of changing fluid velocities. Higher Stokes number indicates that the particle tends to show a different flow path line than the actual fluid flow path. This phenomenon is also known as slip velocity (Kulick et al., 1994). The Stokes number can be calculated as:

$$S_t = \frac{\tau_p}{\tau_f} \tag{2.27}$$

where, τ_p is the particle relaxation time and τ_f is the characteristic time scale of the fluid. Particle relaxation time can be estimated as:

$$\tau_p \cong \frac{\rho {d_p}^2}{\mu} \tag{2.28}$$

According to the seeding particle properties, the relaxation time can be in the range of 0.01 s. The value of τ_f is particularly connected to the acceleration or deceleration of fluid. It is the time required for the fluid to change its velocity. To calculate the fluid characteristic time τ_f, the following equation was considered:

$$\tau_f = \frac{l}{\Delta u} \tag{2.29}$$

where, l is the characteristic length and Δu is the maximum change of fluid velocity within that length.

$S_t \leqslant 0.1$, exhibits an accuracy in the measurement with less than 1% error whereas at S_t = 1, the measurement error can be up to 18% (Van Overbrüggen et al., 2016).

Wilson and Smith (2013) reported that the PIV measurements could be 'noisy' at high shear regions such as manhole wall. The uncertainty of vorticity and velocity divergence at high shear regions depends on the spatial correlation error of particle displacement. Particular high-resolution image recording for this region may decrease the noise. Moreover, according to Seol et al. (2013), the uncertainty in Stereo PIV measurement is not homogeneous in the whole measured plane. The test error increases near the image edges and decreases at the image centre.

2.6 CFD Modelling of urban drainage structure and its challenges

2.6.1 CFD modelling

Computational Fluid Dynamics (CFD) is a group of techniques to solve the Navier- Stokes equations by satisfying mass, momentum (with added energy conservation equations in some cases) and predict the flow behaviour of a fluid. CFD gives an insight into flow patterns that are difficult, expensive or impossible to study using traditional (experimental) techniques. However, the CFD model results or modelling methodology needs to be validated with laboratory measurements and/or other validated CFD models. CFD presents itself as a useful tool for investigating physical system design and performance variables as computer-aided engineering (CAE) software (Jarman et al., 2008). With the advances in computer and hardware tools, CFD modelling has been making itself an excellent competitive tool with physical modelling (Butler and Davies, 2011, p. 347).

High turbulence phenomena and multi-phase flow is often seen at an urban drainage structure. In some cases, the flow collects water through different runoffs after the rainfall and adds the sand particles to it. After that, it can be termed as a three-phased flow containing solid-liquid and gas phases within. Moreover, when the flow enters a hydraulic structure, like for example a manhole, the flow undergoes a sudden expansion, decrease of Froude number, drop of head loss,

added vorticity, change of turbulence energy, mixes with air bubbles. When modelling such phenomena, a particular set of mathematical equations needs to be chosen that can address all these issues. Three dimensional CFD modelling can be the best option to model these types of flow as the Navier-Stokes equation can describe all the fluid property described. The multi-phase physics can also be modelled with the proper interpretation of multi-phase physical properties such as surface tension, elasticity, viscosity, drag force etc. There is the inherent complexity of multiphase flows, from both physical and numerical point of view. Still, numerous application examples can be found in the chemical, petroleum, pharmaceutical, agricultural, biochemical, food, electronic, and power-generation industries, where authors addressed different problems by simplifying assumptions of some properties so that the primary goal of the modelling remains valid. Here we will address some challenges in multiphase flow connected to urban drainage structures modelling.

2.6.2 Prediction of water surface

The most common issue with multiphase modelling is the prediction of the free surface, i.e. the interface between air and water phases. The reasons of difficulties in predicting the surface are the following:

- Phase interface separating the liquid-gas is extremely thin. Hence it involves a numerical discontinuity
- Density change across the phase interface is significant (in the order of 1000)
- Phase interface has a localised force known as surface tension which acts tangentially to the interface
- The topology may subject to rapid change (in case of unsteady flow)

The methodologies to predict the location of free surface can be classified into two groups (Ubbink, 1997).

1. Surface methods
2. Volume methods

Surface Methods

The surface method can represent the interface in many ways. The first way is to use spatial marker points which can be tracked explicitly. Between two marker positions, the surface position is interpolated using piecewise polynomial. The second way to represent the surface using this method is to attach the surface position at the edge/surface of a moving mesh (Ubbink, 1997). The accuracy of the surface tracking is dependent on the stability and precision of the

interpolation method (Hyman, 1984). There are some ways of representing the interface (Ubbink, 1997):

a) Particles on interface method (Daly, 1969)
b) Height function method (Nichols and Hirt, 1973)
c) Level set method (Osher and Sethian, 1988)
d) Surface fitted method (developed by various authors)

With this method of surface tracking, the interface remains sharp throughout the calculation. Using this method also reduces the computational approach to mark the interface curvature and the surface tension along with it.

Volume Methods

In the volume method, the interface is not well defined. So, calculation and application of surface tension force is an issue in this method. Special techniques are applied to find the exact position of the interface (Ubbink, 1997). On the other hand, they can only and accurately account for the interactions smooth varying interfaces (Hyman, 1984). Two essential techniques to describe the interface have been developed:

a) Particles on fluid method: Some massless particles are assumed to be spread over the cell volume of one fluid type. A cell volume without any marker particle is considered as empty or filled with gas or filled with another type of fluid. The cells with marker particle adjacent to the empty cells contain the free surface. In this method, the markers do not track the surface directly but track the volume of fluids, and hence the free surface is just the boundaries of volume. One important contribution under this method is Marker-And-Cell (MAC) method, proposed by Harlow and Welch (1965).
b) Volume fraction methods: A scalar indicator function with values ranging from 0 to 1 is the indicator of the volume fraction corresponding to one fluid or the liquid in case of liquid-gas modelling. If the value for a cell is 1, that indicates that the cell is occupied fully with the fluid. A value of 0 represents, the cell contains no fraction of the fluid. Thus, cells containing values between 0 and 1 is considered to contain the interface. Authors report three important volume fraction methods:
    i. DeBar's method (DeBar, 1974)
    ii. SLIC method (Noh and Woodward, 1976)
    iii. Hirt and Nichols' VOF method (Hirt and Nichols, 1981)

The VOF method has the advantage of the volume occupied by one fluid not being able to be occupied by the other and thus the continuity is always verified (Ubbink, 1997). The flow

properties (i.e. density and viscosity) are a weighted mixture of the properties of both phases. The main downside of the VOF technique is that in numerical simulation with large grid sizes, the formation of small bubbles or droplets, smaller than the minimum grid size, is ignored.

2.6.3 Choice of turbulence modelling

Turbulent flows are highly unsteady. The direction of the velocity field fluctuates rapidly in all three spatial dimensions. These flows fluctuate on a broad range of time and length scales. Therefore it can be tough to correctly simulate these types of flows (Furbo et al., 2009).

High Reynolds number and unsteadiness characterise the flow regime inside a drainage system. To model flow inside a hydraulic structure using CFD, the model must resolve the turbulent characteristics of the flow structure. For most urban drainage problems of practical interest, the flows can generally be turbulent. However, there are exceptions such as in low depth flows or low-velocity surface run-off flows.

Turbulence energy can be dissipated in several length scales, starting from the smallest length scale, the viscous scale to the largest scale, the productive scale (Kolmogorov, 1941). A Direct Numerical Simulation (DNS) can resolve all the length scales of a turbulence structure by solving the complete Navier-Stokes equation numerically (Moin and Mahesh, 1998; Pope, 2000). However, solving all the length scale of a turbulence structure requires too much computational effort as the mesh resolution must be very fine as well as with very small timestep is required, which is impractical to apply in most cases. The applications of DNS are consequently limited to turbulence research and results from DNS simulations can be important to verify results from other turbulence models. Several assumptions can be made to minimise the computational cost.

Large Eddy Simulation (LES) is a less computationally expensive approach which models only the large-scale eddy motions. Large-scale motions are generally more energetic than the small-scale ones. This method is proposed by Smagorinsky (1963) and developed by Deardorff (1970). LES is an implication of Kolmogorov's (Kolmogorov, 1941) theory of self-similarity is that the large eddies of the flow are dependent on the geometry while the smaller scales more universal. This feature allows one to solve for the large eddies in a calculation explicitly and implicitly; accounting the small eddies by using a subgrid-scale model (SGS model). LES is considered good enough to resolve near-wall flows, reacting flows and multiphase flows.

Although LES is less computationally expensive compared to DNS, but still very costly for many engineering applications. Reynolds-averaged Navier-Stokes (RANS) modelling is another turbulence approach which is cheaper than both DNS and LES. In the RANS approach, all of the unsteadiness in the flow is averaged out and regarded as part of the turbulence (Furbo et al.,

2009). Averaging the non-linearity of the Navier-Stokes equations give rise to terms that must be modelled, called the Reynolds stresses. These are the turbulent scalar fluxes. The presence of these new quantities in the conservation equations means that they contain more variables than the number of the equations. Therefore, one must introduce approximations for the Reynolds stresses and the turbulent scalar fluxes. Depending on the approximations and number of additional equations required, there are several RANS models available. Such as zero-equation model (Mixing-length), one-equation model, two-equation model (k-ε, k-ω, SST k-ω) and seven-equations (RSM - Reynolds Stress Model). The computer requirements to use these models are modest, so RANS is primarily used on most of the CFD problems.

Many authors have reported using k-ε models for modelling flow behaviour in a manhole. Some examples of using turbulence models in modelling of manhole and gully are presented here. Beg et al. (2016a) used the standard k-ε model in a two-phase VOF model results to compare with discharge and surcharge water depth in a prototype type 1 manhole and compared flow fields of at different inflow and surcharge level. Saiyudthong and Guymer (2005) also used the standard k-ε model to check head loss at a manhole due to change in pipe direction at a manhole.

The standard k-ε model is widely used and highly validated for specific flows and performs particularly well in confined flows. Despite the success of the model under some conditions, it has an only moderate agreement in unconfined flows. It has been reported that the model does not perform well in weak shear layers and drastically overpredicts the spreading rate of axis-symmetric jets in stagnant surroundings (Bennett, 2012; Versteeg and Malalasekera, 1995). This weakness may be apparent in the 'above threshold' surcharge condition where the flow is dominated by an axis-symmetric jet surrounded by stagnant (or gently recirculating) flow.

Realizable k- ε model predicts the spreading rate of both planar and round jets more accurately. It is also likely to provide superior performance for flows involving rotation, boundary layers under strong adverse pressure gradients, separation, and recirculation' (ANSYS Ins, 2009).

RSM model is better in representing streamline curvature, swirl, rotation and changes in rapid strain rate more rigorously than other simpler (one and two equation) models. Thus, use of the RSM is recommended when the flow features of interest are complex (Bennett, 2012).

Stovin et al. (2013) and Sonnenwald (2014) used the Realizable k-ε model for predicting the flow field in a surcharged manhole. Djordjević et al. (2013) used the k-ω model for predicting the flow field at both drainage flow and reversing flow condition of a gully. Bennett (2012) used Standard k-ε, k-ω, SST k-ω RANS model to investigate solute transport characteristics in a surcharged manhole. Stovin et al. (2007) used the Reynolds Stress Model associated with second-order spatial discretisation schemes to investigate the flow field within the surcharged manhole and compared

with velocity data observed with the PIV method. Lau et al. (2007) used the RNG k-ε model to compare solute characteristics in a surcharged manhole.

Despite several applications, it has been reported that RANS models do not perform very well in near-wall flow. It is recommended to use LES model when flow near the wall is essential. Due to the higher computational time required, LES models are less applied in engineering problems.

2.6.4 Choice of appropriate CFD tools

CFD software solves the governing equations of fluid motion, consisting of equations describing mass, momentum and energy conservation, to obtain transient, three-dimensional solutions. Averaging or filtering the Navier-Stokes equations is current practice in hydraulic engineering applications. The equation can be stated as:

$$\frac{\partial \rho}{\partial t} + \nabla.(\rho \boldsymbol{u}) = 0 \tag{2.30}$$

$$\frac{\partial \rho \boldsymbol{u}}{\partial t} + \nabla.(\rho \boldsymbol{u}\boldsymbol{u}) = \rho \boldsymbol{g} + \nabla.\sigma \tag{2.31}$$

$$\frac{\partial \rho e}{\partial t} + \nabla.(\rho e \boldsymbol{u}) = \rho g \boldsymbol{u} + \nabla.(\sigma \boldsymbol{u}) - \nabla.\boldsymbol{q} + \rho Q \tag{2.32}$$

where ρ is the fluid density, $\boldsymbol{u}$ is the velocity vector, $\boldsymbol{g}$ is the acceleration due to gravity, σ is shear stress tensor, e is the total specific energy, Q is the volume energy source and **q** is the heat flux.

To model flow in a hydraulic structure in an unpressurised system, a free surface simulation needs to be included in the model. To model the free surface flow accurately, the volume of fluid (VOF) method (Hirt and Nichols, 1981) is considered one of the best options (Carvalho et al., 2008). Several CFD tools are available that have the VOF method included. The following gives a basic overview of the available software tools that incorporate free surface simulation.

FLOW-3D

FLOW-3D® is a general purpose CFD commercial software tool with a Graphical User Interface (GUI) that solves the governing equations of fluid motion to obtain transient, three-dimensional solutions. FLOW-3D® has been extensively used in hydraulic engineering applications. FLOW-3D uses the Finite Volume Method (FVM)/Finite Differences Methods (FDM) to solve the equations of fluid motion in a Cartesian staggered grid. The Fractional Area/Volume Obstacle Representation (Hirt and Sicilian, 1985), named FAVOR™ method is one of the major features of FLOW-3D. In this tool, obstacles are modelled as zero-volume porosity regions, and the six components of wall shear stress are included implicitly in the equations to avoid numerical instabilities.

ANSYS FLUENT/CFX

ANSYS Fluent is one of the most popular CFD software tools. Similar to FLOW-3D, it is also a commercial software tool and comes with a GUI. The software package includes well-validated physical modelling capabilities that can deliver fast, accurate results for an extensive range of multi-physics applications. Along with ANSYS Fluent, another primary ANSYS product is ANSYS CFX. With the combined capabilities of these products, one can simulate a wide range of phenomena: aerodynamics, combustion, hydrodynamics, mixtures of liquids/solids/gas, particle dispersions, reacting flows, heat transfer, and much more. Steady-state and transient flow phenomena are easily and quickly solved. For fluid interaction, ANSYS Fluent offers finite volume based 2D and 3D simulation results at both staggered and non-staggered grids. The software package has different solvers to give solutions of multi-phase physical and chemical analysis (ANSYS Inc, 2013).

OpenFOAM®

OpenFOAM® meaning "Open source Field Operation And Manipulation" is a freely available open source platform containing several C++ libraries and applications which can numerically solve continuum mechanics problems (Weller et al., 1998). Its implementation is based on a tensorial approach using object-oriented programming techniques and the FVM. The toolbox enables the development of customised numerical solvers and contains pre and post-processing utilities.

Unlike the first two mentioned software packages OpenFOAM is freely available and probably contains the biggest library of solvers to choose from. On top of that, OpenFOAM has its source code freely available. This vast library made it popular with researchers as they can adapt the codes according to their needs. Considering these issues, OpenFOAM is chosen for our research work to consider uncertainty in drainage structures.

Out of several solvers OpenFOAM offers, the interFoam solver is chosen for our research work. This solver includes a VOF method to model free surfaces which is ideal for flow in urban drainage systems. Several turbulence models can be applied within this solver. Moreover, the code of the interFoam solver can be optimised with added equations to calculate solute and suspended materials if needed.

2.7 Description of OpenFOAM model

2.7.1 interFoam Solver

The basic code of OpenFOAM is Navier-Stokes equations, which theoretically can describe all the fluid phenomena. These equations can be applied to both compressible and incompressible fluids.

For engineering application of flow in an urban drainage structure, the following assumptions are made, and corresponding flow steps were taken.

- The compressibility of fluid is not important: All fluids were considered incompressible.
- Resolving smallest temporal and spatial turbulence scale is not necessary: RANS models are good enough to represent the flow.

Moreover, at a fully surcharged sewer junction, the water level position in the structure is important. For these conditions, it is necessary to simulate the flow using a model that can consider free surface flow in the structure. Considering the mentioned assumptions, the code interFoam was considered the best choice. This Section follows the works of Jasak (1996), Ubbink (1997) and Rusche (2002) in describing the solver.

The solver interFoam assumes the fluids as "Newtonian, isothermal and incompressible". The solver uses one single set Navier Stokes equation for both liquid and gas phase. The Reynold's averaged form of Navier Stokes equation used in interFoam is as follows:

$$\nabla . \mathbf{u} = 0 \tag{2.33}$$

$$\frac{\partial \rho \boldsymbol{u}}{\partial t} + \nabla . (\rho \boldsymbol{u}\boldsymbol{u}) = -\nabla p^* + \nabla . \boldsymbol{\tau} + \boldsymbol{g}.\boldsymbol{x}\nabla\rho + \boldsymbol{f_\sigma} \tag{2.34}$$

where $\boldsymbol{g}$ is the acceleration due to gravity, $\boldsymbol{u}$ is the velocity vector in the Cartesian coordinate, $\boldsymbol{\tau}$ is the shear stress tensor, p^* is the modified pressure adapted by removing the hydrostatic pressure ($\rho \boldsymbol{g}.\boldsymbol{x}$) from the total pressure, ρ is the density and $\boldsymbol{f_\sigma}$ is the volumetric surface tension force.

The interFoam solver uses the VOF method presented by Hirt and Nichols (1981) in considering the multiphase flows. It uses the volume fraction as an indicator function (alpha in OpenFOAM® code) to define the portion of the cell is occupied by the fluid equation.

$$\alpha(\mathrm{x,y,z,t}) = \begin{cases} 1 & \text{for a place } (\mathrm{x,y,z,t}) \text{ occupied by fluid 1} \\ 0 < \alpha < 1 & \text{for a place } (\mathrm{x,y,z,t}) \text{ occupied by interface} \\ 0 & \text{for a place } (\mathrm{x,y,z,t}) \text{ occupied by fluid 2} \end{cases} \tag{2.35}$$

The transport of α in time, is expressed by an advection equation:

$$\frac{\partial \alpha}{\partial \mathrm{t}} + \nabla . (\alpha \mathbf{u}) = 0 \tag{2.36}$$

The fluid properties at each cell (ρ and μ) are calculated according to the volume fraction of each fluids:

$$\rho = \alpha\rho_1 + (1-\alpha)\rho_2 \tag{2.37}$$

$$\mu = \alpha\mu_1 + (1-\alpha)\mu_2 \tag{2.38}$$

In case of an incompressible fluid, conservation of volume is equivalent to conservation of mass. Thus with conservation of mass, conservation of α is necessary, particularly in the case of high-density fluids; as small errors on the volume fraction generate significant errors on the physical properties. To respond to this issue, many researchers have presented alternative techniques to conserve α while preserving the interface location. The best alternative was formulated by Weller (2002), introducing an extra term in the phase fraction function, which is known as artificial compression term.

$$\frac{\partial\alpha}{\partial t} + \nabla.(\alpha\bar{\mathbf{u}}) + \underbrace{\nabla.[\mathbf{u}_r\alpha(1-\alpha)]}_{\textbf{artificial compression term}} = 0 \tag{2.39}$$

where, $\mathbf{u}_r$ is the relative velocity vector between the two fluids; also called as compression velocity (Berberović et al., 2009) such as:

$$\mathbf{u}_r = \mathbf{u}_1 - \mathbf{u}_2 \tag{2.40}$$

Mean velocity is calculated by a weighted average of the velocity between the two fluids:

$$\bar{\mathbf{u}} = \alpha\mathbf{u}_1 + (1-\alpha)\mathbf{u}_2 \tag{2.41}$$

Surface Tension Force

The surface tension force acts on the interface between the two phases. However, in the interFoam model, the interface is not tracked explicitly, and the exact location is unknown (Rusche, 2002). Therefore, the source term, $\boldsymbol{f_\sigma}$ in the momentum equation (Equation 2.34) related to the surface tension force, cannot be calculated. The Continuum Surface Force (CSF) model developed by Brackbill et al. (1992) interprets the term in terms of volume force function and solves this issue. In this CSF model, the surface curvature (κ) is formulated from local gradients in the surface normal ($\mathbf{n}$) at the interface, which is a function of the phase fraction (∇α) (Tang and Wrobel, 2005):

$$\kappa = \nabla.\hat{\mathbf{n}} = \nabla.\frac{\mathbf{n}}{|\mathbf{n}|} = \nabla.\left(\frac{\nabla\alpha}{|\nabla\alpha|}\right) \tag{2.42}$$

The volumetric surface tension force (F) is written regarding the surface tension, and subsequently, to the jump pressure across the interface.

$$F = \sigma\kappa \frac{\rho}{0.5(\rho_1 + \rho_2)} \nabla\alpha \cong \sigma\kappa\nabla\alpha \tag{2.43}$$

The dynamic viscosity (μ) is calculated as:

$$\mu = \rho(\nu_t + \nu_0) \tag{2.44}$$

where ν_0 and ν_t are molecular viscosity and turbulent viscosity respectively.

2.7.2 Algorithms

In solving Navier Stokes equation, both the pressure and the velocity term must be solved simultaneously. There are different algorithms that define the sequence to solve them. Three different algorithms are used in OpenFOAM. They are Pressure-Implicit Split Operator (PISO) (Issa, 1985), Semi-Implicit Method for Pressure-Linked Equations (SIMPLE) (Patankar and Spalding, 1972) and a combined algorithm, PIMPLE (Holzmann, 2016).

SIMPLE is the most used algorithm. A few improvements such as SIMPLER or SIMPLEC are also available. However, this algorithm is only applicable for steady state solutions. Both PISO and PIMPLE is applicable for unsteady problems. PISO algorithm has some issues when dealing with the multiphase flow in cases of abrupt change of density (Brennan, 2001). PIMPLE combines the features of SIMPLE and PISO which attains a more robust and generalizable pressure-velocity coupling.

For this condition, PIMPLE algorithm is used in most multiphase applications. The details on the implementation of the algorithm is given by Jasak (1996), Ubbink (1997) and Rusche (2002).

Between PISO and PIMPLE, the letter can be used with a CFL number more than 1 making a comparably faster simulation, while the former is known for better stability.

2.8 The uncertainty involved in urban drainage modelling

Uncertainty is an inherent component to all monitoring programs plus all models and cannot be eliminated (Dotto et al., 2008). But it is necessary to understand the sources of uncertainty, and their consequences on models and decisions. Uncertainty analysis in integrated urban drainage modelling is of growing importance in the field of water quality (Freni et al., 2008). However, very few studies are found to deal with uncertainty quantification. Most studies mainly focus on sewer modelling from the quantity point of view. Considering the uncertainty in model, quantifications of input and model parameter uncertainties are important; as without those considerations, one may lead to any solution that may be significantly over-dimensioned or under-dimensioned (Schellart et al., 2010).

Uncertainties can be classified on a scale ranging from certainty to ignorance, as adapted from (Korving, 2004; Schellart, 2007; Wynne, 1992):

- Certainty: future system performance is predictable
- Risk: system behaviour is understood, and probabilities of failure can be predicted.
- Uncertainty: the important system parameters are known but their probability distributions are unknown.
- Indeterminacy: probability, consequence or both are not known for a given event.
- Ignorance: “we don’t know what we don’t know” (Wynne, 1992)

There are two types of uncertainties as mentioned by (Korving, 2004):

- Inherent uncertainty: represents the randomness or variability in natural processes; also known as natural variability.
- Epistemic uncertainty: represents the lack of knowledge of the fundamental phenomena

Korving (2004) also describes three types of urban drainage models on which the uncertainty depends differently:

1. Empirical models or ‘black box models’
2. Conceptual models or ‘grey box models’. Rainfall-runoff models are often grey box models.
3. Detailed physics based or ‘white box models’ which consist of a set of mathematical equations, which will always return the same output for a particular set of inputs, without considering uncertainty or randomness.

In case of using deterministic models, authors have pointed out uses of several model parameters from different sources in model building and uncertainty involved in determining them (Dotto et al., 2014). As with most models, the calibration of urban drainage models rarely results in one unique parameter set, and instead many equally plausible parameters sets are obtained. This reduces the confidence in the models when they are used for prediction. The uncertainty related to the model calibration parameters and its impact on the model outputs has been extensively studied (Dotto et al., 2014).

In their study, Dotto et al. (2008) evaluated uncertainty in water quality and quantity at a stormwater model using MUSIC model. Model results showed that out of 13 different parameters, it was sensitive to only two parameters, hence a simplification was possible. However, most of the uncertainty analysis related to urban drainage has been focused on water quality modelling. Generalised Likelihood Uncertainty Estimation (GLUE) methodology was reported by Freni et al.

(2008) to evaluate the uncertainty of an integrated water model. They used the influence of the subjective choice of the acceptability threshold in order to gain insights regarding its effect on the model results. The model was applied at Savena case study in Bologna, Italy; which showed a strong influence of the acceptability threshold selection and confirmed the importance of modeller's experience in the application. Dotto et al. (2014) explained the impact of input and calibration errors and their impacts on parameter sensitivity and predictive uncertainty by propagating these errors through rainfall-runoff model KAREN. An error model was developed to disturb the measured input and calibration data. A Bayesian approach was used to model the sensitivity and uncertainty analysis which showed that random errors in measured data had a minor impact on model performance. It was also seen that the parameters fully remunerated the errors in measured data. However, parameters were unable to compensate in some of the scenarios where the systematic uncertainty in the input and calibration data were represented using extreme worst-case scenarios.

Schellart (2007) describes the uncertainty analysis of Ackers-White transport equations and their development, using some of the original calibration data. They showed that the using the equations, the model parameters developed some inherent uncertainties.

2.9 Uncertainty analysis in large-scale hydrological modelling

A hydrological model is a conceptual or 'grey box model', in which the uncertainty stems from both input (rainfall) and parameters involved in the model. The main input of a rainfall-runoff model is the rainfall, which however does not have any easy procedure to be recorded accurately at both temporal and spatial scales. With the advancement of radar technology, it is possible to obtain spatial rainfall data (Codo and Rico-Ramirez, 2018). Though, rain gauge measurement data is still considered better regarding accuracy (Muthusamy et al., 2017). One of the significant challenges of using rain gauge data is to convert the point measurements to spatially distributed data as most of the popular hydrological models are lumped catchment area models and for which the point measurements must be upscaled for the whole catchment area. Some common methods of upscaling are (Chow et al., 1988):

- Arithmetic averaging method
- Thiessen polygon method
- Inverse distance weighting method
- Polynomial interpolation method
- Moving window regression method

Ly et al. (2013) described the performance of all these methodologies as “case dependent”. The average rainfall calculated through these methods cannot give any information about the associated uncertainty which mainly comes from measurement errors and the spatial distribution. The uncertainty contribution of the spatial distribution error becomes important when point rainfall data is needed to be interpolated to an area. Geospatial simulations such as Kriging is a better option for spatial rainfall interpolations as this method considers spatial dependence structures of the data (Ly et al., 2013; Mair and Fares, 2011).

Being a statistical method Kriging requires more significant amount of data to calculate the statistical properties correctly. However, one significant disadvantage of using the kriging method is, it requires the data to be normally distributed.

Operational hydrological forecast with numerical discharge prediction uncertainty is sometimes thought to be originating from input uncertainty only. However, it also involves parameters used in the hydrological models (Kauffeldt et al., 2016). To choose the correct parameters of the hydrological model, hydrological processes needs to be highlighted with proper understanding (Zhang et al., 2016). The most hydrological model requires some parameters whose values are hypothetical in many cases as they cannot be measured. They can be only derived by calibration against catchment response and hence may contain errors (Joseph and Guillaume, 2013) and introduces uncertainty in the model results. These parameters may differ spatiotemporal variations and may be another source of uncertainties (Leandro et al., 2013). Due to lack of parameter uncertainty assessment, it is often difficult to describe the hydrologic process adequately.

One of the widely used methods in assessing uncertainty in hydrological model parameter is Monte Carlo simulation in which the parameter is chosen randomly from a given probability distribution function.

When considering flood forecasting, the hydrological model forcing originates from the forecasted precipitation data. As the parameters used in these types of model are highly uncertain, it is often recommended to generate many model parameters and make not only one forecast, but many ensembles of the same forecast event. This is known as the Ensemble Prediction System (EPS). Operational flood forecasting systems are progressively moving towards adopting Ensemble Prediction System (EPS) (Cloke and Pappenberger, 2009).

2.10 Uncertainty analysis procedure in this research

In this thesis, we approach to analysis uncertainty of two different scales of modelling. In the first step of the work, the focus was given in estimating uncertainty in modelling the hydraulics of

urban drainage structures such as manholes and gullies. In a latter part, the focus was also given to the uncertainty estimation in hydrological modelling in a catchment scale. These are two different approaches in uncertainty estimation as the former lies in the white box model category while the other lies in the grey box model category. When finding input uncertainty or parameter uncertainty through a deterministic model, several authors have reported on using statistical procedures or Monte-Carlo approach by running numerous simulations and checking the corresponding changes in the model results. However, due to very high computational time requirement in running a CFD model, this was not be a feasible strategy for the project. The model cannot measure any uncertainty itself, instead can inspect the possible change in model results when user applies a change in model parameter.

2.10.1 Uncertainty analysis in hydraulic structure modelling

Uncertainty estimation in manhole modelling is rare, mainly due to its physics based deterministic characteristics. In this work, to represent the flow properly the CFD model is used; which is a deterministic model procedure and involves several parameters.

Some set of simulation will be tested in view of finding maximum and minimum possible change in the model results due to the applied changes in order to investigate uncertainty in hydraulic structure modelling. In applying the hydraulic model for manholes and gullies, our best interest is to find the manhole head losses at different circumstances and gully efficiencies. The following factors are analysed in the work:

Uncertainty in the modelling procedure

The velocity distribution of a deterministic RANS hydraulic model is related to the turbulence closure equation it is using. In this scenario, CFD modelling of a scaled manhole is done using four different RANS equation sets (Chapter 4), namely two equation based models: RNG k-ε (Yakhot et al., 1992), Realizable k-ε (Shih et al., 1995) and SST k-ω (Menter and Esch, 2001; Menter et al., 2003); as well as seven equation based Reynold's Stress Model (RSM): Launder-Reece-Rodi (LRR) (Launder et al., 1975).

RNG k-ε model is known for better performance for separating flow and used previously in the manhole model by Lau et al. (2007). Realizable k-ε model can perform better for spreading rate of round jets and were applied effectively by Stovin et al. (2013). Djordjević et al. (2013) used k-ω model, and this model performs better in cases related to near wall flow and flow separation zone. RSM models perform better in cases where the flow is governed by the stress tensor. As in a manhole hydraulics, all these issues may govern at different cases; model results may introduce

uncertainties. The best modelling approach was evaluated by comparing PIV velocity data with these model results.

Uncertainty in involved due to surcharge and flow conditions

The most important flow phenomena of a manhole and a gully are their head loss coefficients and discharge coefficients respectively (Arao et al., 2012; Guymer et al., 2005; Guymer and O'Brien, 2000; Stovin et al., 2007). Their values are connected to flow conditions such as manhole inlet flows and manhole surcharges. The relationship between them is analysed in Chapter 5.

Uncertainty involved due to difference in geometry and mould shape

The turbulent flow of a manhole is very much dependent on the mould shape of its structure. Different cities use different manhole moulds in their drainage system. A construction error may always result in a change in geometry such as a small change in the inlet and outlet pipe orientation that could be responsible for changing hydraulic properties. The head loss coefficients change at these cases, as it directly changes the flow of the inlet jet. Moreover, the manhole to inlet pipe diameter is also another primary source of deviation in head loss coefficients. All these uncertainty issues related to the geometry of the manhole structure are investigated in Chapter 6.

Numerical Uncertainties

Celik et al. (2008) described an error estimation procedure and hence quantified numerical uncertainty in CFD models. Their work gave a specific guideline for calculation and reporting of discretisation error for CFD based studies. This method is also applicable where no experimental data is available. This method is implemented in our CFD modelling to quantify the numerical uncertainties in the CFD model.

2.10.2 Uncertainty analysis in large-scale catchment modelling

Chapter 7 of this thesis deals with uncertainty estimation in large-scale hydrological modelling. In this work, the uncertainty analysis is done considering forecasting of flood discharge of a large catchment using LARSIM (Large Area Runoff Simulation Model) and applying at the city of Kulmbach, Germany. A flood forecasting tool is prepared that can forecast flood considering both input and parameter uncertainties. The tool has two modules: rainfall uncertainty module and a parameter uncertainty module.

The rainfall uncertainty module collects observed or forecasted rain data from several rain gauges situated at different parts of the catchment. Later, it interpolates the rainfall data over the

catchment area using sequential geospatial simulations and creates different possible scenarios of rainfall distributions. For each of the parameters considered, three different values are given to the parameter uncertainty module. They are maximum, minimum and the calibrated value of the parameter in question. The module creates a Gaussian or beta PDF distribution and creates different parameter sets through Monte Carlo method. Later, each rainfall distribution is combined with each parameter sets and applied to the LARSIM model to get corresponding discharge data. Thus, the module collects all the discharge ensembles and create different forecast percentile bands.

CHAPTER 3

FLOW CHARACTERISATION IN A SCALED SURCHARGED MANHOLE USING STEREOSCOPIC PIV

3.1 Abstract

Manholes are a common element of urban drainage systems. The flow through a manhole is complex involving combinations of sudden expansion and contraction with added vorticity. Understanding manhole hydraulics is important when modelling the behaviour of an urban drainage model efficiently. In this work, flow characterisation was done in a scaled surcharged manhole built according to Froude scale as 1:6. Stereoscopic Particle Image Velocimetry was utilised to visualise the manhole flow and record all the three velocity components in two-dimensional planes. Data were recorded at three vertical planes in the manhole. Flow structures were analysed from temporal averaged velocity, vorticity and turbulent kinetic energy. The temporal mean of the spatial velocity pattern showed three distinguished velocity zones in the manhole: a core velocity region, diffusive zone and a dead zone. The core zone is found to change with incoming flow condition while the diffusive zone showed more susceptible to the change in the surcharge. A swirling motion was observed in the manhole which created asymmetric flow pattern in the two lateral planes. The asymmetry was found minimal in high surcharge conditions. The datasets recorded in this work are expected to provide validation data for CFD models.

Keywords: Mean velocity; Manhole; Stereo PIV; Surcharge; Turbulence

3.2 Introduction

Manholes are used within piped drainage systems to accommodate a change in direction, pipe gradient and size and to connect with other sewers (Butler and Davies, 2011). When the flow enters a manhole, the flow undergoes a sudden expansion, a decrease in Froude number, a drop in the specific energy, added vorticity and possible air entrainment. A combined sewer system normally operates with a free-surface flow. However, during a storm event, pressurised flows are

observed, which is often referred to as surcharged flow (Zhao et al., 2006). With the ongoing development of urban areas, existing piped drainage systems are frequently overloaded hydraulically creating surcharged manholes (Martins et al., 2016; Zhao et al., 2004). Surcharging can result in issues such as blowout of manhole covers, release of polluted water and urban flooding (Zhao et al., 2004). A surcharge manhole flow can be subcritical or supercritical, supercritical flows generally create more energy losses (Gargano and Hager, 2002; Hager and Gisonni, 2005).

Previous laboratory-based research has been conducted on surcharged manholes focusing on the head loss. Some early works by Sangster et al. (1958), Marsalek (1984) and Lindval (1984) revealed change in head loss coefficient in different types of manholes. Howarth (1985) also checked hydraulic performance for change in manhole bottom, manhole diameter at steady and unsteady case scenarios. Later Bo Pedersen and Mark (1990) explained the manhole head loss using submerged jet theory. Guymer et al. (2005) showed the dependence of head loss coefficient on the the manhole surcharges and manhole to inlet pipe diameter ratios. Their work introduced a term 'Threshold surcharge level' value which is approximately 20% of the manhole diameter, below which the head loss coefficient increases abruptly and may not follow any trend. At any surcharge higher than its threshold, the head loss remains steady with the increase in surcharge and increase with the increase in diameter ratio. The change in head loss may also become different in a overflowing manhole as described by Rubinato et al. (2017). These works involve use of laboratory based scaled manholes focusing measurements of pressure variation, water levels and discharges. Velocity measurement of surcharged manhole flow can give more detail insight of the manhole hydraulics. Not many works have been reported in measuring velocities. With the advancements of Computational Fluid Dynamics (CFD) algorithms and associated computational power, an increasing number of numerical studies are investigating the hydraulics of manholes. Several authors investigated manhole hydraulics using CFD (Beg et al., 2018, 2017b, 2017a; Bennett, 2012; Stovin et al., 2013, 2010), which is an alternate source of describing manhole veloity. However, to validate a CFD model properly, one needs to compare the results not only with the pressure and water levels but also with the velocity measurements and turbulence patterns.

Lopes et al. (2014) used Acoustic Doppler Velocimetry (ADV) to measure point velocities and turbulence in a laboratory scaled circular surcharged manhole. ADV measurement is time-consuming. Moreover, being an intrusive technique, it may change the original flow structure at the point of measurement. Particle Image Velocimetry (PIV) provides a non-intrusive approach to map spatially instantaneous velocity components in a plane. The measurement technique is based on measuring movements of discrete solid neutrally buoyant seeding particles with the presumption that the particles follow the fluid flow without any deviation. The spatial resolution

provided by PIV can be high, especially near the water surface and the solid boundary. Additionally, Quaresma et al. (2017) compared PIV with ADV and found both measurement techniques provide the same magnitude and pattern for in-plane velocity data with a near perfect correlation. Probably the only application of PIV measurement in manhole is the work by Lau (2008), who used PIV in a scaled manhole having manhole to pipe ratio of 9.1 and to described the velocity structures for pre and post threshold surcharge conditions. Stovin et al. (2013) used the PIV data to validate a manhole CFD model. Nevertheless, evidence based on experimental data (Arao et al., 2013; Guymer et al., 2005) and CFD modelling (Stovin et al., 2013) also suggests that the manhole hydraulics changes abruptly at a certain manhole to pipe ratio. Guymer et al. (2005) suggested this ratio to be 4.4 and considered manholes below and above that ratio as 'Small manhole' and 'Big Manhole' respectively. On the other hand, most manholes found in practice are 'Small manholes', having manhole to pipe ratios less than 4.4. Detail velocity measurements in small manhole at different surcharge and inflow conditions has not been reported before.

A more advanced non-intrusive modified PIV technique is Stereo PIV, where more than one camera is used to measure velocity at the same plane. Stereo PIV measurements have been intensely used in observing flow phenomena where measurement of all the three velocity components are considered necessary, such as measurement of turbulent velocity in a pipe (Van Doorne and Westerweel, 2007; Zhang and Hugo, 2006), and measurement of the turbulent boundary layer (Herpin et al., 2008). Flow in a surcharged manhole is three dimensional and often highly turbulent making it vital to measure all the three components of the flow. A strong out of the plane velocity component is possibly correlated to energy loss, solute mixing and particulate transport within the manhole.

In this paper, we focus to obtain velocity and turbulence characterisation of a surcharged scaled manhole. Results from a series of laboratory measurements using Stereo PIV are presented. The manhole used in this study is a 'small manhole', having manhole to pipe ratio as 3.2. Measurements were taken at combinations of different inflow and surcharge ratio conditions covering both pre and post threshold surcharges. Each measurement was conducted at steady state condition in the manhole flow. Comparative analysis was drawn from the measured data, and turbulence properties of the flow have been analysed.

3.3 Methodology

3.3.1 Laboratory setup

The PIV measurements were done on a scaled manhole. The 240 mm diameter (Φ_m) manhole is unbenched and does not have any sump zone. It is connected to a 75 mm diameter (Φ_p) inlet-

outlet pipe whose axis passes through the centre axis of the manhole and has a slope of 1:1000. The manhole-pipe system is made of acrylic and referenced as a 1:6 Froude scale, based on the diameter of the manhole. The inlet pipe is connected to a constant head tank, a valve and an electromagnetic flow meter. The valve (Valve 1 in Figure 3.1) controls inlet pipe flow. The outlet pipe is connected to a downstream valve (Valve 2 in Figure 3.1) which is used to control water levels in the manhole. Two pressure sensors are installed at 350 mm upstream and 620 mm downstream from the manhole centre respectively. The sensors are calibrated to measure with an accuracy of ±0.72 mm (Rubinato, 2015). A transparent tape was used to check the water levels in the manhole. The inlet and the outlet valves were controlled to get different combinations inflow and surcharge in the manhole.

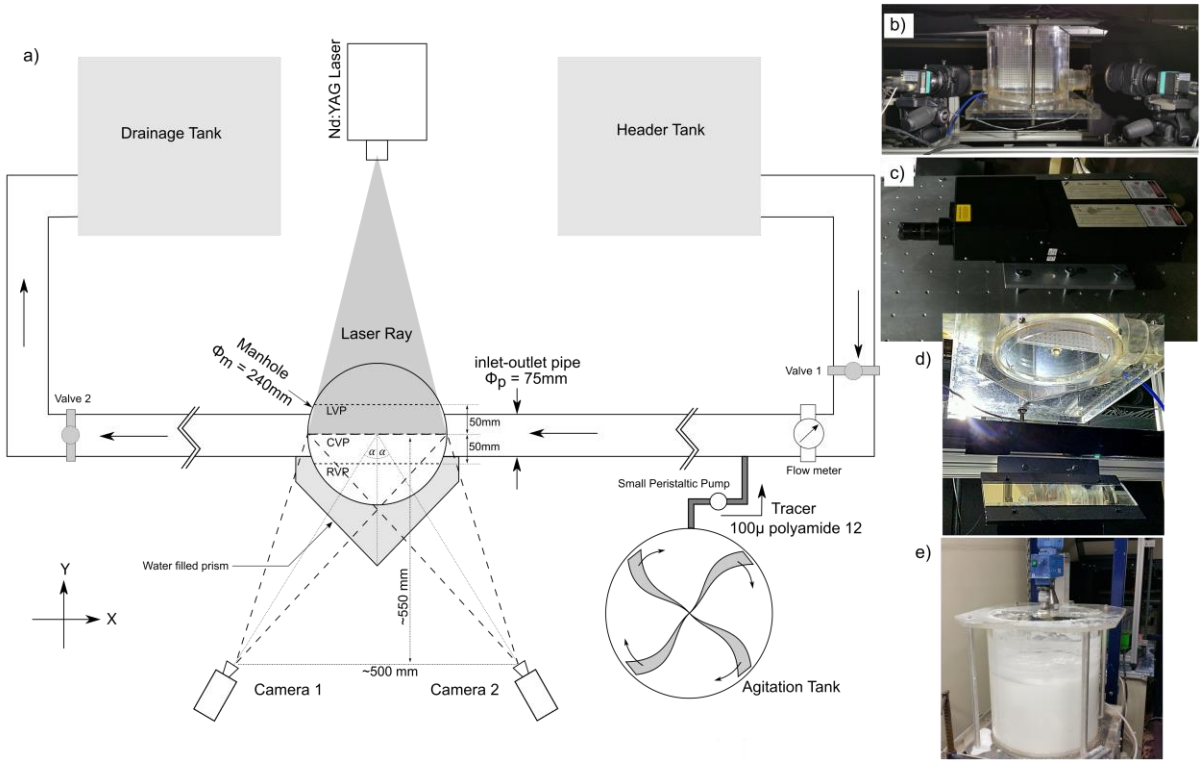

Figure 3.1: Clockwise: a) Top scheme of the PIV setup on the manhole at the laboratory, b) Two cameras focusing calibration plate in the manhole, c) Nd:YAG Double cavity double pulsed laser, d) a 45° mirror under the manhole to reflect the laser light sheet vertically, and e) Agitation tank mixing polyamide 12 seeding particles. The vertical laser light sheet is not shown in the figure.

3.3.2 PIV Setup

A stereo PIV system is installed around the scaled manhole. Beg et al. (2017b) gives a description of the setup. The system uses two PIV cameras (Dantec FlowSense EO 2M) each having CCD of resolution 1600×1200 pixels. The cameras can record 8 bit image pairs as a double frame, double exposure images with inter-frame time gap of 200 ns and at a rate of 35 Hz. Each camera was used with 50 mm Nikon/Nikkor macro lens using Scheimpflug mounts. Scheimpflug mount screw for

each lens was adjusted manually to get the best sharpness in the images. Lens aperture number was set to #2.8 during the data recoding. A dual cavity-pulse Nd:YAG laser was used for illumination the image plane. The laser wavelength was 532 nm with a maximum power output of 50mW. The laser was converted to laser light sheet using a cylindrical lens and then focused onto a laser mirror facing at 45 degree angle to the horizontal at the bottom of the manhole. The mirror reflects the laser sheet vertically through the bottom of the manhole. The final thickness of the laser sheet was around 4 mm in the manhole.

As the measurement plane would have to observe through the curved surface of the manhole, a refraction induced error was possible. A thin-walled flat surfaced prism filled with the same liquid is known to reduce this issue (Prasad and Jensen, 1995). For this reason, an acrylic tank was constructed at the manhole side to be used as a water filled prism, keeping its flat surface perpendicular to the cameras' axes. Two cameras and the laser were connected to the computer using a digital sequencer, which triggers all the components as programmed.

The camera positions were calibrated using a standard calibration plate. The calibration plate uses black dots (ϕ = 3 mm) and spaced at 10 mm centre to centre (Figure 3.2). Each data accusation plane was associated with a set of calibration data. To acquire calibration data at each case, the calibration plate was placed at the image acquisition plane as well as at another plane at a 10 mm lateral offset and calibration image was recorded. Some errors may arise due to misalignments between calibration plane and light sheet, commonly known as disparity (Willert, 2006). Recorded PIV data images from both cameras were back-projected to the calibration plane using multiple images in order to calculate disparity error and the calibration data were thus refined. This calibration procedure was repeated all the three measuring planes. The whole calibration mapping was done using Dantec Studio v3.31.

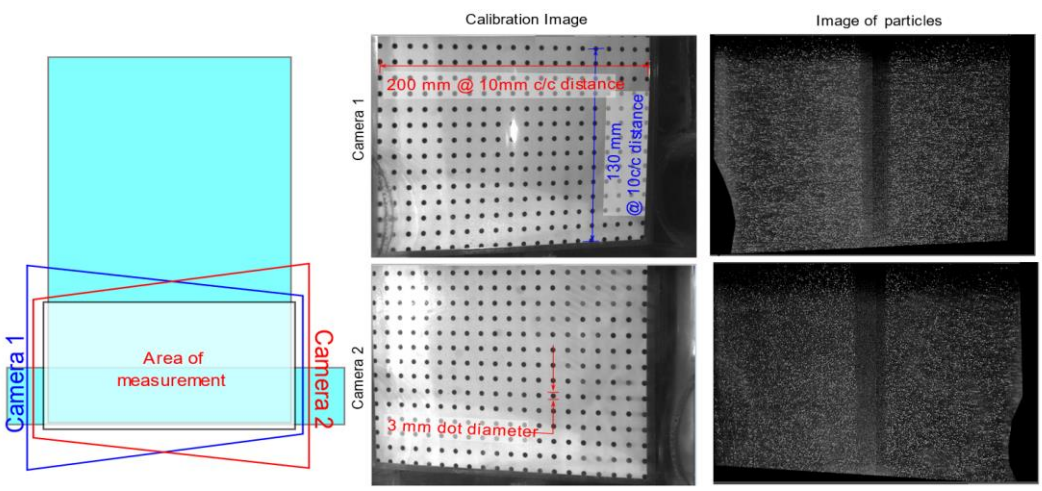

Figure 3.2: Plane of view of each camera, calibration plate and acquired particle image view from both cameras

Polyamide 12 spherical particles with average diameter of 100 µm was used in this work as the tracer. The particle has a specific gravity of 1.01. The particles were kept in a seeding tank with continuous agitation so that they stayed in suspension. The seeding particles were pumped into the manhole inlet pipe at a constant rate at around $50\phi_p$ upstream of the manhole-inlet pipe location.

The injection rate of the seeding particles was chosen by seeing particle density in the PIV image screen. It was selected to ensure that there were always 5-10 particles in each integration area. The particle diameter were around 2-3 pixels in size for this camera setup.

The placement of the cameras was such that they could view only some part of the whole manhole water depth. Importance were given on visualising the manhole jet coming from the inlet and moving out through the outlet. So, the cameras were set to measure only water height between the manhole floor and up to a height of 150 mm from the floor (Figure 3.2, left panel), which was two times to the diameter of manhole inlet-outlet pipe.

3.3.3 Data collection

PIV data were recorded for the central vertical plane (CVP) at different combinations of the inflow and surcharge conditions in the manhole. Four different inflow conditions: 0.51×10^{-3} m^3/s, 1.1×10^{-3} m^3/s, 2×10^{-3} m^3/s and 4×10^{-3} m^3/s were used with combinations of three different water levels: 110 mm, 210 mm and 310 mm. As the soffit level of the manhole outlet pipe was 75 mm, these water levels created surcharge levels (s) of 35 mm, 135 mm and 235 mm inside the manhole. The 2 m^3/s and 4 m^3/s inflow conditions were further used in recording two more vertical planes one located at an offset of 50 mm from CVP towards to the cameras (termed as right vertical plane, RVP) and another located at 50 mm offset from the CVP towards opposite of the camera (termed as left vertical plane, LVP). The left-right convention is given according to the positive x-axis direction; looking towards the upstream from the downstream of the manhole. A full list of all measurement conditions is shown in Table 3.1.

Table 3.1: List of PIV measurement conditions

Inflow ($\times10^{-3}$ m^3/s)	Water Level (mm)	Surcharge ratio		Measurement Plane(s)
		($s/Ø_p$)	($s/Ø_m$)	
0.5	110	0.47	0.147	CVP
	210	1.80	0.563	CVP
	310	3.13	0.978	CVP
1.1	110	0.47	0.147	CVP
	210	1.80	0.563	CVP
	310	3.13	0.978	CVP
2.0	110	0.47	0.147	CVP, RVP, LVP

Inflow ($\times 10^{-3}$ m^3/s)	Water Level (mm)	Surcharge ratio		Measurement Plane(s)
		($s/Ø_p$)	($s/Ø_m$)	
	210	1.80	0.563	CVP, RVP, LVP
	310	3.13	0.978	CVP, RVP, LVP
4.0	115	0.53	0.166	CVP, RVP, LVP
	210	1.80	0.563	CVP, RVP, LVP
	310	3.13	0.978	CVP, RVP, LVP

3.3.4 Data processing

Measurements were made at a rate of 8 image pairs per seconds for 5 minutes for each measurement set. Image pair data were analysed and processed using DynamicStudio v3.31 software. Firstly, collected images were masked for the area of interest. The laser light sheet brightness is non-uniform and Gaussian shaped, making highest intensity at its centre. This issue creates different brightness of the particles in the images according to its position. In addition to that, variation in seeding particle sizes cause particles in the images to show different brightness levels. A local min-max brightness filter was applied to the recorded images to get rid of this issue. This procedure checks the minimum grey value of each particle considering a radius of 2 pixels and subtracts the value form the local zone and later divides it by the local grey value range. This process shifts the particle brightness towards uniformity and subsequently reducing the numbers of erroneous vectors (Adrian and Westerweel, 2011). Adaptive cross-correlation was applied at two steps using 32×32 pixels to 64×64 pixels with 50% overlapping between two consecutive areas and converted to 2D velocity vector data. Later, corresponding 2D vector data from each camera were combined and converted to 3D vector data using the camera calibration data acquired beforehand. Finally, each vector represented approximately a measurement area of 2.8×2.8 mm^2. Local median correction post-processing scheme was applied to the 3D data which corrected approximately 2-8% incorrect vectors from each data set.

Initial observations showed that the data plane contains region with both high and low velocities, ranging from around 1.8 V_{avg} (V_{avg} = ratio of discharge and inlet pipe cross-section area, Q/A_p) near the centre of the inflow jet to almost zero velocity at zones far from the jet, at the upper part of the PIV images. To account for this issue each measurement set was recorded at different image time separation intervals, ranging from 250 µs to 4000 µs, so that both high and low velocities can be appropriately recorded ensuring enough inter-image particle displacement to allow accurate measurement of all vectors. Later, mean velocity maps were created from the ninety-percentiles of each data subsets neglecting lowest and highest five percentile data. Subsequently, a complete velocity map was constructed from each dataset by stitching higher velocity zone data from the faster image separation subsets and lower velocity zone data from slower image separation

subsets in such a way, so that the particle displacement is always below 2 pixels at each case. All velocity datasets were normalised using average inlet velocity V_{avg}.

3.4 Uncertainty estimation in the measurement

For a well conducted experiment, PIV velocity measurement accuracy is typically in the order of one per cent (Adrian, 1997). However, the level of measurement uncertainty depends on a number of factors. Determining the error in PIV measurement is a significant challenge. PIV uncertainties could be a function of experimental conditions as well as the accuracy in the detection and measurement of seeding particle displacement (Huang et al., 1997).

One of the main uncertainties in stereo PIV measurement comes from the viewing angle of the two cameras. Accurate measurement of the out of the plane velocity component is dependent on the intra camera angle. According to Adrian and Westerweel (2011), the random error towards within the plane and out of the plane is two planes are related following equation (3.1).

$$\frac{\delta_y}{\delta_x} = 1/\tan\alpha \tag{3.1}$$

where, δ_y and δ_x are the random errors towards out of the plane and within the plane respectively and α is the camera viewing angle shown in Figure 3.1. Setting the camera viewing angle to 45 degree makes the vector measurement accuracy unbiased to any direction. However, in this work, the camera view angles were constrained due to the experimental conditions and the shape of the scaled manhole used. Three different vertical planes, namely LVP, CVP and RVP were measured using PIV; from which LVP was the furthest and RVP was the closest to the camera. Considering these conditions, the camera measurement angles were maximised as much as possible. At CVP, the camera viewing angles were around 27 degrees, and for LVP, the viewing angles were reduced 21 degrees. However, this issue was less prominent while the measuring of RVP and the camera viewing angle was 41 degrees. Due to all these constraints, the uncertainty in measuring the out of the plane component was higher at LVP and CVP than that of RVP.

In PIV, measurement accuracy is connected to the accuracy in locating the centre of each particle in the image precisely, and it is directly related to the spatial and the temporal resolution of the PIV instruments. In this work, the positioning of each particle was calculated using sub-pixel accuracy method using three-point Gaussian interpolation (Nobach and Honkanen, 2005). The positioning accuracy in this method can be reached up to 0.01 pixel of the image considering each particle are visible as 2-3 pixels in the image (Nobach et al., 2004; Nobach and Honkanen, 2005). As each pixel were in the range of 0.3 mm in the measurement plane, the positioning accuracy would be in the range of µm.

Each PIV instrument has a range considering the minimum to maximum resolvable length (Adrian, 1997), (known as the Dynamic Spatial Range, DSR) and maximum to minimum resolvable velocity (known as Dynamic Velocity Range, DVR). They are related as:

$$(DSR)(DVR) = \frac{L_x}{c_\tau d_\tau} = constant \tag{3.2}$$

where, L_x is a constant depending on the pixels size of the camera, c_τ is a constant concerning the ability of the analysis procedure to calculate the particle displacement between two consecutive images and d_τ is the particle diameter in the recorded image. In this work, the measured data had a very high range of velocity, which effectively increases DVR and subsequently decreases DSR. For this reason, measured data planes were subdivided in several zones considering different velocity ranges and data were collected using several laser pulse interval rates allowing smaller DVR at each measurement sub-groups. Later, velocity data were stitched together to get the velocity of one whole plane. Fast velocity data were acquired from fast acquisitions (shorter Δt) and slow velocity data were acquired from slower acquisitions (longer Δt). Figure 3.3 is showing one example PIV data with and without applying this correction.

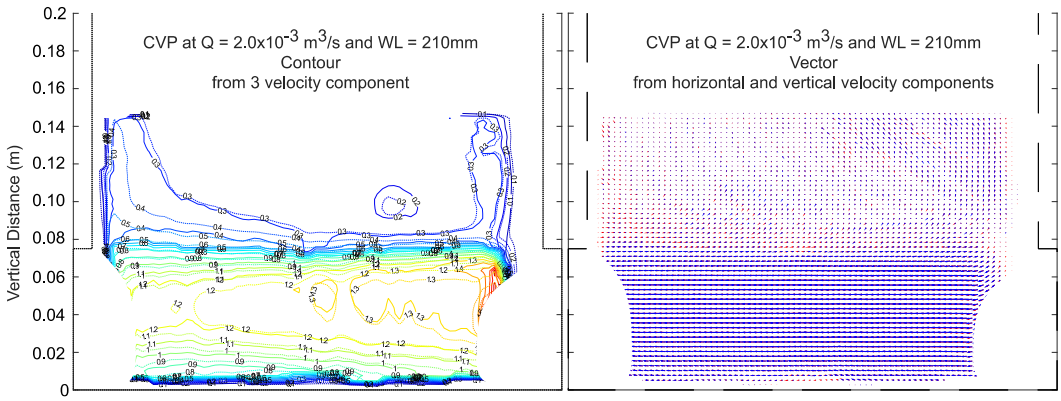

Figure 3.3: Comparison between two different velocity data from the scenario at 2×10^{-3} m^3/s inflow and 210 mm water level. The dotted contour and red vectors showing data after averaging all the instantaneous measurement. Solid contour and the blue vectors are showing data after stitching from different measurements allowing smaller Dynamic Velocity Range

A primary source of error is the influence of the gravitational forces of the seeding particles, which would introduce an additional velocity component (Raffel et al., 2007; Van Overbrüggen et al., 2016). This induced velocity can be calculated using Stoke's law:

$$U_g = {d_p}^2 \frac{\rho_p - \rho}{18\mu} \tag{3.3}$$

where, d_p is the particle diameter (100×10^{-6} m), ρ_p is the particle density (1012 kg/m^3), ρ is the density of water (998 kg/m^3 at 20 ˚C), and μ is the dynamic viscosity of water (1.0016×10^{-3} Pa at 20 ˚C). This makes the downward velocity in the range of 10 µm/s and can be considered negligible compared to the measured velocity for the image separations used in these experiments.

The velocity measurement may also have a strong dependence on the particle diameter (Van Overbrüggen et al., 2016) considering Stokes number in the cases of accelerating or decelerating fluids. Higher Stokes number indicates that the particle tends to show a different flow path line than the actual fluid flow path. This phenomenon is also known as slip velocity (Kulick et al., 1994). The Stokes number can be calculated as:

$$S_t = \frac{\tau_p}{\tau_f} \tag{3.4}$$

where, τ_p is the particle relaxation time and τ_f is the characteristic time scale of the fluid. Particle relaxation time can be estimated as:

$$\tau_p \cong \frac{\rho {d_p}^2}{\mu} \tag{3.5}$$

According to the seeding particle properties, the relaxation time can be in the range of 0.01 s. The value of τ_f is particularly connected to the acceleration or deceleration of fluid. It is the time required for the fluid to change its velocity. To calculate the fluid characteristic time τ_f, the following equation was considered:

$$\tau_f = \frac{l}{\Delta u} \tag{3.6}$$

where, l is the characteristic length and Δu is the maximum change of fluid velocity within that length.

Considering the fact that in this measurement, the velocity is highest near the axis of the inlet-outlet pipe and lowest near the manhole floor wall. Preliminary studies showed that at an inflow of 4×10^{-3} m^3/s, the inlet pipe centre maximum velocity reaches 1.1 m/s while at 0.5×10^{-3} m^3/s inflow, pipe centre maximum velocity was 0.315 m/s. In both cases, the velocity near the manhole floor was near zero. Thus, we consider highest Δu for high flow conditions as 1.1 m/s and 0.315 m/s at low flow conditions within l = 0.0375m. In this way, the highest possible Stokes number becomes 0.29 at high flow and 0.08 at low flow condition. The smaller the Stokes number, the more certainty in the measurement can be achieved; however, the change is not linear. $S_t \leqslant 0.1$, exhibits an accuracy in the measurement with less than 1% error whereas at S_t = 1, the

measurement error can be up to 18% (Van Overbrüggen et al., 2016). With Stokes number of 0.29, one can expect that the error in measurement is below 5%. In case of choosing a smaller size of seeding particles, much smaller Stokes number could have been achieved, making the error due to slip velocity significantly smaller. However, larger particles assure better visibility in the PIV image. For this reason, a trade-off between particle image brightness and flow behaviour has been made.

3.5 Results and discussions

3.5.1 Statistical Convergence

The temporal convergence of the measured data was checked before analysing the results. Figure 3.4 shows fluctuations of the cumulative average data from the measured data at the centre point of the manhole for the condition of 4×10^{-3} m^3/s inflow with 210 mm water level. Three different measurements were taken in this case. It can be seen that the statistical convergence of the flow is very fast. The average flow converges within the first 1500 image data. The convergence of axial flow component is found to be marginally faster than the other two non-axial components. The figure also ensures that averaging velocity data from 2500 images can contain all the required turbulence structures and gives the proper mean velocity field of the measurement plane. Figure 3.5 shows all the average velocities at the three measuring planes of the manhole at the same flow condition mentioned.

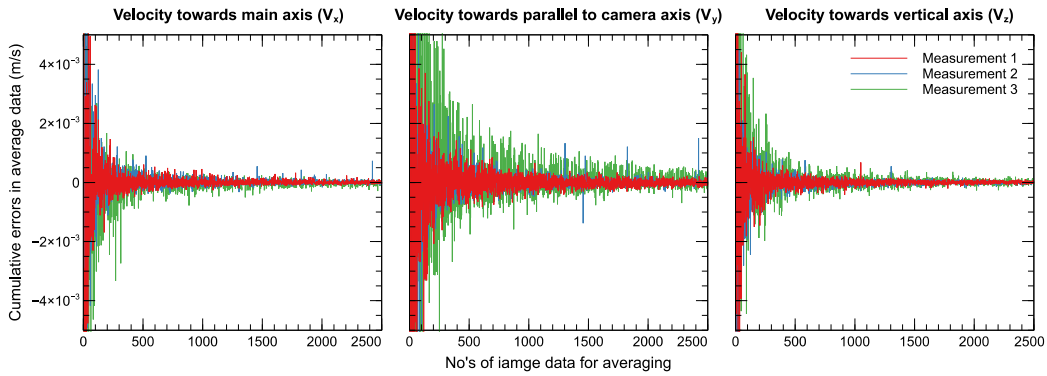

Figure 3.4: Checking of temporal convergence of the measured velocity data

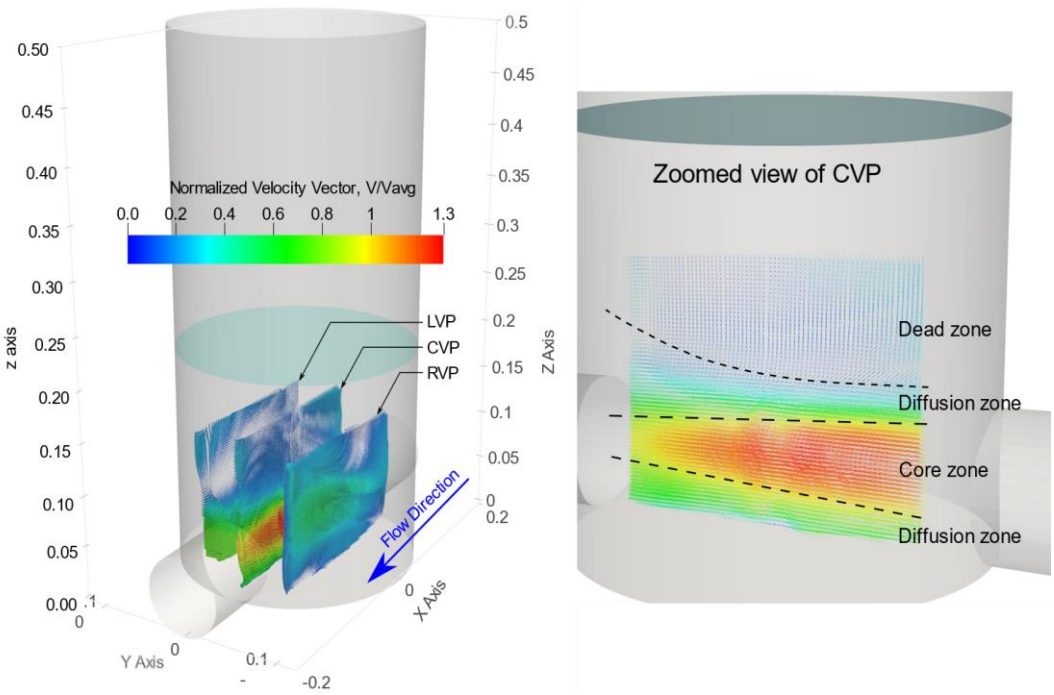

Figure 3.5: Left panel: Mean normalised velocity vectors at three planes in the manhole at inflow, Q = 2×10^{-3} m^3/s with the water level of 210 mm, Right panel: Zoomed view of the central plane with schematic locations of different velocity zones

3.5.2 Spatial mean velocity patterns

PIV data can produce both instantaneous and time averaged velocity information for the planes of investigation. However, the work focuses on the time average velocity for the investigated planes at the mentioned hydraulic conditions.

The following figures show mean velocity data at the CVP of the manhole obtained for four different inflows and three different surcharge conditions. Figure 3.6 shows the measured mean velocity magnitude ($|V_{xyz}|$) at the CVP (in m/s). However Figure 3.7 and Figure 3.8 show the mean velocity magnitude ($|V_{xyz}|$) and out of the plane component (V_y) respectively after normalising to their corresponding averaged inlet pipe velocity (V_{avg}). In all the cases, the flow direction is from right to left.

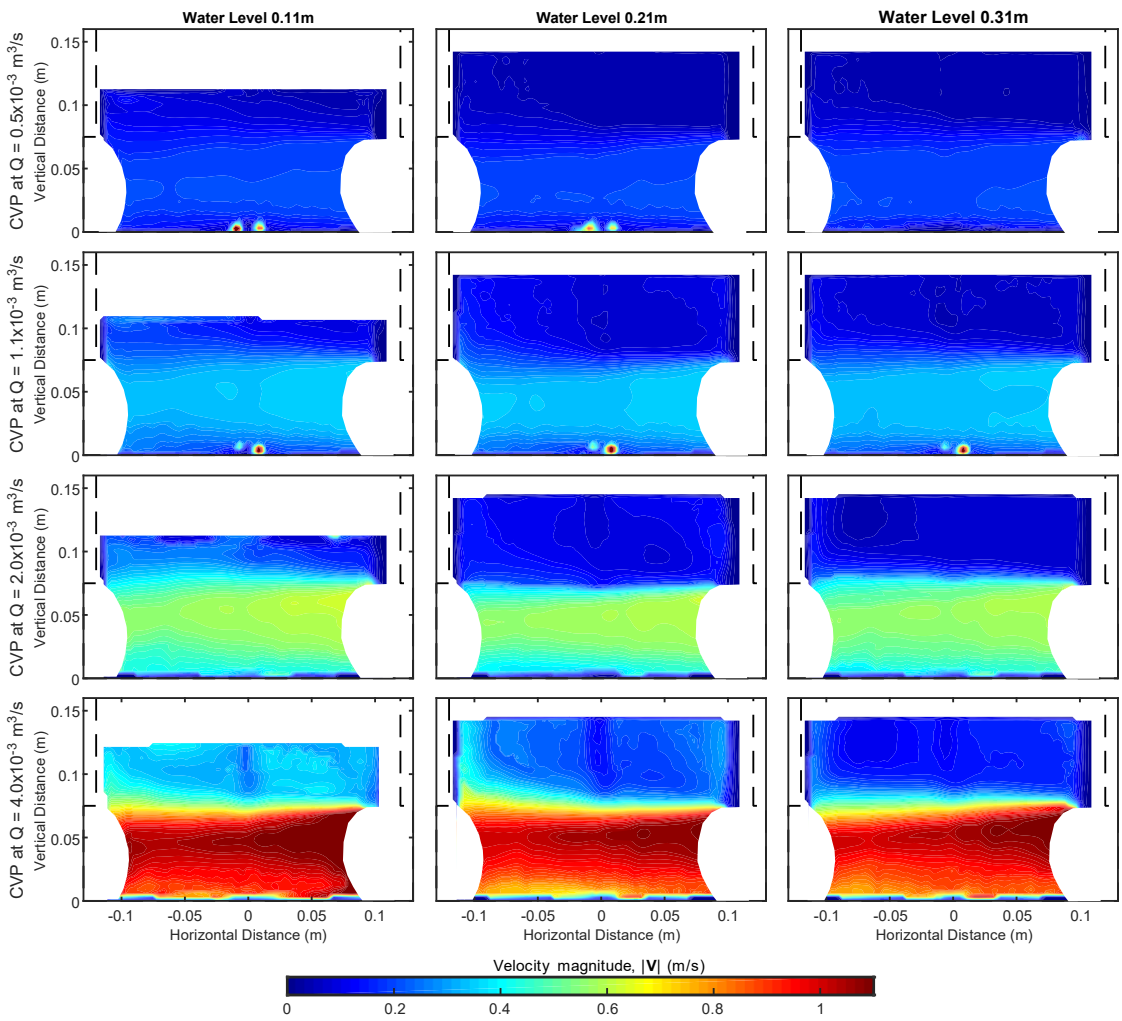

Figure 3.6: Mean velocity magnitude at CVP for different inflow and surcharge conditions

From Figure 3.6, we can see the velocity distribution at the manhole central plane in different conditions. With the increase in inflow, the velocity increases from the top towards the bottom. It shows that the maximum velocity at the slow flow condition ($Q=0.5\times10^{-3}$ m^3/s) is in the range of 0.25 m/s while at the fast flow scenario ($Q=4\times10^{-3}$ m^3/s), the maximum velocity is around 1.1 m/s.

It can be noticed from Figure 3.6 that the highest velocity in the manhole changes from 0.25 m/s at the lowest flow rate conditions (0.5×10^{-3} m/s) to 1.2 m/s at the highest flow rate conditions (4.0×10^{-3} m/s). The maximum velocity at the jet core zone increases around 5 times while the flow rate increases 8 times in the manhole. The Reynold's number at the inlet pipe for the four inflow rate conditions are: 8500, 17000, 34000 and 68000 respectively. Considering the roughness of perplex as 0.0025 and Moody's chart, 0.5×10^{-3} m^3/s inflow rate lies within the transition zone between turbulent and laminar flow. The turbulence level of 1.0×10^{-3} m^3/s inflow is just above the transition flow boundary. The two highest flow conditions are within the range of fully turbulent

flow. The normalised velocity in Figure 3.7 also indicates that the velocity profile at the manhole centre are closer to the averaged velocity of the pipe at the highest two flow conditions.

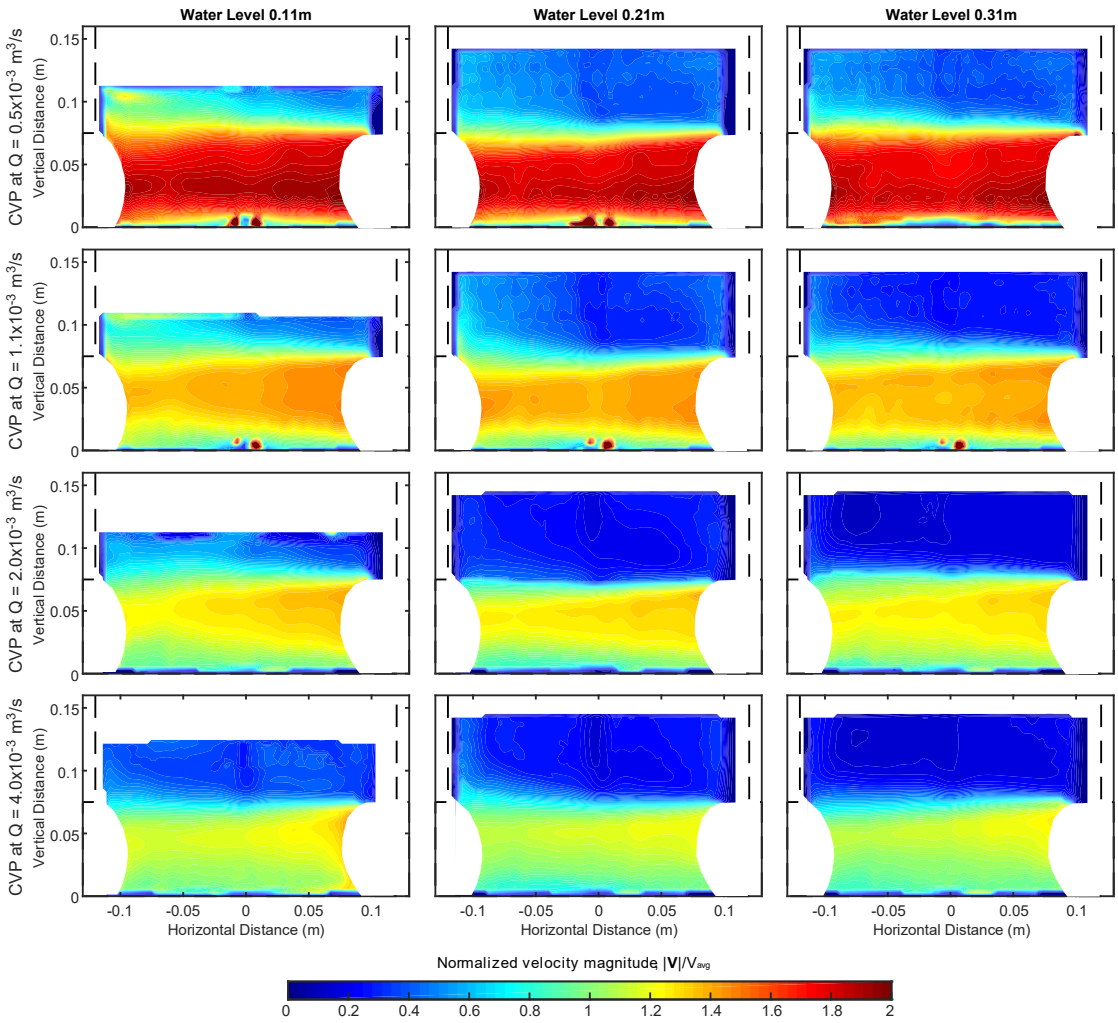

Figure 3.7: Normalized Mean velocity magnitude at CVP at different inflow and surcharge conditions

In Figure 3.7, the spatial distribution of normalised velocity can be distinguished into three regions, which is similar to submerged jet flow as described by Albertson et al. (1950). Near the bottom part of the manhole in-line with the inlet-outlet pipe is the core region where the flow presents higher normalised velocities. The velocity vectors at this zone are almost parallel to the direction from inlet to the outlet. With the increase in the distance from the inlet, the core velocity decreases and as an action-reaction process, the velocity of the surrounding fluid increases. This accelarating zone is known as diffusion zone and is characterised by eddies and strong shear. The third zone is a dead zone, located at the upper part of the manhole, whose magnitude depends on the water level. This zone shows comparably calm water. The first and the second zone forms the whole jet flow of the manhole (Bo Pedersen and Mark, 1990; Guymer et al., 2005; Stovin et

al., 2013) and carries the major part of the mass flow through the manhole. The three zones are also indicated at Figure 3.5 (right panel).

The total jet area increases with the distance from the inlet, however the core region decreases. It creates a conical shape and reduces in its size while moving towards the outlet. It is apparent that the rate at which core region size is reduced is higher at high flow. At low flow condition, the core region size remains close to the pipe diameter even near the outlet pipe. The maximum core velocity reaches up to $1.8V_{avg}$ at low flow condition. With the increase in inflow the manhole flow becomes more turbulent, the core region maximum velocity becomes closer to the average, reaching around $1.2V_{avg}$ at the highest flow measured. It can also be seen that with the increase in inflow, the core region moves away from the manhole bottom when travelling from inlet to outlet, making a more prominent diffusive region between core and manhole floor.

The three water levels created surcharge zones of 0.035 m, 0.135 m and 0.235 m; making a surcharge to manhole diameter ratio (s/ϕ_m) of 0.146, 0.563 and 0.979, respectively. It can be seen that the diffusive region changes with the change of available surcharge ratios.

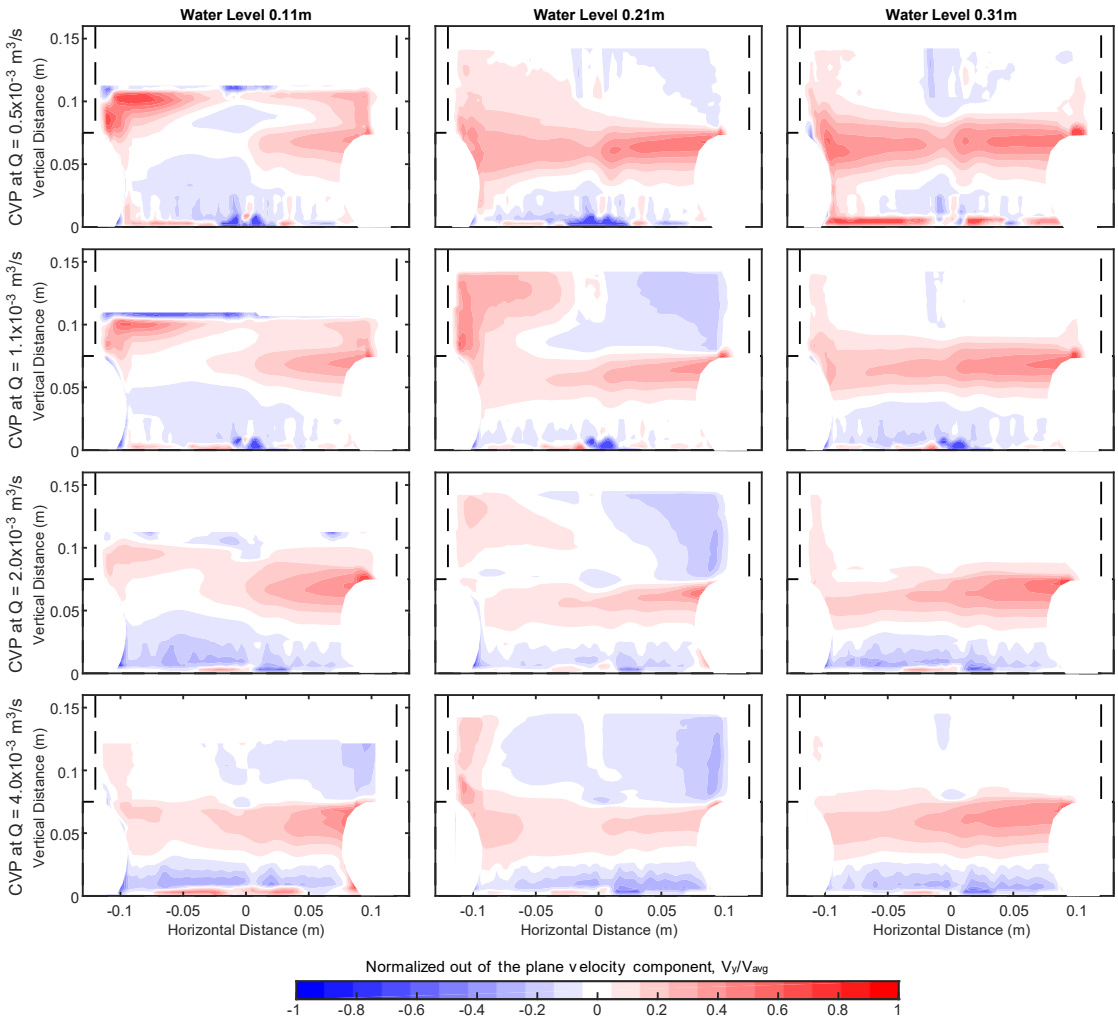

Figure 3.8: Out of the plane normalised mean velocity at CVP at different inflow and surcharge conditions. Positive values are showing velocity away from the camera, and negative values are showing velocity towards the camera

Figure 3.8 shows the out of the plane normalised velocity components for CVP at different conditions. Some part of this component shows flow towards the camera (in blue colour) and some part is showing flow away from the camera (in red colour). The trend shows similar qualitative views of all the inflow and surcharge conditions. This velocity component is stronger at the core velocity zone and can be reached up to $0.3V_{avg}$. A big part of the core velocity region travels away from the camera. The diffusive region shows opposite flow direction, i.e. towards the camera. This velocity structure implies that a non-symmetric flow pattern is apparent in the manhole. This flow behaviour becomes clearer when the flow of RVP and LVP are compared. The out of the plane velocity component is also strong near the surface at low surcharge conditions. The water surface was always oscillating at low surcharge. A strong out of the plane velocity component may be a result of the added turbulence of the wavy water surface.

Figure 3.9 and Figure 3.10 show velocity magnitude and out of the plane velocity component respectively for both LVP and RVP for the inflow and surcharge conditions. It should be noted that the location of LVP was far from the camera positions. Due to the presence of the prism tank installed in front of the manhole, the sides of the LVP (especially the right side) was not visible to the camera correctly and contained poorer data. Therefore, the region with the poorer data is omitted from the results. The location of RVP was the closest to the camera, and the full view of the plane was visible to the camera.

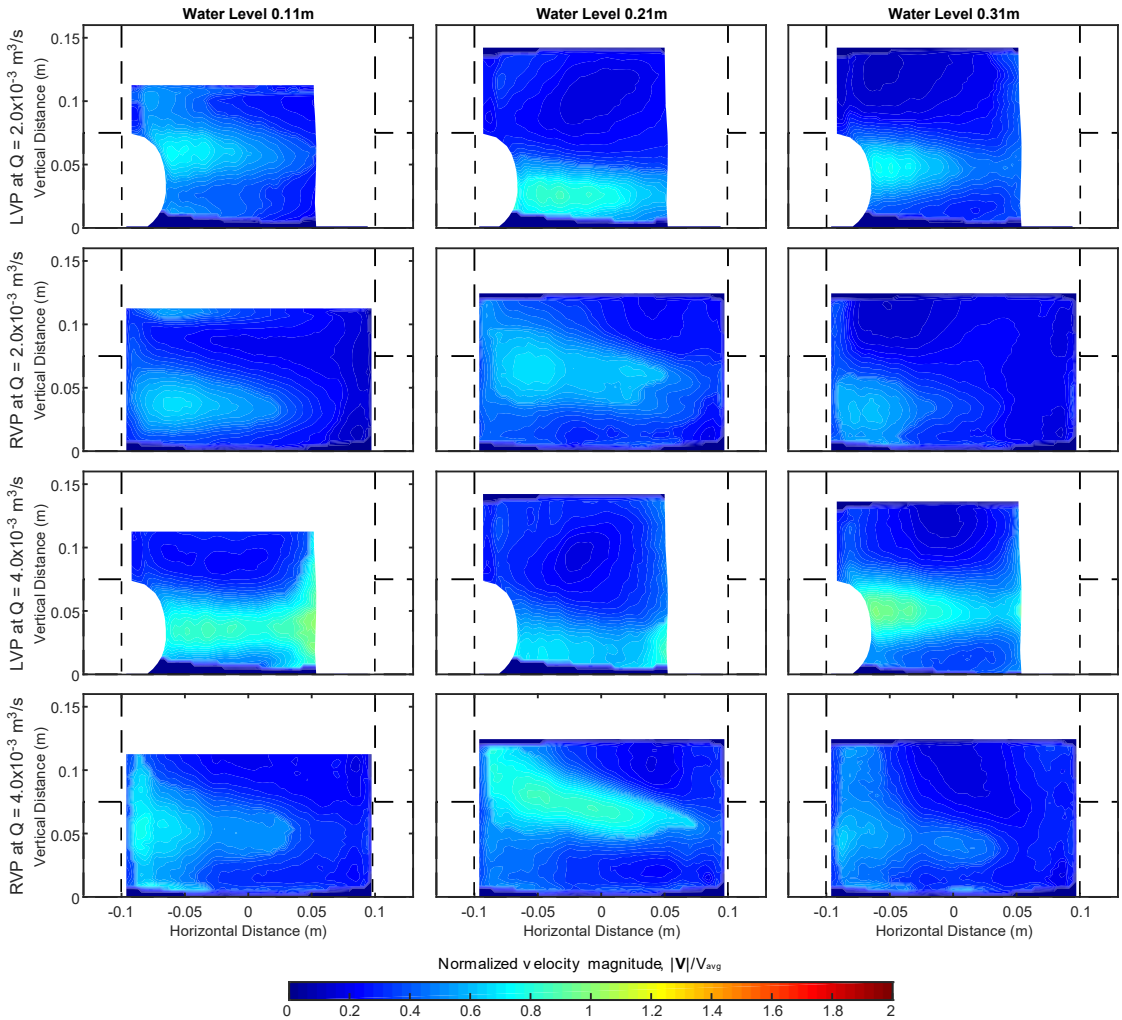

Figure 3.9: Normalised mean velocity magnitude at LVP and RVP

Comparing the flow behaviour from Figure 3.9, it is apparent that the velocity spatial pattern was different at the two planes. This indicates asymmetric flow behaviour in the manhole; especially in the high-velocity region and at low surcharge cases. The flow speed is higher close to the outlet. At inflow of 2×10^{-3} m^3/s, the flow speed at LVP was found marginally higher compared to RVP at all the three surcharge conditions. Similar conditions were observed for the flow condition at the inflow of 4×10^{-3} m^3/s with one exception. At the water level of 0.21 m (surcharge 0.135 m), the

flow speed was higher at the RVP. Moreover, at this condition, the high flow region (zone with flow jet) seems to move upward. The magnitude of the core zone velocity reaches up to $0.8V_{avg}$ at 2×10^{-3} m^3/s flow at LVP, while it is to some extent higher at 4×10^{-3} m^3/s flow reaching $0.9V_{avg}$. The velocity in the two planes at the highest surcharge were more comparable to each other. The jet flow region was at the same height for both planes, although the LVP contained stronger velocity.

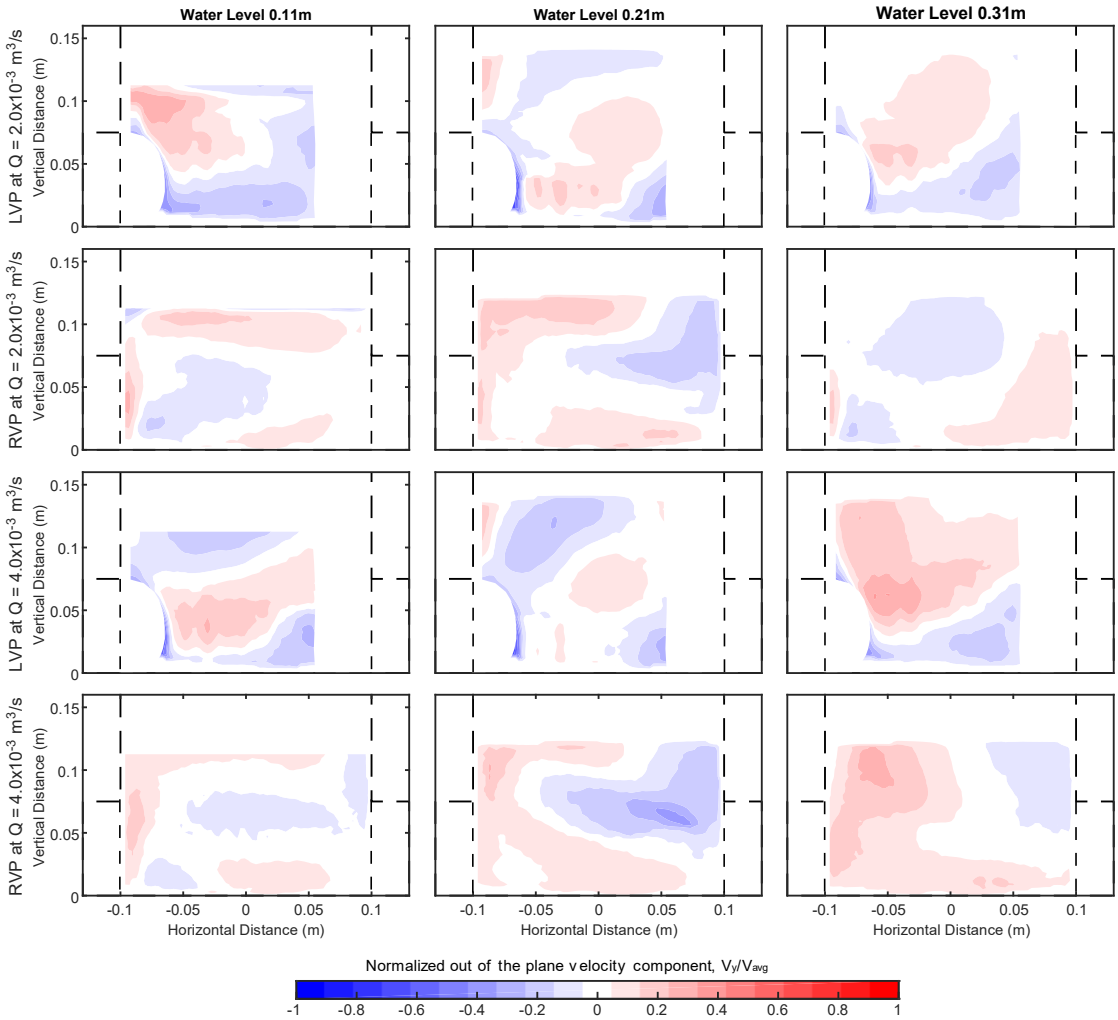

Figure 3.10: Out of the plane normalised mean velocity component at LVP and RVP. Positive values are showing velocity away from the camera, and negative values are showing velocity towards the camera

Examining Figure 3.10, we notice asymmetric flow behaviour of the manhole at different flow conditions, specially at low surcharge. Considering the spatial velocity distribution in Figure 3.10, for RVP, all the red (+ve) zones indicate flow towards the manhole CVP and all the blue zones indicates flow away from CVP; which is exactly opposite for LVP.

At these two planes, the magnitude of the out of the plane velocity component reaches up to 0.3 V_{avg}. For all the condition at LVP, flow towards the camera is observed near the manhole bottom close to the inlet side. In the same region of RVP, an opposite directional flow is observed. Close

to the inlet and manhole bottom, at both planes the mass flow goes towards the manhole centre. Similar phenomena are observed near the outlet. At both planes, water is flowing towards the outlet pipe at this region. A mixed behaviour can be observed in the midzone, where the fluid flows both towards and opposite to the camera.

More symmetrical velocity pattern can be observed at conditions with the highest surcharge. At these cases, flow direction at the bottom part near the manhole floor is towards the manhole CVP (blue zone in LVP and red zone in RVP). The flow direction turns opposite at shallower depths, which is further from the manhole floor.

It is apparent from the observation and the velocity measurement that the manhole flow showed a swirling movement. The swirl intensity was stronger at low surcharge and weaker at higher surcharge. This finding is in agreement with the description provided by Howarth (1985). While investigating surcharged manhole flow, he found 'medium swirl motion' at low surcharge conditions which was weaker or disappeared at higher surcharge. The swirl movement may be the reason of having the asymmetric flow patterns at the manhole LVP and RVP velocity. In our current results, high surcharge flow showed weaker swirl flow. This may also have triggered from small imperfection in the inlet outlet pipe alignment.

3.5.3 Secondary flow and vortex formation in the manhole

Analysing Figure 3.9 and Figure 3.10 and at the same time comparing them with Figure 3.7 with Figure 3.8, one can also have an idea of a swirling flow formation in the manhole. Formation of small vortex are also apparent at the three flow regions due to change in flow speed and directions. For clear analysis, the instantaneous vorticity perpendicular to the three measuring planes are calculated using the following equation:

$$\Omega_y = \frac{\partial V_z}{\partial x} - \frac{\partial V_x}{\partial z} \tag{3.7}$$

where, V_z and V_x are vertical and streamwise velocity components respectively. The values were normalised using respected V_{avg} and later the vorticity value was averaged temporarily. The vorticity maps at CVP as well as at LVP and RVP are shown in Figure 3.11. For simplicity, maps from the inflow of 2×10^{-3} m^3/s and 4×10^{-3} m^3/s are shown.

It can be seen from Figure 3.11 that in the CVP, the vorticity map is similar at all flow and surcharge conditions. At the region close to the manhole floor, a layer is seen with very high negative vorticity. This region indicates the high velocity gradient originated due to the boundary layer at the manhole base and lower diffusive region. At the core flow region, the vorticity magnitude is very small or zero. Strong positive vorticity is observed at the upper diffusive region.

Comparing the vorticity at the LVP and RVP, it can be seen that the locations of the vorticity centres at these two planes are different at all particular inflow and surcharge conditions. It shows that the formed vortex in manhole is not parallel to the manhole floor. With the increase in water level in the manhole, the vorticity characteristics change noticeably.

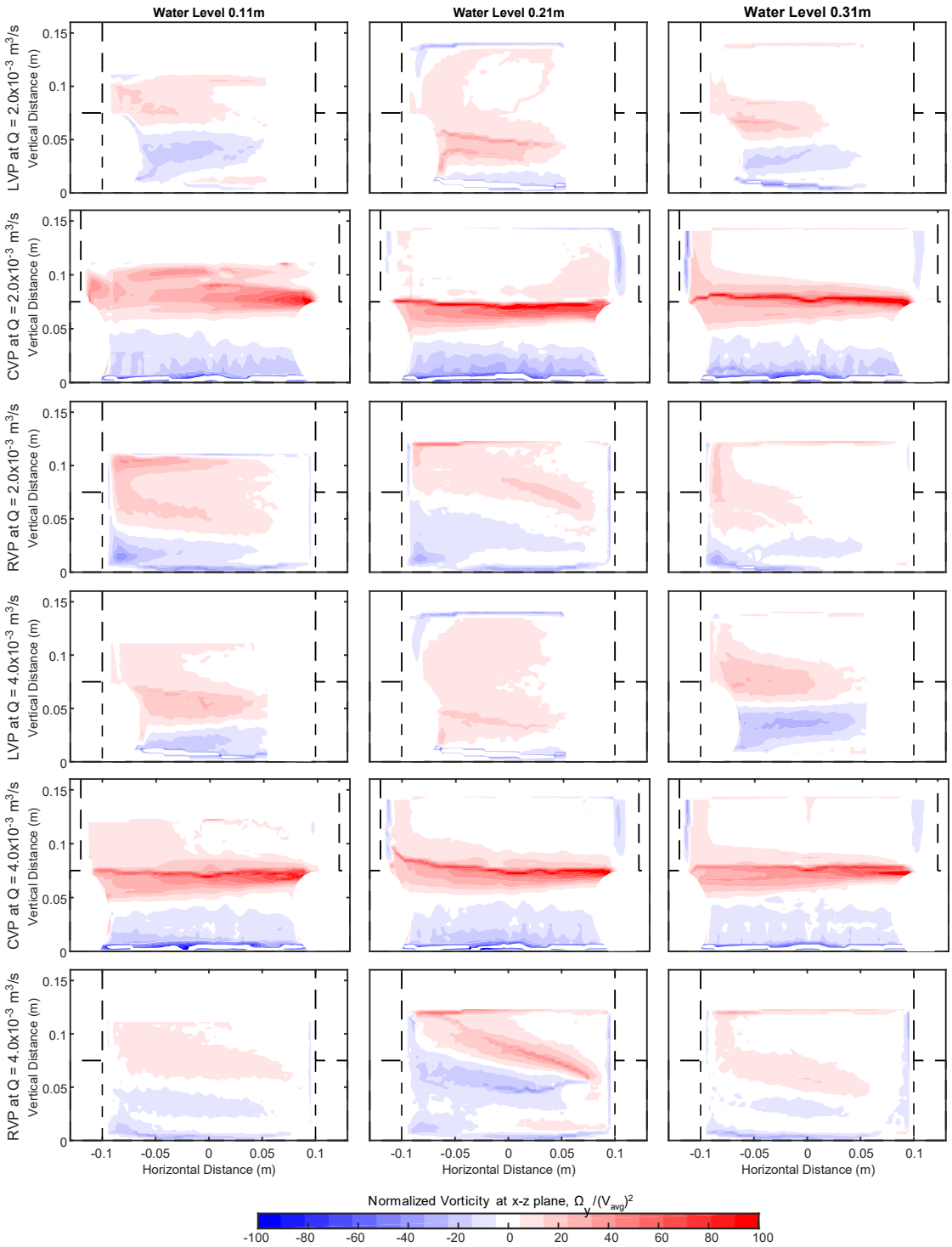

Figure 3.11: Mean normalised vorticity at LVP, CVP and RVP. Positive (red) values showing clockwise rotation and negative values (blue) showing anti-clockwise rotation

3.5.4 Turbulent kinetic energy

The instantaneous Turbulent Kinetic Energy (TKE) of the flow was calculated using the following formula:

$$k = \frac{1}{2}(\acute{u}.\acute{u} + \acute{v}.\acute{v} + \acute{w}.\acute{w}) \tag{3.8}$$

where, $\acute{u}$, $\acute{v}$ and $\acute{w}$ are the difference between instantaneous velocity components and mean velocity components towards x, y and z directions respectively. The value was normalized by dividing with the square of V_{avg} and then the temporal mean was calculated. The mean normalized turbulent kinetic energy at the manhole CVP along with LVP and RVP at different conditions are shown at Figure 3.12 and Figure 3.13 respectively.

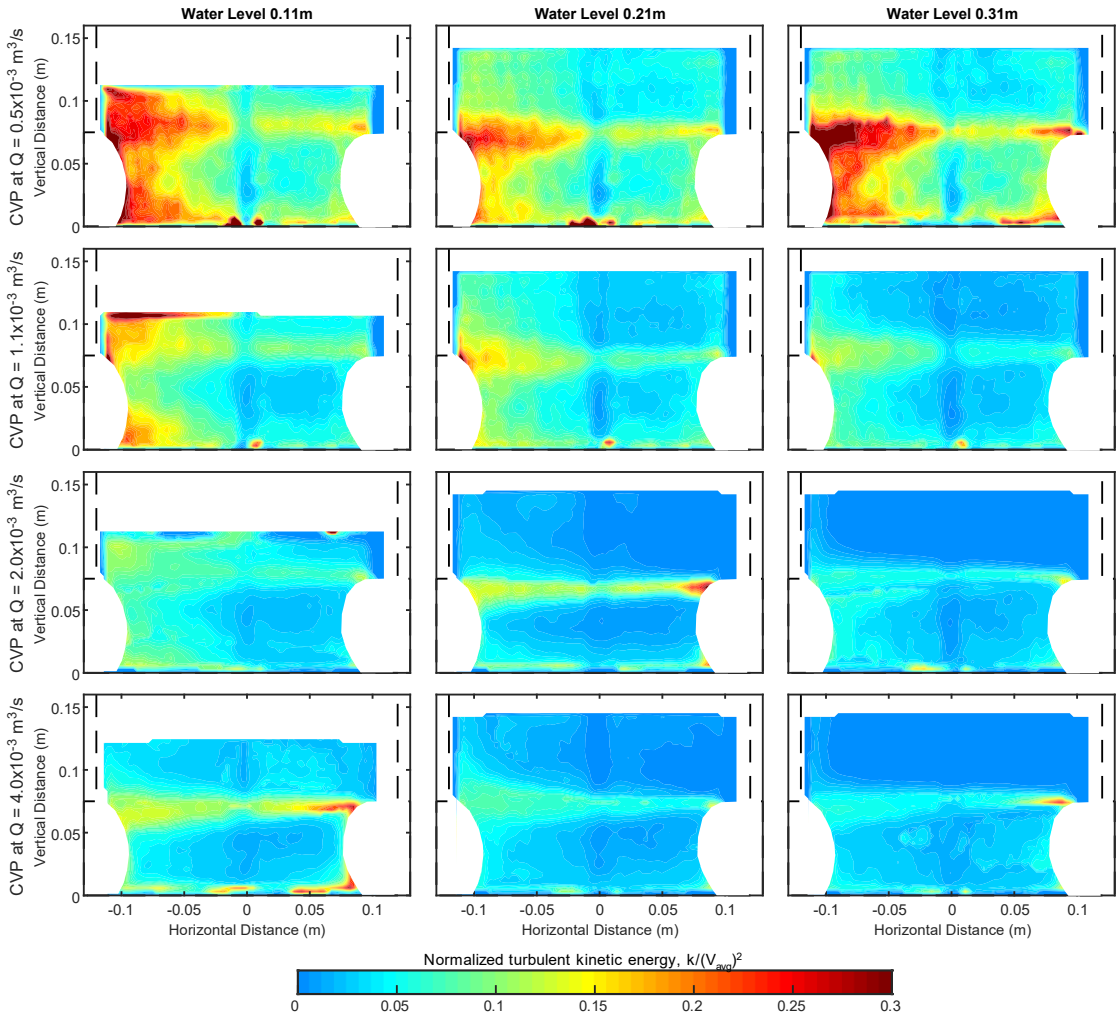

Figure 3.12: Mean normalised turbulent kinetic energy at CVP

Although the turbulence intensities were different, their trends were comparable. At any particular flow condition, highest normalised TKE at the CVP can be seen at the jet diffusion region

where the jet flow coming from the inlet starts dividing between the outlet and the upper part of the manhole (Figure 3.12). When compared to the values with changing inflows, the highest normalised turbulent kinetic energy was found at the lowest flow condition, reaching up to 0.3. Comparing with the changing surcharge, the highest kinetic energy was found at the lowest surcharge, at the water level of 0.11 m. At this low surcharge condition, a big part of the plane near manhole outlet showed higher fluctuations and turbulence. It should also be noted that all the cases presented here showed higher turbulence near the manhole floor, which is one expected phenomenon. The core velocity zone in all cases showed noticeably low TKE. It means that the temporal fluctuation of flow velocity in the core zone is very low.

When compared the turbulent kinetic energy at LVP and RVP (Figure 3.13), it can be seen that turbulence is also seen asymmetric at these two planes, mainly at higher flow. Like CVP, the highest turbulence is also seen at low surcharge conditions. At RVP, highest turbulence is seen near the outlet pipe for all flow conditions. However, for LVP, a part of the data near the inlet is unavailable, and apparently, evidence showed highest LVP turbulence values were probably at the zone of missing data. In contrast to the CVP, in LVP and RVP, we can observe higher turbulent kinetic energy at the zone with highest velocity, mainly because the highest velocity zone at these two planes represent the diffusion region of the inlet jet flow. Generally, the highest TKE levels at were lower in these planes than those of the diffusive regions of the CVP.

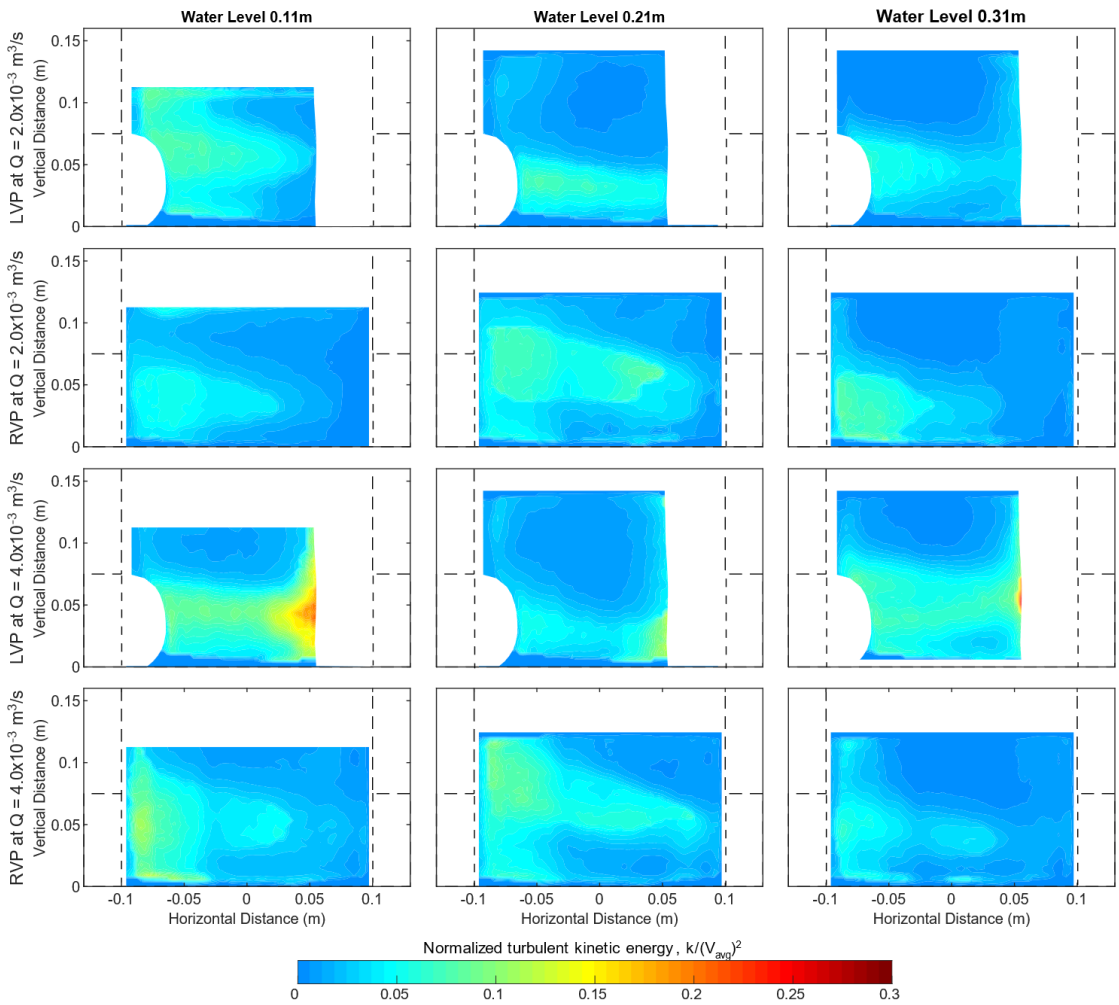

Figure 3.13: Mean normalised turbulent kinetic energy at LVP and RVP

3.5.5 Reynolds shear stresses

The Reynolds shear stress is a good indication of the turbulence characteristics of flow. The instantaneous three stress components are defined by:

$$[R_{xy}, \quad R_{yz}, \quad R_{zx}] = [\acute{u}.\acute{v}, \quad \acute{v}.\acute{w}, \quad \acute{w}.\acute{u}] \tag{3.9}$$

Like others, Reynolds shear stresses were calculated from the measured data and was normalised by dividing them by squared value of the corresponding V_{avg}. Later, the temporal averaged value was calculated and shown in Figure 3.14, Figure 3.15 and Figure 3.16 respectively. The sign of shear stress is dependent on the direction of the axes and do not have any influence on the hydraulics. For this purpose, only the absolute values of Reynolds stress are presented. To avoid redundancy, only data from CVP is shown. It should be noted that the three directions x, y and z are referring towards streamwise, perpendicular to the camera and vertical direction respectively.

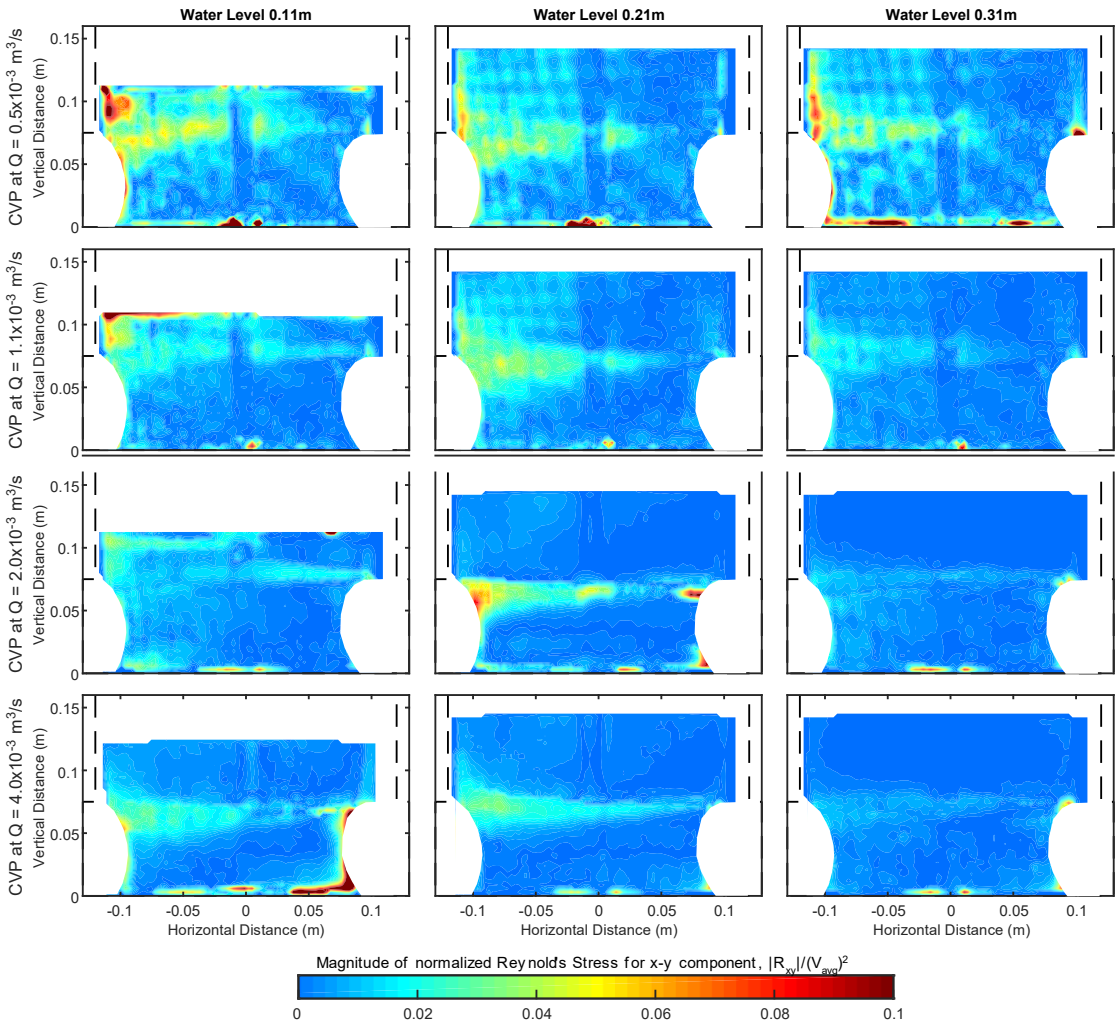

Figure 3.14: Magnitude of mean normalised Reynolds stress component R_{xy} at CVP

Comparing Figure 3.14, Figure 3.15 and Figure 3.16, it can be seen that R_{yz} conveys the highest shear stress at this plane while the value of R_{zx} (Figure 3.16) shows the lowest shear stress of all. This shear stress data is an indicator of low streamwise flow fluctuations (x-direction) and high horizontal/transversal velocity fluctuations. This indicates that the transverse components are more turbulent in the flow. For both R_{xy} and R_{yz}, the highest values are found mainly at the flow separation zone; whereas the highest value of R_{yz} is found near the inlet, manhole floor and outlet. High R_{xy} and R_{zx} are observed near the manhole wall.

Comparing R_{zx} in Figure 3.16, the contour lines of the shear force do not change with the change of inflow condition. However, at lower surcharge condition, the contour shows different orientation near the diffusive zone.

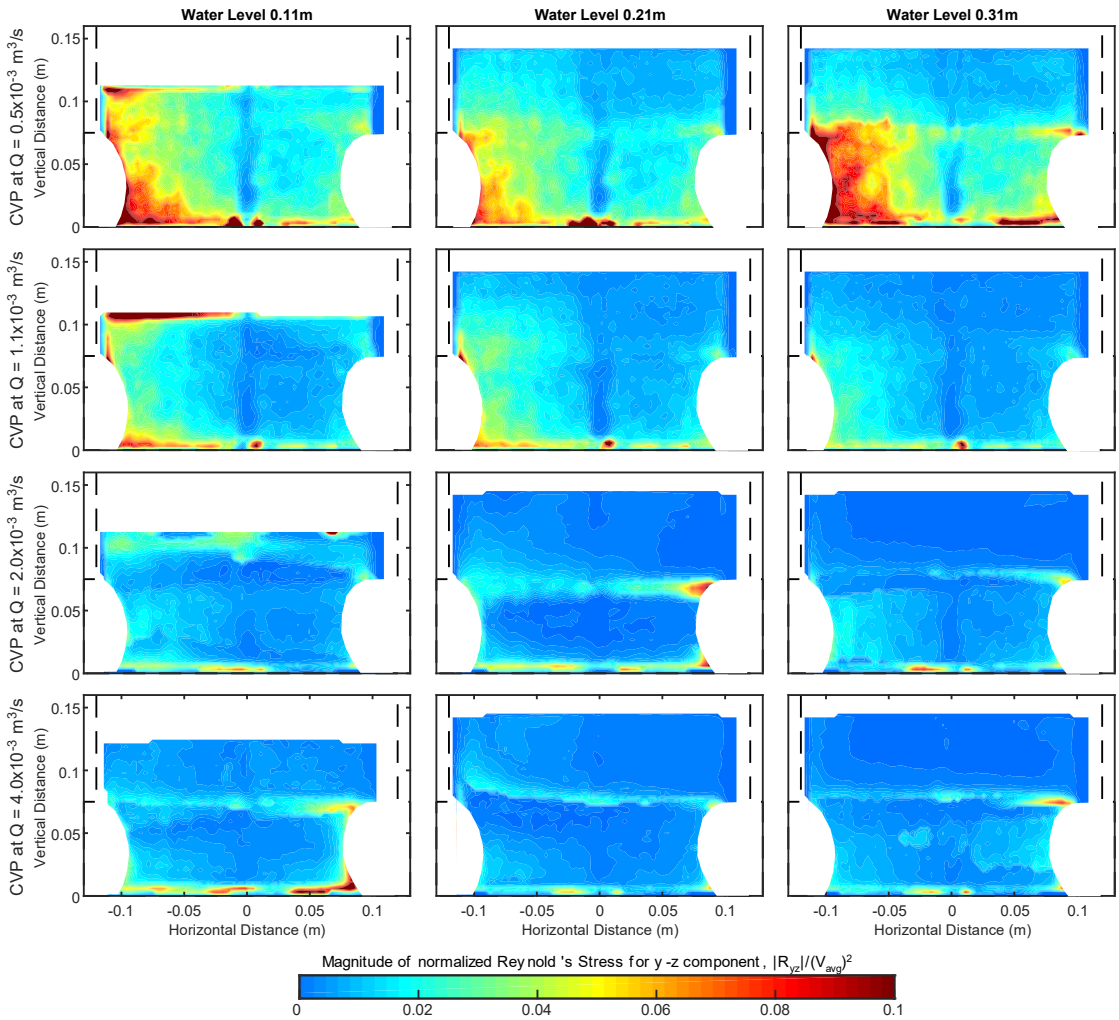

Figure 3.15: Magnitude of mean normalised Reynolds stress component R_{yz}

Reynold's shear stress is an important indicator of the transport and mixing capacity of the fluid. The normalised Reynolds stress was found higher in the low flow condition than that of the high flow conditions This indicates higher mixing potential for each unit flow in case the manhole flow is low. The zone near the manhole wall also showed higher Reynolds stress to all the three components. The flow is more turbulent at the near-wall zone which is causing high shear stress.

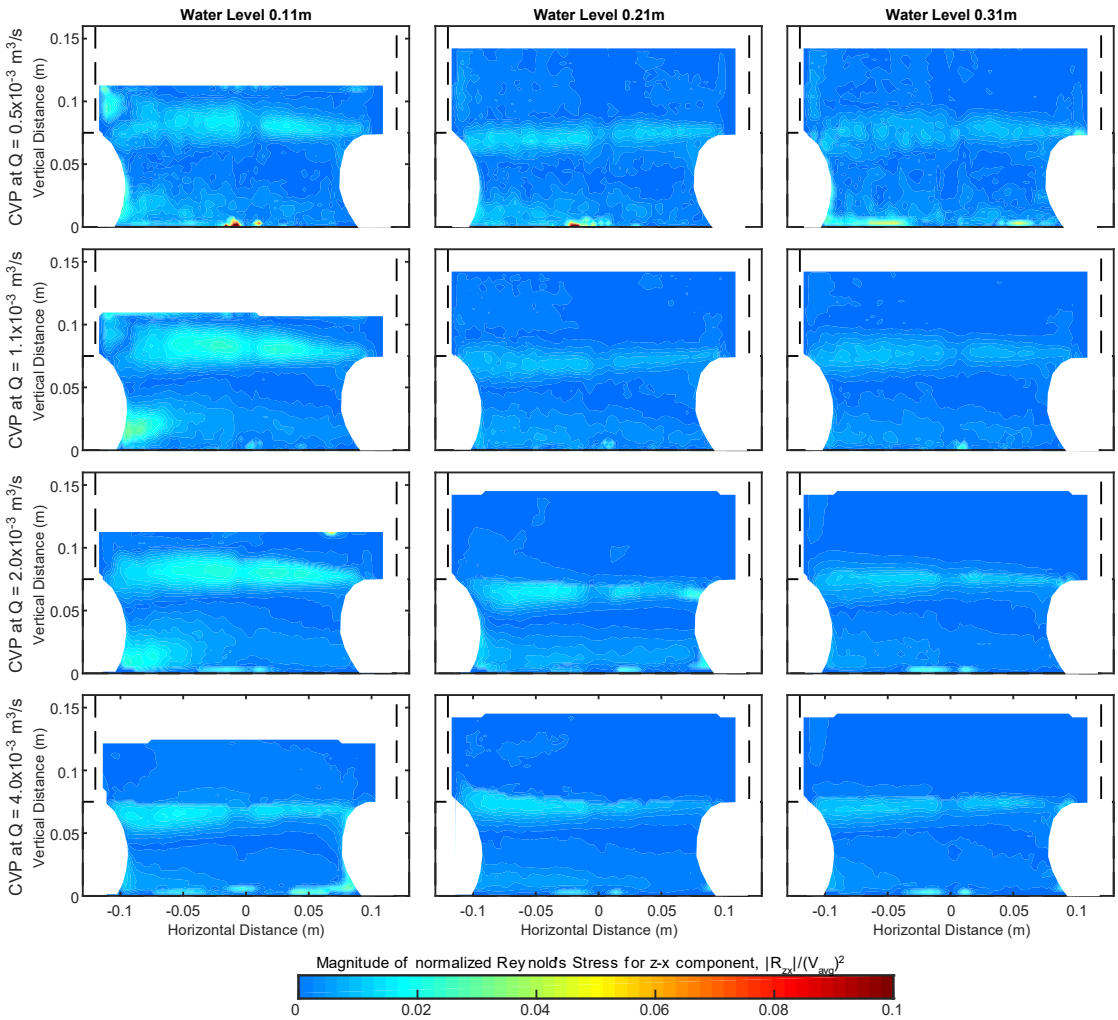

Figure 3.16: Magnitude of mean normalised Reynolds stress component R_{zx}

3.5.6 Changes in core and diffusion region at different conditions

The manhole spatial velocity pattern shows different behaviour at different flow and surcharge conditions. To compare the changes in velocity patterns, the core velocity contour and the diffusive velocity contours from all measured CVP profiles were projected together in one figure (Figure 3.17). For each condition, the normalised flow profile showed different velocity ranges. In this case, contours of eighty and twenty percentiles of the normalised jet velocity were chosen as representatives of the core and diffusion velocity regions respectively for each measurement set. These values not necessarily indicate the boundaries of the core and diffusion region but give comparable contours to analyse the location of these regions among all the flow and surcharge conditions.

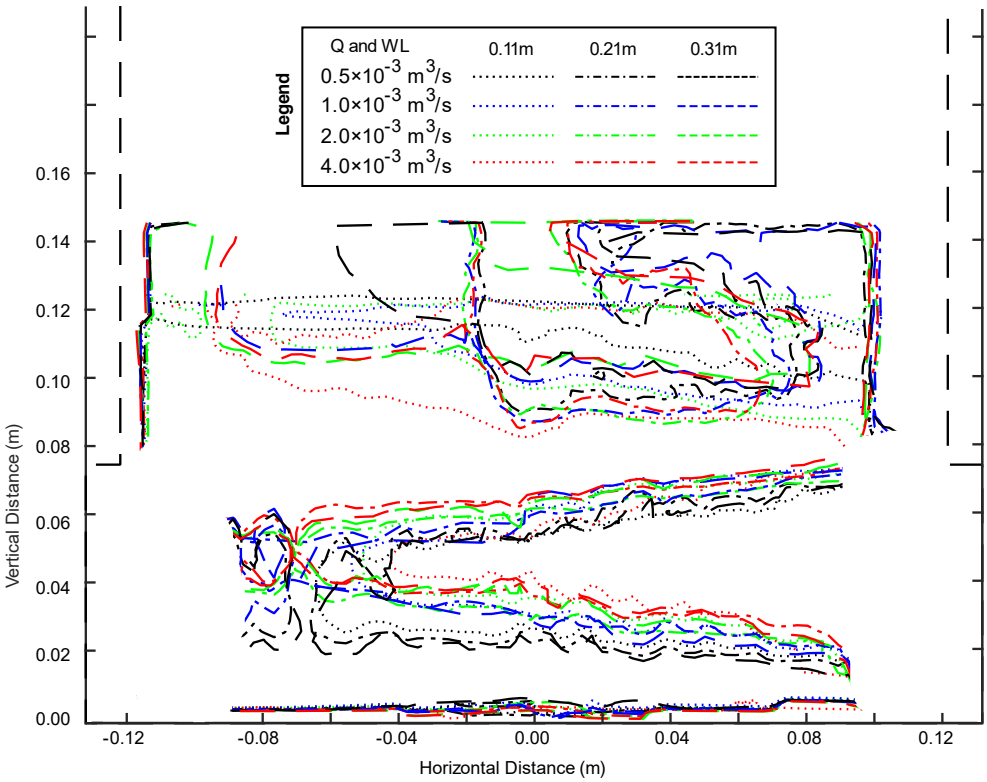

Figure 3.17: Location of the core and diffusion regions from all the measurements at CVP

In Figure 3.17, conically shaped core velocity zone changes its shape and position with the change in inlet flow. At low flow condition, the core zone orientation remains parallel to the inlet-outlet pipe. The size of the core velocity region also becomes smaller and narrower while the flow moves from the inlet towards the outlet. With the increase in velocity of the inlet jet flow, the core velocity tends to deviate from the manhole bottom. The diffusion region also tends to increase its size as the distance from the inlet increases. However, the region becomes constrained at the manhole bottom and creates additional pressure to the core velocity region. This upward pressure may increase with the increase inlet flow and creates pushes the core velocity zone away from the manhole bottom. However, the core region showed little to no deviation due to a change in surcharge.

The diffusive region showed different characteristics than the core region. The location of the velocity contour at this region was found to change with changing manhole surcharges. At low surcharge (comparable to WL= 0.11m) conditions, the diffusive regions were found much closer to the core velocity due to the unavailability of more water depth. However, at high surcharge, when more depth of water was available (comparable to WL= 0.21 m and 0.31m), the diffusive region contours were found to move upward and further from the outlet. The changes in the diffusive region with the change in inlet flow was comparably low and does not show any trend.

3.6 Conclusions

In this work, Stereo Particle Image Velocimetry was used to measure instantaneous velocity in a scaled surcharged 240 mm diameter manhole with a manhole to pipe ratio of 3.2. Two cameras were used at the same side of the manhole to characterise velocity field at three vertical planes; one being the central vertical plane and the other two being two vertical planes at 50 mm offset towards either side of it. Combined data from both cameras were used to reconstruct three-dimensional instantaneous velocity field. This is a novel approach in measuring all three velocity components of a surcharged manhole at combinations of different inflow and surcharge. Tests were conducted at four different inflows and three different surcharge conditions. Each temporal averaged data was obtained from at least 2000 instantaneous velocity data, recorded at a frequency of 8 Hz. Several possible measurement uncertainty sources were identified, and their possible effect was analysed. The uncertainty effect was found very limited and was rather small compared to the measured data range. The measured velocity showed different flow and turbulence phenomena. The analysed flow conditions have various Reynold's number, covering transition and turbulent flow through the manhole inlet pipe.

The findings can be summarized as follow:

- Analysis shows that it requires at least 1500 instantaneous data to attain statistical convergence of the temporal mean.
- The central vertical plane spatial velocity measurements showed that the normalised maximum manhole velocity is higher at lower flow. At high flow rate, the inlet Reynold's number increased, and the maximum velocity became closer to the averaged value.
- The spatial mean velocity distribution at the central plane can be distinguished at three different regions. The first one is the core jet region containing faster flow. This region reduces its size with the distance from the inlet and the velocity vectors remains parallel to the inlet-outlet pipe. The second region is diffusion region located around the jet core. This region is characterised by diverging flow from the jet core and it increases its size as the core size decreases. The third region is the dead zone containing the slowest fluid velocity.
- Additional velocity measurements at LVP and RVP for higher inflows indicated a swirling motion in the manhole. The swirl was less prominent at high surcharge.
- The mean flow field for all flow rates shows that the manhole flow was asymmetrical concerning the axis plane drawn through manhole centre and inlet-outlet pipe axis. The out of the plane velocity component and the vorticity created by flow showed lack of symmetry. A swirl flow was observed in the manhole, which is in agreement to the observation described by Howarth (1985). The swirl flow could also be a result of small

imperfection in the inlet-outlet pipe. This could not be explored further within the scope of this work.

- Turbulent Kinetic Energy (TKE) trends were comparable at all the cases in CVP. The normalised TKE was found higher in low flow condition. In all the measurements at CVP, the highest TKE was observed at the diffusion zone and at the flow separation zone. The core velocity zone had low TKE close to zero. At RVP and LVP, the highest TKE was found near at the region with highest velocity. The maximum TKE at these two planes were comparable to that of the TKE of the diffusive zone of the CVP.
- The location of the core region and diffusive region was found to change with in different measurement conditions. The location of core velocity region was found to be dependent on the inlet flow velocity while the diffusive region changes with the available surcharge in the manhole.

3.7 Acknowledgement

The work presented is part of the QUICS (Quantifying Uncertainty in Integrated Catchment Studies) project. This project has received funding from the European Union's Seventh Framework Programme for research, technological development and demonstration under grant agreement No. 607000. The laboratory facility was made possible through EPSRC, project EP/K040405/1.

CHAPTER 4

A COMPARATIVE STUDY ON MANHOLE HYDRAULICS USING STEREO PIV AND DIFFERENT RANS MODELS

4.1 Abstract

Flows in manholes are complex and may include swirling and recirculation flow with significant turbulence and vorticity. However, how these complex 3D flow patterns could generate different energy losses and so affect flow quantity in the wider sewer network is unknown. In this work, 2D3C stereo Particle Image Velocimetry (PIV) measurements are made in a surcharged scaled circular manhole. A CFD model in OpenFOAM® with four different Reynolds Averaged Navier Stokes (RANS) turbulence model is constructed using a VOF model, to represent flows in this manhole. Velocity profiles and pressure distributions from the models are compared with the experimental data in view of finding the best modelling approach. It was found among four different RANS models that the RNG k-ε and k-ω SST gave a better approximation for velocity and pressure.

Keywords: Manhole; OpenFOAM®; RANS model; Stereoscopic PIV; VOF

4.2 Introduction

Manholes are one of the most common features in urban drainage networks. They are located at changes in slope and orientation of the sewer pipes, as well as at regular intervals along the pipes to enable maintenance. The flow pattern in a manhole is complex, especially during high flows, and involves several hydraulic phenomena such as local flow contraction, expansion, rotation, recirculation as well as possible air entrainment and sediment mixing. These flow phenomena can control the overall energy loss, transport and dispersion of solute and particulate materials in the manhole structure. PIV measurement can provide a good representation of the complex velocity field of a manhole. Previously Lau (2008) studied two-dimensional PIV in a surcharged scaled

manhole. Attempts to measure stereo PIV data in a scaled manhole are however new and to the authors' knowledge, has not been done before. Several researchers studied flow patterns in surcharged manholes using CFD models. Use of different RANS modelling approach like RNG k-ε model (Lau et al., 2007), Realizable k-ε (Stovin et al., 2013), k-ω model (Djordjević et al., 2013) have been reported. A little research study has been conducted on how these flow patterns could affect flow movement and flow quality in the wider piped network. In the current work, the flow phenomena of a scaled manhole are measured by stereo Particle Image Velocimetry (PIV) and modelled numerically using OpenFOAM® CFD tools. Four different RANS models, i.e. RNG k-ε, Realizable k-ε, k-ω SST and Launder-Reece-Rodi (LRR) were used, and the differences in flow structures among them were compared and discussed.

4.3 Methods and Materials

4.3.1 Experimental model

The experimental facility was installed in the Hydraulic Laboratory of the University of Sheffield. It consists of a transparent acrylic circular scaled manhole, linked to a model catchment surface (Rubinato et al., 2017). The manhole has an inner diameter (Φ_m) of 240 mm and connected with a 75 mm diameter (Φ_p) inlet-outlet pipes. Both pipes are co-axial, and the pipe axis passes through the centre of the manhole vertical axis (Figure 4.1). Two butterfly valves (one at >48Φ_p upstream the manhole, the other one at >87Φ_p downstream the manhole) are used to control the inflow and the water depth of the manhole respectively. The inflow was monitored using an electromagnetic MAG flow meter fitted within the inlet sewer pipe (10Φ_p from the butterfly inlet valve). The ratio of the manhole diameters to inlet pipe diameters (Φ_m/Φ_p) is 3.20. Two Gems series pressure sensors (Product code 5000BGM7000G3000A, serial number 551362, range 0-70 mb) were installed vertically at the inlet and outlet pipes, the first one at 350 mm upstream from the centreline of the manhole, the second one, 520 mm downstream from the centreline of the manhole by making a hole in the pipe of Φ = 5 mm. They can measure piezometric pressures for both free surface and pressure flow conditions within the inlet-outlet pipes. These transducers were calibrated such that transducer output signal (4-20 mA) can be directly related to gauge pressure. For the calibration of the pressure transmitter 10 different water levels were measured (range 50 to 500 mm, no discharge) and checked with a point gauge. Rubinato (2015) found an overall accuracy can be defined as ±0.72 mm. A transparent measuring tape was attached vertically to the manhole side in order to check the manhole water levels during the experiments. The tape position was at the other side of the camera, keeping an equal distance from both inlet and outlet.

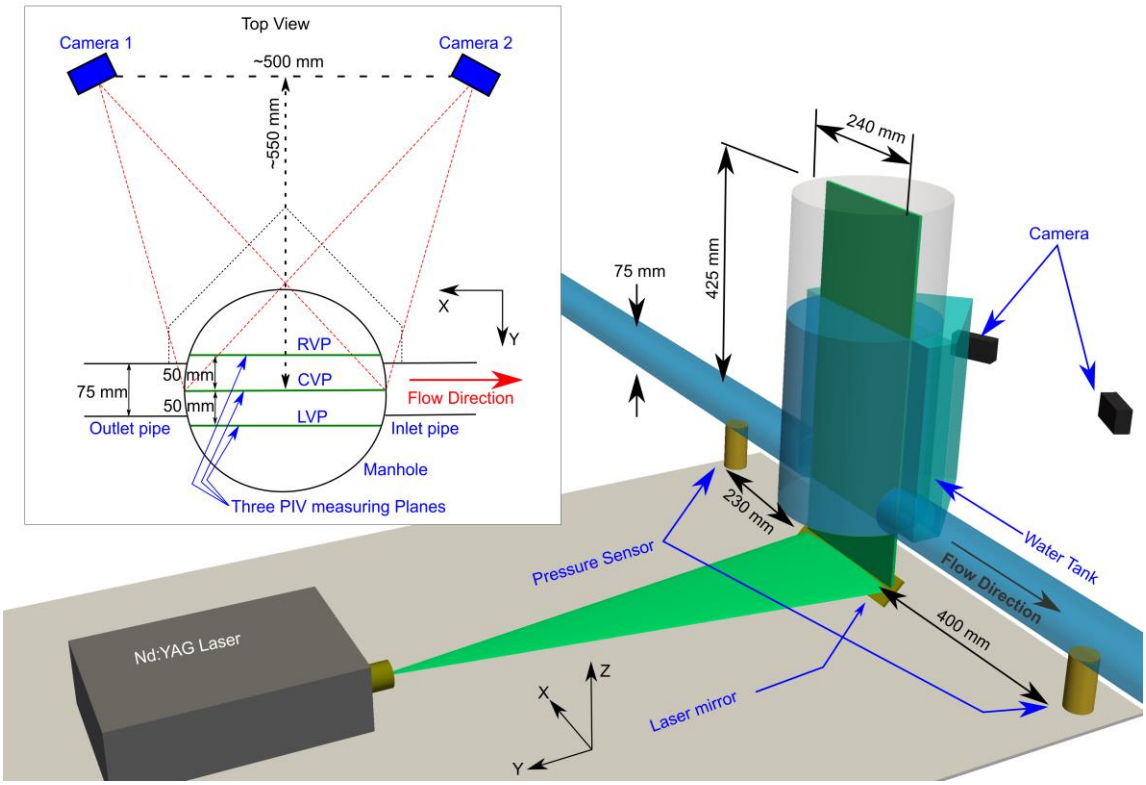

Figure 4.1: Experimental setup for 2D3C stereo PIV measurement at the manhole

4.3.2 PIV measurement

A stereo PIV measurement setup was installed. Two Dantec FlowSense EO 2M cameras and an Nd:YAG pulsed laser was placed at opposite sides of the scaled manhole. Each camera resolution was 1600x1200 pixels (Figure 4.1) and was set at the same distance from the manhole making more than 45° angle at the vertical centre of the measuring plane. To reduce error due to refraction through the curved manhole wall, a transparent acrylic tank was constructed around it and filled with water, keeping flat surfaces parallel to both camera lens axes. The laser was directed from the bottom of the acrylic manhole as a laser sheet with the help of a flat mirror set at 45° to the horizontal direction. The laser sheet thickness was around 4mm.

Conventional 2D PIV can give the velocity vectors perpendicular to the camera direction only, which is typically parallel to the laser sheet (known as the in-plane velocity (Leandro et al., 2014a)). However, the use of two cameras can give the reading of the third component of the velocity vector (referred as out of plane velocity) with proper regeneration of the 2D velocities from each camera images; provided that appropriate calibration is done beforehand. As both of the cameras see the same stationary image from two different angles, the calculated velocity vectors from the two successive snapshots of a moving particle will also orient differently on both cameras. This change in orientation is the result of the different camera position and out of the plane velocity vectors. If the camera position is known and distortion of a still image at each

camera is known, the out of the plane velocity component can be calculated. Standard calibration plates were used in this study to calibrate the cameras.

When the manhole surcharge level is below a certain limit (typically around $0.2\Phi_m$), then the manhole inlet flow reacts vigorously with the surface, creating irregular flow pattern and a very high head loss. This surcharge limit is known as threshold surcharge (Stovin et al., 2013). At higher surcharge, the flow pattern inside the manhole is regular. This work focuses to analyse above threshold surcharge flow. The PIV measurements condition was chosen as 4 dm^3/s of inflow through the inlet pipe and a water level of 310 mm which resulted in a surcharge level of 235 mm (s) at the manhole centre; making surcharge to manhole diameter ratio (s/Φ_m) 0.98. This was well over the estimated threshold surcharge level. Initial inspection showed that the measurement zone has two different distinctive velocity characteristics. One part of the measuring plane is approximately in line with the inlet-outlet pipes and is characterised by a fast, slowly expanding jet flow. The second part is outside the jet flow zone and is characterised by a recirculation in which the velocity magnitude is around 10% of the jet flow. For these two distinctive velocity zones, data were taken at different image time separation intervals ranging from 250 ms to 4000 ms; so that velocities of both zones can be estimated accurately using the PIV cross-correlation algorithm.

For seeding, 100 µm polyamide 12 particles were chosen (density = 1010 kg/m^3). The particles were mixed with water and kept in a seeding tank with continuous circulation so that they remain in suspension. The particles were pumped from the seeding tank at a constant rate into the inlet pipe approximately $40\Phi_p$ upstream on the manhole so that they were well mixed before entering the manhole.

The seeding rate was adjusted by checking the PIV images to facilitate at least five particles in any selected interrogation area. Data were recorded at three vertical planes; one passing through the central axis of the inlet-outlet pipes and the other two at 50 mm offset from it (see Figure 4.1). Each data set was measured for five minutes, at a rate of 8 image pairs per second, totalling 2400 pairs of images.

The data was analysed using Dantec Dynamics' DynamicStudio v3.31 software. The collected data was pre-processed after masking the area of interest. The fluid velocity was calculated using an adaptive cross-correlation technique keeping an interrogation area of 128x128 pixels with consideration of 50% overlap between two adjacent areas. Median correction post-processing was applied to remove erroneous vectors and which removed approximately 2 to 8% vectors from each measurement set.

Due to the resolution and positioning of the laboratory setup, neither of the cameras was able to cover the whole manhole height. Emphasis was given to the incoming jet to see how velocity is distributed over the length of the manhole. Hence the data was recorded covering the lower zone of the manhole; from the manhole bottom until the height of 150 mm of the manhole; which is two times of the inlet-outlet pipe diameter.

4.3.3 Numerical model

The open source CFD model tool OpenFOAM®v4.1 was used in this work. The solver *interFoam* is selected as it can predict the velocity patterns and the free-surface for sharp interfaces. This solver uses a single set of Navier-Stokes/Reynolds-Average equations where the velocity is shared by both phases and a Volume of Fluid (VOF) method (Hirt and Nichols, 1981) captures the free-surface position. The length of the inlet pipe was chosen as 1000 mm (more than $13\Phi_p$) based on some other previous works (Lau, 2008; Stovin et al., 2013), and the outlet pipe was kept as 400 mm, which is until the position of the pressure sensor at the downstream of the manhole (Figure 4.2a). The computational mesh for the simulation was prepared with hexahedral Cartesian mesh using *cfMesh* (Juretić, 2015).

Some pre-analysis of CFD simulations were performed to test the mesh independence. For this case, three computational meshes were constructed having dx = 2 mm (Mesh 1), 4 mm (Mesh 2) and 6 mm (Mesh 3) respectively keeping the global refinement ratio as 3. Number of cells at these meshes are: 2.4 million, 861,500 and 380,000 respectively. The inlet flow condition was prescribed as constant discharge of Q = 4 dm^3/s. The meshes were simulated using k-ϵ turbulence model and the velocity profiles at the manhole centre and at the outlet pipe were extracted from the results (Figure 4.2c). The mesh analysis was performed applying Richardson extrapolation (Celik et al., 2008). The meshes gave similar results at the manhole jet zone and at the pipe. However, the velocity profiles showed different results closed to the manhole water surface (at around z = 0.29 m to 0.31 m) and close to the bottom (around z = 0 m). Mesh 3 predicted slightly slower velocity at the near surface zone. The apparent order (*p*) and the Grid Convergence Index (GCI) was calculated at each grid point of the meshes. The average value of p at the manhole centre and pipe were found 2.76 and 2.32 respectively. The GCI values were found higher close to the surface and the walls. Analysis showed that 50% cells in the manhole has GCI value below 10% when comparing Mesh 2 and Mesh 3; while 65% cell showed below 10% GCI in case of comparing Mesh 1 and Mesh 2. However, in case of results at the pipe, 70% and 76% cells showed GCI value below 10% in case of comparing Mesh 3-Mesh 2 and Mesh 2-Mesh 1 respectively. It was apparent that the results go towards mesh independence and Mesh 1 and Mesh 2 show almost similar results. Average approximate relative error between Mesh 2 and Mesh 1 was found to be 2.7%, whereas the simulation time requirement for Mesh 1 was more than three times to that of Mesh 2.

Considering the accuracy level and computational time required, Mesh 2 with dx = 4 mm was found best suited for this work.

The model considers all the manhole borders as *noSlip* wall (i.e. zero velocity at the wall) and three open boundaries: *inlet*, *outlet* and *atmosphere* (Figure 4.2b). Wall roughness was not considered as the aim was to characterize the flow velocity patterns in the manhole in which the wall energy losses were considered small in comparison with the entry, exit and mixing losses. The inlet boundary conditions were prescribed as fixed velocity approving for fully developed pipe flow profile using inverse power law of pipe flow (Çengel and Cimbala, 2006, chap. 8):

$$v_r = v_{max}\left(1 - \frac{r}{R}\right)^{1/n} \tag{4.1}$$

where v_r is the longitudinal velocity at a radial distance of r from the pipe axis, R is the pipe radius, v_{max} is the maximum longitudinal velocity at the developed profile section and n is a constant which is dependent on the Reynold's number of the flow. To find the best combination of v_{max} and n, pre-analysis was done considering a pipe flow CFD model. The pipe diameter was made the same as the inlet pipe (Φ_p=0.075 m) and pipe length was kept 3 m (40 Φ_p). The model was simulated using k-ϵ model applying the same inflow (Q = 4 dm^3/s). It was found that the pipe becomes fully turbulent at flow reach of 27Φ_p (2 m length) and after 20 s of simulation time. It produces v_{max} = 1.128ms^{-1} at fully turbulent condition and n = 6.5 gives the best fit curve of the development profile. These values were chosen to calculate inlet boundary condition of the manhole model using equation (4.1). The outlet boundary condition was prescribed as fixed pressure boundary corresponding to average water column pressure head, measured with the outlet pipe pressure sensor (shown in Figure 4.1). The pressure at atmosphere boundary condition (at the manhole top, shown at Figure 4.2b) was prescribed as equal to *atmospheric pressure* and *zeroGradient* for velocity to have free air flow, if necessary.

The mentioned condition was simulated with four different Reynolds Average Navier-Stokes (RANS) turbulence modelling approaches; namely: RNG k-ε model, Realizable k-ε model, k-ω SST model and Launder-Reece-Rodi (LRR) model to evaluate if they are able to characterize the flow properly. The first two models use a two-equation based approach calculating turbulent kinetic energy (*k*) and turbulent energy dissipation (*ε*). These two models are and formulated by Yakhot et al. (1992) and Shih et al. (1995) and known to be better than the standard *k-ε* model to give better prediction at separating flow and spreading rate of round jets respectively. The k-ω SST model used in OpenFOAM is based on Menter and Esch (2001) with updated coefficients from Menter et al. (2003) and addition of the optional F3 term for rough walls (Hellsten, 1998). This model uses rate of dissipation (*ω*) instead of *ε* at the near wall zone and standard *k-ε* model at the zones far from the wall influence and is supposed to give better prediction at the near wall and

turbulence separating flow. Wall-functions are applied in this implementation by using Kolmogorov-Prandtl expression for eddy viscosity (Hellsten, 1998) to specify the near-wall omega as appropriate. The blending functions are not currently used in OpenFOAM version because of the uncertainty in their origin. The effect is considered negligible in case of small y+ cell at the wall (Greenshields, 2017) and hence can be applied to models with low y+ cells. The fourth model uses the seven-equation based Reynolds Stress Model (RSM); using turbulent kinetic energy (*k*) and six component of stress tensor (R) directly and therefore may predict complex interactions in turbulent flow fields in a better way. The initial condition was prescribed as filling the manhole up to the expected level. Inlet pipe, outlet pipe and the manhole zone in line with the inlet-outlet pipe was initialized with a fully developed velocity profile which was same as the inlet boundary condition. The inlet turbulent boundary and initial conditions *k*, *ε*, *R* and ν_t were calculated using standard equations as follows:

$$k = \frac{3}{2}\left(I\left|\boldsymbol{u}_{ref}\right|\right)^2 \tag{4.2}$$

$$\epsilon = \frac{{C_\mu}^{0.75} k^{1.5}}{L} \tag{4.3}$$

$$\nu_t = C_\mu \frac{k^2}{\epsilon} \tag{4.4}$$

$$\omega = \frac{k^{0.5}}{C_\mu L} \tag{4.5}$$

where $\boldsymbol{u}_{ref}$ is the velocity to be considered, I is the turbulent intensity (chosen as 0.05 at this case), C_μ is a constant (=0.09) and L is the characteristic length of the inlet pipe.

Standard wall function was considered in k-ω SST model only as according to the model description, it requires wall function for y+>1. The rest of the models require wall function when 30<y+<300.

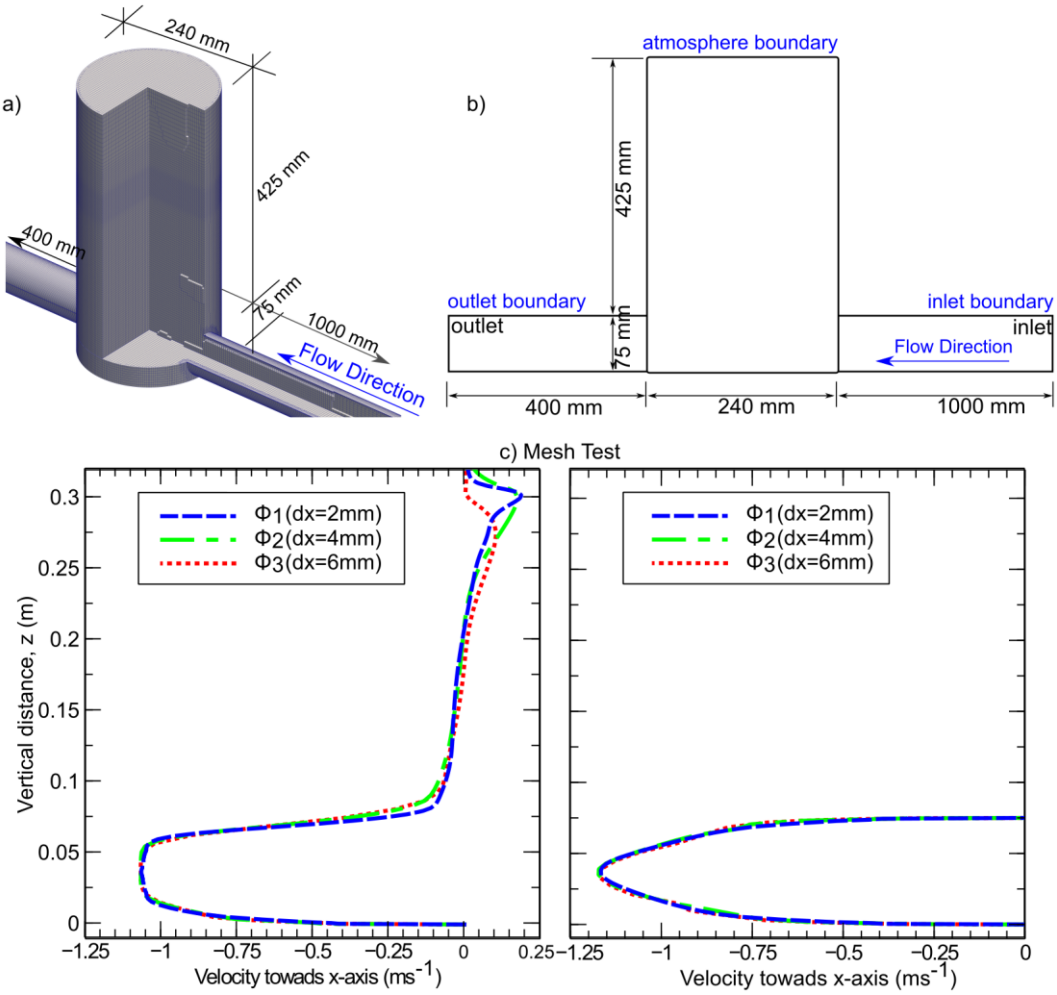

Figure 4.2: a) Numerical model mesh (top left panel), b) Boundary locations (top right panel) and c) Mesh convergence test (bottom panel)

During the simulations, the adjustableRunTime code was used keeping maximum Courant–Friedrichs–Lewy (CFL) number to 0.95. Cluster computing system at the University of Coimbra was used to run the simulations using MPI mode. Each simulation was run for 65 seconds. The steady condition was ensured by checking the residuals of p, alpha.water, k, epsilon and Rxx (where applicable). The first 60 seconds were required to reach steady state condition and the results of 101 velocity profiles in the last 5 seconds were averaged and all the numerical analysis were made using averaged data of these mentioned time step results.

4.4 Results and Discussion

The processed PIV velocity data were compared with velocity data of the manhole model. The PIV measurement was taken at the central vertical plane (CVP) along with the left vertical plane (LVP) and right vertical plane (RVP) (Figure 4.1). However, the position of LVP was much further from the camera, and light ray coming from the two edges of the LVP have to travel through the

manhole inlet-outlet pipe. Although the scaled manhole model is made of transparent acrylic, the joints between the model components were semi-transparent to non-transparent. Due to this limitation, the LVP image edges had bad data in some cases, as the camera could not see the seeding particles due to the obstruction made by the model joints. So, in this work, PIV data comparison is only done to the CVP and RVP of the manhole. Figure 4.3 shows the axial (V_x) and vertical (V_z) velocity components comparison between the PIV data and numerical model results. All the comparison is shown as dimensionless velocities as a ratio of the average inlet velocity (V_{avg}), where V_{avg} is the ratio between inlet discharge (Q) and pipe cross section (A_p). Both PIV data and CFD data are showing temporal mean velocities from the measurements and simulation results. PIV data at the CVP near the manhole inlet and outlet pipe were not collected as it was not visible clearly by the cameras due to the joints between pipe and manhole.

It can be seen from the velocity comparison at the CVP of PIV (1st and 3rd column of row 1 at Figure 4.3), that the jet flow in the experimental results starts expanding slowly as it proceeds from the inlet towards the outlet. The CVP axial velocity (V_x) (1st column of Figure 4.3) reaches up to 110% of V_{avg} at the experimental results. It dampens down at the manhole centre. The maximum velocity near the outlet pipe is the same as V_{avg}. However, in the CFD data, this damping effect is not seen. The high-velocity core stays as 110% of V_{avg} until it reaches the outlet. While the jet flow trying to escape through the outlet pipe, it hits the manhole wall at the top of the outlet (near x = -100 mm and y = 75 mm) and creates a vertically upward velocity component which is up to 20% of V_{avg} (3rd column of Figure 4.3). However, in all the CFD, the vertical velocity component at this zone reaches up to 30% of V_{avg}. Comparing the velocity contours of V_x and V_z at the CVP, it can be seen that LRR model could not predict the velocity profile properly. This model shows different axial velocity contour at CVP which is dissimilar to PIV measurements.

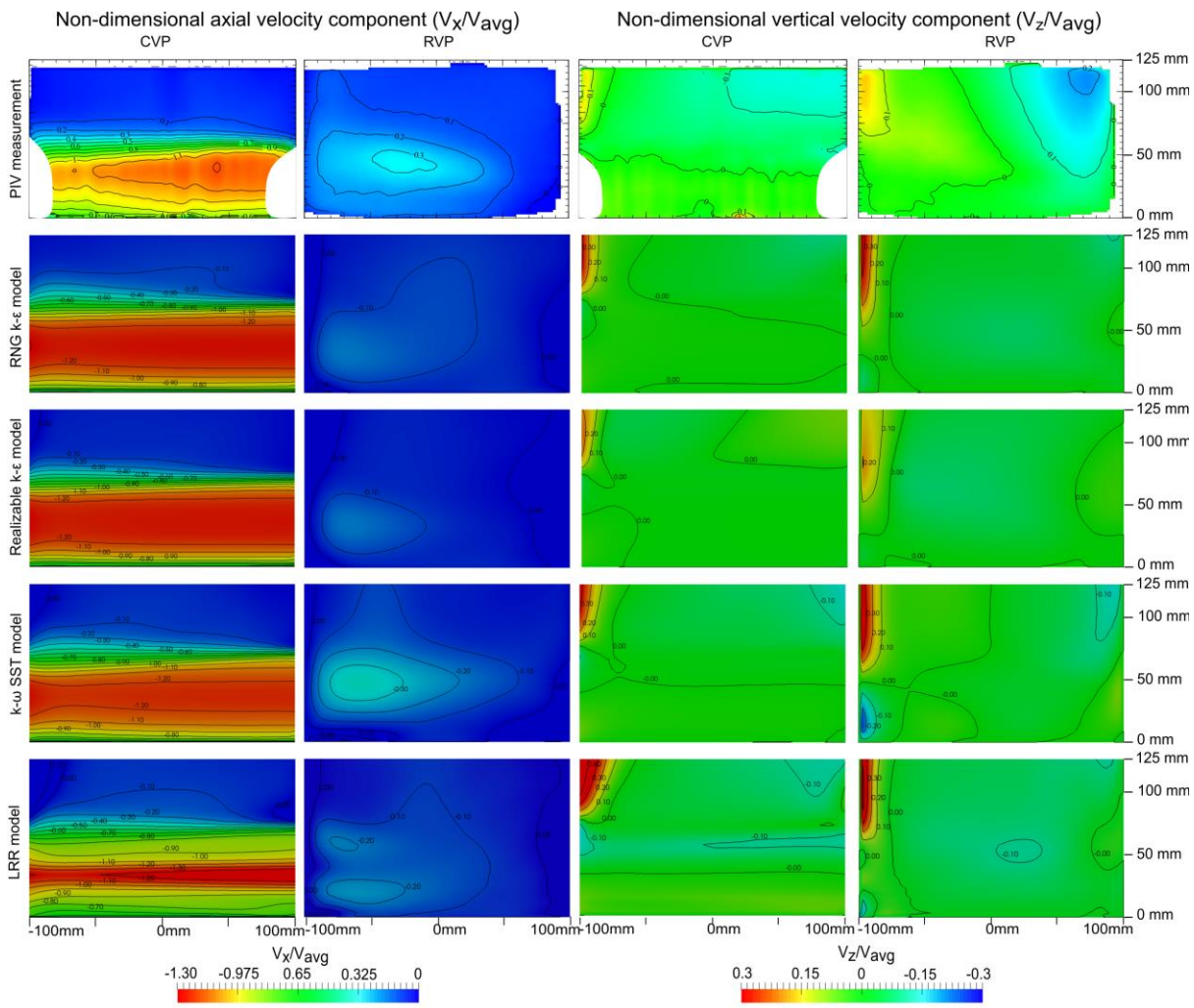

Figure 4.3: Comparison of non-dimensional velocity components from the numerical models and PIV measurement at both CVP and RVP of the manhole. The flow direction is from right to the left

Comparing the velocity towards the pipe axis at the RVP (2nd column of Figure 4.3), RNG k-ε and Realizable k-ε models slightly underestimate the axial velocity component in compared to the PIV experiment. The PIV data showed axial velocity up to $0.3V_{avg}$ whereas, in these two numerical models, the highest velocity is found $0.25V_{avg}$. The axial velocity at this plane is properly estimated by k-ω SST model. The shape of the velocity contour is almost similar to that of the PIV data. The vertical velocity component (V_z) (4th column of Figure 4.3), at PIV is observed between $-0.2V_{avg}$ and $0.2V_{avg}$. The numerical models show similar results of V_z near the outlet of the manhole. However, at the upper part of the measuring plane near the inlet, the V_z was measured in PIV as around $-0.2V_{avg}$, which was not predicted by the numerical models. Only k-ω SST model in this plane shows a negative (downward) velocity near the inlet, however still underestimated than the PIV.

The velocity comparison was not done for out of the plane component (V_y) as at CVP, this component is very close to zero and considered not significant (Figure 4.4).

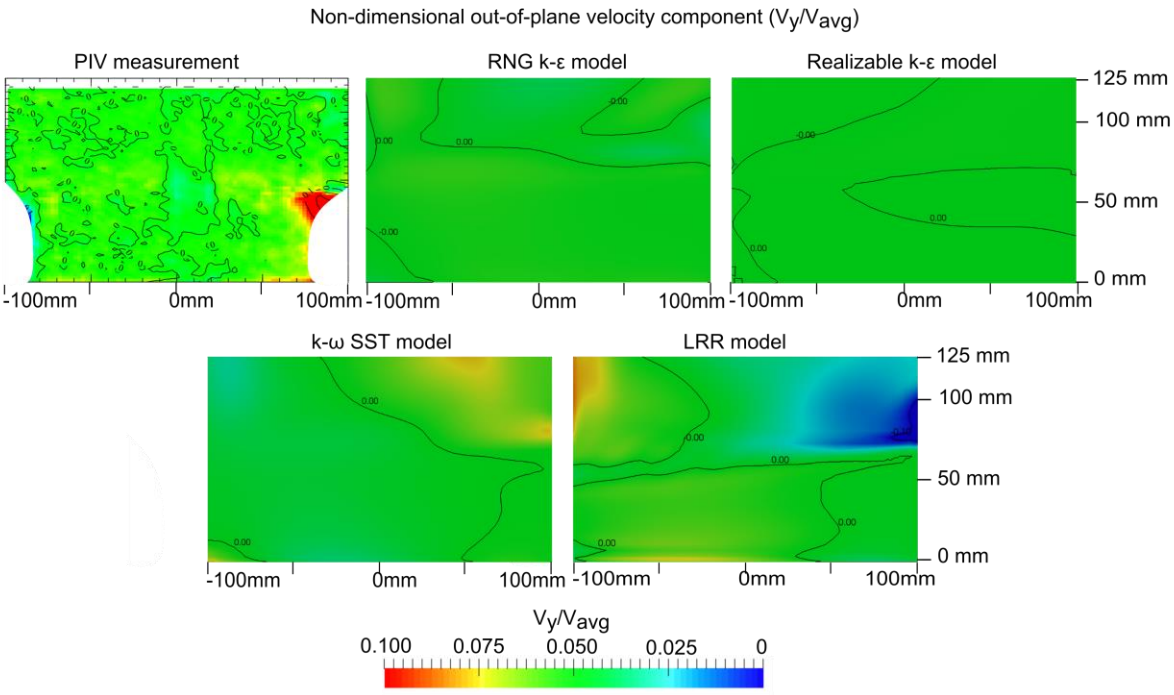

Figure 4.4: Out of the plane velocity component at the CVP from PIV and four RANS models

The standard deviation of the data was also compared at both CVP and RVP for axial and vertical velocity components (Figure 4.5). The comparison was also made on dimensionless velocities as a ratio of V_{avg}.

It can be seen that for axial velocity component (V_x) at CVP and RVP (1st and 2nd column at Figure 4.5), the PIV data shows high standard deviation near inlet, outlet and jet expansion zones. High standard deviation can also be seen near the manhole floor of CVP. Vertical velocity component (V_z) showed lower deviation compared to V_x. The standard deviation was found to be significantly low at both planes in CFD results in compared to PIV data. All CFD results show marginally higher standard deviation values close to the jet expansion zone. The Realizable k-ε model shows the minimum fluctuation in the velocity fields, resulting almost zero standard deviation. The k-ω SST model shows the highest standard deviation among all the four RANS models, still, the value is lower than that of the PIV data. As these numerical models are formulated from Reynolds Averaged Navier Stokes (RANS) equations, a big part of the turbulence variabilities is averaged out from the results already. Perhaps Large Eddy Simulation (LES) model could show better standard deviation match with the PIV data. Moreover, for this work, only 5 seconds of numerical simulation data was considered. In case the longer period of data was taken into consideration, probably the standard deviation in the CFD results would come higher. Turbulence coming from pipe rather than the standard turbulence inlet conditions could also be a reason for the differences in numeric.

Examining the velocity contours at Figure 4.3 and Figure 4.5, it can be stated that k-ω SST model creates the closest approximation of the manhole velocity field followed by RNG k-ε model. The LRR model overestimates the axial velocity component in this plane and the velocity contour is significantly different than the PIV measurement.

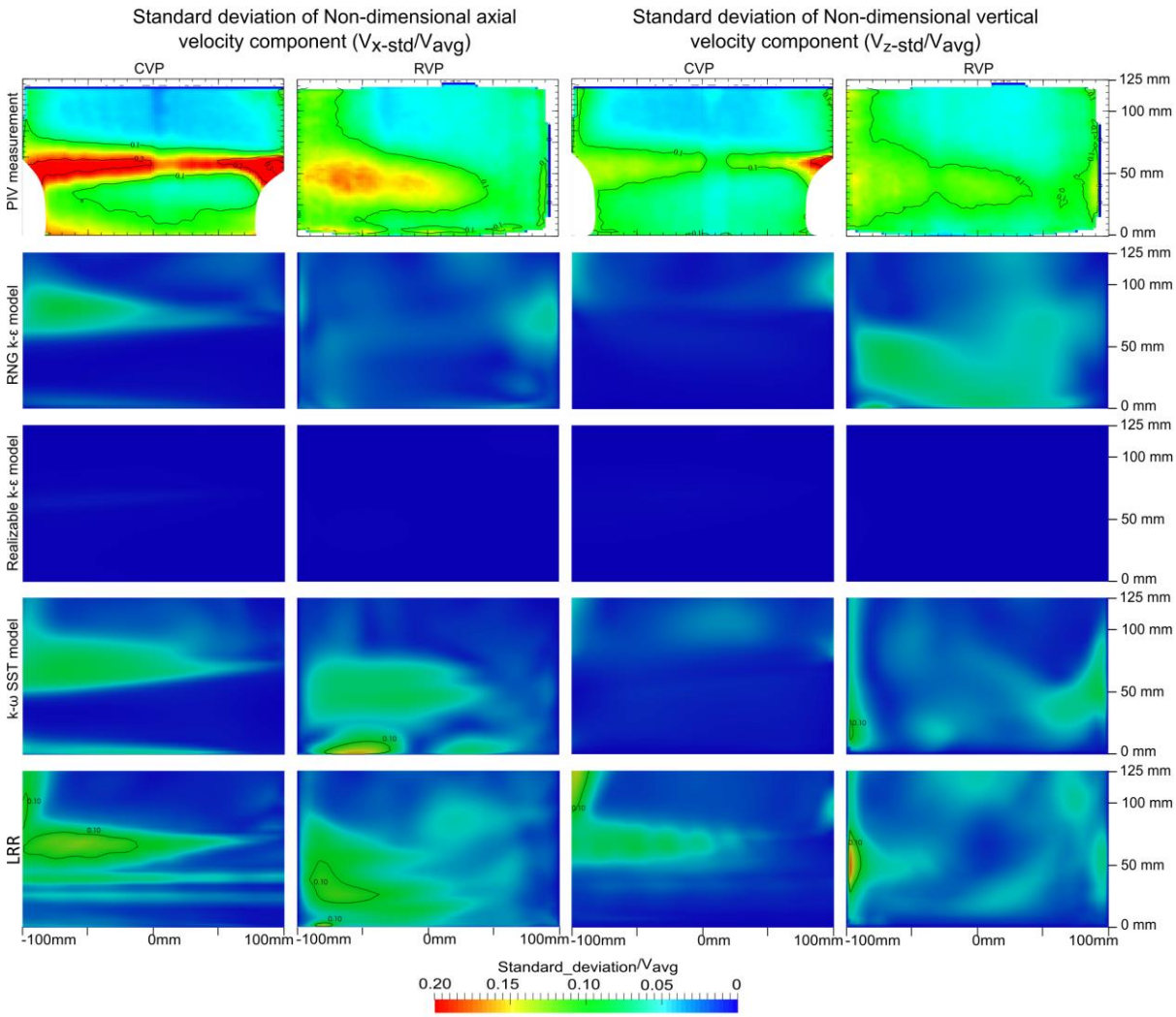

Figure 4.5: Temporal standard deviation of different velocity component at CVP and RVP, measured from PIV data and four RANS models

To understand the manhole flow more clearly, streamline and water level fluctuation was analysed from the numerical model results (Figure 4.6). It can be seen that the inflow jet originating from the inlet, marginally spread in the manhole (termed as the diffusive region). When exiting the manhole through the outlet pipe, the diffusive region impinges the manhole wall and after that part of the jet flow moves vertically upward. This flow region reaches the manhole water surface, starts moving opposite to the core jet direction and makes a clockwise circulation. Due to this constant circulation, the free surface of the manhole fluctuates slightly. The fluctuation was found more towards the inlet of the manhole. In this case, the water level was observed

varying between 0.295 m to 0.320 m. The fluctuation level was found different in the four numerical models. In RNG k-ε model, the water level varies from 0.300 m to 0.310 m. While the water level fluctuations in the other three manhole models were found as Realizable k-ε: varying between 0.300 m and 0.305 m; k-ω SST: varying between 0.300 m and 0.310 m and LRR: varying between 0.310 m and 0.320 m. In the experimental work the average water level at the manhole was observed as 0.310 m. The fluctuation of the manhole level was not possible to measure in the experimental work as it would require installing a pressure sensor at the manhole bottom, which would create an obstacle in the laser ray path line and hence was not used.

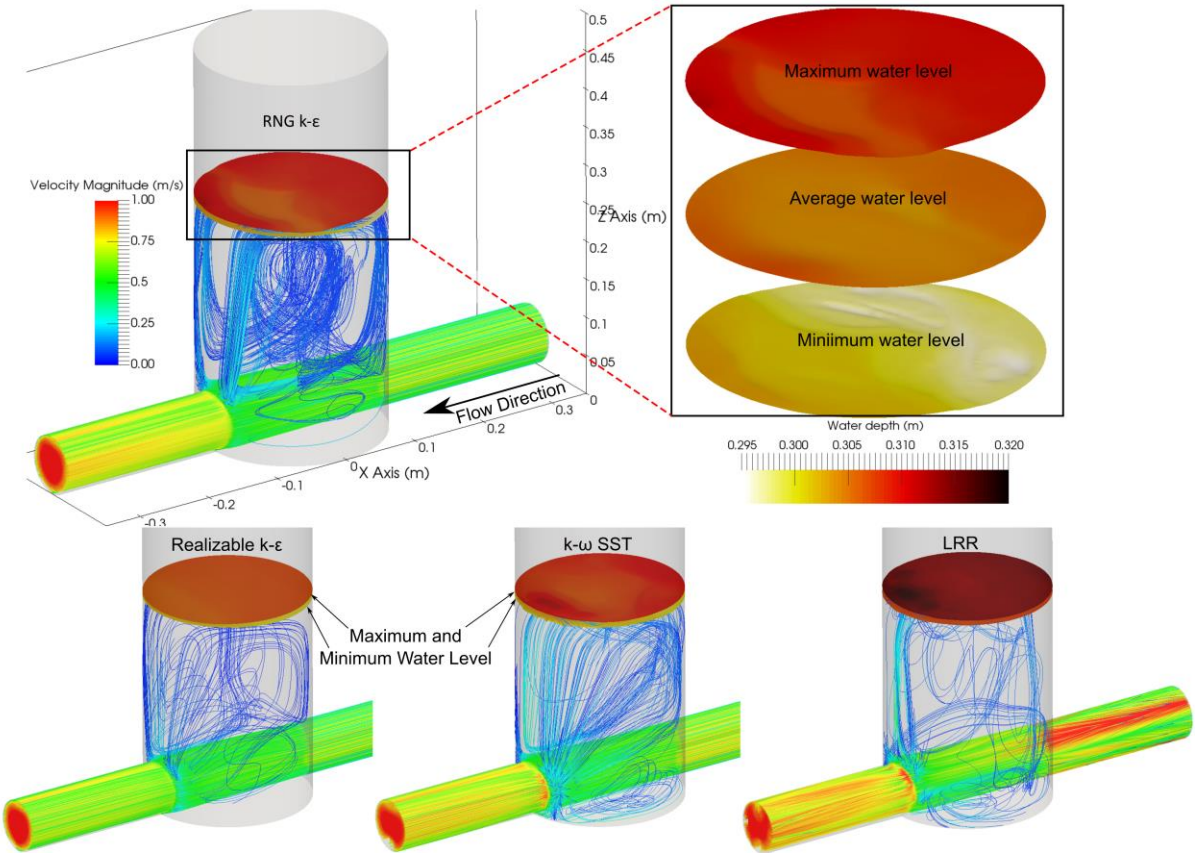

Figure 4.6: Flow streamline through the manhole and water level range from different models

The pressure distributions in different CFD models were also compared with experimental data and can be seen in Figure 4.7. All distances showed at the horizontal axis are measured from the manhole centre. The inlet and outlet pipes are connected at distance of 0.12 m and -0.12 m respectively. The bottom pressure in between these two distances also represents free surface water level inside the manhole. Two box plots represent pressure data recorded during the experimental measurement using pressure sensors. The left box plot shows the pressure at the outlet pipe, whose average value was used to generate boundary condition of the numerical models. As the downstream pressure is same for all the four models, all the model results pass through the average value of this box. Pressures at the upstream side were calculated from the

models. All the line plots are showing maximum, minimum and average bottom pressure from each of the four CFD models. The circular marker at the manhole centre (at x=0 m) is showing the product of recorded average water height at the manhole during the experimental works (h = 0.310 m), water density (ρ) and gravitational acceleration (g).

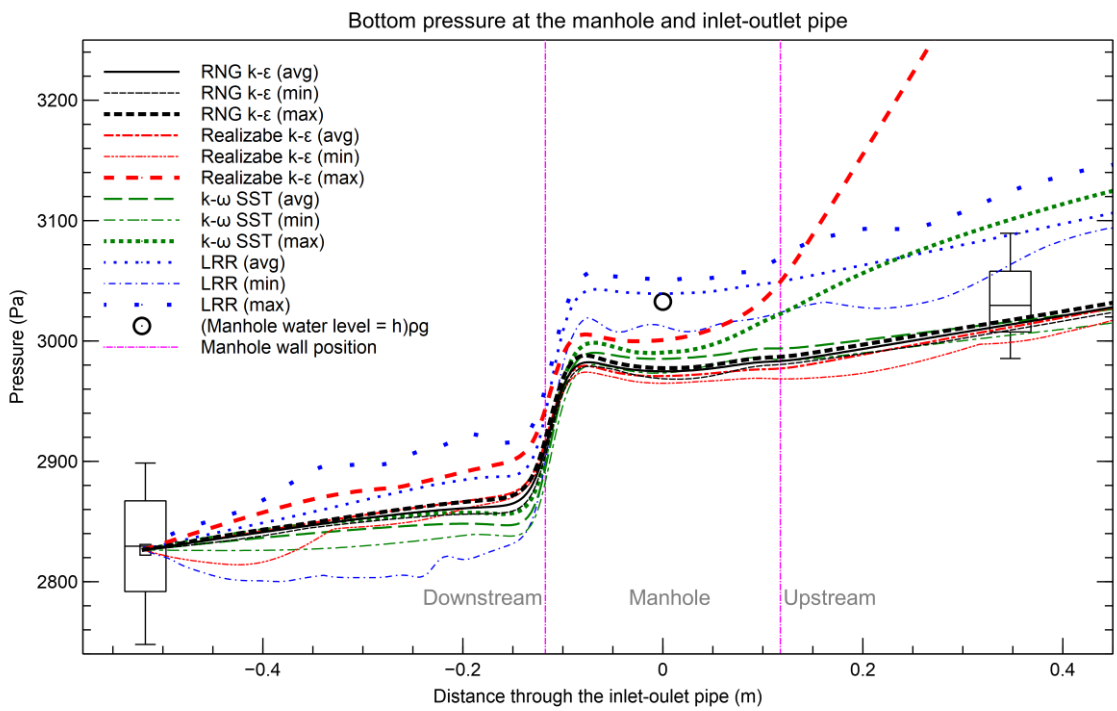

Figure 4.7: Bottom pressure comparison from different RANS models and the experimental pressure sensor data

From Figure 4.7, it can be seen that when the upstream flow through the inlet pipe enters the manhole, the flow experiences a pressure drop, which is due to the expansion of the flow. The second pressure drop can be observed when the flow exits the manhole and enters the outlet pipe. This drop is due to the flow contraction and much bigger in magnitude. The average pressure line of RNG k-ε, Realizable k-ε and k-ω SST models produce a similar pressure pattern throughout the computational domain. The LRR model overestimates the bottom pressure of the manhole, although the difference found is in the range of few millimetres of water column head. The maximum, minimum and the average bottom pressure from RNG k-ε model shows almost the same line which presents that the RNG k-ε model shows almost zero pressure fluctuation. Apparently, the LRR model overestimated the pipe loss in compared to the other three models. This results in an overestimation of upstream pressure at the inlet direction.

The coefficient of head loss (K) in the manhole is known as the ratio between head loss and the velocity head and is calculated using equation (4.6).

$$K = \Delta H / \left(\frac{v^2}{2g}\right) \tag{4.6}$$

where ΔH is the head loss, v is the average longitudinal velocity at the outlet pipe (= 0.89 m/s) and g is the acceleration due to gravity.

As the numerical model reached steady state before extracting any results, and as both inlet and outlet pipes were full, the temporal averaged velocity at each pipe can be considered equal. In this case, a difference in bottom pressure would give the same value as head loss. To compute the pressure drop at the manhole centre for a certain CFD result, each line showing the average bottom pressure (Figure 4.7) was projected to the manhole centre from both inlet and outlet pipe. The vertical difference of pressure value between these two lines at the manhole centre gives the value of pressure drop for the manhole, which is later divided by ρg and considered as ΔH.

The value of manhole head loss coefficient has been reported in different literature. This is directly related to the structural mould types of the manhole, manhole to pipe diameter ratios, as well as manhole surcharge ratio. A comparable analysis of the coefficients of head loss (K) with those of the values reported in different literature are shown in Table 4.1. It should be noted that only the research works reporting the same manhole mould type are considered here. In the work of both Arao and Kusuda (1999) and Lau et al. (2008), authors reported high head loss coefficient at below threshold surcharge conditions and comparably lower coefficient at above threshold surcharge condition. As in this research, the manhole surcharge condition is comparable to above threshold surcharge, only the coefficient range covering this condition are shown.

Table 4.1: Different values of head loss coefficient (K) at different models

Works done	Head loss coefficient	Experimental condition	Surcharge ratio range	
			$s/Ø_m$	$s/Ø_p$
Marsalek (1981)	0.21	1.923		
Arao and Kusuda (1999)	0.18-0.58	3.60	0.55-1.67	2-6
Lau et al.(2008)	0.28-0.69	9.08	0.65-0.82	5.90-7.45
This Work				
RNG k-ε	0.193	3.20	0.98	3.13
Realizable k-ε	0.156			
k-ω SST	0.284			
LRR	0.265			

Table 4.1 shows that the four models calculate the manhole flow differently and hence give different values of manhole head loss coefficient. It is reported by different authors the head loss coefficient becomes higher when manhole to pipe diameter ratio (Φ_m/Φ_p) is high and vice versa (Bo Pedersen and Mark, 1990; Stovin et al., 2013). The manhole reported at Arao and Kusuda

(1999) has a similar Φ_m/Φ_p. Comparing the findings from the literature, it is apparent the Realizable k-ε model gives rather low head loss coefficient for this case. From the rest three models, the coefficient given by k-ω SST model is almost 50% more than that of value given by RNG k-ε, however, both values lie within the range specified by other researchers.

4.5 Conclusions

In this work, two-dimensional three component (2D3C) stereo PIV measurement was done on a scaled inline manhole with manhole to pipe diameter ratio of 3.20, in order to evaluate CFD model constructed in OpenFOAM® and four different RANS models with VOF method. From the analysis, it can be apparent that each model calculates the velocity inside manhole differently. Comparison with PIV measurement at the central vertical plane showed similar velocity as compared to all the numerical models. However, comparison of the velocity at another vertical plane 50 mm offset to the centre, showed that all the CFD models slightly underpredicts the axial velocity. The velocity and locations of vortex structures centres were found marginally different among the models. The k-ω SST model showed the closest approximation of velocity contour followed by the RNG k-ε model. All the models showed very good approximations of the average water surface level at the manhole. However, the LRR model could not quite capture the velocity profile in compared to PIV data. This model predicts considerably higher axial velocities for central vertical plane as compared to PIV. Nonetheless, the temporal standard deviations of the axial and vertical velocity components were found significantly low when compared to those of experimental measurement through PIV. As a RANS model is formulated based on time-averaged turbulence data, which could be the reason of having a lower standard deviation in the CFD model.

Bottom pressure analysis through the computational domain shows that the average pressure line is almost similar at RNG k-ε, Realizable k-ε and k-ω SST models. However, the comparison could be made with data from only two pressure sensors installed at the inlet and outlet pipe respectively. RNG k-ε model showed almost no pressure fluctuation while maximum pressure line predicted by the Realizable k-ε model was found much higher than the measurement. The calculated head loss coefficients were compared with the values reported in the literature. It was seen that the Realizable k-ε model shows much lower value compared to the values reported.

Considering all the aspects of the four models analysed here, it can be said that both RNG k-ε model and k-ω SST models give a very good approximation of manhole hydraulics. However, it should be noted while using k-ω SST model, the wall boundary cell size must be made considerably small for the proper formulation of the model.

4.6 Acknowledgements

The work presented is part of the QUICS (Quantifying Uncertainty in Integrated Catchment Studies) project. This project has received funding from the European Union's Seventh Framework Programme for research, technological development and demonstration under grant agreement No. 607000. The laboratory facility was made possible through EPSRC, project EP/K040405/1. All the numerical results showed here were performed on the Centaurus Cluster of the Laboratory for Advanced Computing of University of Coimbra, Portugal.

CHAPTER 5

EFFECT OF SURCHARGE ON GULLY-MANHOLE FLOW

5.1 Abstract

In an urban drainage system, surface system and buried system are connected through several linking elements like gullies and manholes. To model an urban flood through a 1D or 2D routing model, proper representation of these linking elements is mandatory. This paper focuses on the effects on inline manhole head loss coefficient and gully flow due to change in manhole surcharges to get knowledge of their characteristics, flow patterns and influence in the overall flow. The solver *interFoam* with VOF capability under open source CFD toolbox OpenFOAM® is used for the numerical simulations. The CFD model created is a real scale model following the experimental setup installed at the University of Coimbra. The CFD model results were compared with discharge and water depth data at the manhole and velocity data at the gully, measured from the physical model. The manhole head loss coefficient was found very high at low surcharge level and reaching a constant value of 0.3 for higher surcharge levels. The gully flow was found to follow typical orifice flow equation with different discharge coefficients for different water depth conditions of the manhole. Three different surcharged zones were identified at the manhole on which discharge coefficients are dependent. The shear stress pattern at the manhole floor is also found varying due to surcharge depth as well as the gully flow. The variation showed distinctive configuration at different surcharge zones.

Keywords: Computational Fluid Dynamics (CFD); Gully; Manhole; Head-loss coefficient; OpenFOAM®; Urban drainage;

5.2 Introduction

The Urban drainage system is termed as the main conveyance route for draining extensive rainfall and flood in a busy city. The system is composed of many linking elements that convey the flow during a rainfall event from the major or surface system to the minor or buried system. Manhole and gully are two very common drainage structures where the flow is usually complex, highly

turbulent and possibly multiphase. When entering to a manhole or gully, the drainage flow undergoes a sudden expansion and/or contraction with several hydraulic losses, which are important in flood routing simulations. Most urban flood routing models are one or two dimensional and therefore cannot represent the complex flow pattern of these structures (Leandro et al., 2009b). These structures usually are not modelled but connected as a point entity and translated by discharge and head loss coefficients calculated using empirical equations (J. Leandro and Martins, 2016). State-of-the-art routing models in urbanised areas are Dual Drainage (DD) models as they simulate both surface flow and flow in buried pipes simultaneously among other urban key features (Djordjević et al., 2004; Leandro et al., 2016). These models use discharge coefficients to connect the two systems through linking elements. However, they also have weaknesses in considering linking elements as very few existing models are available to calibrate these coefficients (Djordjević et al., 2005). The hydraulic losses and efficiencies are very much dependent on the flow conditions and should be studied to allow the translation of the different structures behaviours throughout the possible flow conditions in a model. At low flow conditions, drainage pipes are partially filled, and the estimation of the head loss in a manhole can be calculated considering an open channel flow. However, in the case of flood events, the system becomes pressurised, uses its storage potential and creates surcharged flow conditions. In those cases, estimation of head loss is complex, involving more structural and hydraulic factors of the system. The flow through the gully can also vary due to the surcharge heights of the manhole. This paper aims to determine manhole head loss coefficients and gully discharge coefficients at different surcharge levels of a manhole.

Researchers pointed out many factors that influence the head loss in a manhole using experimental model facilities. The shape of the manhole is a major factor in determining the flow conditions. Four different types of manholes are mainly found in the various countries (Asztely, 1995), which are known as Type I, II, III and IV. Type I has the simplest design with no guided channel. Type II and III has guided channel where the channel is half circular invert and U-type invert respectively. Type IV is a modified form of type II, where the manhole bottom is sloped towards the guided channel. Out of different kinds of the manhole, Type I is the most investigated. Sangster et al. (1958) studied Type I surcharged manhole where the inlet pipe invert was at the same level with the manhole bottom. The head loss coefficient varied between 0 and 0.3 with different inlet-outlet pipe diameters ranging from 76 to 145 mm. A unsystematic variation on energy losses at small manholes was reported by Sangster et al. (1958) and Lindval (1984). Lindval (1984) also found the head loss coefficients varying between 0.08 and 0.88 by using different manhole and inlet pipes with manhole to inlet diameter ratios ranging from 1.7 to 4.1. Many authors reported an oscillatory surface with high head loss coefficients at shallow surcharge conditions (Bo Pedersen and Mark, 1990; Howarth and Saul, 1984; Lindval, 1984). The coefficient

of head loss was as high as 1.3 for reduced surcharge flow, as reported by Arao and Kusuda (1999). Pedersen and Mark (1990) investigated Type I, II and III manholes with scaled physical models with a pipe to manhole diameter ratios of 1.22, 2.11, 3.20 and 4.94. They reported the loss coefficient to increase with manhole to pipe diameter ratios. They also explained this phenomenon through submerged jet theory; originally described by Albertson et al. (1950). Guymer et al. (2005) and Lau (2008) checked the velocity distribution of surcharged manholes and described their results in line with submerged jet theory.

Several researchers studied surcharged manholes using CFD. Stovin et al. (2008) explained the approach to validate a CFD manhole model. One major issue in CFD modelling of drainage structure is locating the position of the free surface. Two different techniques are commonly followed for modelling the free surface; namely: Rigid lid approximation and Volume of Fluid (VOF) method. In the Rigid lid approximation, the free surface is assumed as a frictionless lid at a fixed positioned. Lau (2008) and Stovin et al. (2013) used Rigid lid approximation using CFD modelling tool Fluent (ANSYS Ins, 2009) to simulate scaled surcharged manhole behaviour and to predict solute transport through it. However, rigid lid approximation requires prior knowledge of the exact location of the free surface. In Volume of Fluid (VOF) method (Hirt and Nichols, 1981), the position of the free surface is not approximated but modelled by introducing the concept of volume fraction. This approach is considered as the recommended procedure when the position of the free surface is not known (Bennett, 2012; Lau, 2008). However, not much work has been done to model a manhole flow using VOF method. Moreover, all studies mentioned here used scaled manhole models. Uses of prototype scale manholes are rare.

In compared to manholes, fewer works have been done on the hydraulics of a gully. A typical gully collects runoff from the roadside curbs and delivers it to a nearby manhole. The gully outlet is typically placed at a higher location than the manhole floor. So, at a low surcharge condition, the gully outflow enters the manhole as a plunging jet. This could be related to the typical hydraulics of a drop manhole structure. Some researchers focused on the hydraulics of a drop manhole but mainly discussing the energy dissipation of the drop (Arao et al., 2012; Carvalho et al., 2013; Carvalho and Leandro, 2012; Chanson, 2004; Granata et al., 2014, 2011). Martins et al. (2014) described the hydraulic performance of the gully at drainage condition. They used weir and orifice equations to explain the flow through the gully outlet. Carvalho et al. (2011) investigated flow through a gully using VOF based 2DV numerical model. They compared water depths, streamlines, velocities, pressures and the inlet discharge coefficients at different outlet sizes and positions. Gómez and Russo (2009) and Lopes et al. (2016a) described flow efficiency of transverse gully grate using experimental and CFD models respectively. Although the main task of a gully is to drain surface flow to the underground system, the opposite directional flow may occur due to any exceptional event when gully becomes pressurised and surcharged water flood the surface area.

Leandro et al. (2014c) and Lopes et al. (2015) described the reverse flow in a surcharged gully. Romagnoli et al. (2013) measured the velocity of a typical gully at reverse flow condition using Acoustic Doppler Velocimetry (ADV). Few research has been reported on effects of manhole surcharge on gully flow. Noh et al. (2016) used scaled urban drainage model along with Monte-Carlo simulations to estimate discharge coefficients between different sewer network components. However, the research did not consider other structural elements such as manhole types and surcharge heights corresponding to the height of gully as these are responsible for different coefficient values.

In this work, the effect of manhole surcharge on manhole head loss coefficients and manhole-gully discharge coefficients have been studied. The analysis has been done using open source CFD tools OpenFOAM®. The CFD model replicated the real scale experimental facility installed at the hydraulic lab of the University of Coimbra. The work uses VOF model to examine the flow behaviour of the drainage system. Numerical model data was compared with discharge, water depth or pressure data measured at the manhole and ADV velocity data measured at the gully. The work describes the experimental and the numerical model at the 'Methodology' section. In the 'Results and Discussion' section, comparisons were drawn between numerical and experimental works. Attempts were also made to describe the manhole and gully flow using basic hydraulics. The last section concludes the work.

5.3 Methodology

5.3.1 Experimental Setup

The Multiple Linking Element (MLE) installation at the hydraulic laboratory of University of Coimbra was used to validate the CFD modelling procedure. The facility has been described in other literature such as Leandro et al. (2009a) and Carvalho et al. (2013). A part of the facility has been used in this work containing a rectangular surface drain (0.48 m wide) with a slope of 1:1000, a rectangular gully pot (0.6 m × 0.24 m × 0.30 m) and a circular manhole (1 m diameter) (Figure 5.1). The manhole is a "Type I" (Asztely, 1995) manhole with no guided channel. A 300 mm horizontal inlet-outlet pipe is connected to the manhole, whose invert level is at a height of 0.10 m from the manhole floor. The manhole to inlet-outlet pipe diameter ratio (Φ_m/Φ_p) is 3.33. The manhole does not receive any flow from its top. A lid is loosely connected that ensures equal pressure between inside and outside of the manhole. An 80 mm angular pipe connects the gully to the manhole; which is angled 90º and 63º towards vertical and in plan direction.

The gully-manhole element replicates a typical drainage system in Portugal. Data from three electromagnetic flow meters were used to define boundary conditions and to verify simulations. The first one is located at the upstream of *Drain Inlet*, the second one is referred at the pipe

between manhole and gully and the third is at the downstream of *Pipe Outlet*; from which different discharges at the drain, gully and manhole can be measured (Figure 5.1). The first and the third flow meters are just outside the computational domain. The second flow meter is within the domain, and it is represented by a small contraction in the numerical model. The contraction zone has a diameter of 60 mm. Three pressure sensors are also installed in the setup located at the outlet pipe shown in Figure 5.1 as P18, P22 and the manhole centre, shown as P23.

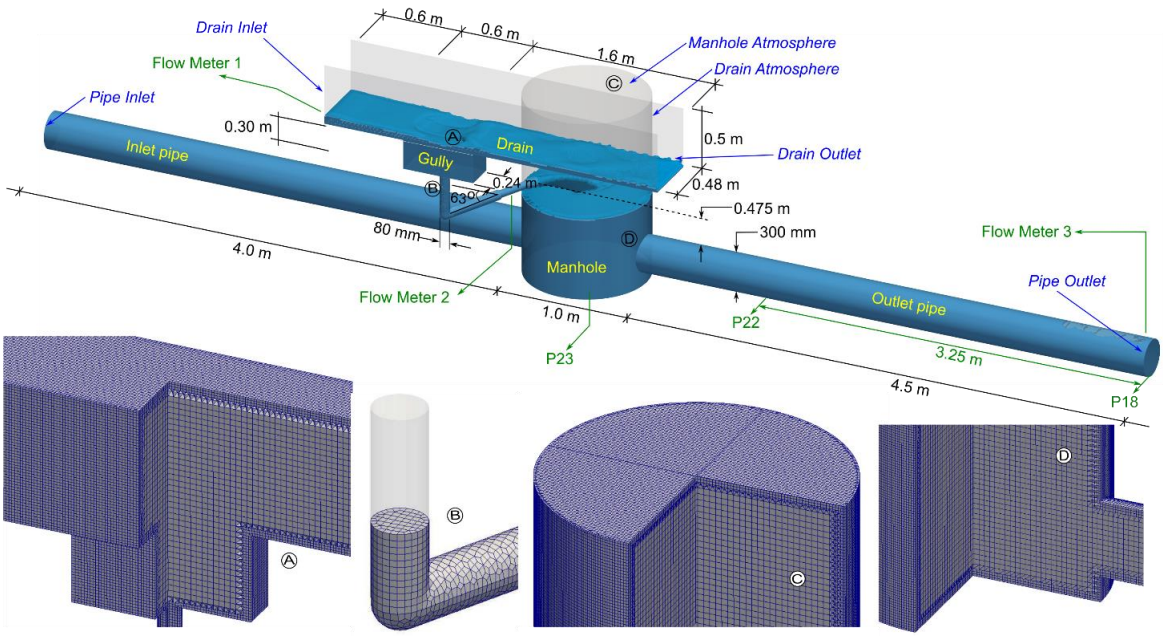

Figure 5.1: Upper Panel: Experimental setup; Lower panel: Computational mesh of different parts of the domain A: Gully with outlet pipe, B: Outlet Pipe, C: Manhole and D: Pipe connected with Manhole

5.3.2 Experimental Test Cases

The grate of the gully was removed throughout the experiment. Two experimental data sets have been used for the numerical model validation. In the first set (SE1), flow through the drain and gully was observed and measured giving 19.8 l/s flow at upstream of the *Drain Inlet*. The flow through the rectangular drain upstream of the gully was a free surface flow with a depth of 0.068 m; which yielded a Froude number of 0.6. A part of the incoming drain flow passed through the gully outlet and entered the manhole, the rest being overflown through the drain and falling as a free fall to the reservoir tank through the *Drain Outlet* (Figure 5.1). The intercepted flow by gully enters the manhole as a free fall plunging jet generating a recirculation zone in the manhole. This flow mixes with the inflow coming through the *Pipe Inlet* and drains out through the *Pipe Outlet*. The gully was given special attention. The velocity fields at the gully were measured using Acoustic Doppler Velocimetry (ADV) at three vertical planes parallel to the longitudinal flow direction of the drain. The first and the third planes (Plane 1 and Plane 2 of Figure 5.2 left panel) are at 0.05 m distance from the two longitudinal walls of the gully; which made each of the planes 0.07 m apart

from the central line of the gully. The second plane is the central plane (Plane C). Each plane had 121 point velocity measurements, at an interval of 0.050 m and 0.025 m towards horizontal and vertical directions respectively (Figure 5.2 right panel). Since the drainage capacity of the gully was lower than the flow in the drain, the water level was higher than the top level of the gully. The velocity measurement was taken inside the gully only and was not extended to the water surface. Detail description of the measurement can be found at Beg et al. (2016b).

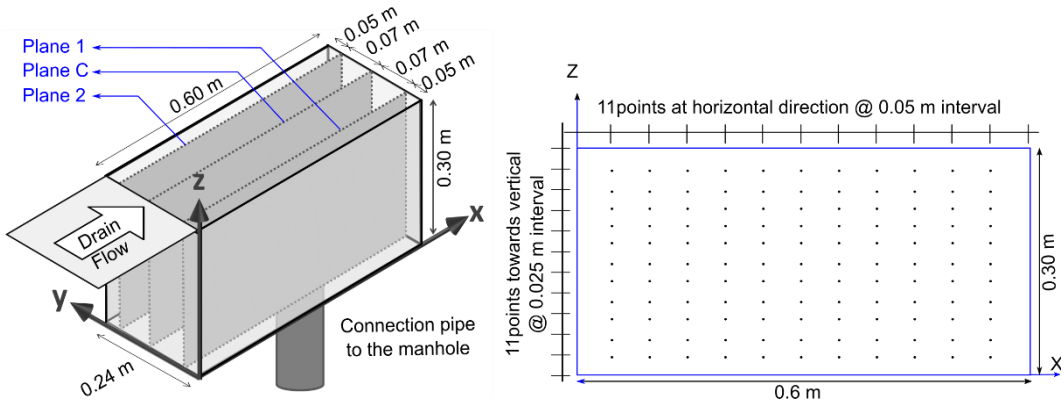

Figure 5.2: Velocity measurement locations using ADV. Left panel shows the location of the three planes and the right panel shows the point measurement locations at each plane

In the second set of experimental works (SE2), only flow in the pipe passing through the manhole inlet was used and recorded using a discharge flow meter. The three pressure sensors (P23, P22 and P18 shown in Figure 5.1) were also used to check the pressures of the flow at different sections. The inflows and the manhole surcharges were controlled using two valves at the inlet and outlet pipe. The pressure sensors measured piezometric pressures for both free surface and pressure flow conditions, which were converted to piezometric head considering the bottom of the manhole as the zero datum. Eighteen experimental runs were performed, keeping the outlet valve opened at 30% (low flow), 40% (medium flow), and 60% (high flow) to observe different flow velocities inside the pipe and the manhole. All discharges and corresponding water pressures throughout the system were recorded at a steady flow condition. This setup was utilised at different combinations of inflows ranging from 12 l/s to 145 l/s and manhole surcharge heights up to 1.40 m (Beg et al., 2016a).

5.3.3 Numerical Model Description

The objective of the numerical modelling validated with experimental measurements was to characterise the incoming flow through the gully and check the flow path in the manhole during drainage condition. Open source three dimensional CFD model tools OpenFOAM® v2.3.0 was used in this study. The solver *interFoam* was chosen which includes Volume of Fluid (VOF) method (Hirt and Nichols, 1981) to track the free surface or interface location between two fluids. This method

uses volume fraction indicator function α to determine the amount of liquid present in each cell. In the case of α = 0 or 1, the cell volume is considered filled with air or water respectively; while 0 < α < 1 represents that the cell contains the free surface as it is partially filled with water.

The *interFoam* solver uses a single set of Navier-Stokes equations for the two fluids independently for water and air, and additional equations to describe free-surface where the velocity at free-surface is shared by both phases. The solver considers a system of isothermal, incompressible and immiscible two-phase flow. The model deals with Reynolds averaged conservation of mass and momentum expressed according to Rusche (2002) as:

$$\nabla . \boldsymbol{u} = 0 \tag{5.1}$$

$$\frac{\partial \rho \boldsymbol{u}}{\partial t} + \nabla . (\rho \boldsymbol{u}\boldsymbol{u}) = -\nabla p^* + \nabla . \boldsymbol{\tau} + \boldsymbol{g}.\boldsymbol{x}\nabla\rho + \boldsymbol{f_\sigma} \tag{5.2}$$

where $\boldsymbol{g}$ is the acceleration due to gravity, $\boldsymbol{u}$ is the velocity vector in the Cartesian coordinate, $\boldsymbol{\tau}$ is the shear stress tensor, p^* is the modified pressure adapted by removing the hydrostatic pressure ($\rho\boldsymbol{g}.\boldsymbol{x}$) from the total pressure, ρ *is the density* and $\boldsymbol{f_\sigma}$ is the volumetric surface tension force.

The viscous stress term is defined by the Newton's law of viscosity for incompressible fluid,

$$\nabla . \boldsymbol{\tau} = \nabla(\mu(\nabla \boldsymbol{u})) + (\nabla \boldsymbol{u}).\nabla\mu \tag{5.3}$$

The advection equation to describe free-surface in VOF method uses an interfacial compressive term to keep the interface region confined in a small space (Rusche, 2002; Weller, 2002) and is described as:

$$\frac{\partial \alpha}{\partial t} + \nabla . (\alpha \boldsymbol{u}) + \nabla . [\boldsymbol{u_c}\alpha(1-\alpha)] = 0 \tag{5.4}$$

The last term of equation (5.4) is the compressive term. The term $\alpha(1-\alpha)$ ensures that the compressive term or compressive velocity $\boldsymbol{u_c}$ is calculated only at the interphase (when 0 < α < 1). This velocity acts at the perpendicular direction to the interface and defined as:

$$\boldsymbol{u_c} = C_\alpha |\boldsymbol{u_c}| \frac{\nabla\alpha}{|\nabla\alpha|} \tag{5.5}$$

C_α is a Boolean term (value is 0 or 1) which activates (C_α=1) or deactivates (C_α=0) the interface compressive term. The volumetric surface tension $\boldsymbol{f_\sigma}$, shown at equation (5.2) is calculated by the Continuum Surface Force model (Brackbill et al., 1992).

$$\boldsymbol{f_\sigma} \approx \sigma\kappa\nabla\alpha \tag{5.6}$$

where κ is referred as the surface curvature.

While modelling the turbulence phenomena considering RANS approach, two different *k*- ε model families were considered for the gully and manhole flow. For the simulations considering gully outlet flow, importance was given to the pipe flow at the gully outlet and Standard *k*- ε turbulent modelling approach was used as this is considered to give good prediction of fully turbulent flow (ANSYS Inc, 2013; Ghoma, 2011). For the manhole head losses simulations, resolving the complex flow inside the manhole was considered essential. Therefore, the Renormalization group of *k*- ε turbulent model (Yakhot et al., 1992) was used for these simulations. This approach is described to be more accurate to predict complex shear flow with separation (Speziale and Thangam, 1992) and more responsive to the effects of rapid strain and streamline curvature (ANSYS Inc, 2013; Bennett, 2012; Carvalho et al., 2008). Both of these turbulence calculation approaches use two closure equations for *k* (turbulent kinetic energy) and ε (Energy dissipation).

The dynamic viscosity (μ) is calculated as:

$$\mu = \rho(\nu_t + \nu_0) \tag{5.7}$$

where ν_0 and ν_t are molecular viscosity and turbulent viscosity respectively.

5.3.4 Mesh Generation

Three different computational meshes were simulated with three grid sizes to check the mesh grid convergence using RNG k- ε turbulent model. The three meshes have dx = 6.6 mm (Mesh 1), 20 mm (Mesh 2) and 25 mm (Mesh 3) respectively. The number of cells in these meshes were 8.64 million, 310 thousand and 156 thousand respectively. Richardson extrapolation was considered in the mesh convergence study following Celik et al. (2008). The global refinement ratio was 3.8; which is bigger than the recommended minimum value of 1.3. The three meshes were simulated with 30 l/s inflow and 0.6 m of surcharge depth in the manhole. The axial velocity profile at the centre of the manhole and the centre of the outlet pipe were compared for the mesh analysis. A total of 38-point velocities were compared. The longitudinal velocities from the three meshes are shown in Figure 5.3.

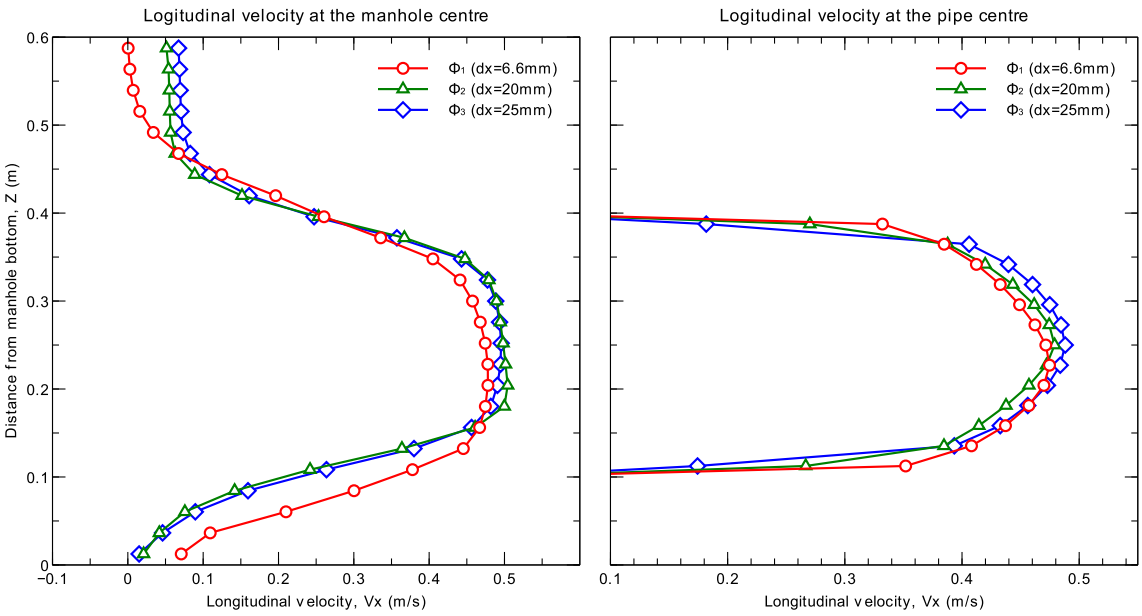

Figure 5.3: Mesh analysis using three different mesh sizes. Left panel shows longitudinal velocity profile at the manhole centre and the right panel shows longitudinal velocity profile at the outlet pipe

To calculate the mesh convergence study, different parameters of the three meshes were calculated. The apparent order p was calculated for each 38 velocity points by the iteration of the following equations:

$$p = \frac{1}{ln(r_{21})}|ln|\varepsilon_{32}/\varepsilon_{21}| + q(p)| \tag{5.8}$$

$$q(p) = ln\left(\frac{r_{21}^{p} - s}{r_{32}^{p} - s}\right) \tag{5.9}$$

$$s = sgn(\varepsilon_{32}/\varepsilon_{21}) \tag{5.10}$$

where r_{21} and ε_{21} indicate average mesh sizes ratio between Mesh 2 & Mesh 1 and difference of data at a certain point from Mesh 2 and Mesh 1 respectively. Values of r_{21} and ε_{21} indicate similar data from Mesh 3 and Mesh 2. Negative s values indicate oscillatory convergence. The Grid Convergence Index (GCI) can be calculated with the value of p.

$$GCI_{fine}^{21} = \frac{1.25e_a^{21}}{r_{21}^{p} - 1} \tag{5.11}$$

where e_a^{21} is the approximate relative error between Mesh 2 and Mesh 1 and calculated as:

$$e_a^{21} = \left|\frac{\Phi_1 - \Phi_2}{\Phi_1}\right| \tag{5.12}$$

where Φ_1 and Φ_2 are the data from Mesh 1 and Mesh 2 respectively.

In the analysis, oscillatory convergence was found at 22 points (57%). The approximate relative error close to the wall was found 53% comparing mesh 1 and 2, and 30% when comparing mesh 2 and mesh 3. However, at the centre where the jet stream is located, the approximate relative error was found 7.24% comparing mesh 1 and 2, and 6.2% comparing mesh 2 and 3. Large uncertainty close to the wall was found due to high gradient of velocity. The average GCI for mesh 2 was found 16%. From Figure 5.3 (left panel), it can be seen that the fine mesh of 6.6 mm creates different flow structure close to the manhole bottom. The remaining two meshes (20 mm and 25 mm) create similar flow in the manhole. The location of vortex formation was changed at different meshes. A high percentage of oscillatory convergence, as well as change in vortex formation, resulted in high GCI values. As for this work, the focus is given to manhole head loss coefficient k, the value was checked at all the three meshes. The K value in mesh 1, mesh 2 and mesh 3 were found 0.321, 0.324 and 0.371 respectively. It can be said that although mesh 2 showed different flow structure on a small scale compared to mesh 1, considering the flow at the large scale, mesh 2 gives similar results for head loss coefficient, k. Considering the simulation time required, Mesh 1 demands very high computational cost as the number of cells is significantly high. Considering the accuracy level and computation costs the cell size of mesh 2 is chosen (cell size = 20 mm) for this work. The maximum cell size is kept 20 mm towards all the three directions. The mesh was further refined at the walls and joints of different geometrical shapes. The created final computational mesh has 821 500 computational cells with a little more than 1.01 million nodes. Some of the mesh properties can be seen in Figure 5.1 and Table 5.1.

Table 5.1: Quality parameters of the computational mesh

Parameter Name	Max. Aspect ratio	Max. skewness	Max. non-orthogonality	Avg. non-orthogonality	Min. face area (m^2)	Max. face area (m^2)	Min. volume (m^3)	Max. volume (m^3)
Parameter Value	7.27	1.708	51.32	4.13	3.45×10^{-06}	4.72×10^{-04}	4.19×10^{-09}	1.06×10^{-05}

5.3.5 Definition of boundary conditions and simulation control parameters

Six open boundaries were prescribed to the numerical model (Figure 5.1): *Drain Inlet, Drain Atmosphere, Drain Outlet, Pipe Inlet, Manhole Atmosphere* and *Pipe Outlet*. The closed boundaries were prescribed as *walls*. The *Drain Inlet* was further divided into two parts for the incoming water

and air phases respectively. The boundary data were calculated from the experimental model completed beforehand.

As the simulation used *k*- *ε* turbulent modelling and RNG *k*- *ε* turbulent modelling, OpenFOAM® requires six types of Boundary Conditions (BC) for each boundary. They are *alpha.water* (water fraction in each cell volume), *U* (velocity vector in Cartesian domain), *p_rgh* (relative bottom pressure corresponding to datum), *k* (turbulent kinetic energy), *ε* (energy dissipation) and *nut* (turbulent viscosity). The first three BC's are required for hydraulic modelling while the last three are required for turbulence calculation.

For both inlets, fixed velocities/discharges were applied using *alpha.water* and *U*. Pressure data (*p_rgh*) were prescribed at the outlet boundaries. Both of the atmosphere boundaries were kept as *zeroGradient* velocity and relative air pressure as zero; so that air could be exchanged if necessary. All the *wall* BC's were kept as no-slip condition (i.e. velocity = 0). For the turbulent approach, values of *k*, *ε* and *nut* were calculated using the equations in FLUENT manual (ANSYS Ins, 2009), considering medium turbulence at the gully and manhole. All the walls are prescribed as *wallFunction* as this eliminates the necessity of fine layered boundary mesh and hence reduce the computational time (Greenshields, 2015). The numerical model represents the experimental facility, which was made of acrylic. The roughness was considered not important at the acrylic surface and thus was not taken into account at the wall BC's.

The model was ready to run after the boundary setup. During the simulation, *adjustableRunTime* was used keeping maximum CFL number to 0.8. Cluster computing system at the University of Coimbra was used to run the simulations at MPI mode using 16 processors. Each simulation took 40 s to reach a steady state; which took 138 hours of effective computational time. For each case scenario, results were saved for 5 s of simulation run (considering the simulation reached steady state already) at an interval of 0.5 s, making a total of 11 time steps. Each analysis was done with the averaged result of these 11 time steps.

5.4 Results and Discussion

5.4.1 Comparison with experiments

During the experimental model run, pressure levels were recorded at different lengths of the pipe as well as the bottom centre of the manhole. The numerical model was validated with experimental data of flow depth/pressure head and discharge inside the structure. The comparison of the pressure and discharge has been presented in an earlier study (Beg et al., 2016a). The comparison was checked with the pressure data at transducer P23, P22 and P18 (see Figure 5.1). Figure 5.4 shows the comparison between experimental and numerical simulations in

a pressure head vs discharge plot. The dot markers of different colours show data from different experimental models while the pentagons show data from numerical models. Figure 5.5 illustrates the comparison between the two data sets in a scatter plot.

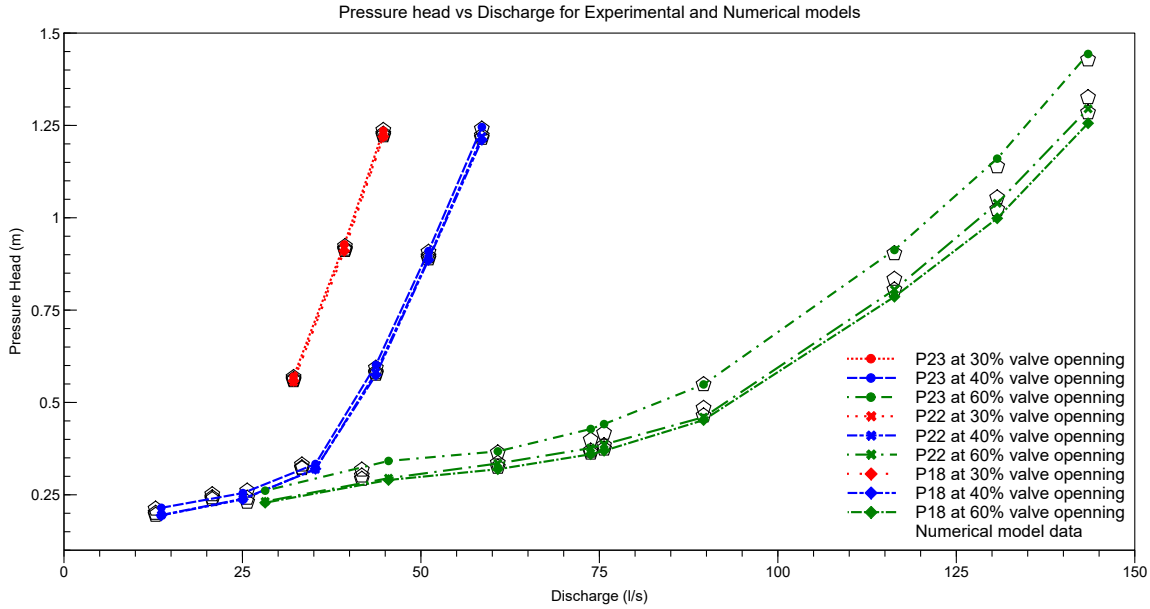

Figure 5.4: Pressure level vs Discharge in the two manholes from experimental and numerical simulation (after Beg et al. (2016a)

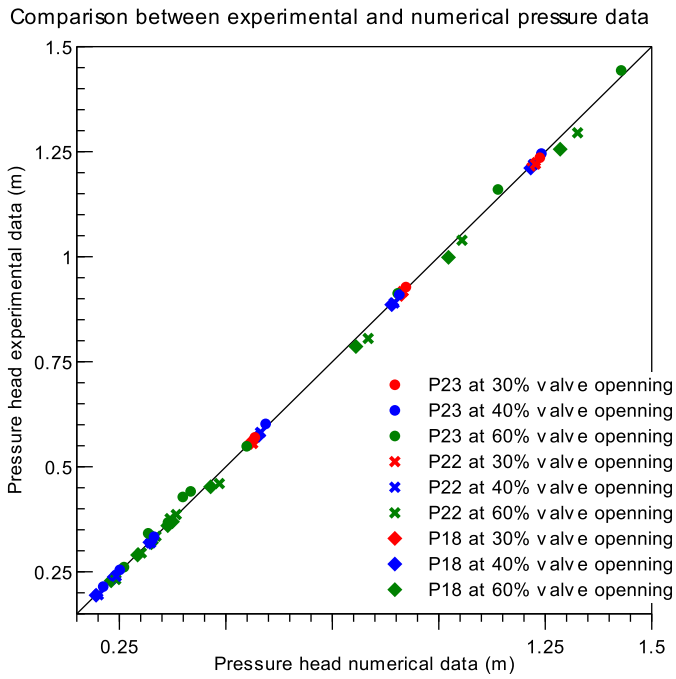

Figure 5.5: Comparison of pressure head between numerical and experimental model

It can be seen from Figure 5.5 that the numerical model showed great match with the recorded pressure head of the experimental data. A maximum of 7% error was reported in pressure data; which indicates that the numerical model can give a very good estimation of water depth/pressure head.

The numerical model results were also compared with the experimental study data of the velocity profiles at the gully obtained by the Vectrino acoustic velocimetry. Figure 5.6 shows contours at the three different planes and Figure 5.7 shows a comparison of longitudinal and vertical velocity profiles at different locations of the gully.

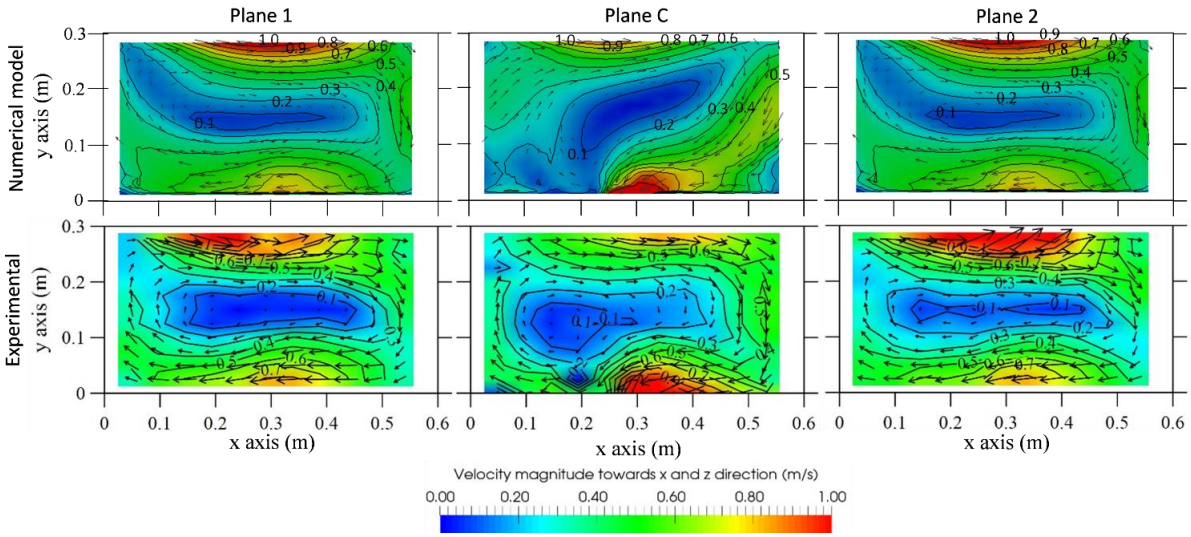

Figure 5.6: Comparison of velocity between numerical (upper panel) and experimental (bottom panel) study at three longitudinal planes of the gully

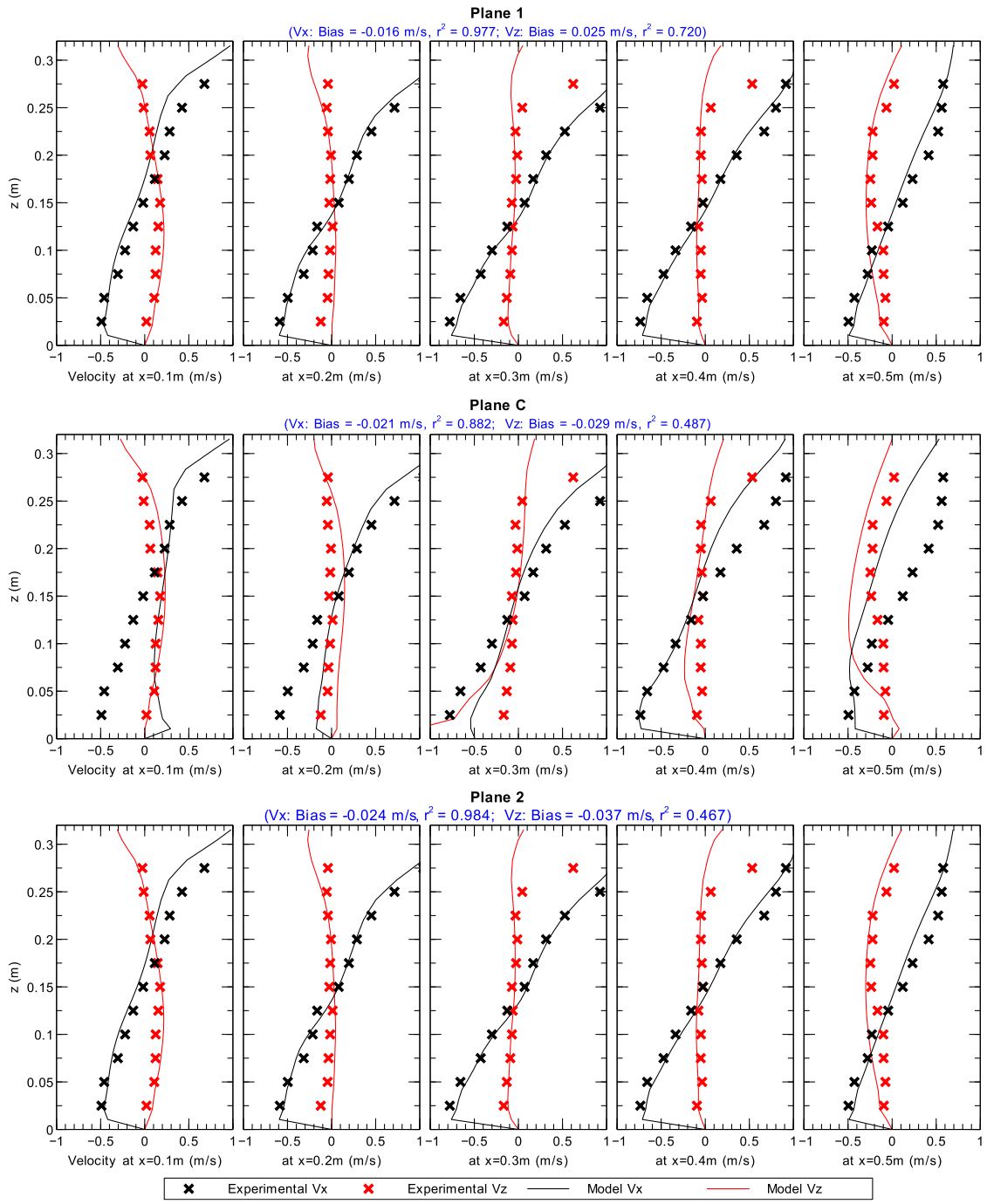

Figure 5.7: Velocity profile at different locations of the gully. Firm lines showing numerical model data and cross (x) markers showing data from experimental study

It can be seen from Figure 5.6 and Figure 5.7 that the numerical model shows good agreement with experimental data. The vertical vortex size and location created in the numerical result shows similarity to those observed in the experimental model data. Average statistical comparison between the two data is also shown in Figure 5.7. It indicates that the model can reproduce the longitudinal velocity component (Vx) very well (average r2 = 0.95 and BAIS = -0.004 m/s). The

representation of vertical velocity component (V_z) in the gully is at a satisfactory level (average BIAS 0.011 m/s and r^2 = 0.56).

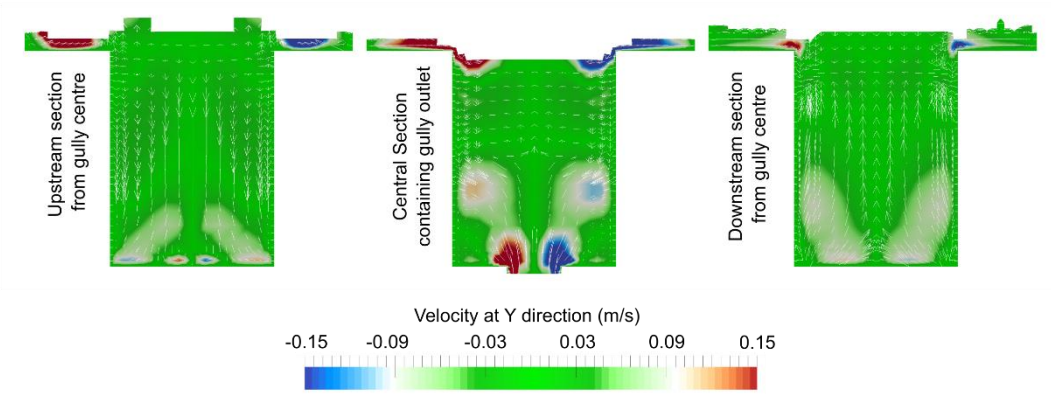

Figure 5.8: Transverse velocity (V_y) at the gully

Figure 5.8 shows the transverse velocity (V_y) in the gully at three different transects. It can be seen that transverse velocity is very low, in the range of -0.03 m/s to +0.03 m/s. This velocity component was found insignificant to compare with experimental results.

5.4.2 Velocity field and manhole head loss at different surcharge

The velocity field at the manhole was checked for various inflow and surcharge conditions. For this part, different numerical simulations were checked to compare the surcharge effect on the manhole. The gully inflow was disconnected. Four different inflows were applied through the *Pipe Inlet* with combinations of different piezometric pressure heads at the *Pipe Outlet* for each numerical simulations (see Figure 5.1). The applied inflows were 30, 60, 90 and 120 l/s with different piezometric pressure head ranging from 0.4 m to 1.5 m. Different surcharge levels were obtained from the simulations, ranging from 0.20 m to 0.85 m. Figure 5.9 shows velocity contours at both horizontal and vertical planes through the main axis of inlet-outlet pipes from four simulations. The four contours are from simulations having 30 l/s and 120 l/s inflows at the *Pipe Inlet* (lowest and highest among the simulations) with and 0.45 m and 1.2 m piezometric pressure heads at the *Pipe Outlet*. The corresponding water depths found at the manhole centre are 0.45 m, 1.21 m, 0.54 m and 1.27 m respectively.

Figure 5.9 shows that for all the cases, highest velocity can be observed at the central axis of the pipe. The main core velocity does not change much during its travel through the manhole but reaches to the outlet pipe. This denotes a ‘short circuiting’ as reported by other authors (Stovin et al., 2013). The longitudinal velocity shows symmetric view at the horizontal cross sections at high surcharge conditions. At the vertical sections, the longitudinal velocity of the jet core decreases with the increase in vertical distance from the central line of the pipe. However, at the bottom of

the manhole near the outlet pipe, the longitudinal velocity is found very low. At lower surcharge conditions (a1 and c1), almost the whole vertical section has high longitudinal velocity towards the outlet. Comparing a2 and c2 conditions, it can be observed at c2 with higher discharge; the jet core does not show a symmetric pattern. On the other hand, at higher surcharge conditions (b1 and d1), the longitudinal velocity has been found towards the opposite at the upper part of the manhole. The horizontal sections show that the longitudinal velocity turns towards the opposite direction near the manhole wall at both higher and lower surcharges.

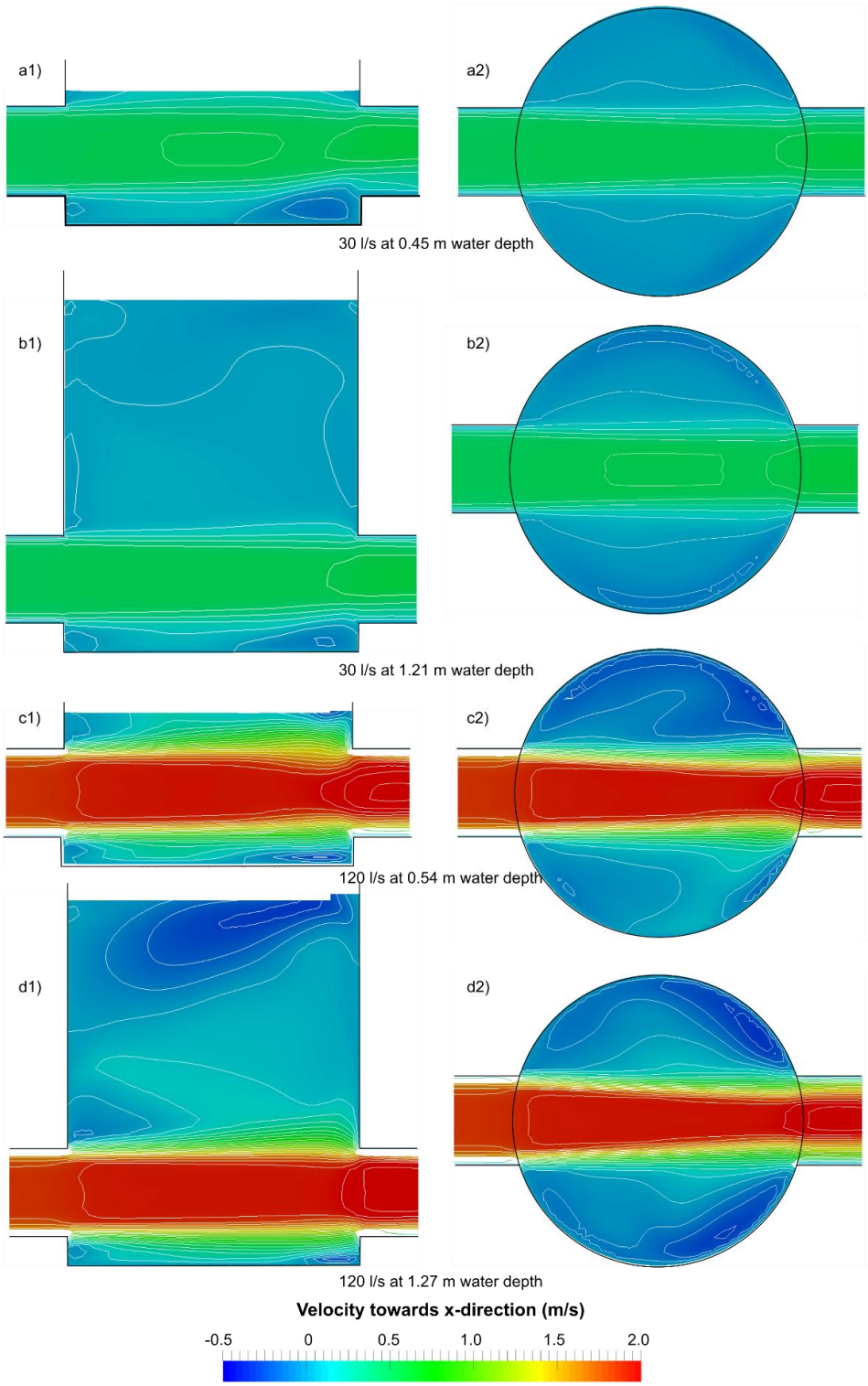

Figure 5.9: Longitudinal velocity at the centreline of the manhole from different simulations. Left panel shows vertical section and right panel shows horizontal section through the axis of the inlet-outlet pipe. a, b, c and d show velocities at 30 l/s-0.45 m depth, 30 l/s-1.21 m depth, 120 l/s-0.54 m depth and 120 l/s-1.27 m depth of water at the manhole centre respectively

Comparing b1 and d1 of Figure 5.9, it can be seen that the longitudinal dispersion of the jet velocity increases with increasing discharge. The horizontal section with higher inflow and surcharge (d2) shows that unlike c2 case, the velocity is symmetric at a higher surcharge.

Head loss coefficient of the manhole was also checked at different manhole surcharges (s). The surcharge levels are calculated as the difference between water levels and outlet pipe soffit levels. From each simulation, the surcharge ratio was calculated as the ratio between surcharge level and inlet pipe diameter (s/Φ_p). The head loss coefficient (K) was calculated as a ratio between pressure head difference and velocity head. The comparison is shown in Figure 5.10.

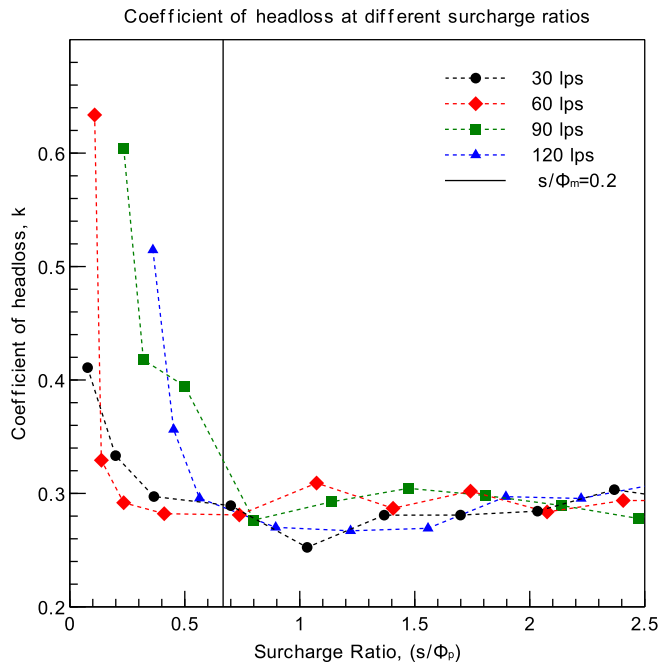

Figure 5.10: Coefficient of head loss vs Surcharge ratio at the manhole

Figure 5.10 indicates that at higher surcharge, the coefficient stays fairly around 0.3 for all discharges. However, the head loss coefficient rises very high when the surcharge ratio goes below a certain limit. The change occurs at around $s/\Phi_m < 0.2$. The line $s/\Phi_m = 0.2$ is shown by a dashed line in Figure 5.10; which is also equivalent to $s/\Phi_p = 0.67$, as $\Phi_m/\Phi_p = 3.33$. This phenomenon can be explained using submerged jet theory described by Albertson et al. (1950). Several authors (Bo Pedersen and Mark, 1990; Guymer et al., 2005; Stovin et al., 2013) applied the submerged jet theory for characterising manhole head loss coefficient. According to Authors, the incoming flow from the inlet pipe enters the manhole as a submerged jet. The jet core expands after entering the manhole and creates two jet regime; a) core region and b) diffusion region (Figure 5.11). Guymer et al. (2005) and Stovin et al. (2013) verified that the diffusive region diverges from the inlet pipe with the travelling lengths inside the manhole at a ratio of 1:5 and the core region keeps

the high jet velocity and maintains a conical shape. The core region diminishes as the jet travels through the manhole and remains until the distance of $6.2\Phi_p$, where Φ_p is the diameter of the inlet pipe.

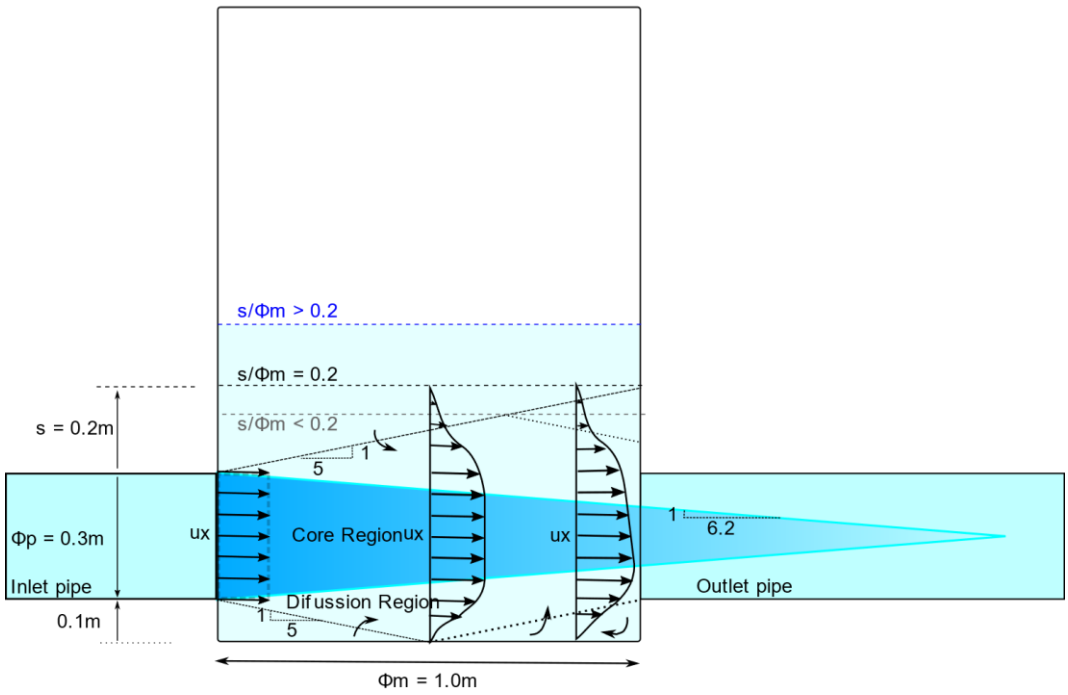

Figure 5.11: Velocity distribution and diffusion region in circular free jet (adapted from the works of Guymer et al. (2005) and Pedersen and Mark (1990)

For an inlet pipe of 300 mm, the core region of the submerged jet can travel (6.2x0.3=) 1.85 m before diminishing completely. As in this work, the manhole diameter is 1.0 m, the core region of the jet should enter directly to the outlet before diminishing completely. This condition can be compared with Figure 5.9.

The diffusive region expands from the line of axis of the inlet pipe. The downward facing diffusive region can expand for 0.10 m towards the bottom of the manhole then reaches the manhole floor. Upon reaching the manhole floor, the flow reflects back to upward direction. This phenomenon occurs for all the applied discharge and surcharge combinations. But the upward facing diffusive region may vary according to the available surcharge depth. As the region expands to a ratio of 1:5 towards vertical to horizontal, it may expand to 0.20 m towards the vertical direction until it reaches the manhole wall at the opposite side. But in case, the available manhole surcharge is less than 0.20 m, the diffusive region cannot develop completely. It interacts with the surface violently and creates additional head losses. This phenomenon is reflected in Figure 5.10 as the head loss coefficient increases drastically in the cases where the available surcharge is low ($s/\Phi_m < 0.2$). Although, the change of head loss coefficient at different inflow conditions do not follow any

particular trend. As for example, the head loss coefficient at 60 l/s at low surcharge was found less than those of at 30 l/s. Similarly, at surcharge ratio within 0.1 to 0.2, flow rate of 90 l/s made higher head loss in compared to those of at 120 l/s. However, in other low surcharge simulations, the higher discharges showed higher head losses. No justification could be drawn for these variations.

5.4.3 Effect of manhole surcharge on the gully flow

The flow distribution from the gully to the manhole at different surcharge heights were checked from the numerical models. A schematic diagram of the gully-manhole system is drawn in Figure 5.12. The depth of the gully was 0.315 m with the bottom level at 1.3 m. This made the bottom level of the drain 1.615 m (Z). The water depth in the drain at the immediate upstream of the gully was 68 mm (h), which made the water level at the drain 1.683 m (Z+h). The gully outlet pipe has a diameter of 80 mm with a contraction for discharge meter at the end of the pipe, which has a diameter of 60 mm. The soffit level of the outlet pipe is at a level of 0.945 m (Z_o). The manhole water depth was increased from 0.53 m to 2.2 m (H) at different numerical simulations and corresponding changes in the intercepted flow of the gully (Q) were checked. In all the numerical simulations, the pressure flow through manhole inlet (Q_1) and surface flow through the drain inlet (Q_3) were kept the same; 42.2 l/s and 19.8 l/s respectively.

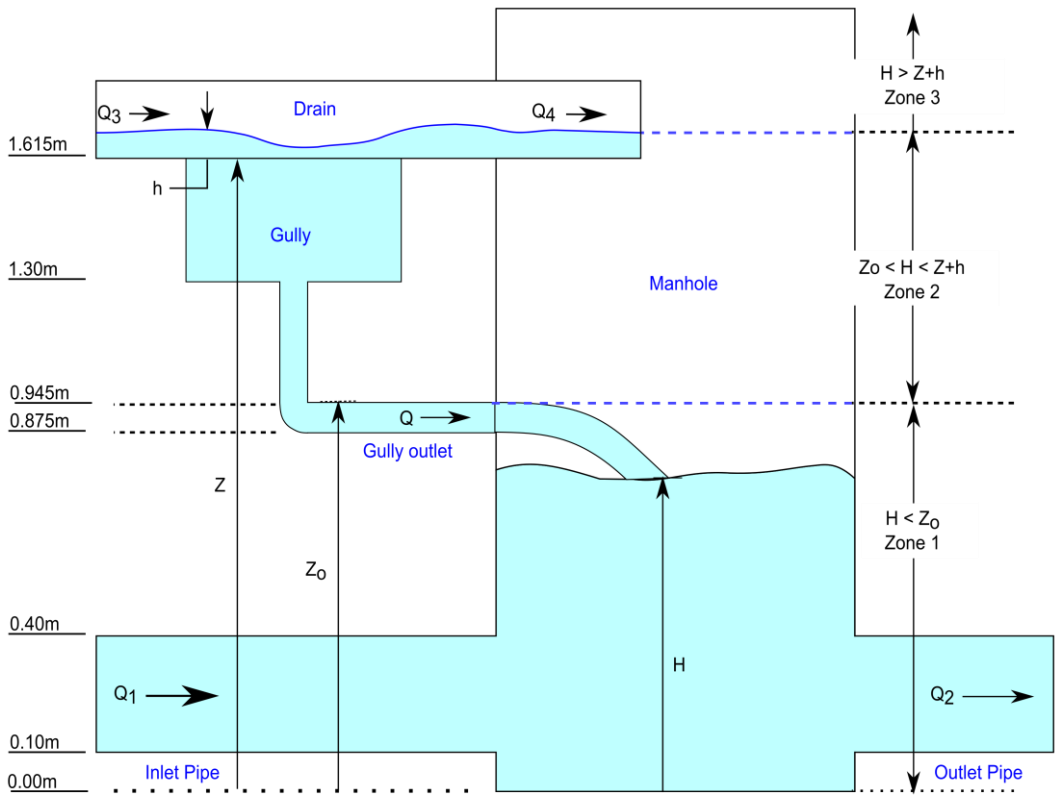

Figure 5.12: Schematic diagram of gully flow to the manhole

Examining the discharge from the gully, the manhole can be divided into three zones according to different surcharge levels.

- Zone 1: the surcharge water level in the gully is less than the soffit level of the gully outlet pipe ($H<Z_o$). At this zone, the gully flow falls into the manhole as a plunging jet.
- Zone 2: the surcharge level is more than the gully outlet pipe soffit level but less than water level at the drain ($Zo < H < Z+h$). At this zone, the gully flow enters the manhole as a submerged jet.
- Zone 3: The surcharge level of the manhole is more than the water level at the drain. At the zone, the gully is unable to drain itself. The surcharge flow from the manhole pushes the water back to surface.

The discharges from the gully to the manhole at different conditions are shown in Figure 5.13. Figure 5.14 shows the gully jet at three different surcharge zones mentioned above.

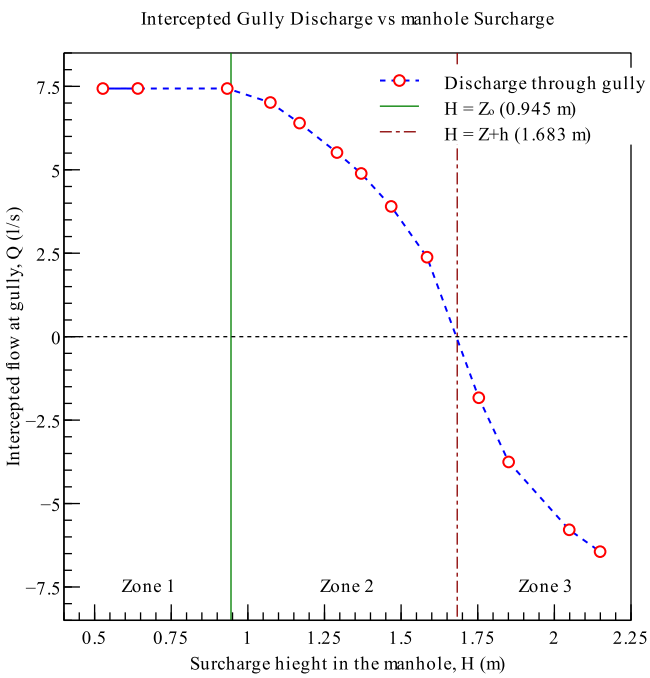

Figure 5.13: Computed intercepted flow at the gully vs surcharge heights at the manhole

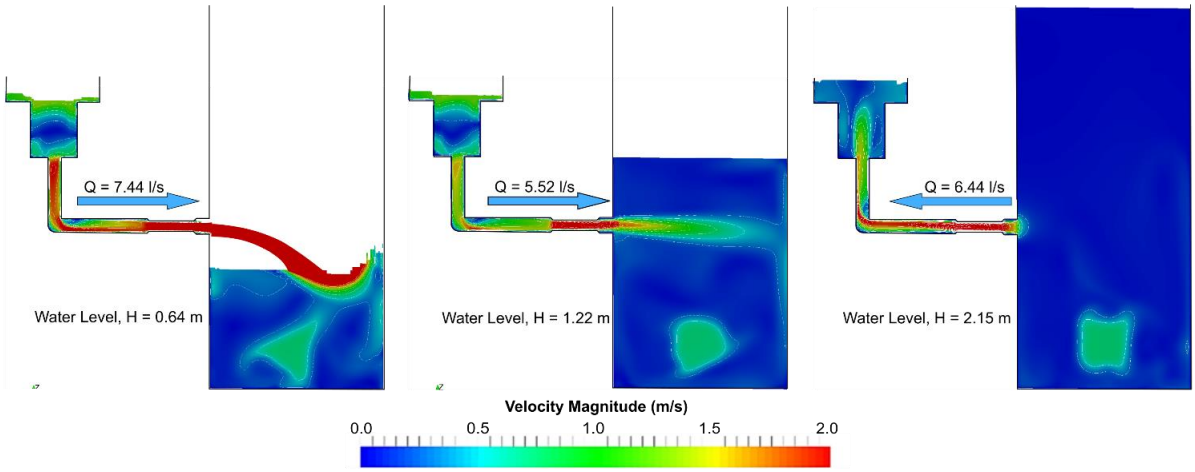

Figure 5.14: Cross section through the gully outlet jet at different surcharges. The figure at left panel represents Zone 1, the middle panel represents Zone 2 and the right panel represents Zone 3.

It can be seen from Figure 5.13 that the decrease in intercepted flow with the increase in surcharge height is not linear. From the simulation results, it can be observed that out of the 19.8 l/s flow on the drain, a maximum of 7.44 l/s flow was intercepted by the gully. The rest of the flow is overflowed through the drain outlet. The intercepted flow remains the same up to the surcharge height of 0.945 m at the manhole. Until surcharge height of 0.945 m, the flow from gully enters the manhole as a plunging jet. When the surcharge in the manhole increases more than 0.945 m, the gully starts to lose its efficiency. From 0.945 m to 1.683 m the jet from gully acts like a submerged jet. At surcharge level more than 1.683 m, the discharge is negative, i.e. the gully cannot drain to the manhole, and instead, the surcharge flow from the manhole creates reverse flow and floods the surface drain.

The gully flow can be characterised like an orifice and can be described according to the following equation:

$$Q = C_d A_o \sqrt{2gh_o} \tag{5.13}$$

where,

Q = discharge from the gully, variable at different manhole surcharge

A_o = Cross sectional area of the orifice, which is ($\pi/4$ x $(0.06m)^2$=) 0.002827 m^2.

h_o = Head difference from the surface drain to the gully outlet. Here, at zone 1, h_o is constant, which is equal to ($h+Z-Z_o$=) 0.786 m. At zone 2 and 3, h_o is a variable and can be calculated as the difference between (Z+h) and H.

C_d = Coefficient of discharge of the orifice and is different at the three different zones. For zone 1, the condition is a free orifice and C_d=0.67, as reported in different literature.

g = Acceleration due to gravity, which is 9.81 ms^{-2}.

The gully discharge vs square root of head difference (h_o) has been drawn in Figure 5.15 (left) to find the discharge coefficient of the gully. The calculated discharge coefficients are used in Figure 5.15 (right) to draw the best fit curve of the discharge vs head difference relationship of the gully. The found discharge coefficients are also listed in Table 5.2.

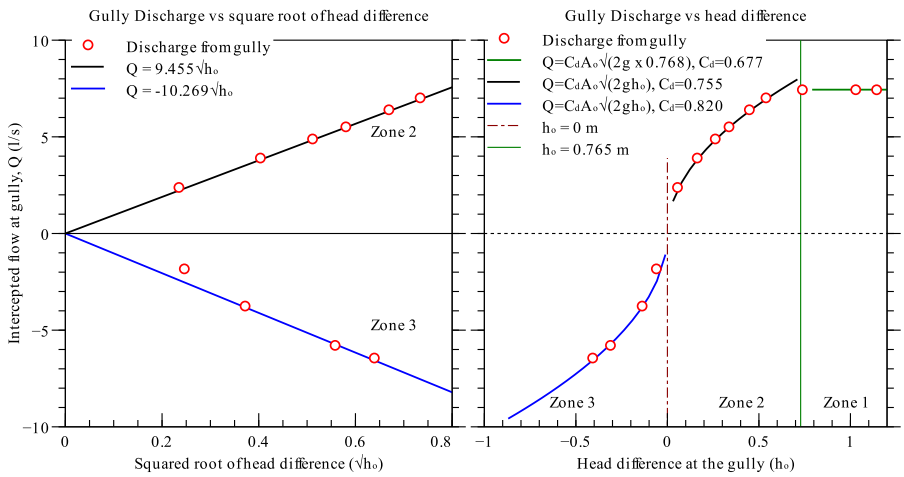

Figure 5.15: Gully discharge vs square root of head difference at the gully at left panel and Gully discharge vs head difference at the gully at right panel

Table 5.2: Numerically determined discharge coefficient of the gully outlet for different surcharge conditions

Zones	C_d	Remarks
Zone 1	0.677	Free outfall to the atmosphere, like a plunging jet to the manhole
Zone 2	0.755	Submerged jet condition
Zone 3	0.820	Reverse flow from manhole to the gully

It has been observed from Figure 5.15 and Table 5.2 that the coefficients of discharge for the discussed type of gully and gully outlet are 0.677, 0.755 and 0.820 at zone 1, 2 and 3 respectively,

Different water depths in the manhole also create significant changes in the shear stress at the manhole bottom. The shear stress maps of the manhole bottom at different depths are shown in Figure 5.16. Depths of 0.53 m, 0.64 m and 0.93 m represent simulations of zone 1 surcharges. The depths from 1.07 m to 1.58 m represent the conditions at zone 2. The depths more than 1.62 m are accounted for the conditions of zone 3.

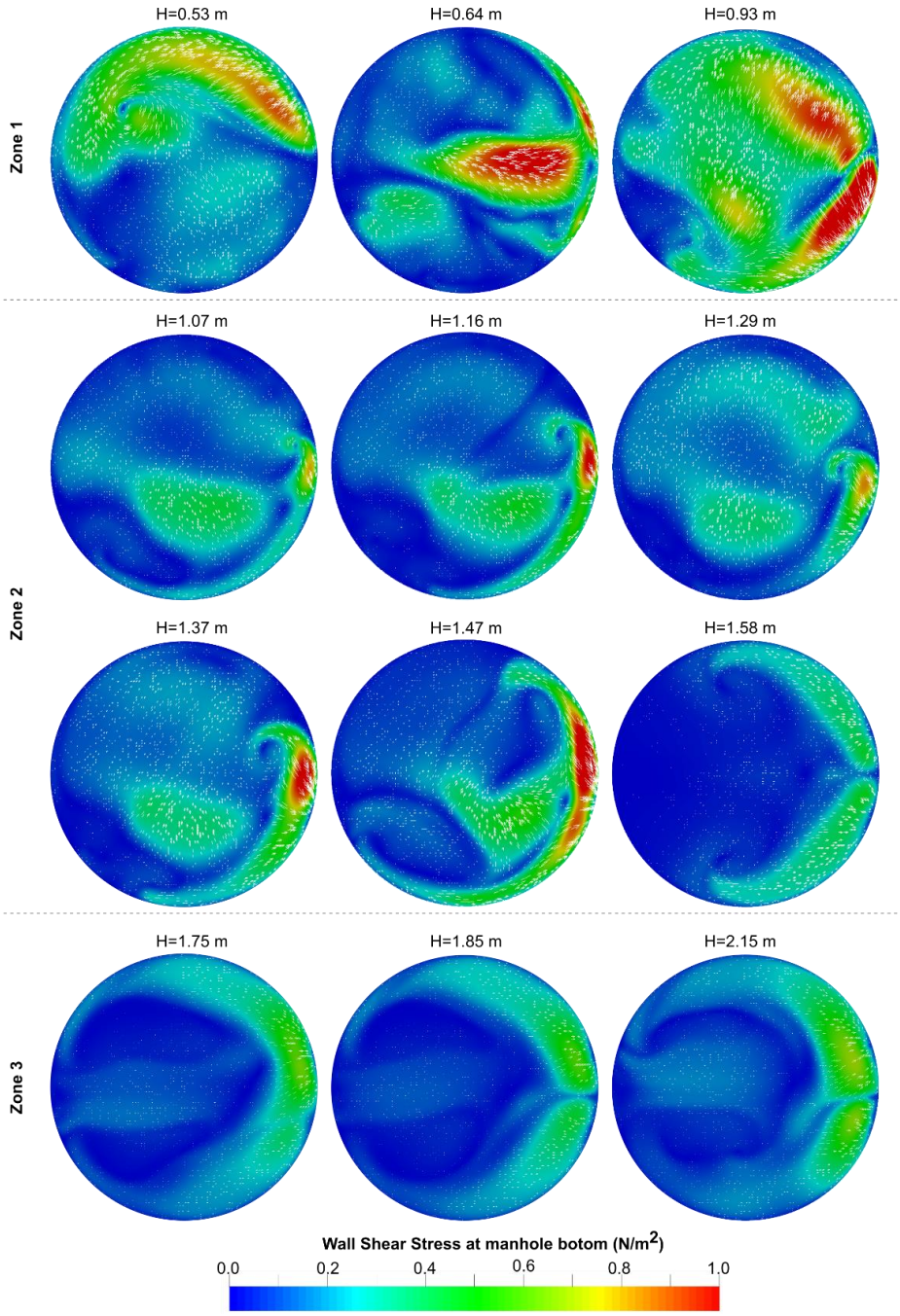

Figure 5.16: Manhole bottom shear stress at different surcharge height of the manhole. The flow direction is from left to the right

It can be seen from Figure 5.16 that shear stress maps at the manhole bottom in case of surcharge heights at zone 1 have significant differences among them. The changes in these simulation results are due to the changes in surcharge heights of the manhole only as the gully discharge at zone 1 is always the same. Moreover, with the change of surcharge heights, the jet impact location in the manhole also changes. This could also be a reason for the change in the shear stress. The maximum shear stress at this zone is around 1 Nm^{-2}. However, in the rest of the stress maps at

zone 2 and 3, the changes in shear stresses are probably an effect of both changes in surcharge level as well as changed flow from the gully. At zone 2, the gully discharge decreases with the increase in water depths in the manhole. The shear stresses at this zone maintain a trend keeping higher stresses close to the manhole outlet pipe. The stress map patterns are not symmetrical at manhole water level below 1.58 m. This indicates an asymmetric circulation pattern at the bottom of the manhole resulting from the gully outlet flow. At water level of 1.58 m, the gully flow is so small that it cannot make any effect on the shear stress pattern of the manhole bottom. With high surcharge and low flow from the gully at water level of 1.58 m, the manhole shear stress was found very low and symmetrical to the main axis of manhole inlet-outlet pipe. The increase in surcharge water level reduces the maximum shear stress at zone 2 to approximately 0.3 Nm^{-2}. At zone 3, the gully starts the reverse flow. The simulation results did not indicate very significant changes in the shear stress pattern at this zone. The shear stresses at this zone always remain asymmetrical but very low, having maximum stress in the range of 0.3 Nm^{-2}.

The shear stress diagrams are indicative of possible sedimentation inside the manhole. As the shear stress reduces for higher surcharges, sedimentation is more likely.

5.5 Conclusions

The article presents the ability of VOF model to reproduce the flow phenomena of a manhole and gully flow at different surcharge conditions. The numerical model reproduces quasi-real scale model using open source CFD modelling tools OpenFOAM® with *interFoam* solver. Standard k-ε model and RNG k-ε model was used to replicate the turbulence condition at the gully and manhole respectively. The model validation was examined using velocity data at the gully as well as discharge and water depth data at the manhole.

The study results show that different surcharge level has a significant effect on gully-manhole flow. The head loss coefficient through the manhole was found very high at low surcharge condition and the flow could be explained using submerged jet theory. The flow through the gully can be comparable to an orifice flow and the surcharge level can be divided in three distinctive regions. At low surcharge, the flow acts like a plunging jet and the discharge coefficient was found as 0.677. When the surcharge level stays between the gully water surface level and soffit level of the gully outlet pipe, the gully discharge acts like a submerged jet to the manhole and a discharge coefficient of 0.755 was found. At a very high surcharge, the gully starts reverse flow with a discharge coefficient of 0.82.

The shear stress variation at the manhole bottom has been compared at different surcharge depths. The stress maps were found to be varying due to surcharge depth as well as the gully flow.

The change in shear stress pattern showed distinctive variation in different surcharge zones and indicated that sedimentation is likely to occur at the manhole bottom for a higher surcharge.

For the future work, it will be interesting to see the effect of wall roughness on manhole head loss coefficients. The discharge coefficients for gullies with different outlet pipes may also be investigated. Lastly, the calculated discharge and head loss coefficients may be implemented in urban drainage network models.

5.6 Acknowledgements

The work presented is part of the QUICS (Quantifying Uncertainty in Integrated Catchment Studies) project. This project has received funding from the European Union's Seventh Framework Programme for research, technological development and demonstration under grant agreement no 607000.

The author would also like to acknowledge for the contribution of FCT (Portuguese Foundation for Science and Technology) through the Project UID/MAR/04292/2013 financed by MEC (Portuguese Ministry of Education and Science) and FSE (European Social Fund), under the program POCH (Human Capital Operational Programme).

CHAPTER 6

UNCERTAINTY IN MANHOLE HYDRAULICS DUE TO DIFFERENT MANHOLE MOULD AND SMALL BENDING IN THE PIPE

6.1 Abstract

Manhole is a prevalent and essential element in an urban drainage system. The complex flow pattern in a manhole may include the effects of retardation, acceleration and rotation. Several manholes in a drainage network model are represented mostly with the value of their head loss coefficients. In this study, we focus in finding the uncertainty in manhole head loss coefficient value due to three different factors: manhole structural mould shapes, changes in their inlet conditions and changes in manhole to inlet pipe ratio. Three different manhole types are studied numerically using volume of fluid (VOF) model with opensource CFD modelling tools OpenFOAM®. Results showed that the presence of sump generates the highest head loss while presence of benching results the lowest head loss. Both head loss coefficients and surcharge heights of the manhole are found to increase due to bending in the pipe angle. At very small bend, head loss increases only at post threshold surcharge situations. At large bending situations, the threshold surcharge level is increased, and head loss increases at both pre and post threshold surcharge. Examining manholes with sump zone, according to manhole-inlet pipe diameter ratios (Φ_m/Φ_p), three different head loss characteristics were seen. Head loss in small manholes ($\Phi_m/\Phi_p < 3$) did not change with surcharge. Medium manholes ($3 < \Phi_m/\Phi_p < 4.0$) showed high head losses up to a certain surcharge (around 20% of manhole diameter). Big manholes ($\Phi_m/\Phi_p > 4.5$) showed high head loss at all the surcharges.

Keywords: CFD; Head loss coefficient; Manholes; OpenFOAM®; Urban Drainage

6.2 Introduction

Manhole is one of the most common features of an urban drainage system. It is usually placed at a drainage network connection where a change in pipe direction, size or gradient is necessary. It also serves as an inspection pit for the pipe network (Butler and Davies, 2011). The flow inside a manhole is normally complex, highly turbulent and possibly multiphase. When the flow enters a manhole, it experiences a sudden expansion and contraction involving energy losses. This loss makes it an important element for storm network modelling consideration. The drainage system is usually designed to operate without surcharging. In normal condition, the water level at any point remains below the crown level of the conduit. Thus, the flow is only gravity driven and considered as an open channel flow. During an extreme rainfall event, the water level increases and the system could become surcharged making a significant contribution to the overall head losses in the network. For a large system with several manholes, these head losses become more significant.

Intense rainfall may also cause local flood following surcharging manholes and most urban flood models considers this issue while evaluating flood risks (Martins et al., 2017). However, the urban flood models are one or two dimensional utilizing St. Venant Equations and therefore cannot represent the three dimensional complex flow pattern of manholes (Leandro et al., 2009b; Rubinato et al., 2018). A manhole is rather considered as a point entity in these models and the complex flow inside it is modelled using empirical equations for different local losses (Djordjević et al., 2005; Jorge Leandro and Martins, 2016; Mark et al., 2004). It is essential to incorporate the effect of manhole head losses into the sewer pipe lines modelling so that the system can be predicted including store excess flow without flooding and overflows. Quantifying energy loss in a manhole structure is a source of uncertainty in such urban flood models (Rubinato et al., 2018).

The complex nature of energy losses in manholes can be caused by almost infinite variety of geometrical and hydraulic conditions (O'Loughlin and Stack, 2002). This includes many structural and hydraulic factors, such as the shape of a manhole, inflow rate, surcharge condition, pipe size, angle of connection, pipe to manhole diameter ratios etc. (Arao et al., 2013; Carvalho and Leandro, 2012; Marsalek, 1984; Pfister and Gisonni, 2014; Stovin et al., 2013; Wang et al., 1998). Due to different design criteria and practices, different drainage systems use different manhole mould. These have varrying flow hydraulics, which may contribute to the head loss of a drainage network differently. Howarth and Saul (1984), Pedersen and Mark (1990) and Arao and Kusuda (1999) investigated different manhole moulds using scaled surcharged manholes. Pedersen and Mark (1990), Guymer et al. (2005), Lau (2008) and Beg et al. (2018) checked the velocity distribution of surcharged manholes and described their results in line with submerged jet theory, which was originally described by Albertson et al. (1950). Some authors also described numerical modelling

of a surcharged manhole using CFD tools. Lau et al. (2007) and Stovin et al. (Stovin et al., 2013) used rigid lid approximation to numerically model a scaled manhole and described the associated head losses.

A change in the different manhole inlet orientations may also create changes in head loss coefficients. Marsalek and Greck (1988) and Arao and Kusuda (1999) investigated the head loss of a 90° confluence in a surcharged manhole. Pfister and Gisonni (2014) investigated 45° and 90° pipe bend in a manhole using extensive physical modelling experiments. Arao and Kusuda (1999) have also proposed a set of equations to calculate the head loss in a bent pipe scenario deriving from experimental measurements of surcharge manhole with 0° (straight through pipe), 90° and 135°. However, study on effect of small bending angles in the drainage network is rare, such as angles equal or over 165°. These bending conditions are so close to straight inline manholes, that their additional effects on the drainage network is sometimes overlooked and considered within the range of uncertainty.

The head loss of a manhole is also dependent on the ratio between diameters of a manhole and its inlet-outlet pipe(s). Studies proposed that the hydraulic performance increases when the manhole to pipe diameter decreases (Arao et al., 2012; Bo Pedersen and Mark, 1990; Guymer et al., 2005; Guymer and O'Brien, 2000; Howarth, 1985; Stovin et al., 2013). Bo Pedersen and Mark (1990) explained the head loss coefficient to proportional to be manhole diameter to pipe ratio, where the proportional constant is dependent on the manhole mould type. However, the work did not explain the effect of changing surcharge in relation to the different size of manhole. Later, Stovin et al. (2013) applied CFD model on a manhole without sump and showed that the hydraulics of the manhole alters at manhole to the pipe ratio of 4.4. However, this characteristics is not checked for other types of manholes, such as manholes containing sump zone.

In this work, we investigated the uncertainty in flow hydraulics and head losses due to different geometrical changes in the manhole moulds. Three different uncertainty issues related to manhole head loss were investigated: a) due to difference in manhole mould types, b) due to changes in the small bending between inlet and outlet pipes and c) due to change in manhole to pipe diameter. The investigated manholes are prototype scale manholes and comparable to the physical size commonly found in urban drainage networks. Analysis has been done numerically using open source CFD tool OpenFOAM®. In previous works, the authors used Volume of Fluid (VOF) model to analyse different flow in both prototype and small scale manhole and validated CFD modelling methodology with comparison of velocity and pressure from the experimental measurements (Beg et al., 2018, 2017b). The validated modelling methodology will be applied to assess the head loss uncertainty on the surcharge manhole.

The work describes the manhole geometric characteristics, computational domain and numerical model at the 'Methodology' section. 'Mesh Analysis' section follows with the mesh independence test. Comparisons were drawn among the manhole hydraulic behaviours in the 'Results and Discussions' section. The last section summarizes and concludes the work.

6.3 Methodology

6.3.1 Manholes considered for uncertainty analysis

To analyse the hydraulic effects of different manholes, three different inline manholes were chosen. Each manhole has a diameter of 1.0 m, connected with a 300 mm inlet-outlet pipe. The geometrical differences in these three manholes are shown in Figure 6.1. The Type A manhole has a bottom depression relative to the pipes which depth is 100 mm from the inlet pipe invert level. This manhole replicates the experimental facility of the University of Coimbra and is considered as the base structure for all the issues analysed. The second type (Type B) does not have a depression and its bottom level is merged with the inlet pipe invert. Type C manhole has a more hydraulically shaped bottom. The entrainment is further restricted and has a more complex interior geometric shape with a guided flow channel where the channel is a U-type invert. The inlet-outlet pipe at all the three manholes have a 1:1000 slope towards the downstream. The ratio between the manhole diameters to inlet pipe diameters (Φ_m/Φ_p) in all the three cases is 3.33.

To analyse the effect of pipe bending, Type A manhole is investigated only for this case. The outlet pipe is bended slightly for four different cases, making an orientation angle of 178°, 175°, 170° and 165° respectively (Figure 6.2).

For the investigations of manhole to pipe diameter ratios, Manhole type A is investigated only. For this case, eight additional manhole models were considered having manhole to pipe ratios ($Ø_m/Ø_p$) from 1.5 to 5.0 at an interval of 0.5. The inlet-outlet pipe diameter was kept 300 mm, similar to previous cases and the manhole diameters were changed accordingly to match different cases.

6.3.2 Computational domain and mesh

The computational meshes were generated using *cfmesh v1.1* (Juretić, 2015). The maximum size of the computational mesh was chosen as 20 mm towards all three Cartesian directions. The boundary meshes were kept as small as 2 mm; keeping three boundary layers at the all close boundaries. The length of the inlet and outlet pipes were kept 4.5 m each, which is 15 times of the pipe diameter. Figure 6.1 shows the computational meshes of all Type A, B and C manholes.

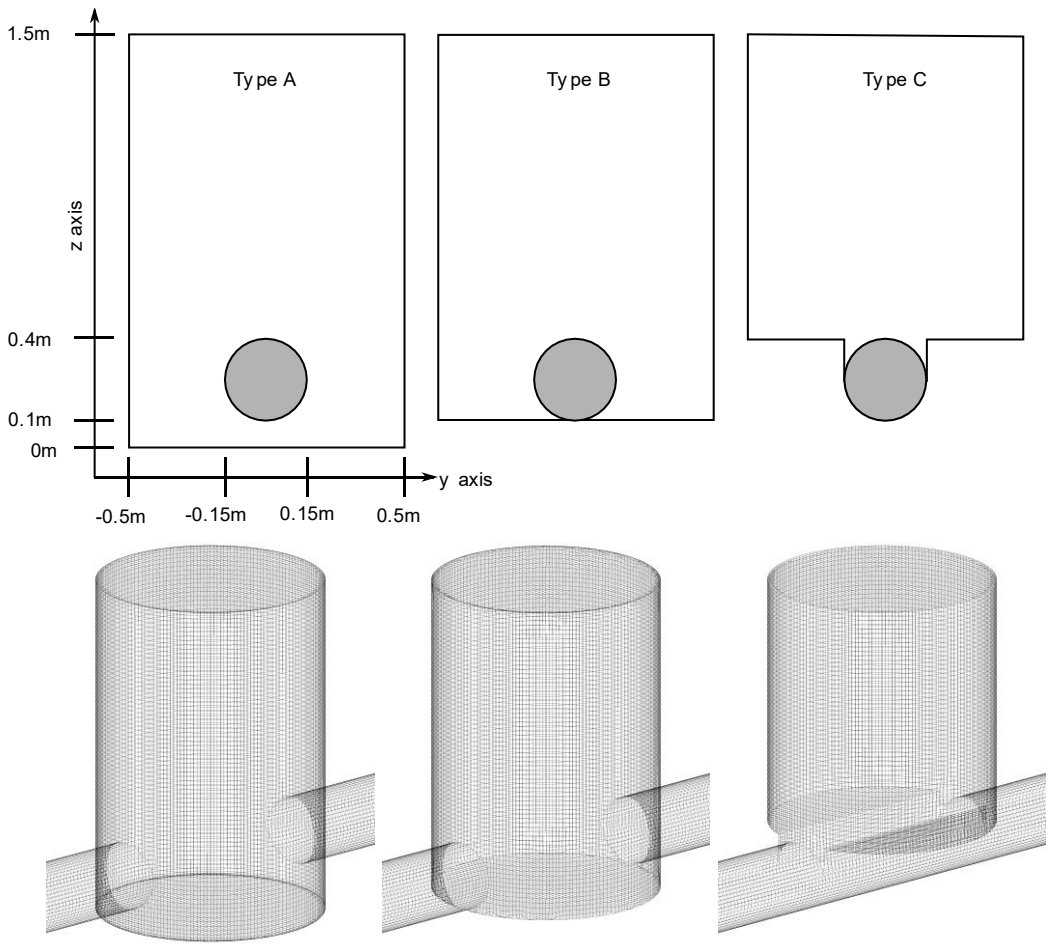

Figure 6.1: Schematic views of the sides of the three manholes showing sizes and positions of different components (upper panel) and their computational meshes (bottom panel). Left panel shows Type A, middle panel shows Type B and the right panel shows Type C

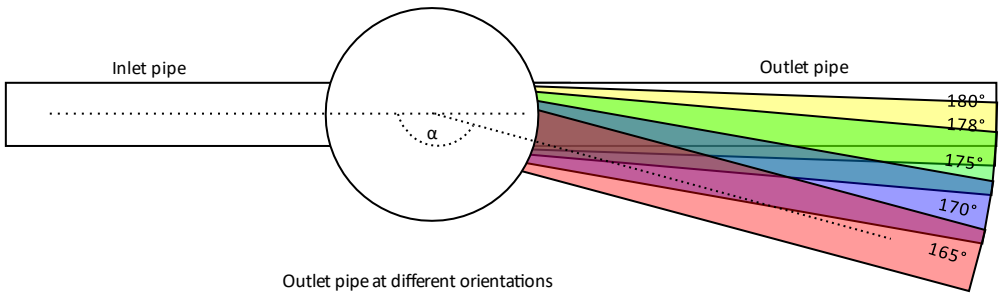

Figure 6.2: Top view of different orientations of inlet-outlet pipe for Type A manhole

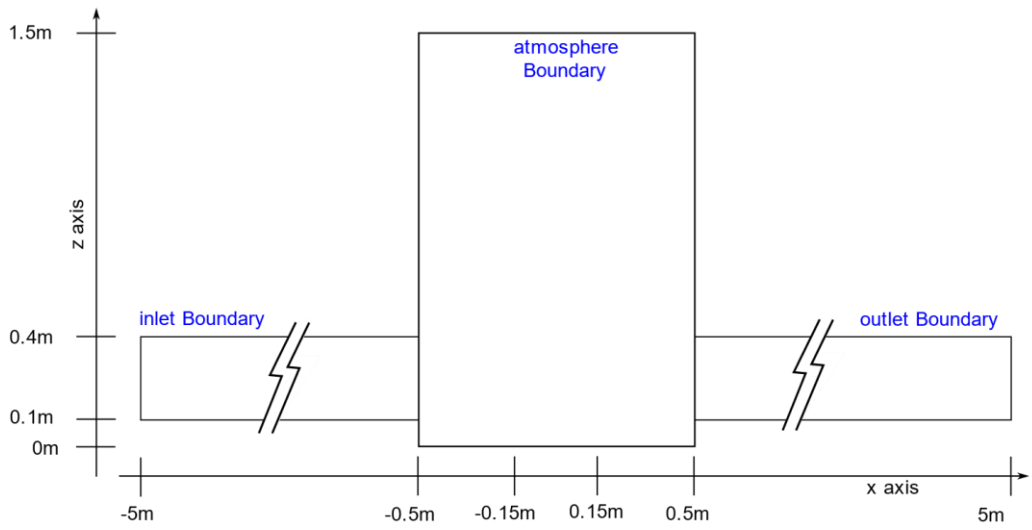

Figure 6.3: Three open boundaries of the model

6.3.3 Numerical Model

All the manhole hydraulic models considered here are fully surcharged manholes connecting full pipe flows. But the water level at the manhole chamber is unknown and needs to be considered to calculate the head loss. For this reason, numerical model with free surface flow model was used in this work.

Open source CFD tools OpenFOAM® v5.0 was utilized in this work. The solver *interFoam* was used to model the flow phenomena which considers the fluid system as isothermal, incompressible and immiscible two-phased flow. The solver utilizes Volume of Fluid (VOF) method (Hirt and Nichols, 1981) to capture the free surface location. VOF utilizes an additional volume fraction indicator term α to determine the amount of each fluid amount in a computational cell volume.

$$\alpha(x,y,z,t) = \begin{cases} 1 & \text{for a place } (x,y,z,t) \text{ occupied by fluid 1} \\ 0 < \alpha < 1 & \text{for a place } (x,y,z,t) \text{ occupied by interface} \\ 0 & \text{for a place } (x,y,z,t) \text{ occupied by fluid 2} \end{cases} \quad (6.1)$$

The solver uses a single set of Navier-Stokes equations for the both fluids, (here in this case water and air) and additional equations to describe the free-surface (Carvalho et al., 2008). The velocity at free-surface is shared by both the phases. The solver deals with Reynolds averaged conservation of mass and momentum for incompressible flow (Jasak, 1996; Rusche, 2002) considering the volumetric surface tension force acting at the two fluids' interface (Brackbill et al., 1992). The details of mathematical equations involved in the model is described in Beg et al. (2018).

6.3.4 Modelling procedures and boundary Conditions

The modelling procedure followed two complementary previous works: Beg et al. (2017b) and Beg et al. (2018). In the first study, stereo PIV analysis was done in a scaled manhole model and the measured velocity was compared with CFD model. The study made four different RANS model namely RNG k-ε, Realizable k-ε, SST k-Ω and LRR. Comparison to PIV data showed that SST k-Ω model and RNG k-ε model has better accuracy in replicating the complex flow in the scaled manhole. The SST k-Ω model requires boundary flow to be resolved utilizing very small mesh of y+ below 5; which makes it significantly expensive in terms of computational time requirement. On the other hand, RNG k-ε model can have almost similar accuracy utilizing mesh consisting 30 < y+<300. For this reason, RNG k-ε model is chosen for this study.

Beg et al. (2018) study replicates a real scale Type A manhole and validates a CFD model comparing discharge and water depth data measured at the laboratory. The CFD model replicated the flow structure in the manhole effectively which was also comparable to the literatures. The study showed that 20 mm hexahedra mesh can was adequate to replicate the flow of the manhole. The inlet flow rate examined in the study was 30×10^{-3} m^3/s, 60×10^{-3} m^3/s, 90×10^{-3} m^3/s and 120×10^{-3} m^3/s. The current study follows the same flow rates.

The model utilizes three open boundaries; i.e. *inlet*, *outlet* and *atmosphere* (Figure 6.3). The *inlet* boundary conditions were prescribed as fully developed pipe flow considering inverse power pipe flow profile (Beg et al., 2017b; Çengel and Cimbala, 2006). The *outlet* boundary conditions were prescribed as fixed pressure boundaries corresponding to different water column pressure heads respectively. No inflow was added at the *atmosphere* boundary conditions. The pressure at this boundary was prescribed as equal to atmospheric pressure and *zeroGradient* for velocity to have free air flow when necessary. All the close boundaries were prescribed as *noSlip* conditions (zero velocity at the wall).

Combination of different inlet discharges and outlet pressures was applied in each simulation. All the three manholes were tested using same sets of boundary conditions and corresponding head losses and surcharges at the manhole centre were recorded. Table 6.1, Table 6.2 and Table 6.3 show all the types of *inlet* and *outlet* boundary conditions used in different simulations.

Table 6.1: Combinations of numerical simulations to check manhole mould effect

Manhole Types	Inlet Discharges ($\times10^{-3}$ m^3/s)	Outlet pressure heads (m)	Simulations
Type A	30, 60, 90 and 120	0.4, 0.425, 0.45, 0.5, 0.55, 0.6, 0.7 and 0.8	32 simulations
Type B			32 simulations
Type C			32 simulations
Total: 3 types	4 options	8 options	96 simulations

Table 6.2: Combinations of numerical simulations to check manhole inlet orientation effect

Inlet orientations	Manhole Types	Inlet Discharges ($\times 10^{-3}$ m^3/s)	Outlet pressure heads (m)	Simulations
178°	Type A	30, 60, 90 and 120	0.4, 0.425, 0.45, 0.5, 0.55, 0.6, 0.7 and 0.8	32 simulations
175°				32 simulations
170°				32 simulations
165°				32 simulations
Total: 4 types	1 type	4 options	8 options	128 simulations

Table 6.3: Combinations of numerical simulations to check manhole inlet orientation effect

Manhole to pipe ratio	Manhole Types	Inlet Discharges ($\times 10^{-3}$ m^3/s)	Outlet pressure heads (m)	Simulations
1.5	Type A	60	different outlet pressures to create surcharges up to 60% of the manhole diameter	8 simulations
2.0				8 simulations
2.5				8 simulations
3.0				8 simulations
3.1				8 simulations
3.2				8 simulations
3.3 (Manhole A)				No additional simulations
3.6				9 simulations
4.0				10 simulations
4.5				11 simulations
5.0				12 simulations
Total: 9 types	1 type	1 option	-	90 simulations

The inlet turbulent boundary conditions *k*, *ε* and *nut* were calculated using the equations described by Beg et al. (2017b), considering 5% turbulence intensity at the manhole. All the wall turbulent boundary conditions were prescribed as *wallFunction* as this eliminates the necessity of fine layered boundary mesh and hence reduce the computational time (Greenshields, 2015). A list of the model parameters used in the model is shown in Table 6.4.

Table 6.4: Parameters for the CFD simulations

Parameter Name		**Parameter value**
Mesh		
	Mesh type	Hexahedral, Unstructured
	Inlet boundary	Velocity inlet, Fully developed velocity profile
	Outlet boundary	Pressure boundary, hydrostatic pressure
	Atmosphere boundary	Atmospheric pressure
	Wall boundary	noSlip, no roughness
	Mesh size	20 mm

Parameter Name		Parameter value
	Boundary mesh size	2 mm and 3 layers with increasing size
	y+ size	30 < y+ < 300
Solver		
	Multi-phase	VOF
	Turbulence	RNG k-ε
	Pressure-Velocity coupling	PIMPLE
	Pressure	Preconditioned conjugate gradient (PCG)
	Velocity	symmetric Gauss Seidel
	Near wall treatment	wallFunction

The model was ready to run after the boundary setup. During the simulations, *adjustableRunTime* was used keeping maximum CFL number to 0.8. Cluster computing system at the University of Coimbra was used to run the simulations using MPI mode. Each simulation was run for 120 seconds. The first 100 seconds were required to reach steady state condition and the results of last 20 seconds were saved at an interval of 0.1 seconds as 201-time steps. All the analysis was made using averaged data of the mentioned time step results.

6.3.5 Identification of Manhole head loss coefficient and threshold surcharge

The flow through a manhole experiences sudden expansion and compression when entering and exiting a manhole respectively. These changes involve loss of energy head of the flow. The head loss coefficient, K of the manholes is calculated using the following equation:

$$K = \frac{\Delta H}{v^2/2g} \tag{6.2}$$

where, ΔH is the change in energy head of the manhole centre and v is the averaged flow velocity towards the flow direction at the outlet pipe. Figure 6.4 explains the change in energy head in a manhole. When determining the head loss, the energy grade lines from inlet and outlet pipes are extrapolated to the manhole centre and the difference between the extrapolated lines at the centre gives the measurement change in pressure head at the manhole centre.

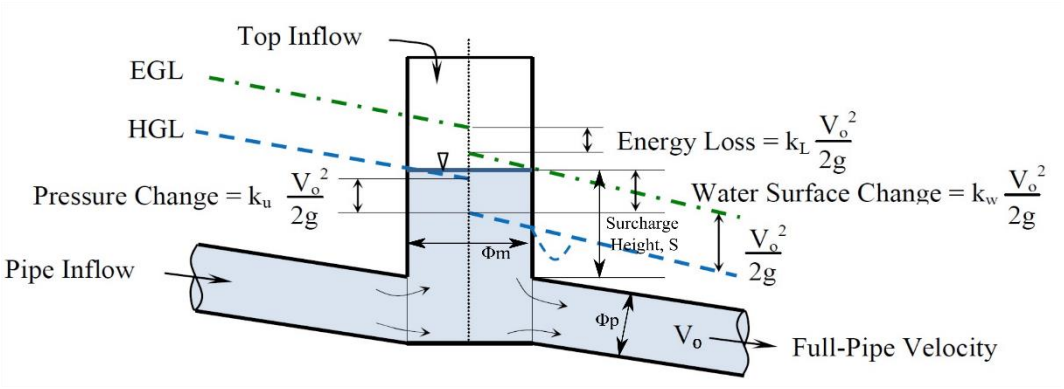

Figure 6.4: Head loss in a surcharged manhole, adapted from Pang & O'Loughlin (2011)

The total energy head is the sum of hydraulic grade line and velocity head. In case of manholes having only one inlet and one outlet, due to continuity, at surcharge condition inlet velocity head and outlet velocity head is equal and the difference between inlet and outlet hydraulic grade line will be equal to the difference in energy grade line.

The head loss coefficients of the manholes were checked at different manhole surcharge levels. The surcharge height (s) for a condition was calculated by subtracting the soffit level of inlet-outlet pipes from the water level of the manhole. Surcharge ratio (s/Φ_p) was calculated from each simulation results, as the ratio between surcharge heights (s) and inlet pipe diameter (Φ_p). At fewer cases, the surcharge ratio was also calculated as the ratio of manhole diameter (s/Φ_m).

6.4 Mesh analysis

A mesh independence test was done for the current work. For this purpose, three different meshes were created for the manhole Type C. The meshes had dx = 10 mm (Mesh C1), 14 mm (Mesh C2) and 20 mm (Mesh C3) with total cell counts as 2 137 000, 865 000 and 329 000 respectively. The mesh convergence study was checked using Richardson extrapolation method described by Celik et al. (2008). The refinement ratio between Mesh C2 and C1 as well as Mesh C3 and C2 were more than the recommended value of 1.3.

All the three meshes were simulated with a combination of 120×10^{-3} m^3/s inlet discharge and 0.8 m of outlet pressure head. Only for this part only, the inlet boundary forcing was applied using constant discharge. The axial velocity profiles were extracted at the manhole centre and at the pipe outlet centre. A total of 60-point velocities were compared. The comparisons between the three meshes are shown at Figure 6.5 and In the analysis, 32 points (53%) showed oscillatory convergence. The average uncertainty at the outlet pipe were found 4.0% comparing Mesh C3 and C2, and 2.4% comparing Mesh C1 and C2. At the manhole centre near the jet stream, the

uncertainty was found less, average uncertainty was 4.37% comparing Mesh C3 and Mesh C2, and 2.71% comparing Mesh C1 and C2.

Table 6.5.

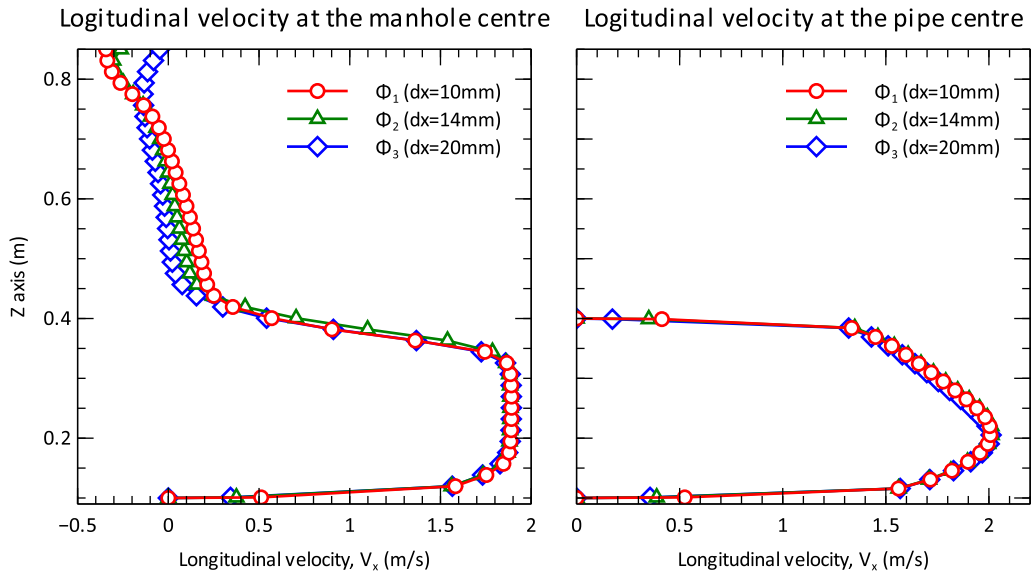

Figure 6.5: Mesh analysis using three meshes for Manhole Type C. Left panel shows longitudinal velocity profile at the manhole centre and the right panel shows longitudinal velocity profile at the outlet pipe

In the analysis, 32 points (53%) showed oscillatory convergence. The average uncertainty at the outlet pipe were found 4.0% comparing Mesh C3 and C2, and 2.4% comparing Mesh C1 and C2. At the manhole centre near the jet stream, the uncertainty was found less, average uncertainty was 4.37% comparing Mesh C3 and Mesh C2, and 2.71% comparing Mesh C1 and C2.

Table 6.5. Comparison between different mesh properties

Name of mesh	Mesh size, dx (mm)	No. of cells	Grid Convergence Index, GCI	Coefficient of head loss, K
Mesh C1	10	2,137,000	1.38%	0.086
Mesh C2	14	865,000	2.7%	0.086
Mesh C3	20	329,000	---	0.088

However, the velocity is very small near the free surface (in the range of 0.1 m/s) and model prediction uncertainty at this zone rises to 32% comparing Mesh C1 and C2, and 54% comparing Mesh C2 and Mesh C3. Large uncertainty close to the free surface was found due to high gradient of velocity. The average grid convergence index (GCI) at the outlet pipe were recorded as 1.38% and 2.7% for Mesh C1 and Mesh C2 respectively, compared to their immediate coarser meshes.

In Figure 6.5 (left panel), the coarse mesh of 20 mm (Mesh C3) creates different flow structure close to the water surface. While the other two meshes (14 mm and 10 mm) creates similar flow in the manhole. As for this work, focus is given to manhole head loss coefficient K ($=2g.\Delta H/v_x^2$), the value was checked for all the three meshes. The K value in Mesh C1, Mesh C2 and Mesh C3 were found 0.086, 0.086 and 0.088 respectively, which are very similar to each other. So, it can be concluded that although Mesh C3 showed different flow structure in the small scale compared to Mesh C1 and Mesh C2, but when considering the flow at the large scale, Mesh C3 gives considerably good results, which justifies the use of similar mesh size for all the simulations.

6.5 Results and discussions

6.5.1 Comparison of head loss values with the literature

The numerical results obtained in the study were compared with the manhole head loss calculated in different literatures. Arao and Kusuda (1999) tested the head loss in Type B manhole where the manhole to pipe diameter ratio was ($Ø_m/Ø_p$) 3.6. Stovin et al. (2013) compared different size of Type B manholes using CFD models. One manhole had had $Ø_m/Ø_p = 3.5$, which is closest to our case and the results are compared in Figure 6.6 (left panel). Arao and Kusuda (1999) found the manhole head loss to be up to 1.25, while Stovin et al. (2013) found the maximum head loss as 0.8 approximately. In our results, four different discharge conditions were tested, and the highest head loss was found to vary between 0.6 and 0.8. Our model showed threshold surcharge around $0.75Ø_p$ (~$0.225Ø_m$). On the other hand, the findings of Arao and Kusuda (1999) showed the threshold surcharge in the range of $1.4Ø_p$ (~$0.39Ø_m$). However, Stovin et al. (2013) found the threshold surcharge around $0.2Ø_m$, which is similar to our findings.

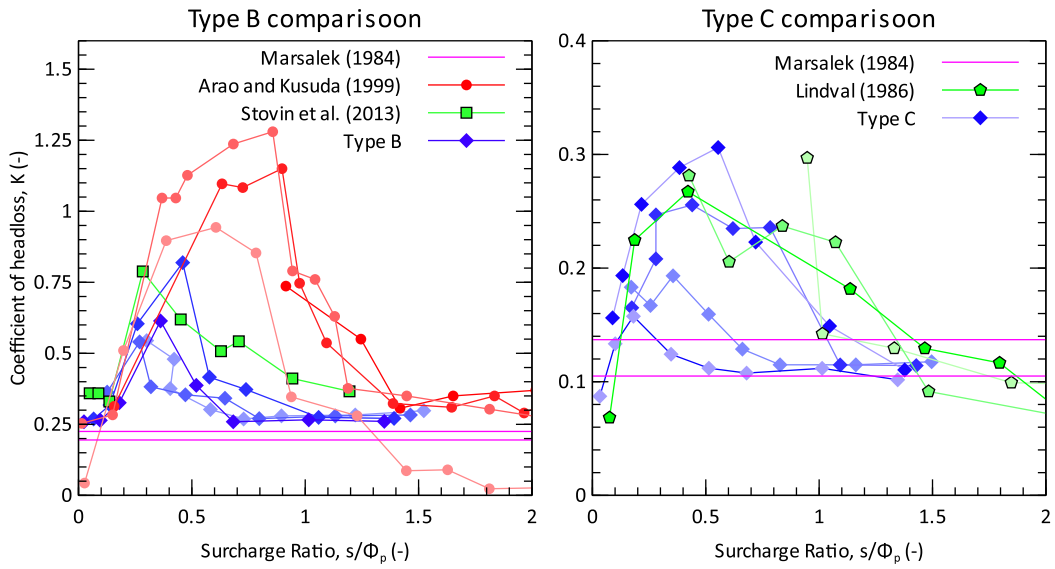

Figure 6.6: Head loss coefficients comparison for manhole Type B (left panel) and Type C (right panel). Data adapted from Bo Pedersen and Mark (1990), Stovin et al. (2013) and Guymer et al. (2005) respectively.

Lindvall (1986) measured head loss in a Type C manhole using experimental models. Their used scaled manhole had manhole to inlet pipe ratio ($Ø_m/Ø_p$) as 4.1. Comparing to their works with our current results (Figure 6.6, right panel), we see that the CFD model shows good agreement with the data. The maximum head loss coefficients at pre-threshold condition was found the same, up to 0.3. The surcharge threshold observed in Lindvall (1986) was around $1.4Ø_p$. While in our current CFD model, the threshold surcharge was found in the range of $1.1Ø_p$. However, if the surcharge is compared as a ratio of manhole diameter ($Ø_m$), both of the two threshold surcharges are equivalent to $0.33Ø_m$, as the value of $Ø_m/Ø_p$ is different in these cases.

Marsalek (1984) tested head loss in Type B and Type C inline manholes using laboratory experiments (mentioned as M1 and M3 manholes respectively in their research). The work did not describe head loss variation for change of surcharges, rather describes a range of head loss for each manhole type. The found head loss coefficients were 0.195-0.225 for Type B and 0.105-0.137 for Type C manhole. These values are fairly below from the results in our findings. In their experimental setup, the manhole to pipe ratio ($Ø_m/Ø_p$) was 1.93, which is much smaller than our tests (3.33). The head loss coefficient also varies due to manhole to pipe diameter ratio; the head loss decreases with the increase in $Ø_m/Ø_p$ (Bo Pedersen and Mark, 1990; Stein et al., 1999; Stovin et al., 2013). This might be a reason of the difference.

6.5.2 Head loss coefficient at different manhole moulds

The surcharge ratios and the head loss coefficients were calculated for the three different manhole mould mentioned at Figure 6.1. The plots are shown in Figure 6.7.

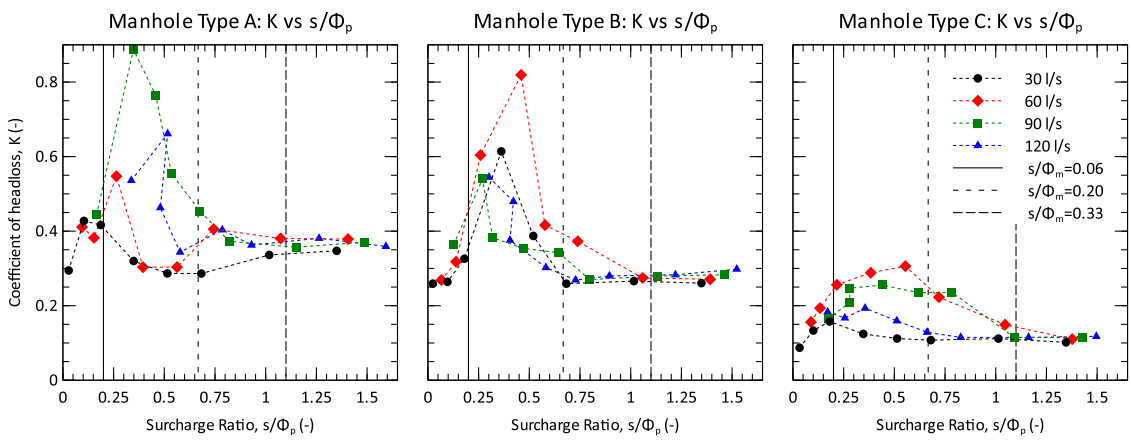

Figure 6.7: Manhole Head loss coefficient (K) vs Surcharge ratio ($s/Φ_p$) for manhole types A, B and C

It can be seen from Figure 6.7 that out of the three manholes, Type A and Type B has comparably higher head losses in all scenarios than those of manhole Type C. All three manholes showed higher head loss coefficients at low surcharge conditions.

For both manhole Type A and Type B, the head loss coefficient stays around 0.35 and 0.3 respectively at higher surcharge conditions (for $s/\Phi_m>0.20$ or $s/\Phi_p>0.67$) with all types of inflow. When the surcharge ratio becomes low (for $s/\Phi_m<0.20$), the head loss coefficient starts to increase. This can be explained by submerged jet theory (Albertson et al., 1950). When the inlet flow enters a manhole, the incoming flow acts like a submerged jet and expands as a diffusive zone at a ratio 1:5 with the travelling length inside the manhole. While travelling through the diameter of the manhole (1 m), the diffusive zone may expand up to 200 mm. When the surcharge height is below 200 mm, the diffusive zone interacts with the free surface and creates additional head losses. In Figure 6.7, the surcharge height of 200 mm is shown at each graph with a dotted line at $s/\Phi_m=0.2$, which is also equivalent to the line $s/\Phi_p=0.67$ as $\Phi_m/\Phi_p=3.33$ for all the three manholes. This surcharge limit is termed as 'Threshold Surcharge' by some authors (Bennett, 2012; Lau, 2008; Stovin et al., 2013). The results from Type A and Type B manholes show that at the surcharge ratios (s/Φ_p) below 0.67, the coefficient of head loss becomes very high; which represents threshold surcharge level is around 20% of the manhole diameter for these two types.

However, for manhole Type C, at high surcharge conditions, the coefficient of head loss stays around 0.1 (for $s/\Phi_m>0.33$). The benching in the manhole tends to confine the round jet and keeps the head loss to minimal. But the head loss is high at very low surcharge and remains high up to a surcharge ratio of $s/\Phi_m = 0.33$; (i.e. $s/\Phi_p = 1.11$). The phenomenon can be checked in Figure 6.8, which shows the velocity profiles at the centre line (y=0 m) of the three manholes.

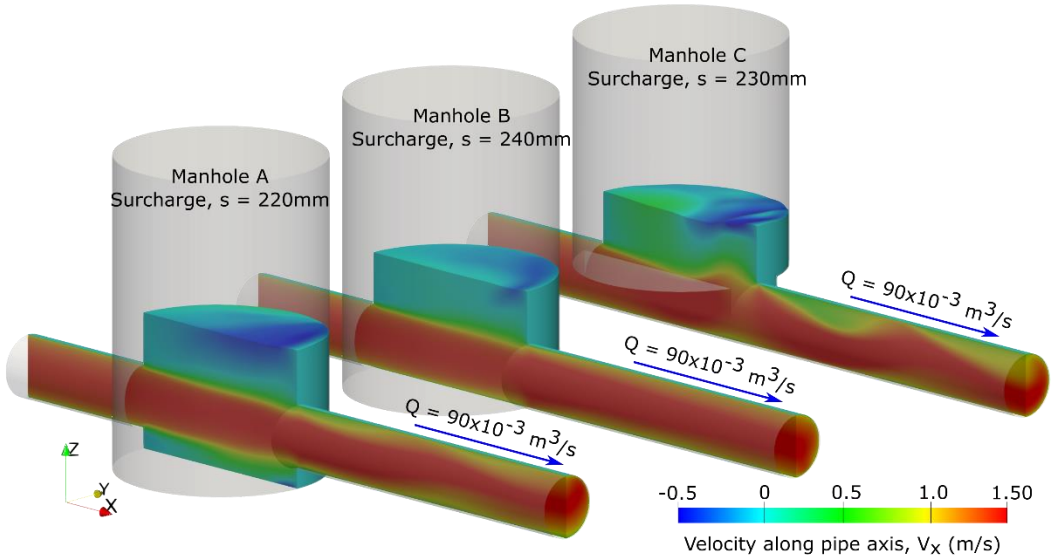

Figure 6.8: Instantaneous velocity profile at the central axis of the manhole. From left to right: Manhole Type A, Type B and Type C. The flow direction at each manhole is from left to right

Figure 6.8 shows the manhole Type A, B and C at surcharge conditions such as $0.20 < s/\Phi_m < 0.33$. Type A and B show steady flow at this surcharge level. But the jet velocity at Type C manhole expands more towards the vertical and interacts with the free surface creating oscillation inside the manhole and outlet pipe. This indicates that threshold surcharge level is higher than 0.20 Φ_m in Type C manhole. From the Figure 6.7, it is apparent that the threshold surcharge ratio for Type C manhole is around 33% of the manhole diameter.

When the surcharge level is below threshold, the head loss coefficient (K) vs Surcharge ratio (s/Φ_p) plot do not follow any particular trend. At manhole Type B and C, the head loss decreases at very low surcharge conditions (for $s/\Phi_m < 0.06$). Too low surcharge was not possible to create in the manhole model due to high speed of the flow.

6.5.3 Free surface location at different manhole moulds

The free surface position of a manhole varies at different surcharge and inflow conditions. This has been analysed from the numerical model results. To analyse this, the Hydraulic Grade Lines (HGL) of the manholes with inlet-outlet pipes were checked. Where,

$$\text{HGL} = \text{Elevation Head (Z)} + \text{Pressure Head } ({}^{P}/_{\rho g}) \tag{6.3}$$

Figure 6.9 shows the change of HGL at the manhole and its immediate upstream and downstream pipes from different simulation results. Each subplot represents one inflow and downstream pressure condition for all three manholes. It should be noted that the inlet pipe and the outlet

pipe is connected to the manhole at x=-0.5 m and x=+0.5 m respectively. The value of HGL between them is also representable of the free surface heights inside the manholes.

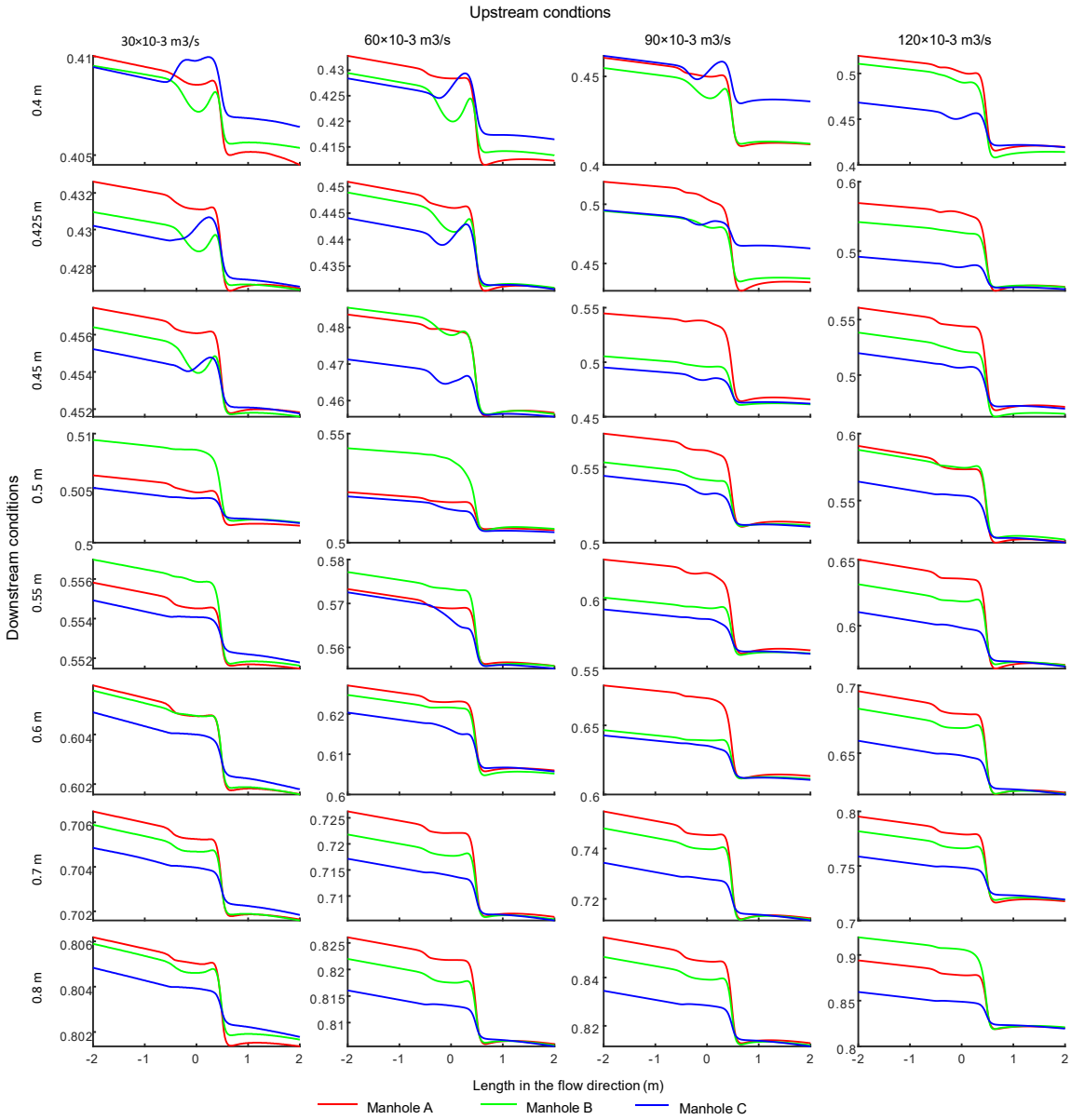

Figure 6.9: Bottom pressure in three types of manhole at different upstream (u/s) and downstream (d/s) cases. Red, Green and Blue lines show the pressure data of Manhole Type A, B and C respectively. Manhole centre is at x = 0 m

Analysing Figure 6.9, it can be concluded that all the three manholes experience two different types of loss. The first head loss is seen at the inlet junction (near x = - 0.5 m) due to expansion of flow and the second head loss is observed much higher at the outlet junction (near x = 0.5 m) due to contraction. Figure 6.9 also shows that head loss experienced by manhole Type C is significantly less than those of Type A and B in most cases. This difference may play a significant role at the time of very high surcharge scenarios. For any flood water level at the downstream, there is

significantly higher chance of flooding at the upstream when the drainage network is based on Type A or Type B manholes other than Type C.

The total head losses at any manhole are greater at high discharge conditions than those of low discharge conditions. Comparing the simulation results at different inflow conditions with 0.8 m water pressures, the head loss at manhole Type A or B is in the range of 30 mm per manhole when the inflow is 30×10^{-3} m^3/s. But this increases to 70 mm per manhole when the inflow is as high as 120×10^{-3} m^3/s. This shows that in higher drainage inflow conditions, it is more likely that the drainage congestion will increase, and the chance of street flooding will be more. However, for the same surcharge and inflow scenarios, the head loss at Type C manhole is as low as 10 mm at 30×10^{-3} m^3/s and 30 mm at 120×10^{-3} m^3/s, making lower chance to any possible local flooding.

6.5.4 Change in head loss coefficient due to pipe bending

Figure 6.10 shows the comparisons of flow velocity at the horizontal section for different pipe bending of the surcharged manhole. All the conditions are showing time averaged velocity distribution of the manhole at upstream condition of 60×10^{-3} m^3/s with downstream condition of 0.6 m of water pressure.

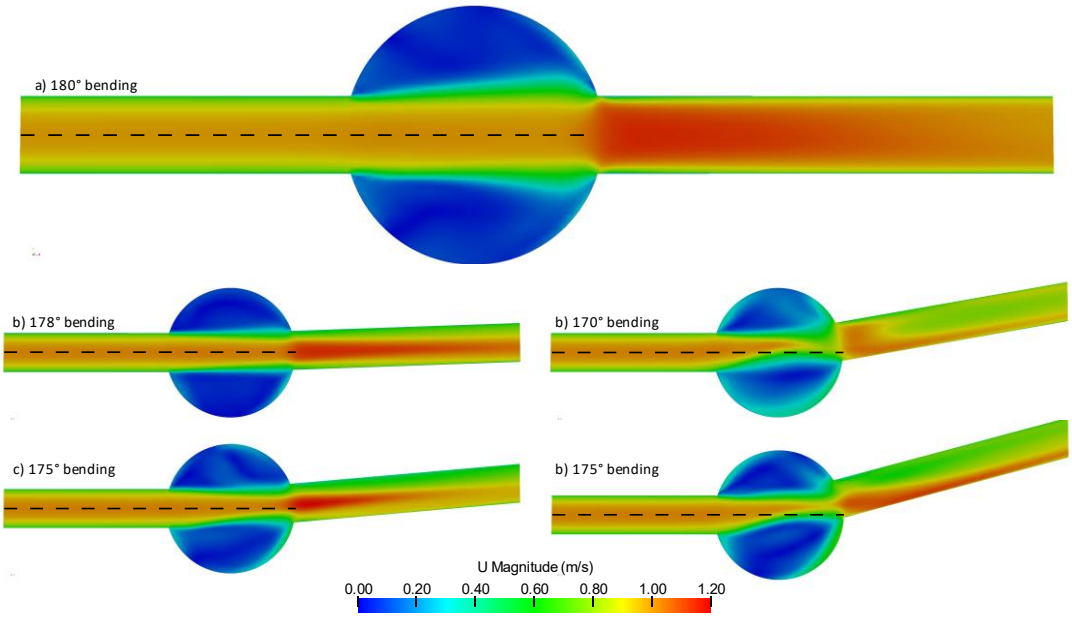

Figure 6.10: Flow velocity at different inlet conditions of the manhole. All figures representing inlet condition of 60×10^{-3} m^3/s and outlet condition of 0.6 m of water column pressure. The flow direction is from left to right.

Figure 6.10 shows that at 180° pipe (straight pipe/normal condition) of the manhole, the incoming jet flow from the inlet pipe shows two zones namely core zone and diffusive zone. The core zone with strong velocity enters the outlet pipe without much variation. This normal condition starts

changing with the change in inlet-outlet orientation. At small bending angle, such as 178° and 175° angles, the core zone can still enter to the outlet pipe without much variation. However, at higher bending angles such as 170° or 165° angles, the core jet becomes discontinued. Although the central axis of the inlet pipe can still point towards the outlet pipe, but the outlet pipe cannot accommodate the full width of the core jet region. Part of the core jet zone hits the manhole wall and results in discontinuity in the core jet. At these bending situations, the whole jet becomes weak or discontinued, making comparably higher contribution the manhole head loss. These phenomena are reflected in Figure 6.11 which shows the variation in head loss coefficients due to different inlet orientations.

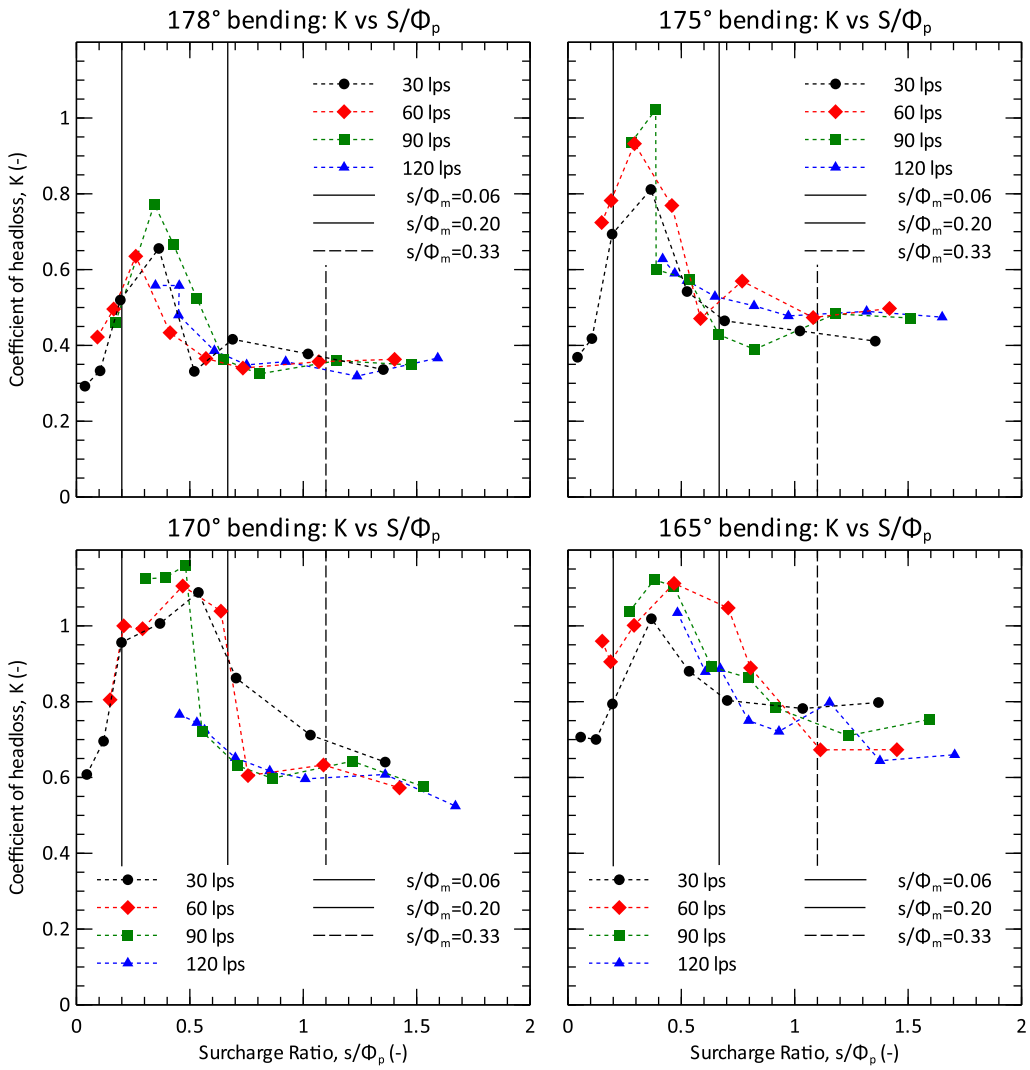

Figure 6.11: Manhole head loss coefficients for different horizontal angle difference between inlet and outlet

From Figure 6.11, comparing with the similar plot at normal condition of Manhole type A (Figure 6.7 left panel), we can see that the overall qualitatively the head loss coefficients show similar trend, i.e. high head loss at low surcharge and comparatively lower head loss at high surcharge.

At 178° bend, the high surcharge head loss is close to 0.38. It is very close to the normal condition high surcharge condition (below 10% increase). At 175° orientation, the high surcharge head loss coefficient is seen around 0.45; which is more than 30% increment from the normal condition. At both cases, the threshold surcharge remains around 20% of the manhole diameter, which is the comparable to the straight pipe scenario.

On the other hand, at the bending angles of 170° and 165° cases, the threshold surcharge is found to increase up to 33% of the manhole diameter, which is around 50% increase from the normal condition. The maximum head loss can be seen at $0.5Ø_p$ and found in the range of 1.15 at both cases. The head loss become consistent at surcharges more than $1.5Ø_p$. The post threshold surcharge scenario, the head loss at 170° bend is found to be around 0.6; which is almost 75% increase compared to the straight pipe case. A further 5° increase in the bending angle accelerates the changes even more. At 165° bend, the post threshold surcharge condition, the head loss coefficient becomes around 0.75; which is a 25% increase compared to 170° bend case and almost double to the straight pipe case. At pre-threshold surcharge condition, the head loss coefficient increase up to 1.25 at both 170° and 165° bend pipe conditions. This is around 80% increase when compared to a straight pipe manhole.

6.5.5 Effect of manhole to pipe ratio

The change of head loss due manhole to pipe ratio at different surcharge condition is shown in Figure 6.12. With the increase in manhole to pipe ratio, the manhole head loss ratio was found to increase. However, between manhole to pipe ratio of 3.0 to 3.1 and 4.0 to 4.5, the hydraulic regime changed showing a different characteristic. For small diameter manholes, considering $Ø_m/Ø_p < 3.0$, the flow from the inlet pipe passes through the outlet making comparably less head loss at all the surcharge conditions. At $Ø_m/Ø_p = 1.5$, the head loss ranges from 0.21 at low surcharge to 0.17 at high surcharge condition. With the increase in manhole ratio and up to the ratio of 3.0, the head loss increases at all the surcharge ratio conditions. At $Ø_m/Ø_p = 3.0$, the head loss on the manhole ranges between 0.4 and 0.6. These manhole models did not show any indication of having threshold surcharge zone.

At slightly bigger manhole, at $Ø_m/Ø_p = 3.1$, the head loss was found to decrease suddenly. At this case, the head loss showed high value at the low surcharge until the surcharge condition reaches around 0.17 $Ø_p$ (around 0.2 $Ø_m$). At higher surcharge than this value, the manhole head loss reduces. This phenomenon can be seen to all the manholes with medium sized diameter ($3.1 < Ø_m/Ø_p < 4.0$). At even bigger diameter manholes, when $Ø_m/Ø_p \geq 4.5$, the manhole showed very high head loss at all surcharge conditions. This changes in the head loss is explained through Figure 6.13.

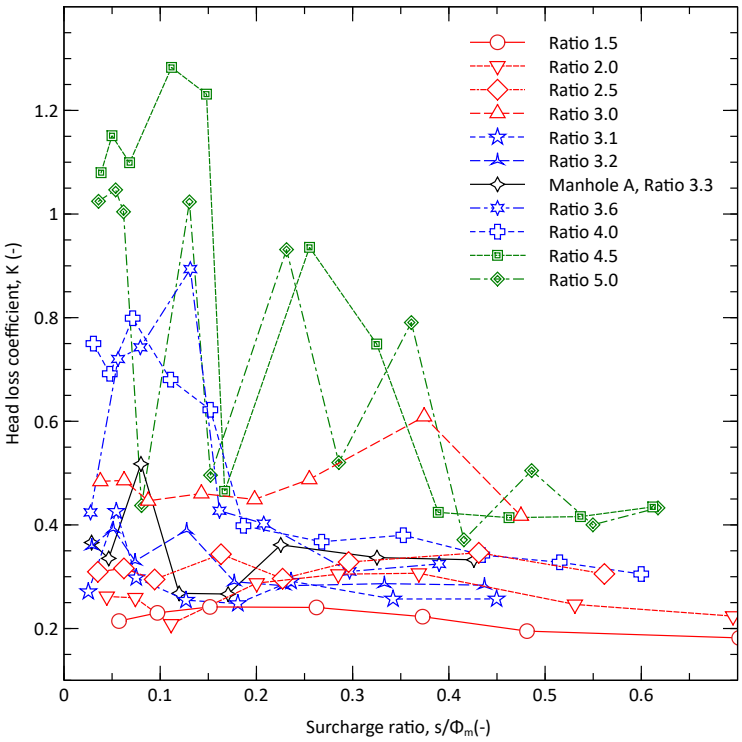

Figure 6.12: Effect of head loss on manhole to pipe ratio

The change in the hydraulic behaviour can be observed in Figure 6.13, which shows different conditions of the jet flow at the vertical section of the manhole. As the flow travels through the manhole, the core jet flow starts weakening. Theoretically, this change happens at a ratio of 1:6.2 towards the manhole travel length (Albertson et al., 1950). This indicates that at a manhole with inlet pipe diameter of 0.3 m, the core jet would travel a distance of (6.2×0.3=) 1.86 m before it diminishes completely. This ratio also tells us that for any manhole with $Ø_m/Ø_p$<6.2, the jet core would not dissipate in the manhole, rather would pass through the outlet. Figure 6.13 indicates a deviation from that ideal condition, showing that the core jet flow zone becomes too weak at $Ø_m/Ø_p$ = 4.5 and diminishes within the manhole. At the small manholes, the fast-moving jet flow does not change its shape and the core jet remains strong enough when it reaches the outlet pipe. At large manholes, especially at $Ø_m/Ø_p$ > 4.5, the jet core becomes too weak before it reaches the outlet. This results a diminish of the jet core as well as an oscillating at the main core jet. This type of hydraulic behaviour was also reported by Guymer et al. (2005) and Stovin et al. (2013) while investigating a Type B scaled manhole using laboratory experiment and CFD modelling.

At small manholes, the core region remains so strong until the outlet that the diffusion region cannot influence to the core jet and hence the head loss of the manhole does not change much. At large manholes ($Ø_m/Ø_p$ > 3.0) with lower surcharge (at around $s/Ø_m$ < 0.2), the diffusion region hits the water surface and creates oscillation in the flow. The core jet zone cannot enter the outlet

smoothly, which creates additional head loss. This phenomenon is applicable for small surcharge until s < 0.2$Ø_m$ for all the manholes

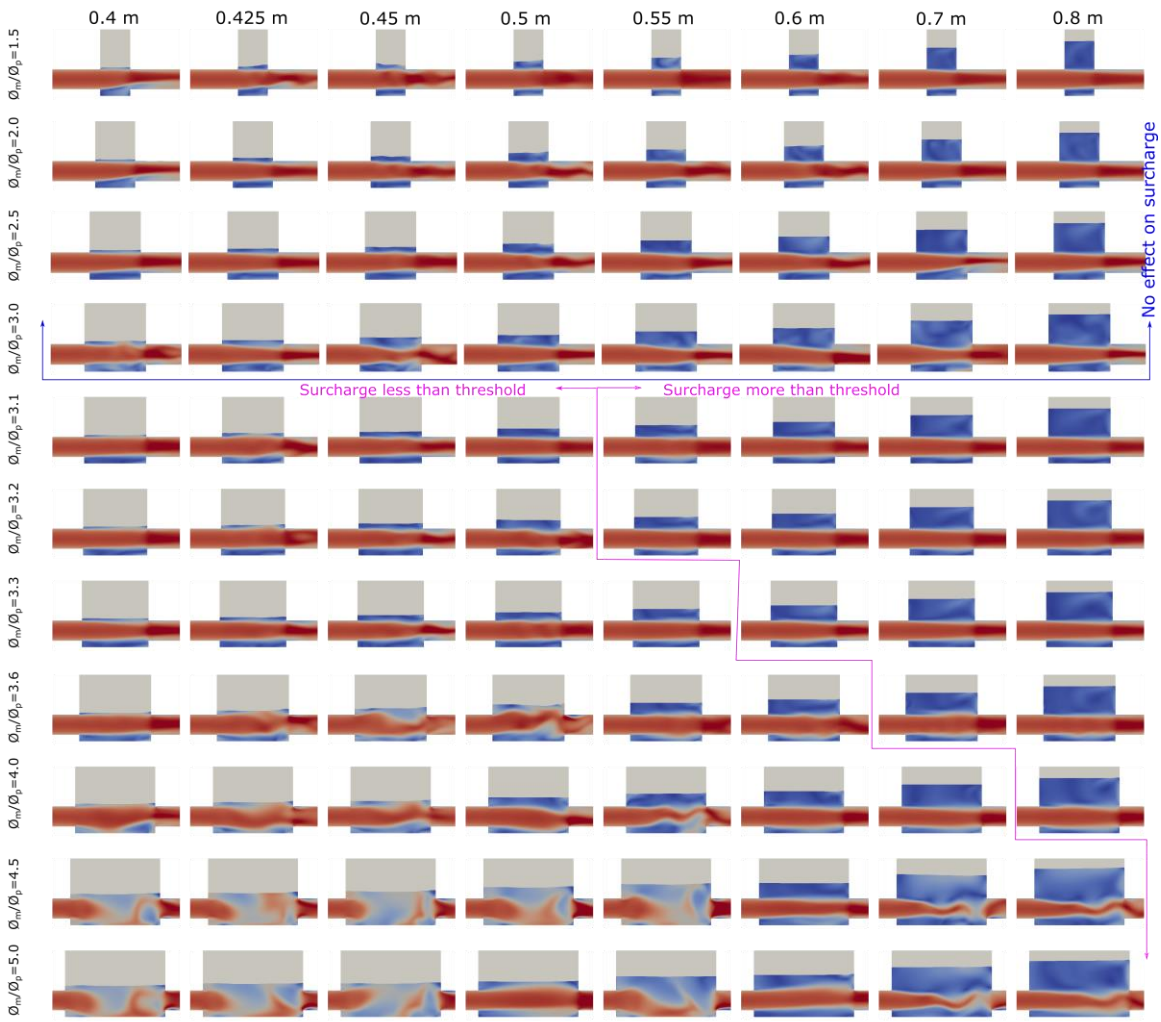

Figure 6.13: Instantaneous velocity at the vertical cross section of the manhole at all manhole ratio and surcharge conditions

6.6 Conclusions

The work presented here compares the hydraulics and head loss coefficients of surcharge manhole due to various changes in their structural properties. All the three manholes are in real scale having 1.0 m diameter and connected with 300 mm inlet-outlet pipes. This makes the manhole to pipe diameter ratio equal to 3.33. Three different types of surcharged manholes moulds were tested: Type A, with no guided channel and a 100 mm sump zone below the inlet outlet pipe invert level; Type B, like Type A but without sump zone at the bottom and Type C, with a U-invert shaped guided channel at the manhole bottom. The manholes were modelled

numerically using open source CFD modelling tools OpenFOAM® with interFoam solver. RNG *k-ε* model was used to replicate the turbulence condition. Each manhole showed different head loss coefficients at different surcharge levels. The threshold surcharge level for Type A and B was found approximately as 20% to that of manhole diameter; whereas for Type C manhole, it was more than 20%. All the three manholes showed higher head loss coefficients at surcharge conditions lower than threshold surcharge level. For any inflow and surcharge condition, manhole Type C was found to be most hydraulically efficient as it showed the lowest head loss coefficients at all inflow and surcharge conditions.

The Hydraulic Grade Lines for all the manholes at different simulations were compared. Analysis showed that at higher inflow, the head loss becomes higher and makes the pressure or water surface level high at the upstream. This may increase the chance of flooding/local flooding at the upstream of the drainage network. Analysis also showed that the chance of manhole overflow is higher at Type A and Type B manholes compared to that of Type C manholes.

The effect of pipe bending in the manhole connection was found to have different characteristics according to the bending angles. At very small bend, jet flow core region can still dissipate through the outlet pipe and very small increase in the post threshold head loss coefficient is seen. The changes in pre-threshold head loss is found insignificant. At higher bending angles, the core jet flow disappears in the manhole and comparably higher head loss coefficients are observed in the manhole at both pre and post threshold conditions.

In a changing manhole to pipe ratios, it was found that the hydraulic regime changes between $Ø_m/Ø_p = 3.0$. Below this ratio, the head loss does not show any susceptibility to the available surcharge. For $Ø_m/Ø_p > 3$, manholes showed another change in hydraulic regime between $Ø_m/Ø_p = 4.0$ and 4.5. A distinctive threshold surcharge which is around 20% of the $Ø_m$ for all manhole with $3.0 < Ø_m/Ø_p < 4.0$. Below this surcharge, the head loss is significantly higher. At $Ø_m/Ø_p \geq 4.5$, the jet flow from the inlet becomes too weak when it reaches the outlet. The head loss at these cases is also found much higher at all the surcharges.

6.7 Acknowledgements

The work presented is part of the QUICS (Quantifying Uncertainty in Integrated Catchment Studies) project. This project has received funding from the European Union's Seventh Framework Programme for research, technological development and demonstration under grant agreement No. 607000. The cluster computing system of the University of Coimbra was utilized to run the CFD simulations. The authors would also like to acknowledge for the support of FCT (Portuguese Foundation for Science and Technology) through the Project UID/MAR/04292/2013 financed by

MEC (Portuguese Ministry of Education and Science) and FSE (European Social Fund), under the program POCH (Human Capital Operational Programme).

CHAPTER 7

FLOOD FORECASTING WITH UNCERTAINTY USING A FULLY AUTOMATED FLOOD MODEL CHAIN: A CASE STUDY FOR THE CITY OF KULMBACH

7.1 Abstract

Real-time flood forecasting can help authorities in providing reliable warnings to the public. Ensemble prediction systems (EPS) have been progressively used for the operational floods forecasting by many hydrometeorological agencies in recent years. This process is, however, non-deterministic such that uncertainty sources need to be accounted before issuing forecasts. In the FloodEvac project, we have developed a tool which takes as inputs rainfall forecasts and links a hydrological with a hydraulic model for producing flood forecasts. The tool can handle calibration/validation of the hydrological model (LARSIM) and produces real-time flood forecast with the associated uncertainty of flood discharges. In this case study, we focus on the linkage with the hydrological model and on the real-time discharge forecasts generated. The tool was found efficient in hindcasting four different historical flood events. A new methodology of flood forecasting named Discharge Interval Method is proposed. This method uses at least one historical event hindcast data run in Monte Carlo ensembles to select a pair of best ensemble discharge results for every certain discharge interval level. Later, the tool uses the same parameter settings of the chosen ensemble discharge pair to forecast any certain flood discharge level. The proposed methodology is very much computationally efficient which could be ideal for real-time forecasts. The result using the Discharge Interval Method was found comparable to 90 percentile forecasted discharge range obtained from the Monte Carlo method.

Keywords: Calibration, Forecasting, Hydrological modelling, Uncertainty, Validation

7.2 Introduction

The economic loss within European Union due to flood issue exceeded 60 billion Euros from 1998 to 2009 with 1126 fatalities (EEA, 2010; Kauffeldt et al., 2016) making flood resilience one of the prominent issues. The loss increased in the past decade as a result of climate change, increasing city population and increase in per capita wealth (EEA, 2017, 2010). Improved disaster risk management is one of the critical procedures to reduce the flood loss. An early flood warning system can also minimise the possible economic loss to a great extent.

Forecasting of flood events is a non-deterministic process in which uncertainty stems from different sources (Deletic et al., 2012). Significant success in flood forecast lies in the accuracy of weather forecast stations to predict the state of future atmospheric condition. However, the atmosphere is a non-linear and complex system, and it is, therefore, difficult to predict its exact state (Lorenz, 1969). Numerical weather forecasts are also inaccurate due to its limitation in representing atmospheric physics numerically and also because of the limited resolution of simulated atmospheric dynamics (Buizza et al., 1999; Kauffeldt et al., 2016). There are also inherent issues with hydrological model structures. For these reasons, hydrological model forecasts contain uncertainty in a great extent (Beven and Binley, 1992; Boyle et al., 2000; Refsgaard et al., 2007; Wani et al., 2017). Assessing uncertainty in the model results is an integrated part for hydrologic modelling and considered necessary in many scientific literatures specially when models are used for water management issues (Barbetta et al., 2017; Beven, 2002; Refsgaard et al., 2007, 2005; Todini, 2009; Vandenberghe et al., 2007). Disregarding its non-deterministic nature leads to disregarding events with lower probability (Leandro et al., 2013) which may already trigger warnings to specific sensitive areas.

Hydrological Ensemble Prediction System (widely known as HEPS or only EPS: Ensemble Prediction System) is one of the most practised methodologies to predict river flow. In this process, the system generates an ensemble of river flow forecasts for the same forecast period considering a range of probabilistic assessment of future river flow instead of only one projection. Several case studies are published in the literature indicating its decent performance in forecasting flood particularly in the case of issuing flood alert with more confidence (Cloke and Pappenberger, 2009). Due to the success of EPS in flood forecasting, several hydrological and flood forecasting centres now use EPS operationally or semi-operationally; such as European Flood Alert System (EFAS) (Thielen et al., 2005), Advanced Hydrologic Prediction Services from NOAA (Brown, 2014), Royal Meterological Institue of Belgium (Roulin, 2006), Météo France (Regimbeau et al., 2007), Bavarian Flood Forecasting Centre (Laurent et al., 2010) among others. The advantage of EPS forecasts that it can be instantly used for flood forecasting system.

Recent advances in computation power enable both hydrological connected with hydraulic modelling forecasts to improve forecast through data assimilation (Barthélémy et al., 2018; Costabile and Macchione, 2015; Madsen and Skotner, 2005). This method enables better forecasting through updating the model state, parameters, initial and boundary states at every forecast repetition and with more reliable model results. In the FloodEvac project, we develop a real-time flood forecasting tool which can forecast flood discharges and flood extents with the inclusion of uncertainties. The hydrological forecasting tool is connected to a 1D and 2D hydraulic modelling system to forecast the flood extent and flood depth in a more reliable way (Figure 7.1). In this work, we will focus on the hydrological forecast part of the FloodEvac tool. The tool can be utilised using ensemble-based prediction to consider both model input and model parameter uncertainties with forecast uncertainty. The current study explains the tool and its hydrological forecast efficiencies.

We also propose a new methodology to reduce forecast computational time. In a study by Wetterhall et al. (2013) showed that reporting past performance of the forecast systems is given the highest priority to the hydrologists, researchers and end users to evaluate the forecast performance of a hydrological model. In the current work, the proposed methodology is checked by hindcasting few historical flood events.

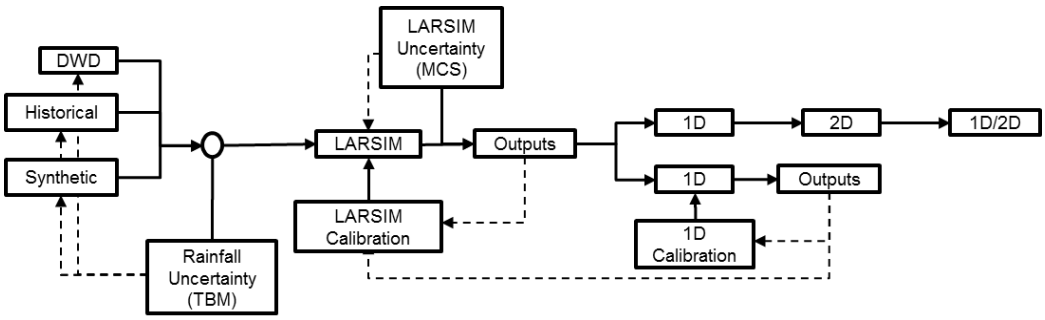

Figure 7.1: FloodEvac Tool and Model chain

7.3 The FloodEvac Tool

The FloodEvac tool is developed within the FloodEvac project funded by the *Bundesministerium für Bildung und Forschung* (BMBF, FKZ 13N13196 (TUM)). The tool allows the simulation of the rainfall-runoff process while including uncertainty from different sources (Figure 7.1). The tool can be run in simulation or forecast modus. The former is suitable for reproducing specific flood events or for the simulation of long time series (e.g. yearly). The latter is suitable for real-time flood forecasting. The model chain includes a rainfall uncertainty module, an uncertainty and calibration module for the hydrological model, and a link to several hydraulic models.

In the rainfall module, rainfall data can be introduced in three different ways: using 1) observed/forecast rainfall from German Meteorological Services (Deutscher Wetterdienst, DWD), 2) generated rainfall based on historical data, or 3) generated rainfall based on synthetic data. Uncertainty can then be added to catchment rainfall based on the sequential conditional simulation (Seo et al., 2014).

LARSIM (Large Area Runoff Simulation Model) is the conceptual hydrological model used in the tool. The hydrological processes are simulated in a series of subarea elements connected by flood routing elements in a predetermined sequence. The model simulates the hydrologic processes for one element for a defined period. The resulting output hydrograph is the input information for the next element according to the general model structure rules. The model structure can be both grids based or based on hydrologic sub-catchments.

The soil module consists of three storages: upper, middle and lower soil storage which contribute to the discharge components modelled as a linear storage system (Figure 7.2). It includes 34 parameters which allow modelling of different processes such as direct discharge, interflow and groundwater flow (please see (Haag et al., 2016) for a complete description of the parameters). The tool also includes a calibration module for LARSIM, based on the Shuffled Complex Evolution Algorithm (SCE-UA) (Deubler, 2017), which is widely used in hydrology for model calibration (Seong et al., 2015). In this module, it is possible to define the calibration and validation time windows, as well as the calibration parameters and ranges.

The final hydraulic module includes the linkage to the Hydro_AS-2D, a 2D fully dynamic model with the unstructured grid, from which the flood inundation extents are generated. Other possible linkages include MIKE 11, MIKE Urban and HEC-RAS 2D.

In forecast modus, the FloodEvac tool generates ensembles by sampling from LARSIM parameters using a beta or a normal probability distribution function. The beta function can produce skewed shapes of the distribution function, and hence take into account asymmetric uncertainty parameter intervals around the calibrated parameter set when generating the ensembles.

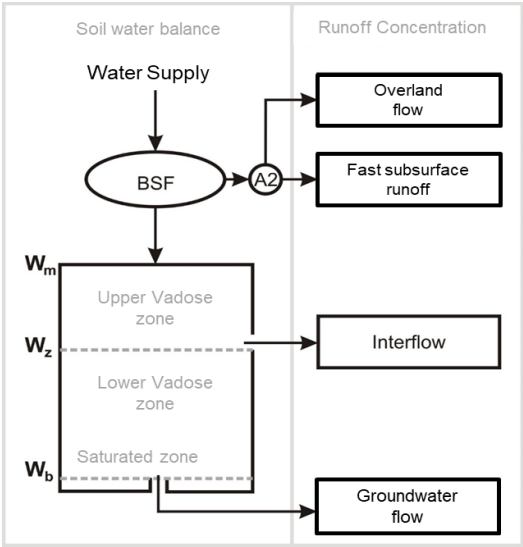

Figure 7.2: LARSIM water balance model

7.4 Pilot catchment and datasets

The FloodEvac tool was applied to the catchment area of the Upper Main located in Bavaria with a total area of 4244 km^2 (Figure 7.3). The topography of the area varies from 0 m to 1000 m above sea level.

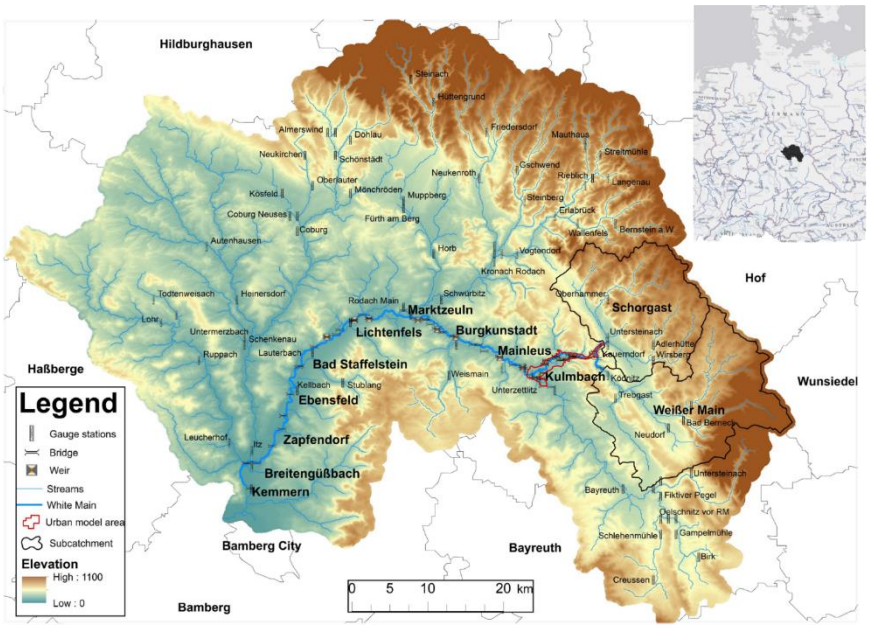

Figure 7.3: Case study: Upper-Main Catchment

Seventy-seven rain gauges were available in the study area. Historical data were available at each rain gauge from 2005 to 2015. The temporal resolution of the rainfall data was 1 hour. The data is collected by Deutscher Wetterdienst (DWD, German German Meteorological Office). There are

also 55 discharge measuring stations in the study area, whose data is also provided by DWD. Like the rainfall data, all the discharge data is available at every hour.

For the evaluation of the tool, we hindcast a flood event from December 2012.

In this work, we are hindcasting the flood discharge of December 2012-January 2013 to exemplify the forecasting tool. In the rest part of the paper, this event is referred to as 'Dec 2012' event (marked in red in Figure 7.4). For the hindcast process, the tool can utilise both forecasted and observed rainfall data. For the sake of simplicity, the actual DWD measured rainfall is used here as a forecast data. The considered flood event had two peaks on 24 and 28 December respectively. The discharge was recorded at the Ködnitz gauge situated just upstream of the city of Kulmbach. The two peak discharges were recorded as 64.2 m^3/s and 58.4 m^3/s on 24 and 28 December respectively. In this work, the uncertainty estimation in the forecast was done at two stages: a) rainfall (input) uncertainty and b) parameter uncertainty.

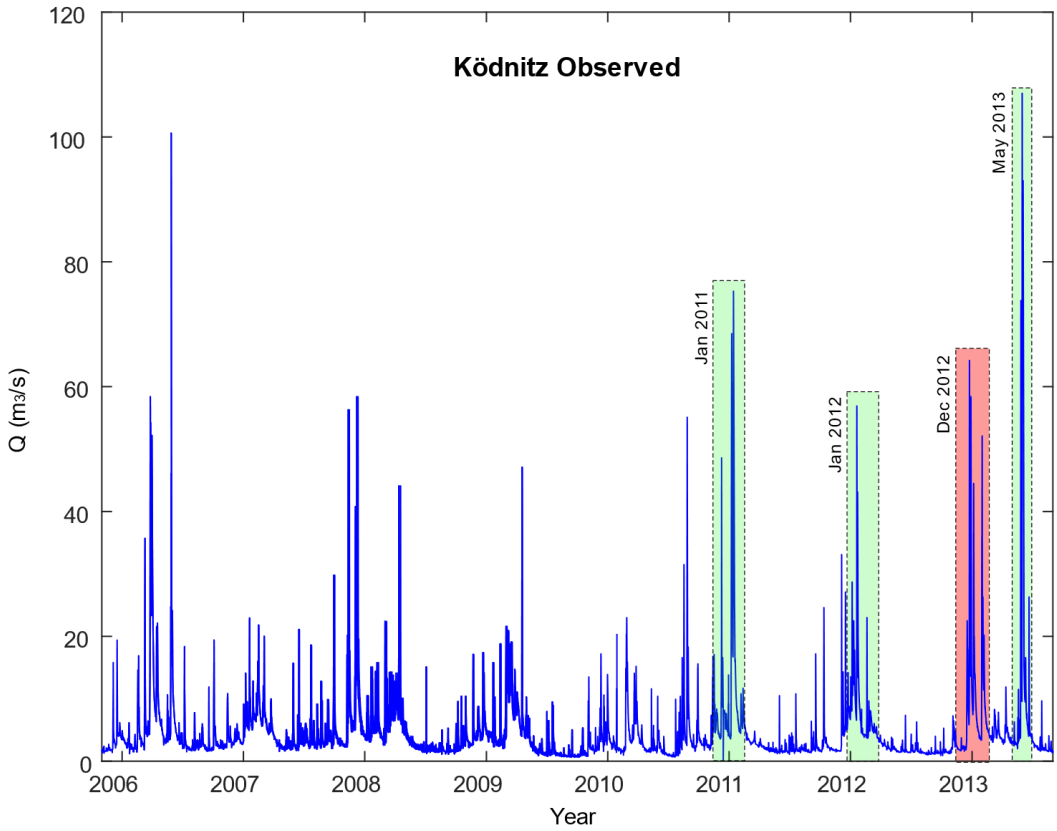

Figure 7.4: Historical observed discharge data at the Ködnitz gauge. The flood event marked with red shade was chosen for the analysis

In a latter part of the work (section 7.7), a new methodology is proposed to reduce the time required in the forecast process. For the new forecast methodology, the Dec 2012 event was used

as the calibration event. Three other events were hindcasted to validate the method. These flood events were during January 2011 (referred as 'Jan 2011' event), January 2012 (referred as Jan 2012 event) and May 2013 (referred as May 2013 event).

7.5 Methods

7.5.1 Generation of rainfall uncertainty

The rainfall uncertainty module checks observed or forecast rainfall data at the seventy-seven rain gauge stations and distribute the data within the whole catchment area considering sequential conditional geospatial simulation. The rainfall variable is considered as normally distributed and continuous. However, using geospatial simulation in case of precipitation has some challenges as due to zero precipitation (no rainfall) at some stations, the distribution is not normal but positively skewed. Moreover, the spatial distribution of rainfall is not constant but varies temporarily. For this reason, a proper mixed distribution is considered here using two variants. The discrete part of the distribution is empirically recorded via the proportion of zeros in the total sample, and the continuous part is mapped on the three-parametric gamma distribution as well as by a nonparametric nuclear density distribution considering *gammaMix* and *kdeMix*. The whole geostatistical simulation is implemented using two different R-packages, namely *gstat* (Gomez-Hernandez and Journal, 1993; Pebesma, 2004) and *RandomFields* (Schalather et al., 2015).

The LARSIM model takes input from distributed rainfall data for the catchment at a spatial resolution of 1 km x 1 km. For this work, ten rainfall simulation sets were considered to estimate the uncertainty of the spatial rainfall distribution. Figure 7.5 shows one example rainfall data on a certain wet day. The data shows ten different rainfall distribution simulation data along with the default rainfall data considered by the LARSIM model.

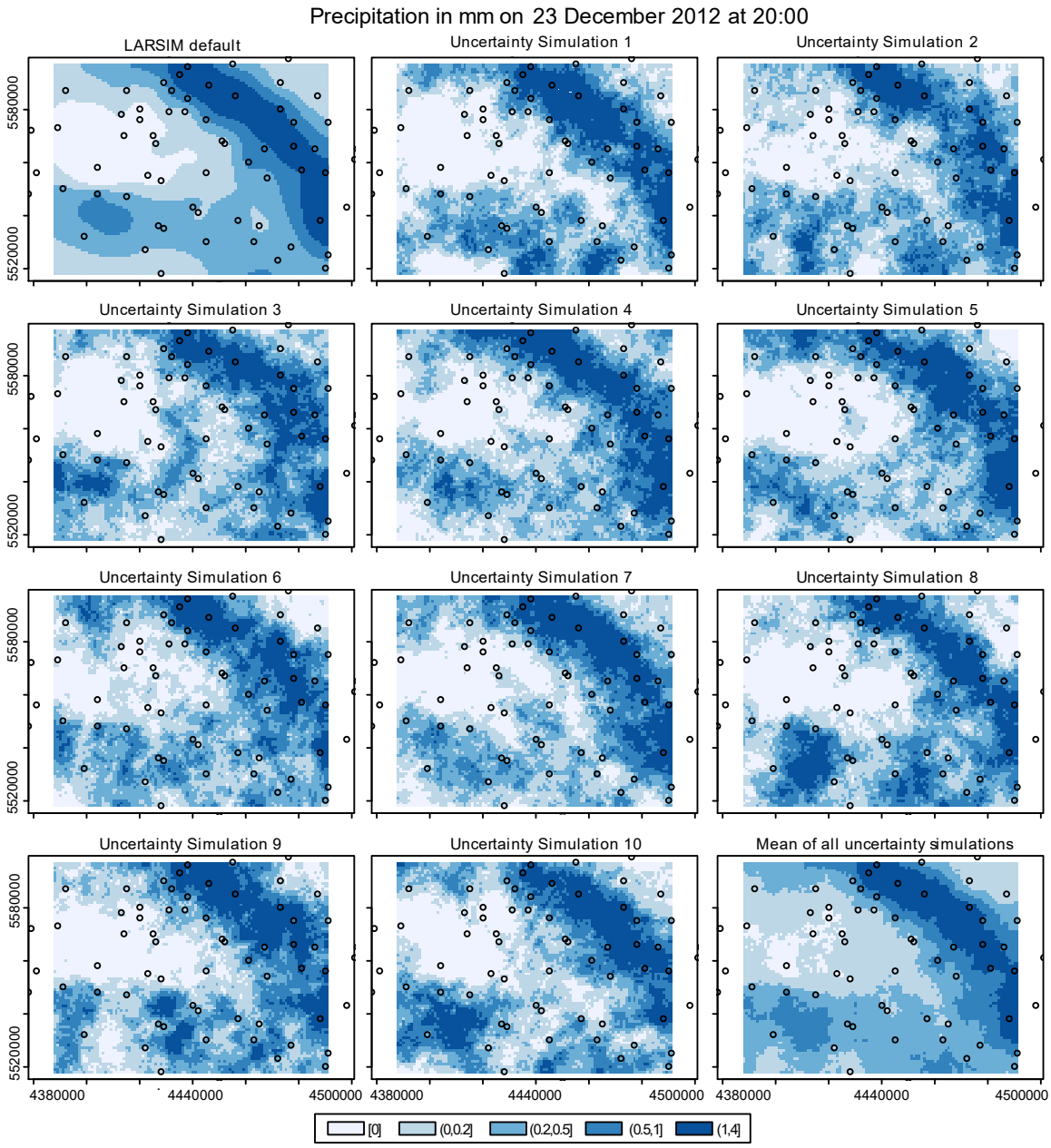

Figure 7.5: Uncertainty quantification of rainfall distribution

7.5.2 Generation of parameter uncertainty

The LARSIM model considers 34 different model parameters in calculating the rainfall runoff simulation. A sensitivity analysis was performed in LARSIM to derive the most sensitive parameters of the model regarding flood discharge at the upstream gages of Kulmbach (Ködnitz and Kauerndorf). Eight parameters were identified as most sensitive such as *EQD*: the index for lateral drainage to the lower soil storage, *beta*: the shape parameter of the soil-moisture – saturated-areas function, followed by *BSF*, *EQB*, *EQI*, *EQD2* and *Dmax* (Härder, 2017). In this work, only these parameters were considered for uncertainty analysis. In a next step, the original model (Haag et al., 2016) currently in use by the Flood Forecast Centre at Bayerisches Landesamt für

Umwelt (Bavarian Water Authorities) - LfU Bayern was compared with the one obtained using the automatic calibrated model. Since similar results were obtained between the original and the automated calibrated model, the original model was kept unchanged. The Upper Main catchment area has 81 sub-catchments. Each sub-catchment has its own set of calibrated model parameters. Different sets of parameters were generated for each sub-catchment and applied accordingly for the forecast runs. The ensembles were generated using Monte Carlo method. The parameters and intervals were selected based on the sensitivity analysis of each sub-catchment. Figure 7.6 shows the probability distribution curve for the eight selected parameters of a sub-catchment in the model area.

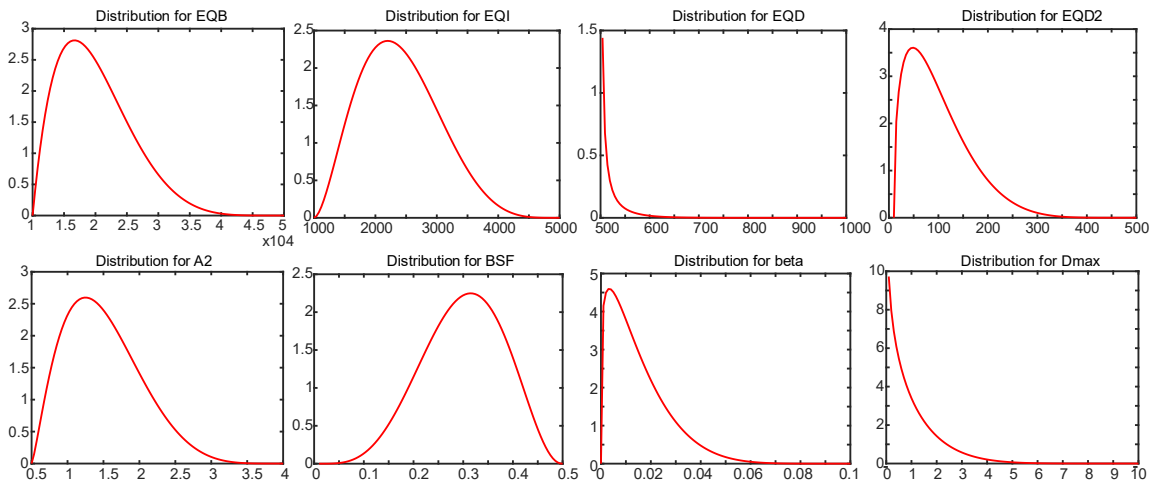

Figure 7.6: Probability distribution curve of the eight considered parameters at one sub-catchment

7.5.3 Forecast of flood discharge

Before the hindcasting process can start, a warm-up period is run. The model is run using observed precipitation and temperature data for one year of the warm-up period until 49 hours before the forecast initialisation time. At this stage, the model uses the previously calibrated parameters. The model results are saved in an '*initial state file*' at the end of the one-year warm-up simulation time. As such, we assure that the internal model states condition of the basins is as close as possible to the real conditions. Later, this initialisation state is used to simulate each forecast ensemble run. However, in the case of starting the simulation from an '*initial state file*', it is recommended to start the flood forecasting for at least 49 hours ahead of the initial time. Therefore, each forecast ensemble simulation was run for 63 hours; the first 49 hours of simulation results are deleted, and the last 12 hours of forecast data are stored. In this process, the model collects 49 hours of observed hourly rainfall followed by 12 hours of forecast rainfall data. These 63 hours of rainfall data are passed through the rainfall distribution uncertainty module, and ten different rainfall uncertainty datasets are prepared. Later, 50 different

parameter sets are produced using parameter uncertainty module. These 50 parameter uncertainty sets are combined with the ten rainfall uncertainty cases linking one rainfall uncertainty scenario with every five-parameter uncertainty sets in sequential order, making 50 sets of hydrological models for the Upper Main catchment. These 50 models are run, and the results of discharge datasets are saved. The total run time for completing this whole process was around 25 minutes in a three-core desktop in parallel mode.

As in this work, the actual measured rainfall data is used, which has a temporal resolution of one hour, the whole process was repeated at every one-hour interval. In the next forecast process, the model simulates new 50 cycles of 63 hours simulation, of which the first 48 hours are a repetition of previously done simulation; the 49th-hour data uses the latest available observed data and the last 12 hours data uses the new weather forecast. At this stage, the model uses the same parameter set which was generated at the first stage. Figure 7.7 shows the results of all the simulations for the flood discharge forecast at Ködnitz gauge point.

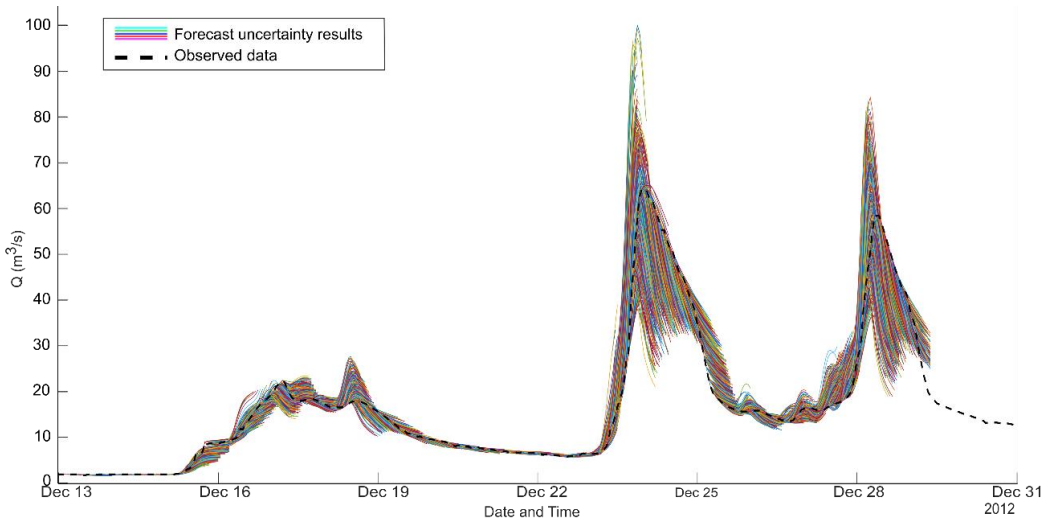

Figure 7.7: All forecast uncertainty results

7.6 Uncertainty analysis in the model results

The quality of the forecast data is assessed from each hourly lead of the forecast (Figure 7.8). It can be seen that the inconsistency between forecast and observed data increases with increasing forecast lead time. It is apparent that the model is excellent for forecasting flood up to 4 hours in advance. The difference between forecast and observed data at 5 or 6 hours lead time is comparably better than forecast data with lead time of 7 to 12 hours. The deviation of the simulated data from the observed is consistent at 9 to 12 hours lead time, which indicates that after a specific lead time, the error in forecast becomes stable and stops increasing.

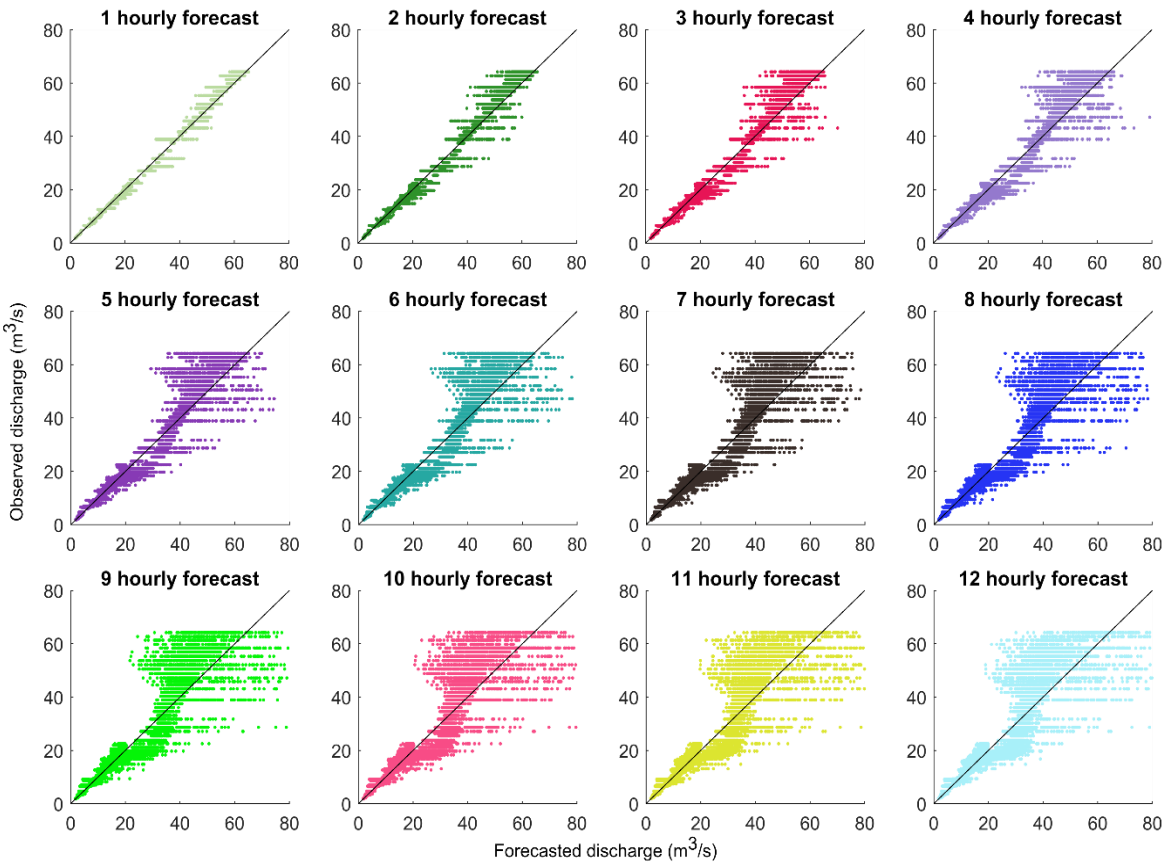

Figure 7.8: Scatter plots of observed vs simulated data for each hourly forecast leads

In assessing the uncertainty of the basin response to spatial and temporal rainfall distribution, confidence intervals are calculated. According to the procedure described above, each temporal result was forecast 12 times using 50 ensembles of uncertainty runs. In this way, each temporal result is predicted 600 times, which are used for the statistical assessments for each time step.

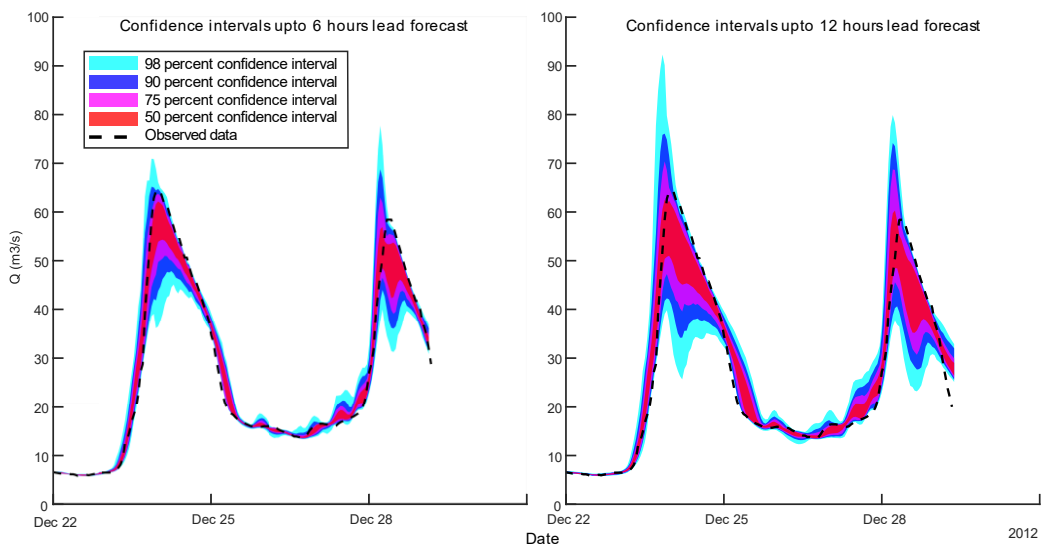

Figure 7.9: Confidence intervals in flood forecasting

A confidence interval chart is shown for all the simulated forecast data (Figure 7.9). We calculate the confidence intervals of the whole forecast data in two parts: considering a forecast lead time up to 6 hours and up to 12 hours. Comparing with the observed flood discharge of the area, it can be seen that the model can forecast the rising limb of the flood peak reasonably well. Both rising limbs of the observed flood discharge lie within the 50 percentiles of the simulated results at both 6 hours and 12 hours lead forecasts. The peak discharge predicted in the model simulation is slightly earlier than the actual flood peak time. However, the uncertainty interval of the model peak is found moderately high. The falling limb of the flood discharge is found within the 98 per cent confidence interval of the simulated discharges. The uncertainty is considerably lower at 6 hours lead forecast than that of 12 hours lead.

7.7 Towards reducing the forecast time requirement

This work was intended to check the effectiveness of the FloodEvac tool in real-time flood forecasting. The rainfall forecast is available at every hour. Considering this fact, it was intended to obtain forecast results within a considerable fraction of an hour. Due to available computational resources, this forecast was done using 50 uncertainty runs only; which took around 25 minutes. The forecast quality might have been improved if more uncertainty runs were used, however, that would require more coputational power. In this section, we propose another option to produce similar uncertainty bands of forecast within a shorter time period.

In this new proposed method, a pair of uncertainty ensembles is chosen within some predefined discharge intervals. Each possible pairs of uncertainty results are investigated to choose one pair of ensemble results that contains the maximum numbers of observation points within them. As the model receives observed discharge data at the time of forecast initialisation, the parameter ranges can be selected considering that discharge observed at that time. This methodology will be termed as “Discharge Interval method” for the rest of the article.

Considering the Discharge Interval method, we divide the observed discharge into seven segments with an interval of 10 m^3/s starting from 0 discharge. One pair of the ensemble is chosen for each segment based on the observed discharge at the forecast initiation time considering that the pair bounds the maximum numbers of observed discharge data. The observed discharge along with the results of these seven ensemble pairs are plotted in Figure 7.10.

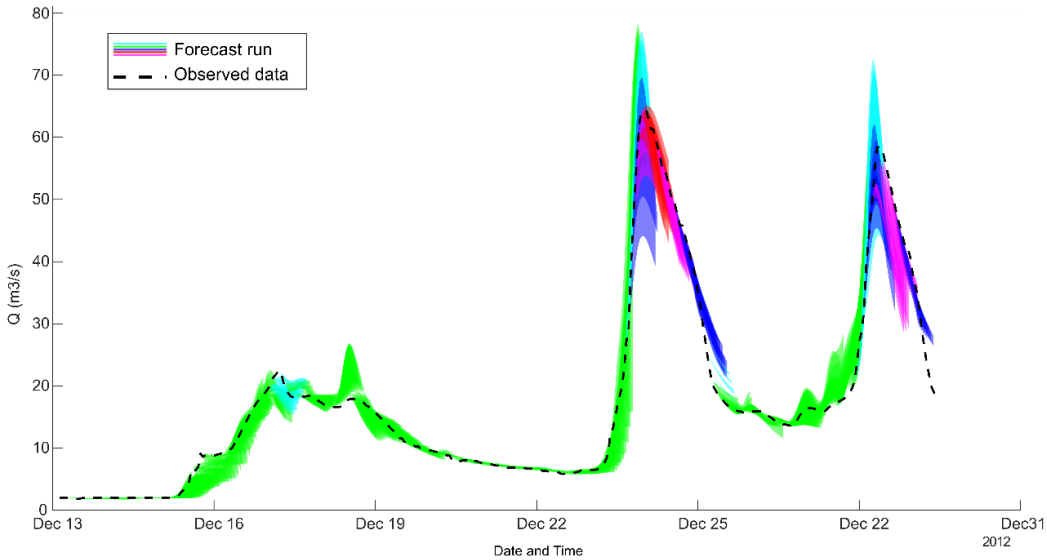

Figure 7.10: Observed discharge with updated forecasts using Discharge Interval method

In this proposed forecasting method, only one pair of uncertainty simulation run is required to predict the flood forecast within a given flood range. The ensemble pair can give a maximum and a minimum limit of flood discharge forecast. However, this method requires prior knowledge of the hydrological response in the catchment area before actual forecast, which can be obtained by running a large number of uncertainties based hindcast simulations. For the basis of validation, flood event of December 2012 was considered to choose flood ensemble pairs, and the applicability was checked for three other flood events.

7.8 Hindcasting other flood events

To check the effectiveness of the proposed Discharge Interval Method in the above section, we applied the methodology to hindcasting with three other flood event scenarios. The chosen three additional flood scenarios were (marked as green in Figure 7.4):

- Event 1: January 2011
- Event 2: January 2012
- Event 3: May 2013

For these cases, the hindcast was run using the traditional Monte Carlo method utilising the same combination as described in section 7.5.3 and later the seven ensemble pairs chosen from the December 2012 event were used to check if they can still be able to predict the forecast discharge at the Ködnitz gauge. The results are shown in Figure 7.11.

During the hindcast of January 2011, the observed discharge showed two peaks with a maximum discharge close to 80 m^3/s. However, hindcast ensembles predicted much higher peak discharge

(160 m^3/s). The seven pairs of selected ensembles showed qualitatively similar flood prediction. During the first flood peak between 6 to 12 January 2011, flood discharges were precisely forecasted using only a pair selected flood forecast ensemble at each hour. The rising limb, peak and the falling limb were accurately forecasted at this case. At the second peak discharge, the selected ensemble pairs showed a much faster rising and falling limb with a higher peak prediction than the observed.

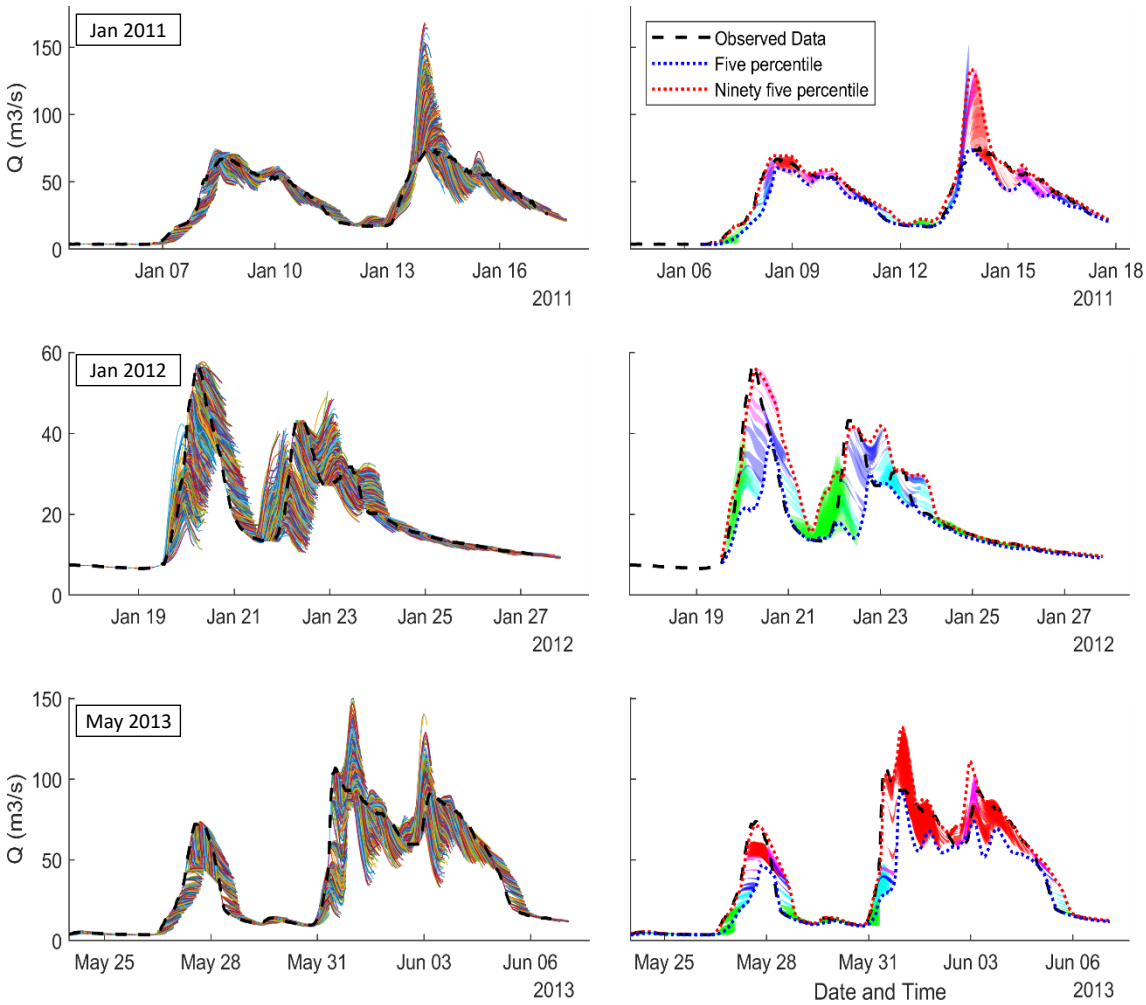

Figure 7.11: Hindcasting three events using traditional Monte Carlo (left panel) and the Discharge Interval method (right panel). The three flood events are January 2011 (top), January 2012 (middle) and May 2013 (bottom). The ninety percentile discharge forecasts from the MC method is shown with the Discharge Interval method data.

In the second flood event scenario of January 2012, selected flood ensemble pairs could not forecast the flood event with enough accuracy. The first flood peak hydrograph has a duration of two days, considering its time of rising, peak and retention time. During the rising of the flood discharge, the forecast model expects the flood to be reduced in all the hourly forecast data even before the observed discharge reaches its peak. The second peak discharge in this event had a

duration of nearly four days. The forecast model along with our selected forecast ensemble showed to some extent better performance. The peak discharge value was underpredicted at both peak flow. The forecast of the falling limb of this flood event was almost accurate.

In the third flood event, the observed discharge peak was found to be up to 120 m^3/s. The whole flood duration was eleven days. Like the other events, it also had two peak discharges. The traditional forecasting model underestimates the first peak but overestimates the latter one. Our proposed methodology for flood forecasting using selected ensemble pairs also followed the same trend. The selected flood ensemble could forecast the falling limb with much better accuracy.

In all the three events, the Uncertainty band of the proposed method gave almost similar uncertainty band comparable to the 90 percentile interval of the traditional Monte Carlo simulation results. Still, the time requirement for forecast was considerably small as it required only two ensemble prediction simulations to produce the uncertainty band. However, if the forecast is made using this procedure, the conventional uncertainty band calculation will not be possible.

7.9 Determining the forecast quality

To check the forecast quality, a likelihood table was constructed considering the forecasted discharge using both Monte Carlo approach as well as our proposed Discharge Interval method. The table was formed considering yes/no forecasts and yes/no observed discharge consideration after dividing the forecasted discharge range into several subgroups/discharge interval thresholds. Hindcasted discharge data and observed discharge at each hour were checked if they fall within a given threshold bin and a data table were prepared considering a “yes” if the data is below the given threshold and a “no” if the data is over the threshold. An example table is shown in Table 7.1. When both forecast and observed data shows “yes”, that is considered as a hit (a) and when both shows “no”, that is considered as another success (d) of the forecast. The other two conditions (b and c) are considered not success. After the likelihood table construction, hit ratio (=a/(a+b)) (also known as the probability of detection-yes or PODy) and false alarm ratio (=b/(b+d)) (also known as the probability of false detection or POFD) are counted for every discharge threshold considered. The results are represented as Receiver Operating Characteristics (ROC) (Liguori et al., 2012; Marzban, 2004; Mason and Graham, 2002) which describes the occurrence of hit and false alarm rate for a defined event, helping in crucial decision-making issues (Mason and Graham, 2002).

The area under the curve is a good indicator of the forecast quality and applied in many studies to assess the goodness of numerical forecasts (Mullen and Buizza, 2001; Murphy and Winkler, 1987;

Zhang and Casey, 2000). A good forecast is indicated by higher area under the curve which is more closer to the unity. If a forecast can predict a predefined event perfectly, the corresponding event would calculate a PODy = 1 and POFD = 0, and the point would be located at the left top corner of the plot. The first diagonal line represents the line of “No skill”. Whenever a point is located below the diagonal line, it is termed as worst scenario than no prediction. The computational method is not parametric without suggesting any hypothesis regarding probability distribution of the forecast. The ROC curve characteristics is however dependent to the number of discrete values used in creating the plot (Mason and Graham, 2002).

Table 7.1: Likelihood table for calculating a forecast category

Threshold Discharge = x	Observed Discharge <= x	Observed Discharge > x
Forecast Discharge <= x	a	b
Forecast Discharge > x	c	d

In the work, the forecast quality was assessed using the 5th and 95th percentile forecast data from the traditional Monte Carlo discharge ensembles. The Discharge Interval Method provides two discharge ensembles considering the upper and the lower bound of the forecasted discharge. Both ensembles were used to construct the ROC plots. The predefined discharge intervals were chosen at an interval of 5 m^3/s, starting from 0. Figure 7.11 shows one example ROC plots from hindcast results of all the four flood events each using all the four different forecast results with 6 hours of forecast lead.

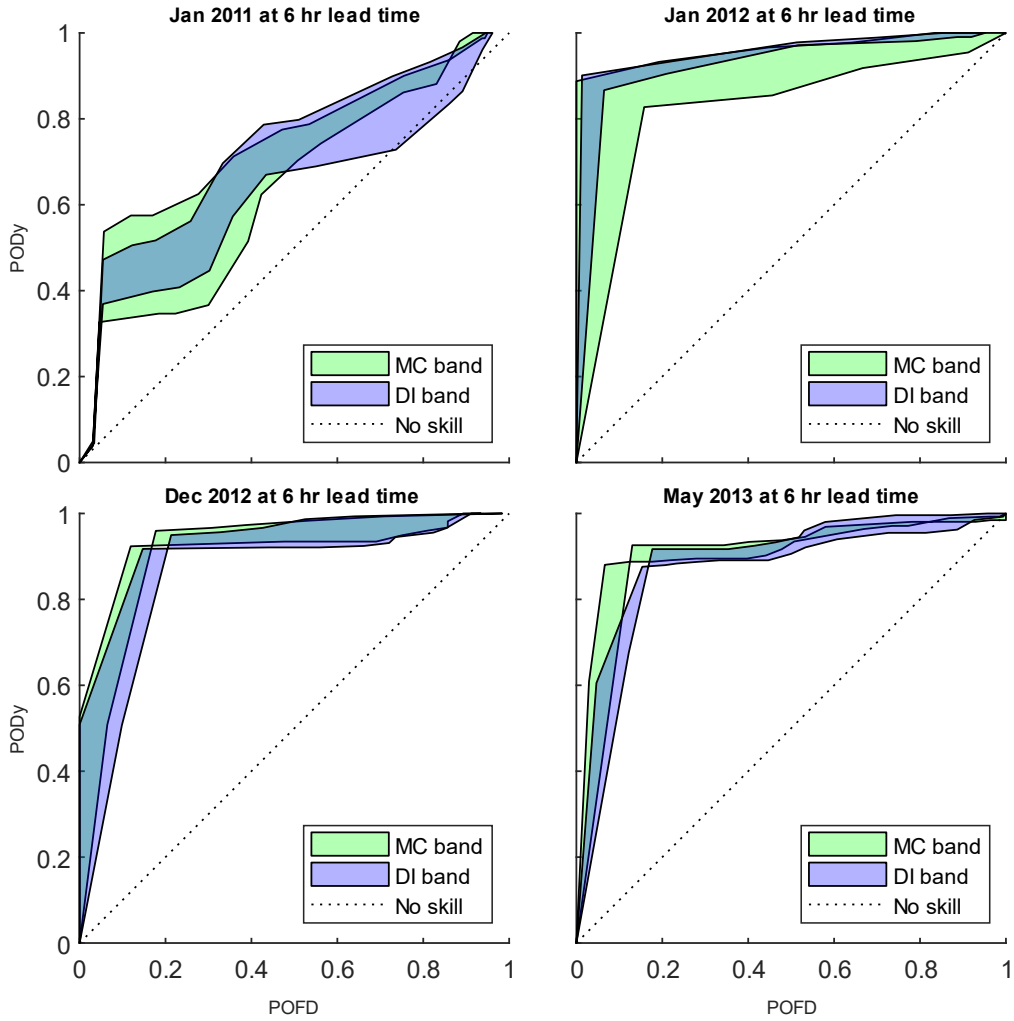

Figure 7.12: ROC plot of the four hindcasted events at 6 hrs lead time using Monte Carlo approach and Discharge Interval Method

From Figure 7.12 it can be seen that both the Monte Carlo method and the discharge interval method show almost similar forecast quality. However, out of the four events, the January 2011 event had the worst forecast quality in both Monte Carlo and Discharge Interval method. Forecasts of the other three events showed a better performance. At forecasting higher discharges, the PODy was much closer to the unity for the January 2012, December 2012 and May 2013 events. It can be more explained in Table 7.2 which shows the areas under the ROC curves for different forecasts. During the Dec 2012 and May 2013 events, the 95th percentile and the 5th percentile ensemble's ROC plot cross each other. The ROC plots check the forecast quality at specific discharge intervals. For a particular discharge interval, if observation and the 95th percentile fall in the same interval while the 5th percentile remains below, the 95th percentile will contribute to higher ROC area. It may change for another case where the 5th percentile and the observation may fall in the same category keeping 95th percentile outside. In that case, the 5th percentile will contribute to higher ROC area. For these reasons, the ROC plots may cross each

other. It indicates that either of the percentiles may not necessarily be the better than the other. Same condition is applicable to the upper and the lower bound forecasts of the Discharge Interval Method. In Table 7.2 all the average area under the ROC curve is presented. For the Monte Carlo ensemble method, the average area from 5th and 95th percentile is calculated and for Discharge Interval method, the averaged area between upper bound ROC and the lower bound ROC is considered.

Table 7.2: Average area under the ROC curve for all the four events with both forecasting methods and different forecast leads. MC refers to Monte Carlo; DI refers to Discharge Interval Method

		Forecast lead time (hr)											
Hindcast Event		1	2	3	4	5	6	7	8	9	10	11	12
Jan 2011	MC Ensemble	0.717	0.649	0.635	0.635	0.608	0.593	0.578	0.550	0.531	0.523	0.513	0.519
	DI Method	0.669	0.692	0.679	0.695	0.734	0.727	0.695	0.686	0.666	0.721	0.661	0.631
Jan 2012	MC Ensemble	0.825	0.841	0.934	0.940	0.952	0.963	0.954	0.944	0.955	0.932	0.908	0.908
	DI Method	0.775	0.843	0.882	0.871	0.875	0.920	0.892	0.927	0.912	0.905	0.921	0.926
Dec 2011	MC Ensemble	0.869	0.868	0.906	0.913	0.916	0.917	0.929	0.941	0.949	0.954	0.961	0.956
	DI Method	0.893	0.893	0.912	0.923	0.884	0.882	0.857	0.833	0.823	0.823	0.806	0.814
May 2013	MC Ensemble	0.843	0.873	0.875	0.879	0.904	0.904	0.903	0.903	0.909	0.907	0.909	0.895
	DI Method	0.875	0.869	0.882	0.901	0.890	0.872	0.872	0.868	0.874	0.861	0.858	0.859

Comparing the two forecast bands, we can see that the ROC curve areas at both two forecast methods are very close to each other. The flood events of January 2012, December 2012 and May 2013 forecasts had ROC curve area between 0.85 and 0.95. These results show that the predictability of discharge decreases slightly with forecast lead.

Table 7.2 also shows the fact that the forecast data provided by the Discharge Interval Method is qualitatively like that of the traditional Monte Carlo Method. The forecast band provided by this method can be comparable to the 90th percentile interval of the Monte Carlo method. This indicates that the Discharge Interval Method can compute very fast forecast data with reliable accuracy.

7.10 Conclusions

The work can be summarised as follows:

- In this work, we present real-time flood forecasting using FloodEvac tool. The tool was applied to the LARSIM hydrological model. The tool utilises observed and forecasted weather predictions to generate real-time flood discharge hydrograph.
- The FloodEvac tool considers both input uncertainty and parameter uncertainty in simulating flood scenario ensembles. It creates rainfall distribution uncertainty scenarios

using geospatial simulations and parameter uncertainty scenarios considering Monte Carlo simulations and provides the combinations of scenarios to a hydrological model to generate flood discharge ensembles.

- The tool was applied to hindcast flood at the city of Kulmbach located at the catchment of Upper Main river. In this case study, the tool effectively hindcasted a flood event of December 2012-January 2013. The tool was found useful to predict flood discharge with 12 hours of lead time.
- This work utilises 50 Monte Carlo based hydrological ensemble simulations to describe the results. The total number of ensembles which can be generated in forecasting mode is limited by the available computation time. In any case, a more significant number of ensembles could be used depending on of available computation power.
- A new flood forecast methodology has been proposed, namely Discharge Interval method, which selects best forecast ensemble pairs considering hindcast model results and use the selected ensembles to create flood forecast data. The ensemble pair provides an upper and lower limit of the flood discharge forecast.
- The new proposed forecasting methodology is very fast as it runs only a pair of ensemble simulations for the forecast. However, this method is unable to produce any confidence interval band estimations in the forecast scenarios.
- ROC plots of the Monte Carlo based ensembles and Discharge Interval Methods showed that the latter methodology can deliver qualitatively similar forecast data when compared with the data provided by the former.

7.11 Acknowledgements

The tool is developed within the FloodEvac project funded by the Bundesministerium für Bildung und Forschung (BMBF, FKZ 13N13196 (TUM)). The first author would also like to acknowledge to QUICS project. QUICS has received funding from the European Union’s Seventh Framework Programme for research, technological development and demonstration under grant agreement no 607000.

CHAPTER 8
FINAL REMARKS

8.1 Conclusions

The work presented in this thesis was carried out to analyse uncertainty in a) hydraulic modelling of drainage structures and b) hydrological modelling of a catchment. Uncertainty in the hydraulic modelling was investigated through laboratory measurements of gully and manhole using ADV and Stereo PIV respectively. The measured data were used to validate CFD models, and later the validated CFD models were utilised to check uncertainties in calculating head loss coefficients for manhole and discharge coefficients of the gully. Uncertainty in hydrological modelling was studied using LARSIM rainfall-runoff model, which was used for forecasting flood discharge of the city of Kulmbach in Germany. Input and parameter uncertainties of the hydrological modelling were studied at this part.

Chapter 2 provides a literature review on the hydraulics of urban structures drainage flow, the importance of modelling manholes and gullies using three-dimensional models, procedures and practices of flow measurements in manholes/gullies and general code description of VOF based modelling using OpenFOAM®. The chapter also reviews the uncertainty investigation steps in hydrological models and describes the steps taken in this research in assessing uncertainties in both hydraulic and hydrological modelling. From the literature, it was identified that CFD with VOF modelling is one of the most popular numerical procedures for free surface modelling.

Chapter 3 describes flow measurement techniques at a scaled experimental model using Stereo PIV. The measurement was carried out at the hydraulic laboratory of the University of Sheffield. The manhole used was a 1:6 Froude scaled inline manhole, which does not have any benching or sump zone. Three different vertical planes were illuminated using Nd:YAG pulsed laser and the flow velocities were simultaneously recorded using two cameras. Data were measured at the different inflow and surcharge conditions. The mean velocity and turbulence characteristics were analysed. The manhole flow was found to be sub-divided in three different zones: core zone, diffusion zone and dead zone. The core zone was seen to change its size and location with the changing inflow, while the diffusive zone was found to be controlled by the surcharge level of the

manhole. The experimental datasets were further used to compare and validate with the CFD model data.

Chapter 4 compares stereo PIV data with different VOF based CFD models. For this work, four different CFD models were constructed using different RANS modelling approaches by replicating the scaled manhole model as discussed in Chapter 3. The numerical model was compared with pressure measurements at the inlet and the outlet pipes as well as the measured velocity fields at the manhole. The appropriate mesh size to represent the flow was calculated following recommended mesh analysis procedure. Results showed that RNG k-ε and SST k-ω models have almost similar result quality and perform better then Realizable k-ε and LRR models while representing water level and velocity of a surcharged manhole. In contrast to RNG k-ε, SST k-ω model requires very small mesh size at the wall zone ($y+ < 5$), making the computational cost significantly higher. For this reason, RNG k-ε model was considered appropriate choice to represent the manhole flow at surcharge conditions.

Chapter 5 analyses the surcharge effect on a full-scale manhole and gully using CFD model and experimental measurements. Laboratory setup at the University of Coimbra was utilised for this work. The manhole was an unbenched inline manhole with a sump zone. The CFD modelling procedure applies RNG k-ε and Standard k-ε for modelling the manhole and the gully flow respectively. The numerical results were compared with discharge and pressure measurements from the experimental manhole model and ADV point velocity measurements at the gully. The CFD model showed good performance against measured data. The CFD model was further applied to check gully discharge coefficients and manhole head loss coefficients at different surcharge conditions. The flow through the gully was found to follow the orifice equation. The surcharge level of the manhole was divided into three zones for which the gully discharge coefficients show different values. The manhole head loss coefficients were analysed for different inflow and surcharge levels. Results showed that the manhole has a threshold surcharge level which is approximately 20% of the manhole diameter. Below that surcharge, the manhole head loss shows very high value, and over this surcharge, the head loss was found comparably small and stays around 0.30.

Chapter 6 applies the CFD modelling procedure knowledge, gathered from the previous chapters to investigate head loss coefficients at different full-scale manholes. Different manhole mould types and manholes with very small bending angles between the inlet and the outlet pipes were investigated. Three different common manhole mould designs were chosen, of which the first and the second types (Type A and Type B) were unbenched manholes having a sump and without sump zones while the third type (Type C) was a benched manhole. Results showed that Type A has the highest and Type C has the lowest head loss coefficients at all surcharge and inflow conditions.

The threshold surcharges at Type A and B were found to be around 20% of the manhole diameter while at Type C, the threshold surcharge rises to 33%. Type A manhole was further examined to check the effect of bending between inlet and outlet pipes. The analysed head loss vs surcharge plot showed two different characteristics. At very small bending angles, the core jet velocity zone can flow out through the outlet pipe without hitting the opposite manhole wall. At these cases, the threshold surcharge level remains the same as straight through manhole; however, the head loss coefficient increases at high surcharge conditions. At higher bending angles, the core velocity cannot pass through the outlet pipe and becomes discontinued. At these cases, the threshold surcharge was found to increase. The effect of manhole to inlet pipe ratio was also analysed on the same manhole type. The results showed the existence of two different hydraulic regimes. At small manholes ($Ø_m/Ø_p \leq 3$) the head loss coefficients increase with the increasing manhole to pipe ratios. These manholes do not show any existence threshold surcharge; the head loss was found almost the same with increasing surcharge conditions. Bigger manholes ($Ø_m/Ø_p > 3$), also show increasing head loss coefficients with increasing manhole to pipe ratios; however, in contrast to the small diameter manholes, they show a clear threshold region. The head loss is significantly higher at the below threshold surcharge.

Chapter 7 deals with the hydrological modelling uncertainty in a rainfall-runoff model LARSIM. A flood forecasting tool was developed for the LARSIM model which can make automated flood forecast with possible uncertainty estimation. The tool collects observed or forecasted rainfall data from different point gauge rainfall stations and make different interpolations throughout the catchment area using different geospatial simulations. The parameter uncertainty part considers 34 different model parameters for each sub-catchment. Each parameter is given with a maximum, minimum and pre-calibrated parameter value. The model makes a Gaussian or Beta distribution and generates new parameter sets using Monte Carlo method. These parameter sets are combined with generated rainfall distribution data. Later, each combination is utilised to simulate LARSIM model and generate forecasted discharge ensemble. The tool was applied to hindcast four different flood events. It was found that the tool can hindcast the flood discharge effectively. Another new methodology was proposed named as 'Discharge Interval Method'. In this method, the model chooses only a pair of ensemble simulations instead of running many, based on at least one previously simulated hindcast event data. Analysis showed that the forecast quality of this proposed method is comparable to the 90-percentile forecasted discharge band of the Monte Carlo based forecast.

8.2 Research Questions

In Chapter 1, three questions were presented to be discussed in the thesis. Answers to these questions and how these answers are obtained in this PhD thesis, is discussed below.

Q1: What are the uncertainty sources in modelling urban drainage flow related to hydraulic structures such as manholes or street gullies?

A1: The question is answered through a review of literature on manhole and street gully. It is apparent that the governing equations used in the mathematical modelling of urban drainage flow is unable to replicate the flow physics of a drainage structure as the structures contain the more complex three-dimensional flow. Theoretically, it is possible to model a drainage structure such as manhole and gully separately using a three-dimensional CFD model, by resolving all (or certain level of) spatial and temporal scales of flow physics and couple it to a drainage flow model. However, this is still ambitious and might be considered an impractical task as it will be too time-consuming considering the current development of computational power. This results in choosing the remaining option to use empirical equations of different coefficients and use them in the flow model. The values of these coefficients are very much case dependent and using a generalised coefficient is the primary source to create uncertainty in the drainage flow model.

Q2: How to reduce the uncertainty caused by the non-representation of the hydraulic structures and their 3D effects on the flow?

A2: To answer this question, a series of experimental and numerical simulations were conducted during the PhD research. Prototype scale interface tracking VOF model of manhole and gully was developed, and modelled data was validated with measured velocity, discharge and pressure/water level. Out of the numerous manhole head loss controlling factors mentioned in the literature, only a few could be addressed in this thesis. The examined factors were different manhole types, variation in manhole surcharge, small changes in manhole inlet orientation and changes in manhole to inlet pipe diameter ratios. For gully, the examined discharge coefficient controlling factor was water level condition at the gully outlet. Three different gully discharge coefficients were proposed for three different water level condition of the gully outlet. A matrix of manhole head loss values at different cases were also proposed. Using different values at the different situation may reduce the uncertainty in considering the effects of hydraulic structures in the flow. However, in cases where accuracy is an essential issue, a specific study using 3D model (experimental or numerical) may be necessary. Nevertheless, with the increase in computational power in the near future, it might be more feasible to apply 1D/3D sewer network models to allow 3D calculation for the hydraulic structures and simplified 1D calculation for the piped network.

Q3: How to quantify the uncertainty in flood discharge forecasting so that the predicted discharge can be used more reliably for drainage flow model?

A3: This research question is answered by developing a tool that can consider rainfall input uncertainties in combination with hydrological model parameter uncertainties to create

ensemble-based discharge forecast. The tool was applied using LARSIM model at the city of Kulmbach located in the catchment of Upper Main river. The tool was found to be efficient in hindcasting historical flood events with reasonable accuracy. A new methodology named Discharge Interval Method is proposed in this study. The proposed method makes real-time flood forecasting much less computationally expensive with consistent accuracy. The tool can be coupled with urban drainage models to ensure more reliable boundary data for forecasting possible inundation.

8.3 Future works

This research aimed at reducing and quantifying uncertainty in modelling of urban drainage systems by better predicting flow through the drainage structures and model boundary conditions. For the flow through structures, the focus was given to inline manhole head losses to find their values at various structural and hydraulic changes. Different values of gully discharge coefficients were also explored due to change in the hydraulic condition of the gully flow. However, complex scenarios of manholes such as cases where more than two drainage pipes connect, could not be explored due to time constraints. Regarding gully flow, discharge coefficients related to variations in gully structural moulds and outlet pipe orientations was not assessed in this research. Some literature also explained variations in gully deposit at different seasons; which might also constrain the gully outlet flow and govern to the discharge coefficient values. They need to be addressed to quantify gully discharge uncertainty. The results of manhole head loss coefficients and gully discharge coefficients need to be added to a dual drainage model with consideration of uncertainty in their values. The uncertainty of water quality modelling in urban drainage systems is also an important issue, which is currently being explored focusing solute and particulate transport in the drainage flow at the multiphase flow.

In future research, the urban drainage model could be coupled to the hydrological model, so that the flow uncertainty could be directly incorporated to the hydraulic modelling uncertainty as well as a forecast of possible local flooding inundations could be assessed.

Considering all these, the following tasks are proposed for the next steps of the research.

Research related to modelling of the urban drainage structures:

- The uncertainty of gully discharge coefficients related to change in gully outlet orientation and manholes with several pipes crossing
- The uncertainty of gully discharge coefficients related to the different amount of sediments and trash
- Water quality modelling for the urban drainage structures

- Implement manhole head loss coefficients to 1D network model with added uncertainty estimation

Research related to hydrological model

- Coupling of a hydro-dynamic model for forecasting urban drainage inundation with consideration of uncertainty in the results.

REFERENCES

Ackers, J., Butler, D., Leggett, D., May, R., 2001. Designing Sewers to Control Sediment Problems, in: Urban Drainage Modeling. American Society of Civil Engineers, Reston, VA, pp. 818–823. https://doi.org/10.1061/40583(275)77

Ackers, P., 1959. An investigation of head losses at sewer manholes. Civ. Eng. Public Work Rev. 54, 882–884.

Adrian, R.J., 1997. Dynamic ranges of velocity and spatial resolution of particle image velocimetry. Meas. Sci. Technol. 8, 1393–1398. https://doi.org/10.1088/0957-0233/8/12/003

Adrian, R.J., 1986. Image shifting technique to resolve directional ambiguity in double-pulsed velocimetry. Appl. Opt. 25, 3855–3858. https://doi.org/10.1364/AO.25.003855

Adrian, R.J., Westerweel, J., 2011. Particle Image Velocimetry, 1st ed. Cambridge University Press, Cambridge, New York.

Albertson, M.L., Dai, Y.B., Jensen, R.A., Rouse, H., 1950. Diffusion of Submerged Jets. Am. Soc. Civ. Eng. 115, 639–664.

Alvarez-Harnandez, E.M., 1990. The influence of cohesion on sediment movement in channels of circular cross-section. PhD Thesis. University of Newcastle upon Tyne.

ANSYS Inc, 2013. ANSYS Fluent Theory Guide, ANSYS Inc., USA. Canonsburg, PA, USA.

ANSYS Ins, 2009. ANSYS Fluent 12.0 User ’s Guide. https://doi.org/10.1111/j.1600-0447.2011.01711.x

Arao, S., Hiratsuka, S., Kusuda, T., 2013. Formula on Energy losses at three-way circular drop manhole under surcharge flow (in Japanese). J. Japan Soc. Civ. Eng. Ser. B1 (Hydraulic Eng. 69, 105–122. https://doi.org/10.2208/jscejhe.69.105

Arao, S., Kusuda, T., 1999. Effects of pipe bending angle on energy losses at two-way circular drop manholes, in: 8th International Conference on Urban Storm Drainage. 8th International Conference on Urban Storm Drainage, Sydney, Australia, pp. 2163–2168.

Arao, S., Kusuda, T., Moriyama, K., Hiratsuka, S., Asada, J., Hirose, N., 2012. Energy losses at three-way circular drop manholes under surcharged conditions. Water Sci. Technol. 66, 45–52. https://doi.org/10.2166/wst.2012.164

Archer, B., Bettes, F., Colyer, P.J., 1978. Head losses and air entrainment at surcharged manholes. Wallingford, England.

Arnbjerg-Nielsen, K., 2011. Past, present, and future design of urban drainage systems with focus on Danish experiences. Water Sci. Technol. 63, 527–535. https://doi.org/10.2166/wst.2011.253

Arnbjerg-Nielsen, K., Willems, P., Olsson, J., Beecham, S., Pathirana, A., Bülow Gregersen, I., Madsen, H., Nguyen, V.T.V., 2013. Impacts of climate change on rainfall extremes and urban drainage systems: A review. Water Sci. Technol. 68, 16–28. https://doi.org/10.2166/wst.2013.251

Ashley, R.M., Bertrand-Krajewski, J.-L., Hvidtvej-Jacobsen, T., Verbanck, M. (Eds.), 2004. Solids in Sewers: Characteristics, effects and control of sewer solids and associated pollutants, 1st ed. IWA Publishing. Scientific and Technical Report n° 14, May 2004, London.

Ashley, R.M., Crabtree, R.W., 1992. Sediment Origins, Deposition and Build-Up in Combined Sewer Systems. Water Sci. Technol. 25, 1–12. https://doi.org/10.2166/wst.1992.0173

Asztely, M., 1995. Literature Review of Energy Losses in a Manhole. Chalmers University of Technology, Goteborg.

Barbetta, S., Coccia, G., Moramarco, T., Brocca, L., Todini, E., 2017. The multi temporal/multi-model approach to predictive uncertainty assessment in real-time flood forecasting. J. Hydrol. 551, 555–576. https://doi.org/10.1016/j.jhydrol.2017.06.030

Barnhart, D.H., Adrian, R.J., Papen, G.C., 1994. Phase-conjugate holographic system for high-resolution particle-image velocimetry. Appl. Opt. 33, 7159–7170. https://doi.org/10.1364/AO.33.007159

Barthélémy, S., Ricci, S., Morel, T., Goutal, N., Le Pape, E., Zaoui, F., 2018. On operational flood forecasting system involving 1D/2D coupled hydraulic model and data assimilation. J. Hydrol. 562, 623–634. https://doi.org/10.1016/j.jhydrol.2018.05.007

Bazin, P.-H., Nakagawa, H., Kawaike, K., Paquier, A., Mignot, E., 2014. Modeling Flow Exchanges between a Street and an Underground Drainage Pipe during Urban Floods. J. Hydraul. Eng. 140, 04014051. https://doi.org/10.1061/(ASCE)HY.1943-7900.0000917

Beg, M.N.A., Carvalho, R., Lopes, P., Leandro, J., Melo, N., 2016a. Numerical Investigation of the Flow Field inside a Manhole-Pipe Drainage System, in: Crookston, B., Tullis, B. (Eds.), Hydraulic Structures and Water System Management. 6th IAHR International Symposium on Hydraulic Structures. Utah State University, Portland, Oregon, USA, pp. 1–11. https://doi.org/10.15142/T370628160853

Beg, M.N.A., Carvalho, R.F., Leandro, J., 2018. Effect of surcharge on gully-manhole flow. J. Hydro-environment Res. 19, 224–236. https://doi.org/10.1016/j.jher.2017.08.003

Beg, M.N.A., Carvalho, R.F., Leandro, J., 2017a. Comparison of flow hydraulics in different manhole types, in: Ghani, A.A. (Ed.), Managing Water for Sustainable Development: Learning from the Past for the Future: Proceedings of the 37th IAHR World Congress. IAHR & USAINS HOLDING SDN BHD, Kuala Lumpur, Malaysia, pp. 4212–4221.

Beg, M.N.A., Carvalho, R.F., Leandro, J., Lopes, P., Cartaxo, L., 2016b. Investigation of the Flow Field inside a Drainage System : Gully - Pipe - Manhole, in: International Junior Researcher and Engineer Workshop on Hydraulic Structures. Utah State University, Lübeck, Germany, pp. 1–11. https://doi.org/10.15142/T3859Z

Beg, M.N.A., Carvalho, R.F., Tait, S., Brevis, W., Rubinato, M., Schellart, A., Leandro, J., 2017b. A comparative study of manhole hydraulics using stereoscopic PIV and different RANS models. Water Sci. Technol. 87–98. https://doi.org/10.2166/wst.2018.089

Begum, S., Rasul, M., Brown, R., 2008. A comparative review of stormwater treatment and reuse techniques with a new approach: Green Gully. WSEAS Trans. Environ. Dev. 4, 1002–1013.

Bennett, P., 2012. Evaluation of the Solute Transport Characteristics of Surcharged Manholes using a RANS Solution. PhD Thesis. University of Sheffid.

Berberović, E., van Hinsberg, N.P., Jakirlić, S., Roisman, I. V., Tropea, C., 2009. Drop impact onto a liquid layer of finite thickness: Dynamics of the cavity evolution. Phys. Rev. E 79, 036306. https://doi.org/10.1103/PhysRevE.79.036306

Bertrand-Krajewski, J.-L., 2006. Modelling of Sewer Solids Production and Transport, in: Hydrologie Urbaine. Laboratoire Hydrologie Urbaine, INSA de Lyon, Lyon, France, p. 39.

Beven, K., Binley, A., 1992. The future of distributed models: Model calibration and uncertainty prediction. Hydrol. Process. 6, 279–298. https://doi.org/10.1002/hyp.3360060305

Beven, K.J., 2002. Towards a coherent philosophy for environmental modelling. Proc. R. Soc. A Methematical, Phys. Eng. Sci. 458, 2465–2484. https://doi.org/10.1098/rspa.2002.0986

Biron, P., Best, J.L., Ror, A.G., 1996. Effects of Bed Discordance on Flow Dynamics At Open Channel Confluences. J. Hydraul. Eng. 2, 676–682.

Bo Pedersen, F., Mark, O., 1990. Head losses in sewer manholes: Submerged Jet Theory. J. Hydraul. Eng. 116, 1317–1328.

Boyle, D.P., Gupta, H. V., Sorooshian, S., 2000. Toward improved calibration of hydrologic models: Combining the strengths of manual and automatic methods. Water Resour. Res. 36, 3663–3674. https://doi.org/10.1029/2000WR900207

Brackbill, J.U., Kothe, D.B., Zemech, C., 1992. A continuum method for modeling surface tension. J. Comput. Phys. 100, 335–354. https://doi.org/10.1016/0021-9991(92)90240-Y

Brennan, D., 2001. The Numerical Simulation of Two-Phase Flows in Settling Tanks. PhD Thesis. University of London.

Brown, J., 2014. Verification of temperature, precipitation and streamflow forecasts from the Hydrologic Ensemble Forecast Service (HEFS) of the US national weather service.

Brown, S.A., Schall, J.D., Morris, J.L., Doherty, C.L., Stein, S.M., Warner, J.C., 2013. Urban Drainage Design Manual, Hydraulic Engineering Circular 22, Third Edition. Washington D. C.

Buizza, R., Miller, M., Palmer, T.N., 1999. Stochastic representation of model uncertainties in the ECMWF Ensemble Prediction System. Q. J. R. Meteorol. Soc. 125, 2887–2908. https://doi.org/10.1256/smsqj.56005

Burgi, P.H., Gober, D.E., 1978. Hydraulic and safety characteristics of selected grate inlets. Transportation Research Board Session 43, Denver, Colorado

Butler, D., Davies, J.W., 2011. Urban drainage, 3rd ed, Taylor & Francis. Spon Press, London.

Butler, D., Karunaratne, S.H.P.G., 1995. The suspended solids trap efficiency of the roadside gully pot. Water Res. 29, 719–729. https://doi.org/10.1016/0043-1354(94)00149-2

Butler, D., Memon, F.A., 1999. Dynamic modelling of roadside gully pots during wet weather. Water Res. 33, 3364–3372. https://doi.org/10.1016/S0043-1354(99)00050-0

Butler, D., Xiao, Y., Karunaratne, S.H.P.G., Thedchanamoorthy, S., 1995. The gully pot as a physical, chemical and biological reactor. Water Sci. Technol. 31, 219–228. https://doi.org/10.1016/0273-1223(95)00339-O

Carvalho, R., Páscoa, P., Leandro, J., Abreu, J., Lopes, P., Quinteiro, R., Lima, L.M.P.L., 2013. Experimental investigation of the linking element gully - drop manhole, in: Proceedings of 35th IAHR World Congress 2013. 35th IAHR World Congress 2013.

Carvalho, R.F., 2015. ADV data processing. (Presentation) http://www.civil.ist.utl.pt/~ruif/SUMMER_SCHOOL/presentations/Seditrans_ADV_RCarvalho.pdf

Carvalho, R.F., Leandro, J., 2012. Hydraulic Characteristics of a Drop Square Manhole with a Downstream Control Gate. J. Irrig. Drain. Eng. 138, 569–576. https://doi.org/10.1061/(ASCE)IR.1943-4774.0000437

Carvalho, R.F., Leandro, J., David, L.M., Martins, R., Melo, N., 2011. Numerical Research of the Inflow Into Different Gullies Outlets. CCWI, Urban Water Manag. Chall. Oppor. Exet. Sept. 2011 2–7.

Carvalho, R.F., Lemos, C.M., Ramos, C.M., 2008. Numerical computation of the flow in hydraulic jump stilling basins. J. Hydraul. Res. 46, 739–752. https://doi.org/10.3826/jhr.2008.2726

Celik, I.B., Ghia, U., Roache, P.J., Freitas, C.J., Coleman, H., Raad, P.E., 2008. Procedure for Estimation and Reporting of Uncertainty Due to Discretization in CFD Applications. J. Fluids Eng. 130, 78001. https://doi.org/10.1115/1.2960953

Çengel, Y.A., Cimbala, J.M., 2006. Fluid Mechanics, 1st Editio. ed. McGraw-Hill, New York, USA.

Chanson, H., 2004. Hydraulics of Rectangular Dropshafts. J. Irrig. Drain. Eng. 130, 523–529. https://doi.org/10.1061/(ASCE)0733-9437(2004)130:6(523)

Chanson, H., Takeuchi, M., Trevethan, M., 2008. Using turbidity and acoustic backscatter intensity as surrogate measures of suspended sediment concentration in a small subtropical estuary. J. Environ. Manage. 88, 1406–1416. https://doi.org/10.1016/j.jenvman.2007.07.009

Chebbo, G., 1992. Solides des rejets pluviaux urbains - Caractérisation et traitabilité (Solids of urban storm discharges - characterization and treatability). PhD Thesis, (in French). Ecole Nationale des Ponts et Chaussées, Paris, France.

Chen, A., Leandro, J., Djordjevic, S., 2015. Modelling sewer discharge via displacement of manhole covers during flood events using 1D/2D SIPSON/P-DWave dual drainage simulations. Urban Water J. In Press. https://doi.org/10.1080/1573062X.2015.1041991

Cheng, Z., Hsu, T., 2014. A turbulence-resolving eulerian two-phase model for sediment transport. Coastal Engineering Proceedings 1(34):74, 1–10. DOI: 10.9753/icce.v34.sediment.74

Chocat, B., Ashley, R., Marsalek, J., Matos, M.R., Rauch, W., Schilling, W., Urbonas, B., 2004. Urban Drainage - Out-of-sight-out-of-mind?, in: Brelot, E., Chocat, B., Desbordes, M. (Eds.), Novatech 2004. IWA Publishing, Lyon, France, pp. 1659–1690.

Chocat, B., Krebs, P., Marsalek, J., 2011. Urban drainage redefined: from stormwater removal to integrated management. Water Sci. Technol. 43, 61–68.

Chow, V. Te, Maidment, D.R., Mays, L.W., 1988. Applied Hydrlogy. McGraw-Hill Book Company.

Cloke, H.L., Pappenberger, F., 2009. Ensemble flood forecasting: A review. J. Hydrol. 375, 613–626. https://doi.org/10.1016/j.jhydrol.2009.06.005

Codo, M., Rico-Ramirez, M.A., 2018. Ensemble Radar-Based Rainfall Forecasts for Urban Hydrological Applications. Geosciences 8, 297. https://doi.org/10.3390/geosciences8080297

Cooper, P.F., 2007. Historical aspects of wastewater treatment, in: Lens, P., Zeeman, G., Lettinga, G. (Eds.), Decentralised Sanitation and Reuse: Concepts, Systems and Implementation. pp. 11–38.

Costabile, P., Macchione, F., 2015. Enhancing river model set-up for 2-D dynamic flood modelling. Environ. Model. Softw. 67, 89–107. https://doi.org/10.1016/j.envsoft.2015.01.009

Daly, B., 1969. A technique for including surface tension effects in hydrodynamic calculations. J. Comput. Phys. 4, 97–117. https://doi.org/http://dx.doi.org/10.1016/0021-9991(69)90042-4

Deardorff, J.W., 1970. A numerical study of three-dimensional turbulent channel flow at large Reynolds numbers. J. Fluid Mech. 41, 453–480. https://doi.org/10.1017/S0022112070000691

DeBar, R.B., 1974. Fundamentals of the KRAKEN code, Report: UCID-17366, Lawrence Livermore Lab. Livermore, USA.

Deletic, A., 1998. The first flush load of urban surface runoff. Water Res. 32, 2462–2470. https://doi.org/10.1016/S0043-1354(97)00470-3

Deletic, A., Ashley, R., Rest, D., 2000. Modelling Input of Fine Granular Sediment Into Drainage Systems Via Gully-Pots. Science (80-.). 34, 3836–3844. https://doi.org/10.1016/S0043-1354(00)00133-0

Deletic, A., Dotto, C.B.S., McCarthy, D.T., Kleidorfer, M., Freni, G., Mannina, G., Uhl, M., Henrichs, M., Fletcher, T.D., Rauch, W., Bertrand-Krajewski, J.L., Tait, S., 2012. Assessing uncertainties in urban drainage models. Phys. Chem. Earth 42–44, 3–10. https://doi.org/10.1016/j.pce.2011.04.007

Deltares, 2018. SOBEK: 1D/2D modelling suite for integral water solutions, Hydrodynamics, Rainfall Runoff and Real Time Control. Delft, The Netherlands. https://www.deltares.nl/en/software/sobek

Deubler, M., 2017. Der Shuffled-Complex-Evolution-Algorithmus (SCE-UA) - Anwendung für die Kalibrierung des Wasserhaushaltsmodells LARSIM am Beispiel des Einzugsgebiets Oberer Main (The Shuffled Complex Evolution Algorithm (SCE-UA) - Application for the calibration of the water balance model LARSIM using the example of the catchment area Upper Main).

Report (in German), Technische Universität München.

DHI, 2017. Mike zero: User Guide. Horsholm, Denmark. http://manuals.mikepoweredbydhi.help/2017/MIKE_Zero_General.htm

Djordjević, S., Prodanović, D., Maksimović, Č., Ivetić, M., Savić, D., Maksimović, C., Ivetić, M., Savić, D., 2005. SIPSON - Simulation of interaction between pipe flow and surface overland flow in networks. Wat. Sci. Tech. 52, 275–283. https://doi.org/http://wst.iwaponline.com/content/52/5/275

Djordjević, S., Prodanović, D., Walters, G.A., 2004. Simulation of transcritical flow in pipe/channel networks. J. Hydraul. Eng. 130, 1167–1178. https://doi.org/10.1061/(ASCE)0733-9429(2004)(130:12(1167)

Djordjević, S., Saul, A.J., Tabor, G.R., Blanksby, J., Galambos, I., Sabtu, N., Sailor, G., 2013. Experimental and numerical investigation of interactions between above and below ground drainage systems. Water Sci. Technol. 67, 535–542. https://doi.org/10.2166/wst.2012.570

Dotto, C.B.S., Deletic, A., Fletcher, T.D., 2008. Analysis of uncertainty in flow and water quality from a stormwater model, in: 11th International Conference on Urban Drainage, Edinburgh, Scotland, UK, 2008. Scotland, UK, pp. 1–10.

Dotto, C.B.S., Kleidorfer, M., Deletic, A., Rauch, W., Mccarthy, D.T., 2014. Impacts of measured data uncertainty on urban stormwater models. J. Hydrol. 508, 28–42. https://doi.org/10.1016/j.jhydrol.2013.10.025

Durand, R., 1953. Basic Relationships Of The Transportation Of Solids In Pipes — Experimental Research, in: Proceedings of the 5th IAHR Congress,. Minneapolis, Minnesota, pp. 89–103.

EEA, 2017. Climate change adaptation and disaster risk reduction in Europe. Enhancing coherence of the knowledge base, policies and practices, EEA Report No 15/2017. https://doi.org/10.2800/938195

EEA, 2010. Mapping the impacts of recent natural disasters and technological accidents in Europe - An overview of the last decade, Environmental issue report No 35. https://doi.org/10.2800/62638

Ellis, J.B., Harrop, D.O., 1984. Variations in solids loadings to roadside gully pots. Sci. Total Environ. 33, 203–211. https://doi.org/10.1016/0048-9697(84)90394-2

Ellis, J.H., McBean, E.A., Mulamoottil, G., 1982. Design of Dual Drainage Systems Using SWMM. J. Hydraul. Div. 108, 1222–1227.

Elsinga, G.E., Scarano, F., Wieneke, B., Van Oudheusden, B.W., 2006. Tomographic particle image velocimetry. Exp. Fluids 41, 933–947. https://doi.org/10.1007/s00348-006-0212-z

Freni, G., La Loggia, G., Notaro, V., 2010. Uncertainty in urban flood damage assessment due to urban drainage modelling and depth-damage curve estimation. Water Sci. Technol. 61, 2979–2993. https://doi.org/10.2166/wst.2010.177

Freni, G., Mannina, G., Viviani, G., 2008. Uncertainty in urban stormwater quality modelling: The effect of acceptability threshold in the GLUE methodology. Water Res. 42, 2061–2072. https://doi.org/10.1016/j.watres.2007.12.014

Furbo, E., Harju, J., Nilsson, H., 2009. Evaluation of turbulence models for prediction of flow separation at a smooth surface, Project Report - Uppsala Universitet. Uppsala.

Galambos, I., 2012. Improved Understanding of Performance of Local Controls Linking the above and below Ground Components of Urban Flood Flows. PhD Thesis. University of Exeter.

García, C.M., Cantero, M.I., Niño, Y., García, M.H., 2005. Turbulence Measurements with Acoustic Doppler Velocimeters. J. Hydraul. Eng. 1062–1073. https://doi.org/10.1061/?ASCE?0733-9429?2005?131:12?1062? CE

Gargano, R., Hager, W.H., 2002. Supercritical Flow across Sewer Manholes. J. Hydraul. Eng. 128, 660–667. https://doi.org/10.1061/?ASCE?0733-9429(2002)128:11(1014)

Ghoma, M.I., 2011. The Effect of Wall Jet Flow on Local Scour. PhD Thesis. University of Bradford.

Gisonni, C., Hager, W.H., 2002. Supercritical flow in the 90° junction manhole. Urban Water 4, 363–372. https://doi.org/10.1016/S1462-0758(02)00003-1

Gomez-Hernandez, J.J., Journal, A.G., 1993. Joint Sequential Simulation of MultiGaussian Fields, in: Soares, A. (Ed.), Quantitative Geology and Geostatistics Vol 5. Springer, Dordrecht, Netherlands, pp. 85–94. https://doi.org/10.1007/978-94-011-1739-5_8

Gómez, M., Russo, B., 2009. Hydraulic Efficiency of Continuous Transverse Grates for Paved Areas. J. Irrig. Drain. Eng. 135, 225–230. https://doi.org/10.1061/(ASCE)0733-9437(2009)135:2(225)

Goring, D.G., Nikora, V.I., 2002. Despiking Acoustic Doppler Velocimeter Data. J. Hydraul. Eng. 128, 117–126. https://doi.org/10.1061/(ASCE)0733-9429(2002)128:1(117)

Granata, F., de Marinis, G., Gargano, R., 2014. Flow-improving elements in circular drop manholes. J. Hydraul. Res. 1686, 1–9. https://doi.org/10.1080/00221686.2013.879745

Granata, F., Marinis, G. de, Gargano, R., Hager, W.H., 2011. Hydraulics of Circular Drop Manholes. J. Irrig. Drain. Eng. 137–2, 537–552. https://doi.org/10.1061/(ASCE)IR.1943-4774.0000327

Greenshields, C.J., 2017. OpenFOAM User Guide v5.0.

Greenshields, C.J., 2015. OpenFOAM User Guide v2.4.

Grottker, M., 1990. Pollutant removal by gully pots in different catchment areas. Sci. Total Environ. 6, 515–522.

Guymer, I., Dennis, P., O'Brien, R., Saiyudthong, C., 2005. Diameter and Surcharge Effects on Solute Transport across Surcharged Manholes. J. Hydraul. Eng. 131, 312–321. https://doi.org/10.1061/(asce)0733-9429(2005)131:4(312)

Guymer, I., O'Brien, R., 2000. Longitudinal dispersion due to surcharged manhole. J. Hydraul. Eng. 126, 137–149. https://doi.org/10.1061/(ASCE)0733-9429(2000)126:2(137)

Haag, I.M., A, J., M, S., Bremicker, 2016. Guideline for the Calibration of LARSIM Water Balance Models for operational Application in Flood Forecasting; LARSIM-Entwicklergemeinschaft - Hochwasserzentralen. LUBW, BLfU, LfU RP, HLNUG, BAFU.

Hager, W.H., Gisonni, C., 2005. Supercritical flow in manholes, in: I CONVEGNO NAZIONALE DI IDRAULICA URBANA. ACQUA E CITTÀ, Sant'Agnello, pp. 1–15.

Härder, M., 2017. Sensitivitätsanalyse des Wasserhaushaltsmodells LARSIM für das Einzugsgebiet des Oberen Mains (Sensitivity analysis of the water balance model LARSIM for the catchment area of the Upper Main). Report by Technische Universität München (in German).

Hare, C., 1981. Magnitude of Hydraulic Losses at Junctions in Piped Drainage Systems, in: Conference on Hydraulics in Civil Engineering. ACT: Institution of Engineers, Australia, Sydney, N.S.W., pp. 54–59.

Harlow, Welch, J.E., 1965. Numerical Calculation of Time-Dependent Viscous Incompressible Flow of Fluid with Free Surface. Phys. Fluids 8(12), 2182–2189..

Hellsten, A., 1998. Some Improvements in Menter's k-omega-SST turbulence model, in: 29th AIAA Fluid Dynamics Conference. Albuquerque, New Mexico, U.S.A., pp. 1–11.

Herpin, S., Wong, C.Y., Stanislas, M., Soria, J., 2008. Stereoscopic PIV measurements of a turbulent boundary layer with a large spatial dynamic range. Exp. Fluids 45, 745–763. https://doi.org/10.1007/s00348-008-0533-1

Hickin, E.J., 1995. River geomorphology, in: River Geomorphology. p. 255. https://doi.org/10.1023/A:1006813004972

Hirt, C.W., Nichols, B.D., 1981. Volume of fluid (VOF) method for the dynamics of free boundaries. J. Comput. Phys. 39, 201–225. https://doi.org/10.1016/0021-9991(81)90145-5

Hirt, C.W., Sicilian, J.M., 1985. A porosity technique for the definition of obstacles in rectangular cell meshes, in: 4th International Conference on Numerical Ship Hydrodynamics. Washington, DC, p. 19.

Holzmann, T., 2016. Mathematics, Numerics, Derivations and OpenFOAM. https://doi.org/10.13140/RG.2.2.27193.36960

Howarth, D.A., 1985. The hydraulic performance of scale model storm sewer junctions. PhD Thesis. University of Manchester.

Howarth, D.A., Saul, A.J., 1984. Energy loss coefficients at manholes, in: Balmer, P., Malmquist, P.-A., Sjöberg, A. (Eds.), Proceedings of the Third International Conference on Urban Storm Drainage, Göteborg, Sweden, June 4-8, 1984: Planning and Control of Urban Storm Drainage. Chalmers University of Technology, Göteborg, Sweden, pp. 127–136.

Hu, H., 2013. Stereo Particle Imaging Velocimetry Techniques: Technical Basis, System Setup, and Application, in: Zhang, S. (Ed.), Handbook of 3D MAchine Vision: Optical Metrology and Imaging. Taylor and Francis Group, Boka Raton, FL, pp. 71–100.

Huang, H., Dabiri, D., Gharib, M., 1997. On errors of digital particle image velocimetry. Meas. Sci. Technol. Meas. Sci. Technol 8, 1427–1440. https://doi.org/10.1088/0957-0233/8/12/007

Hyman, J.M., 1984. Numerical methods for tracking interfaces. Phys. D Nonlinear Phenom. 12(1-3), 396–407. https://doi.org/10.1016/0167-2789(84)90544-X

Isenmann, G., Bellahcen, S., Vazquez, J., Dufresne, M., Joannis, C., Mose, R., 2016. Stage–discharge

relationship for a pipe overflow structure in both free and submerged flow. Eng. Appl. Comput. Fluid Mech. 10, 283–295. https://doi.org/10.1080/19942060.2016.1157100

Issa, R.I., 1985. Solution of the implicitly discretised fluid flow equations by operator-splitting. J. Comput. Phys. 62, 40–65. https://doi.org/10.1016/0021-9991(86)90099-9

Jarman, D.S., Faram, M.G., Butler, D., Tabor, G., Stovin, V.R., Burt, D., Throp, E., 2008. Computational fluid dynamics as a tool for urban drainage system analysis : A review of applications and best practice, in: 11th International Conference on Urban Drainage. Edinburgh, Scotland, pp. 1–10.

Jasak, H., 1996. Error Analysis and Estimation for the Finite Volume Method with Applications to Fluid Flows. PhD Thesis. Imp. Coll. Sci. Technol. Med. University of London, London.

Johnson, M.C., 2000. Discharge coefficient analysis for flat-topped and sharp-crested weirs. Irrig. Sci. 19, 133–137. https://doi.org/10.1007/s002719900009

Joseph, J.F., Guillaume, J.H.A., 2013. Using a parallelized MCMC algorithm in R to identify appropriate likelihood functions for SWAT. Environ. Model. Softw. 46, 292–298. https://doi.org/10.1016/j.envsoft.2013.03.012

Juretić, F., 2015. cfMesh User Guide (v1.1). Zagreb, Croatia.

Kauffeldt, A., Wetterhall, F., Pappenberger, F., Salamon, P., Thielen, J., 2016. Technical review of large-scale hydrological models for implementation in operational flood forecasting schemes on continental level. Environ. Model. Softw. 75, 68–76. https://doi.org/10.1016/j.envsoft.2015.09.009

Kim, J.-S., Song, J.-I., Jang, S.-J., Yoon, S.-E., 2008. An Experimental Study for Estimation of Head Loss Coefficients at Surcharged Circular Manhole. J. Korea Water Resour. Assoc. 41, 305–314. https://doi.org/10.3741/JKWRA.2008.41.3.305

Kolmogorov, A.N., 1941. The Local Structure of Turbulence in Incompressible Viscous Fluid for Very Large Reynolds Numbers, in: Proceedings of the USSR Academy of Sciences (in Russian). pp. 299–303.

König, A., Sægrov, S., Schilling, W., 2002. Damage assessment for urban flooding, in: 9th International Conference on Urban Drainage. 9th International Conference on Urban Drainage, September 2002, Portland, Oregon USA.

Korving, H., 2004. Probabalistic assessment of the performance of combined sewer systems. PhD Thesis. Technical University of Delft.

Kulick, J.D., Fessler, J.R., Eaton, J.K., 1994. Particle response and turbulenc modification in fully developed channel flow. J. Fluid Mech. 277, 109–134.

Larrarte, F., Chanson, H., 2008. Challenges in Sewer Hydrodynamics , Sediments and measurements, in: Larrarte, F., Chanson, H. (Eds.), International Meeting on Measurements and Hydraulics of Sewers, 2008. pp. 1–10.

Lau, S.-T.D., Stovin, V.R., Guymer, I., 2008. Scaling the solute transport characteristics of a surcharged manhole. Urban Water J. 5, 33–42. https://doi.org/10.1080/15730620701737249

Lau, S.D., 2008. Scaling Dispersion Processes in Surcharged Manholes. PhD Thesis. University of Sheffield, Sheffield, UK.

Lau, S.D., Stovin, V.R., Guymer, I., 2007. The prediction of solute transport in surcharged manholes using CFD. Water Sci. Technol. 55, 57–64. https://doi.org/10.2166/wst.2007.095

Launder, B.E., Reece, G.J., Rodi, W., 1975. Progress in the development of a Reynolds-stress turbulence closure. J. Fluid Mech. 68, 537–566. https://doi.org/10.1017/S0022112075001814

Laurent, S., Hangen-Brodersen, C., Ehret, U., Meyer, I., Moritz, K., Vogelbacher, A., Holle, F.-K., 2010. Forecast Uncertainties in the Operational Flood Forecasting of the Bavarian Danube Catchment, in: Hydrological Processes of the Danube River Basin. Springer Netherlands, Dordrecht, pp. 367–387. https://doi.org/10.1007/978-90-481-3423-6_12

Leandro, J., Abreu, J., de Lima, J.L.M.P., 2009a. Laboratory set-up to validate a dual drainage concept numerical model, in: 8th International Conference on Urban Drainage Modelling. Tokyo, Japan, pp. 1–7.

Leandro, J., Bung, D.B., Carvalho, R., 2014a. Measuring void fraction and velocity fields of a stepped spillway for skimming flow using non-intrusive methods. Exp. Fluids 55, 1–17. https://doi.org/10.1007/s00348-014-1732-6

Leandro, J., Chen, A.S., Djordjević, S., Savić, D.A., 2009b. Comparison of 1D/1D and 1D/2D Coupled (Sewer/Surface) Hydraulic Models for Urban Flood Simulation. J. Hydraul. Eng. 135, 495–504. https://doi.org/10.1061/(ASCE)HY.1943-7900.0000037

Leandro, J., Chen, A.S., Schumann, A., 2014b. A 2D parallel diffusive wave model for floodplain inundation with variable time step (P-DWave). J. Hydrol. 517, 250–259. https://doi.org/10.1016/j.jhydrol.2014.05.020

Leandro, J., Leitão, J.P., de Lima, J.L.M.P., 2013. Quantifying the uncertainty in the Soil Conservation Service flood hydrographs: a case study in the Azores Islands. J. Flood Risk Manag. 6, 279–288.

Leandro, J., Lopes, P., Carvalho, R., Páscoa, P., Martins, R., Romagnoli, M., 2014c. Numerical and experimental characterization of the 2D vertical average-velocity plane at the center-profile and qualitative air entrainment inside a gully for drainage and reverse flow. Comput. Fluids 102, 52–61. https://doi.org/10.1016/j.compfluid.2014.05.032

Leandro, J., Martins, R., 2016. A methodology for linking 2D overland flow models with the sewer network model SWMM 5.1 based on dynamic link libraries. Water Sci. Technol. 73, 1–11. https://doi.org/10.2166/wst.2016.171

Leandro, J., Martins, R., 2016. A methodology for linking 2D overland flow models with the sewer network model SWMM 5.1 based on dynamic link libraries. Water Sci. Technol. 73, 3017–3026. https://doi.org/10.2166/wst.2016.171

Leandro, J., Schumann, A., Pfister, A., 2016. A step towards considering the spatial heterogeneity of urban key features in urban hydrology flood modelling. J. Hydrol. 535, 356–365. https://doi.org/10.1016/j.jhydrol.2016.01.060

Li, W.-H., Goodell, B.C., Geyer, J.C., 1954. Hydraulic Behavior of Storm-Water Inlets: IV. Flow into

Depressed Combination Inlets, Sewage and Industrial Wastes. Water Environment Federation, 26, 8, 967-975..

Liguori, S., Rico-Ramirez, M.A., Schellart, A.N.A., Saul, A.J., 2012. Using probabilistic radar rainfall nowcasts and NWP forecasts for flow prediction in urban catchments. Rainfall Urban Context Forecast. Risk Clim. Chang. 103, 80–95. https://doi.org/10.1016/j.atmosres.2011.05.004

Lindval, G., 1984. Head losses at surcharged manholes with a main pipe and a 90° lateral, in: Balmer, P., Malmquist, P.-A., Sjöberg, A. (Eds.), Proceedings of the Third International Conference on Urban Storm Drainage, Göteborg, Sweden, June 4-8, 1984: Planning and Control of Urban Storm Drainage. Chalmers University of Technology, Göteborg, Sweden, pp. 137–146.

Lindvall, G., 1986. Energiförluster i ledningsbrunnar - Laboratorie Mätninger (Energy losses in pipelines - Laboratory Measurements) Geo Hydrologiska forsknings gruppen 81 (in Swedish). Göteborg, Sweden.

Lopes, P., Leandro, J., Carvalho, R.F., 2018. Numerical procedure for free-surface detection using a Volume-of-Fluid model. J. Hydro-Environment Res. 21, 43–51. https://doi.org/10.1016/j.jher.2018.07.002

Lopes, P., Leandro, J., Carvalho, R.F., Páscoa, P., Martins, R., 2015. Numerical and experimental investigation of a gully under surcharge conditions. Urban Water J. 12, 468–476. https://doi.org/10.1080/1573062X.2013.831916

Lopes, P., Leandro, J., Carvalho, R.F., Russo, B., Gómez, M., 2016a. Assessment of a VOF Model Ability to Reproduce the Efficiency of a Continuous Transverse Gully with Grate. J. Irrig. Drain. Eng. (in production). https://doi.org/10.1061/(ASCE)IR.1943-4774.0001058

Lopes, P., Shucksmith, J., Leandro, J., Carvalho, R.F. de, Rubinato, M., 2014. Velocities Profiles and Air-entrainment Characterisation in a Scaled Circular Manhole, in: Urban Drainage in the Context of Integrated Urban Water Management: A Bridge Between Developed and Developing Countries. 13th International Conference on Urban Drainage, Sarawak, Malaysia, pp. 7–12.

Lopes, P., Tabor, G., Carvalho, R.F., Leandro, J., 2016b. Explicit calculation of natural aeration using a Volume-of-Fluid model. Appl. Math. Model. (in production). https://doi.org/10.1016/j.apm.2016.03.033

Lorenz, E.N., 1969. The predictability of a flow which possesses many scales of motion. Tellus 21, 289–307. https://doi.org/10.3402/tellusa.v21i3.10086

Ly, S., Charles, C., Degré, A., 2013. Different methods for spatial interpolation of rainfall data for operational hydrology and hydrological modeling at watershed scale: a review. Base 17, 392–406.

Madsen, H., Skotner, C., 2005. Adaptive state updating in real-time river flow forecasting - A combined filtering and error forecasting procedure. J. Hydrol. 308, 302–312. https://doi.org/10.1016/j.jhydrol.2004.10.030

Mair, A., Fares, A., 2011. Comparison of Rainfall Interpolation Methods in a Mountainous Region of a Tropical Island. J. Hydrol. Eng. 16, 371–383. https://doi.org/10.1061/(ASCE)HE.1943-5584.0000330

Mark, O., Cerar, U., Perrusquía, G.S., 1996. Prediction of locations with sediment deposits in sewers. Water Sci. Technol. 33, 147–154. https://doi.org/10.1016/0273-1223(96)00381-2

Mark, O., Ilesanmi-jimoh, M., 2016. An analytical model for solute mixing in surcharged manholes. Urban Water J. 9006, 1–9. https://doi.org/10.1080/1573062X.2016.1179335

Mark, O., Weesakul, S., Apirumanekul, C., Aroonnet, S.B., Djordjevic, S., 2004. Potential and limitations of 1D modelling of urban flooding. J. Hydrol. 299, 284–299. https://doi.org/10.1016/j.jhydrol.2004.08.014

Marsalek, J., 1984. Head Losses at Sewer Junction Manholes. J. Hydraul. Eng. 110, 1150–1154. https://doi.org/10.1061/(ASCE)0733-9429(1984)110:8(1150)

Marsalek, J., 1981. Energy losses at straight-flow-through sewer junctions, Research Report No. 111. Ontario, Canada.

Marsalek, J., Greck, B.J., 1988. Head losses at manholes with a 90° bend. Can. J. Civ. Eng. 15, 851–858. https://doi.org/10.1139/l88-110

Martínez-Suástegui, L., 2012. Overview on Stereoscopic Particle Image Velocimetry, in: Jones, P.S. (Ed.), Advanced Methods for Practical Applications in Fluid Mechanics. InTech, pp. 3–20.

Martins, R., Leandro, J., Carvalho, R.F., 2014. Characterization of the hydraulic performance of a gully under drainage conditions. Water Sci. Technol. 69, 2423–30. https://doi.org/10.2166/wst.2014.168

Martins, R., Leandro, J., Chen, A.S., Djordjević, S., 2017. A comparison of three dual drainage models: shallow water vs local inertial vs diffusive wave. J. Hydroinformatics 19, 331–348. https://doi.org/10.2166/hydro.2017.075

Martins, R., Leandro, J., Djordjević, S., 2016. Influence of sewer network models on urban flood damage assessment based on coupled 1D/2D models. J. Flood Risk Manag. In Press, In Press. https://doi.org/10.1111/jfr3.12244

Marzban, C., 2004. The ROC Curve and the Area under It as Performance Measures. Weather Forecast. 19, 1106–1114. https://doi.org/10.1175/825.1

Mason, S.J., Graham, N.E., 2002. Areas beneath the relative operating characteristics (ROC) and relative operating levels (ROL) curves: Statistical significance and interpretation. Q. J. R. Meteorol. Soc. 128, 2145–2166. https://doi.org/10.1256/003590002320603584

May, R.W.P., 1993. Sediment transport in pipes and sewers with deposited beds. Oxfordshire, UK.

McLelland, S.J., Nicholas, A.P., 2000. A new method for evaluating errors in high-frequency ADV measurements. Hydrol. Process. 14, 351–366. https://doi.org/10.1002/(SICI)1099-1085(20000215)14:2<351::AID-HYP963>3.0.CO;2-K

Meierdiercks, K.L., Smith, J.A., Baeck, M.L., Miller, A.J., 2010. Analyses of Urban Drainage Network Structure and Its Impact on Hydrologic Response. J. Am. Water Resour. Assoc. 46, 932–943. https://doi.org/10.1111⁄ j.1752-1688.2010.00465.x INTRODUCTION

Memon, F.A., Butler, D., 2002a. Identification and modelling of dry weather processes in gully pots. Water Res. 36, 1351–1359. https://doi.org/10.1016/S0043-1354(01)00342-6

Memon, F.A., Butler, D., 2002b. Assessment of gully pot management strategies for runoff quality control using a dynamic model. Sci. Total Environ. 295, 115–129. https://doi.org/10.1016/S0048-9697(02)00056-6

Menter, F., Esch, T., 2001. Elements of Industrial heat transfer, in: 16th Brasilian Congress of Mechanical Engineering (COBEM). COBEM 2001, Uberlândia, Brasil, pp. 117–127.

Menter, F.R., Kuntz, M., Langtry, R., 2003. Ten Years of Industrial Experience with the SST Turbulence Model, in: Hanjalic, K., Y.Nagano, M.Tummers (Eds.), Turbulence Heat and Mass Transfer 4. Begell House, Inc., Antalya, Turkey, pp. 625–632.

Moin, P., Mahesh, K., 1998. Direct numerical simulation: A tool in turbulence research. Annu. Rev. Fluid Mech. 30, 539–578. https://doi.org/10.1146/annurev.fluid.30.1.539

Morrison, G.M., Revitt, D.M., Ellis, J.B., 1995. The gully pot as a biochemical reactor. Water Sci. Technol. 31, 229–236. https://doi.org/10.1016/0273-1223(95)00340-S

Mrowiec, M., 2007. Head loss at two-way circular manholes in drainage systems under surcharge conditions. Environ. Prot. Eng. 33, 183–191.

Mullen, S.L., Buizza, R., 2001. Quantitative precipitation forecasts over the United States by the ECMWF Ensemble Prediction System. Mon. Weather Rev. 129, 638–663. https://doi.org/Doi 10.1175/1520-0493(2001)129<0638:Qpfotu>2.0.Co;2

Murphy, A.H., Winkler, R.L., 1987. A General Framework for Forecast Verification. Mon. Weather Rev. https://doi.org/10.1175/1520-0493(1987)115<1330:AGFFFV>2.0.CO;2

Muthusamy, M., Schellart, A., Tait, S., Heuvelink, G.B.M., 2017. Geostatistical upscaling of rain gauge data to support uncertainty analysis of lumped urban hydrological models. Hydrol. Earth Syst. Sci. 21, 1077–1091. https://doi.org/10.5194/hess-21-1077-2017

Nalluri, C., Alvarez, E.M., 1992. The Influence of Cohesion on Sediment Behaviour. Water Sci. Technol. 25, 151–164.

Nanía, L.S., Leon, A.S., García, M.H., 2014. Hydrologic-Hydraulic Model for Simulating Dual Drainage and Flooding in Urban Areas : Application to a Catchment in the Metropolitan Area of Chicago. J. Hydrol. Eng. 20, 1–13. https://doi.org/10.1061/(ASCE)HE.1943-5584.0001080,04014071

Nichols, B.D., Hirt, C.W., 1973. Calculating three-dimensional free surface flows in the vicinity of submerged and exposed structures. J. Comput. Phys. 12, 234–246. https://doi.org/10.1016/S0021-9991(73)80013-0

Nikora, V., Goring, D., 2000. Flow turbulence over fixed and weakly mobile beds. J. Hydraul. Eng. 126, 42–47.

Nikora, V., Goring, D., McEwan, I., Griffith, G., 2001. Spatially Averaged Open-Channel Flow over Rough Bed. J. Hydraul. Eng. 127, 123–133.

Nobach, H., Damaschke, N., Tropea, C., 2004. High-precision sub-pixel interpolation in PIV / PTV image processing, in: 12th Int. Symp. on Appl. of Laser Techn. to Fluid Mechanics. Lisbon, Portugal.

Nobach, H., Honkanen, M., 2005. Two-dimensional Gaussian regression for sub-pixel displacement estimation in particle image velocimetry or particle position estimation in particle tracking velocimetry. Exp. Fluids 38, 511–515. https://doi.org/10.1007/s00348-005-0942-3

Noh, S.J., Lee, S., An, H., Kawaike, K., Nakagawa, H., 2016. Ensemble urban flood simulation in comparison with laboratory-scale experiments: Impact of interaction models for manhole, sewer pipe, and surface flow. Adv. Water Resour. 97, 25–37. https://doi.org/10.1016/j.advwatres.2016.08.015

Noh, W.F., Woodward, P.R., 1976. SLIC (Simple Line Interface Calculation) method, in: Vooren, P.D.A.I. van de, Zandbergen, P.D.P.J. (Eds.), Proceedings of the Fifth International Conference on Numerical Methods in Fluid Dynamics June 28 – July 2, 1976 Twente University, Enschede. Springer, Berlin, pp. 330–340. https://doi.org/10.1007/3-540-08004-X_336

Nortek, 2013. Nortek Vectrino II Product Datasheet. Vollen, Norway.

O'Loughlin, G., Stack, B., 2002. Algorithms for Pit Pressure Changes and Head Losses in Stormwater Drainage Systems, in: Global Solutions for Urban Drainage, Proceeding of 9th ICUD. Portland, Oregon USA, pp. 1–16. https://doi.org/10.1061/40644(2002)297

Osborne, M., Butler, D., Clarke, P., Memon, F., 1998. Management of gully pots for improved runoff quality. CIRIA report. London.

Osher, S., Sethian, J.A., 1988. Fronts Propagating with Curvature Dependent Speed, NASA Contractor Report 178382 ICASE REPORT NO. 87-66. Rampton, Virginia. https://doi.org/10.1007/s13398-014-0173-7.2

Palmer, M., 2002. Experimental Techniques in Fluids [WWW Document]. Massachusetts Inst. Technol. URL http://web.mit.edu/fluids-modules/www/exper_techniques/ (accessed 8.19.16).

Pang, X., O'Loughlin, G., 2011. Pressure Changes at Stormwater Pits with Part-Full Flows, in: 12nd International Conference on Urban Drainage. Porto Alegre, Brazil, pp. 1–8.

Patankar, S. V., Spalding, D.B., 1972. A calculation procedure for heat, mass and momentum transfer in three-dimensional parabolic flows. Int. J. Heat Mass Transf. 15, 1787–1806. https://doi.org/10.1016/0017-9310(72)90054-3

Pebesma, E.J., 2004. Multivariable geostatistics in S: The gstat package. Comput. Geosci. 30, 683–691. https://doi.org/10.1016/j.cageo.2004.03.012

Pfister, M., Gisonni, C., 2014. Head Losses in Junction Manholes for Free Surface Flows in Circular Conduits. J. Hydraul. Eng. 140, 060140151–060140156. https://doi.org/10.1061/(ASCE)HY.1943-7900.0000895

Pitt, R., 2004. Sediment Transport in Storm Drainage Systems. Sediment transport course Material, University of Alambama. pp. 1–26.

Pope, S.B., 2000. Turbulent Flows, 1st ed, Cambridge. Cambridge University Press, Cambridge.

Prasad, A.K., Adrian, R.J., 1993. Stereoscopic particle image velocimetry applied to liquid flows. Exp. Fluids 15, 49–60. https://doi.org/10.1007/BF00195595

Prasad, A.K., Jensen, K., 1995. Scheimpflug stereocamera for particle image velocimetry in liquid flows. Appl. Opt. 34, 7092–7099. https://doi.org/10.1364/AO.34.007092

Pratt, C.J., Elliott, G.E.P., Fulcher, G.A., 1987. Suspended solids discharge from highway gully pots in a residential catchment. Sci. Total Environ. 59, 355–364. https://doi.org/10.1016/0048-9697(87)90459-1

Quaresma, A.L., Ferreira, R.M.L., Pinheiro, A.N., 2017. Comparative analysis of particle image velocimetry and acoustic Doppler velocimetry in relation to a pool-type fishway flow. J. Hydraul. Res. 1686, 1–10. https://doi.org/10.1080/00221686.2016.1275051

Raffel, M., Willert, C.E., Wereley, S.T., Kompenhans, J., 2007. Particle Image Velocimetry: A Practical Guide, 2nd ed. Springer International Publishing, Berlin, Germany.

Ramamurthy, A.S., Zhu, W., 1997. Combining Flows in 90 degree Junctions of Rectangular Closed Conduits. J. Hydraul. Eng. 123, 1012–1019.

Refsgaard, J.C., Henriksen, H.J., Harrar, W.G., Scholten, H., Kassahun, A., 2005. Quality assurance in model based water management - Review of existing practice and outline of new approaches. Environ. Model. Softw. 20, 1201–1215. https://doi.org/10.1016/j.envsoft.2004.07.006

Refsgaard, J.C., van der Sluijs, J.P., Højberg, A.L., Vanrolleghem, P.A., 2007. Uncertainty in the environmental modelling process - A framework and guidance. Environ. Model. Softw. 22, 1543–1556. https://doi.org/10.1016/j.envsoft.2007.02.004

Regimbeau, F.R., Habets, F., Martin, E., Noilhan, J., 2007. Ensemble Streamflow forecasts over France. ECMWF Newsl. No. 111 111, 21–27. https://doi.org/10.21957/sbjdm2xu33

Roberts, A.H., Ellis, J.B., Whalley, W.B., 1988. The progressive alteration of fine sediment along an urban storm drain. Water Res. 22, 775–781. https://doi.org/10.1016/0043-1354(88)90190-X

Romagnoli, M., Carvalho, R.F., Leandro, J., 2013. Turbulence characterization in a gully with reverse flow. J. Hydraul. Eng. 139, 736–744. https://doi.org/10.1061/(ASCE)HY.1943-7900.0000737

Rossman, L.A., Huber, W.C., 2016. Storm Water Management Model Reference Manual Volume I – Hydrology, U.S. Environmental Protection Agency. Cincinnati, OH.

Roulin, E., 2006. Skill and relative economic value of medium-range hydrological ensemble predictions To cite this version : HAL Id : hal-00298726 Skill and relative economic value of medium-range hydrological ensemble predictions.

Rubinato, M., 2015. Physical scale modelling of urban flood systems. PhD Thesis. University of Sheffield.

Rubinato, M., Martins, R., Kesserwani, G., Leandro, J., Djordjević, S., Shucksmith, J., 2017. Experimental calibration and validation of sewer/surface flow exchange equations in steady and unsteady flow conditions. J. Hydrol. 552, 421–432. https://doi.org/10.1016/j.jhydrol.2017.06.024

Rubinato, M., Martins, R., Shucksmith, J.D., 2018. Quantification of energy losses at a surcharging

manhole. Urban Water J. 9006, 1–8. https://doi.org/10.1080/1573062X.2018.1424217

Rubinato, M., Shucksmith, J., Saul, A.J., Shepherd, W., 2013. Comparison between InfoWorks hydraulic results and a physical model of an Urban drainage system. Water Sci. Technol. 68, 372–379. https://doi.org/10.2166/wst.2013.254

Rusche, H., 2002. Computational Fluid Dynamics of Dispersed Two-Phase Flows at High Phase Fractions. PhD Thesis. University of London. https://doi.org/10.1145/1806799.1806850

Saiyudthong, C., Guymer, I., 2005. Simulation os Energy Loss Due To Changes in Pipe Direction Across a Manhole, in: 10th National Convention on Civil Engineering. pp. 5–9.

Sangster, W.M., Wood, H.W., Smerdon, E.T., Bossy, H.G., 1958. Pressure changes at storm drain junctions. Eng. Exp. Station. Univ. Missouri 41, 55.

Schalather, M., Malinowski, A., Menck, P.J., Oesting, M., Strokorb, K., 2015. Analysis, Simulation and Prediction of Multivariate Random Fields with Package RandomFields. J. Stat. Softw. 63, 1–25. https://doi.org/10.18637/jss.v063.i08

Schellart, A.N.A., 2007. Analysis of uncertainty in the sewer sediment transport predictions used for sewer management purposes. PhD Thesis. University of Sheffield. U.K.

Schellart, A.N.A., Tait, S.J., Ashley, R.M., 2010. Towards quantification of uncertainty in predicting water quality failures in integrated catchment model studies. Water Res. 44, 3893–3904. https://doi.org/10.1016/j.watres.2010.05.001

Scott, K.M., 2012. Investigating Sustainable Solutions for Roadside Gully Pot Management. PhD Thesis. University of Hull.

Seo, Y., Kim, S., Singh, V.P., 2014. Assessment of Uncertainty in the Spatial Distribution of Rainfall Using Geostochastic Simulation. J. Hydrol. Eng. 19, 978–992. https://doi.org/10.1061/(ASCE)HE.1943-5584.0000882

Seol, D.., Seo, J.., Rhee, S.., 2013. Towed underwater PIV measurement for free surface effects on turbulent wake of a surface-piercing body. Int. J. Nav. Arch. Ocean Eng. 5, 404–413. https://doi.org/10.2478/IJNAOE-2013-0142

Seong, C., Her, Y., Benham, B.L., 2015. Automatic Calibration Tool for Hydrologic Simulation Program-FORTRAN Using a Shuffled Complex Evolution Algorithm 503–527. https://doi.org/10.3390/w7020503

Shih, T.-H., Liou, W.W., Shabbir, A., Yang, Z., Zhu, J., 1995. A New k-e Eddy Viscosity Model for High Reynolds Number Turbulent Flows. Compurers Fluids 24, 227–238. https://doi.org/10.1016/0045-7930(94)00032-T

Skipworth, P.J., Tait, S.J., Saul, A.J., 1999. Erosion of Sediment Bed in Sewers: Model Development. J. Environ. Eng. 2, 566–573.

Smagorinsky, J., 1963. General Circulation Experiments With the Primitive Equations. Mon. Weather Rev. 91, 99–164. https://doi.org/10.1175/1520-0493(1963)091<0099:GCEWTP>2.3.CO;2

Sonnenwald, F.C., 2014. Identifying the residence time distributions of urban drainage structures

from solute transport data using maximum entropy deconvolution. PhD Thesis. The University of Sheffield.

Speziale, C.G., Thangam, S., 1992. Analysis of an RNG based Turbulence Model for Separated Flows. NASA Langley Research Center, Hampton, Virginia.

Stahre, P., Urbonas, B., 1990. Stormwater Detention: For Drainage, Water Quality, and CSO Management, 1st ed. Prentice Hall, Englewood Cliffs, New Jersey, USA.

Stein, S.M., Dou, X., Umbrell, E.R., Jones, J.S., 1999. Storm Sewer Junction Hydraulics and Sediment Transport, in: Wilson, E.M. (Ed.), WRPMD'99: Preparing for the 21st Century. American Society of Civil Engineers, Tempe, Arizona, United States, pp. 1–11. https://doi.org/10.1088/1751-8113/44/8/085201

Stovin, V., Lau, D., Guymer, I., Nawasara, J., Dunkley, P., Bryanston-cross, P., 2007. Insights into flow field interactions of surcharged manholes, in: 5th International Symposium on Environmental Hydraulics, 4-7 December. Tempe, Arizona, pp. 1–6.

Stovin, V.R., Bennett, P., Guymer, I., 2013. Absence of a Hydraulic Threshold in Small-Diameter Surcharged Manholes. J. Hydraul. Eng. 139, 984–994. https://doi.org/10.1061/(ASCE)HY.1943-7900 .0000758

Stovin, V.R., Guymer, I., Lau, S.-T.D., 2010. Dimensionless method to characterize the mixing effects of surcharged manholes. J. Hydraul. Eng. 136, 318–327. https://doi.org/10.1061/(ASCE)HY.1943-7900.0000183

Stovin, V.R., Guymer, I., Lau, S.D., 2008. Approaches to validating a 3D CFD manhole model. Proceeding of 11th Int. Conf. of Urban Drainage. 1–10.

Tang, H., Wrobel, L.C., 2005. Modelling the interfacial flow of two immiscible liquids in mixing processes. Int. J. Eng. Sci. 43, 1234–1256. https://doi.org/10.1016/j.ijengsci.2005.03.011

Taylor E.H., 1944. Flow characteristics at rectangular open channel junctions. Trans. ASCE 109, 893–912.

Thielen, J., Ramos, M.-H., Bartholmes, J.C., De Roo, A.P.J., Pappenberger, F., Cloke, H.L., Demeritt, D., 2005. 1St Workshop on the Use of Ensemble Prediction System in Flood Forecasting 15.

Todini, E., 2009. Predictive uncertainty assessment in real time flood forecasting: Part of NATO Science for Peace and Security Series, in: Baveye, P.C., Laba, M., Mysiak, J. (Eds.), Uncertainties in Environmental Modelling and Consequences for Policy Making. Springer Netherlands, Dordrecht, The Netherlands, pp. 205–228. https://doi.org/10.1007/978-90-481-2636-1

Ubbink, O., 1997. Numerical prediction of two fluid systems with sharp interfaces. Splash. https://doi.org/10.1145/1774088.1774119

Urban Drainage and Flood Control District (UDFCD), 1969. Urban stormwater design drainage criteria manuals: Volume 1, Management, Hydrology, and Hydraulics, Vol. 1. Denver, CO.

Van Doorne, C.W.H., Westerweel, J., 2007. Measurement of laminar, transitional and turbulent pipe flow using Stereoscopic-PIV. Exp. Fluids 42, 259–279. https://doi.org/10.1007/s00348-006-0235-5

Van Overbrüggen, T., Klaas, M., Soria, J., Schröder, W., 2016. Experimental analysis of particle sizes for PIV measurements. Meas. Sci. Technol. 27. https://doi.org/10.1088/0957-0233/27/9/094009

Vandenberghe, V., Bauwens, W., Vanrolleghem, P.A., 2007. Evaluation of uncertainty propagation into river water quality predictions to guide future monitoring campaigns. Environ. Model. Softw. 22, 725–732. https://doi.org/10.1016/j.envsoft.2005.12.019

Verbanck, M., 1990. Sewer sediment and its relation with the quality characteristics of combined sewer flows. Water Sci. Technol. 22, 247–257.

Versteeg, H.K., Malalasekera, W., 1995. An Introduction to Computational Fluid Dynamics - The Finite Volume Method, Fluid flow handbook. McGraw-Hill …. Longman Scientific and Technical, Essex, Eng.

Verwey, A., 2001. Latest Developments in Floodplain Modelling - 1D/2D Integration, in: Hobart, T. (Ed.), 6th Conference on Hydraulics in Civil Engineering: The State of Hydraulics. Institution of Engineers, Australia, Barton, pp. 13–24.

Virant, M., Dracos, T., 1997. 3D PTV and its application on Lagrangian motion. Meas. Sci. Technol. 8, 1539–1552. https://doi.org/10.1088/0957-0233/8/12/017

Vojinovic, Z., Tutulic, D., 2009. On the use of 1D and coupled 1D-2D modelling approaches for assessment of flood damage in urban areas. Urban Water J. 6, 183–199. https://doi.org/10.1080/15730620802566877

Voulgaris, G., Trowbridge, J.H., 1998. Evaluation of the Acoustic Doppler Velocimeter (ADV) for Turbulence Measurements*. J. Atmos. Ocean. Technol. 15, 272–289. https://doi.org/10.1175/1520-0426(1998)015<0272:EOTADV>2.0.CO;2

Wang, K.H., Cleveland, T.G., Towsley, C., Umrigar, D., 1998. Head Loss at Manholes in Surcharged Sewer Systems. J. Am. Water Resour. Assoc. 34, 1391–1400. https://doi.org/10.1111/j.1752-1688.1998.tb05439.x

Wani, O., Beckers, J.V.L., Weerts, A.H., Solomatine, D.P., 2017. Residual uncertainty estimation using instance-based learning with applications to hydrologic forecasting. Hydrol. Earth Syst. Sci. 21, 4021–4036. https://doi.org/10.5194/hess-21-4021-2017

Weller, H.G., 2002. Derivation modelling and solution of the conditionally averaged two-phase flow equations, Technical Report TR/HGW/02, Nabla Ltd.

Weller, H.G., Tabor, G., Jasak, H., Fureby, C., 1998. A tensorial approach to computational continuum mechanics using object-oriented techniques. Comput. Phys. 12, 620. https://doi.org/10.1063/1.168744

Wetterhall, F., Pappenberger, F., Alfieri, L., Cloke, H.L., Thielen-Del Pozo, J., Balabanova, S., Daňhelka, J., Vogelbacher, A., Salamon, P., Carrasco, I., Cabrera-Tordera, A.J., Corzo-Toscano, M., Garcia-Padilla, M., Garcia-Sanchez, R.J., Ardilouze, C., Jurela, S., Terek, B., Csik, A., Casey, J., Stankunavičius, G., Ceres, V., Sprokkereef, E., Stam, J., Anghel, E., Vladikovic, D., Alionte Eklund, C., Hjerdt, N., Djerv, H., Holmberg, F., Nilsson, J., Nyström, K., Sušnik, M., Hazlinger, M., Holubecka, M., 2013. HESS Opinions “forecaster priorities for improving probabilistic flood forecasts.” Hydrol. Earth Syst. Sci. 17, 4389–4399. https://doi.org/10.5194/hess-17-4389-2013

Willems, P., 2013. Revision of urban drainage design rules after assessment of climate change impacts on precipitation extremes at Uccle, Belgium. J. Hydrol. 496, 166–177. https://doi.org/10.1016/j.jhydrol.2013.05.037

Willems, P., Arnbjerg-Nielsen, K., Olsson, J., Nguyen, V.T. V, 2012. Climate change impact assessment on urban rainfall extremes and urban drainage: Methods and shortcomings. Atmos. Res. 103, 106–118. https://doi.org/10.1016/j.atmosres.2011.04.003

Willert, C.E., 2006. Assessment of camera models for use in planar velocimetry calibration. Exp. Fluids 41, 135–143. https://doi.org/10.1007/s00348-006-0165-2

Wilson, B.M., Smith, B.L., 2013. Uncertainty on PIV mean and fluctuating velocity due to bias and random errors. Meas. Sci. Technol. 24. https://doi.org/10.1088/0957-0233/24/3/035302

Wynne, B., 1992. Uncertainty and Environmental Learning - Reconceiving Science and Policy in the Preventive Paradigm. Glob. Environ. Chang. Policy Dimens. 2, 111–127.

Yakhot, V., Orszag, S.A., Thangam, S., Gatski, T.B., Speziale, C.G., 1992. Development of turbulence models for shear flows by a double expansion technique. Phys. Fluids 4, 1510–1520. https://doi.org/10.1063/1.858424

Yevjevich, V., Barnes, A.H., 1970. Flood Routing Through Storm Drains Part IV Numerical Computer Methods of Solution. Hydrol. Pap. 46 55.

Zhang, H., Casey, T., 2000. Verification of Categorical Probability Forecasts. Weather Forecast. 15, 80–89. https://doi.org/10.1175/1520-0434(2000)015<0080:VOCPF>2.0.CO;2

Zhang, J., Li, Y., Huang, G., Chen, X., Bao, A., 2016. Assessment of parameter uncertainty in hydrological model using a Markov-Chain-Monte-Carlo-based multilevel-factorial-analysis method. J. Hydrol. 538, 471–486. https://doi.org/10.1016/j.jhydrol.2016.04.044

Zhang, Z., Hugo, R.J., 2006. Stereo particle image velocimetry applied to a vortex pipe flow. Exp. Fluids 40, 333–346. https://doi.org/10.1007/s00348-005-0071-z

Zhao, C.-H., Zhu, D.Z., Rajaratnam, N., 2008. Computational and Experimental Study of Surcharged Flow at a 90° Combining Sewer Junction. J. Hydraul. Eng. 134, 688–700. https://doi.org/10.1061/(ASCE)0733-9429(2008)134:6(688)

Zhao, C.-H., Zhu, D.Z., Rajaratnam, N., 2006. Experimental Study of Surcharged Flow at Combining Sewer Junctions. J. Hydraul. Eng. 132, 1259–1271. https://doi.org/10.1061/(ASCE)0733-9429(2006)132:12(1259)

Zhao, C., Zhu, D.Z., Rajaratnam, N., 2004. Supercritical sewer flows at a combining junction: A model study of the Edworthy trunk junction, Calgary, Alberta. J. Environ. Eng. Sci 3, 343–353. https://doi.org/10.1139/S04-019